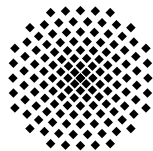


**Frequency-Domain Magnetic Resonance  
Spectroscopy**  
on  
**the  $Mn_{12}$  – acetate Single-Molecule Magnet**

Von der Fakultät Mathematik und Physik  
der Universität Stuttgart  
zur Erlangung der Würde eines  
Doktors der Naturwissenschaften (Dr. rer. nat.)  
genehmigte Abhandlung

Vorgelegt von  
**Suriyakan Vongtragool**  
geboren in Lampang

Hauptberichter: Prof. Dr. M. Dressel  
Mitberichter: Prof. Dr. W. Kaim  
Tag der mündlichen Prüfung: 28.10.2004



1. Physikalisches Institut  
Universität Stuttgart  
2004



# Contents

<b>List of Abbreviations</b>	<b>7</b>
<b>Abstract</b>	<b>9</b>
<b>Kurzfassung</b>	<b>11</b>
<b>1 Introduction to Molecular magnets</b>	<b>17</b>
1.1 An overview . . . . .	17
1.1.1 Magnetic anisotropy and spin Hamiltonian . . . . .	18
1.1.2 Double-well energy potential . . . . .	19
1.1.3 Theory of quantum tunneling and magnetic quantum tunneling	22
1.1.4 Experimental evidences for magnetic quantum tunneling . . . .	25
1.1.5 Magnetic relaxation . . . . .	27
1.1.6 Theoretical concepts of phonon-assisted spin tunneling . . . . .	27
1.2 Examples of the molecular magnets . . . . .	39
1.2.1 Mn <sub>12</sub> -acetate . . . . .	39
1.2.2 Other molecular magnets . . . . .	41
1.3 Molecular magnets in applications . . . . .	41
1.4 Motivation of the Thesis . . . . .	42
1.5 Thesis outline . . . . .	44
<b>2 Wave and the magnetic resonance</b>	<b>45</b>
2.1 Electromagnetic wave propagation . . . . .	45
2.1.1 Electromagnetic waves in space . . . . .	45
2.1.2 Electromagnetic waves in a medium . . . . .	46
2.1.3 Electromagnetic waves at the interface . . . . .	47
2.1.4 Polarization . . . . .	49
2.1.5 Wave propagation geometries . . . . .	51
2.1.6 Dielectric permittivity and magnetic permeability tensor of the second rank . . . . .	53
2.2 Magnetic Resonance . . . . .	59
2.2.1 Transition probability and the transition absorption line in the magnetic resonance . . . . .	61

<b>3</b>	<b>Experimental techniques</b>	<b>63</b>
3.1	Historical background of electron paramagnetic resonance spectroscopy	63
3.2	Frequency-domain magnetic resonance spectroscopy . . . . .	65
3.3	Polarization transforming . . . . .	68
3.4	Operating the magnetic cryostat . . . . .	68
3.5	Sample preparation . . . . .	71
3.6	Simulating FDMRS transmission spectra . . . . .	72
3.6.1	Dielectric medium . . . . .	75
3.6.2	Magnetic medium . . . . .	75
3.7	Phase and transmission measurement . . . . .	78
<b>4</b>	<b>Magnetic Resonance in Mn<sub>12</sub>-acetate</b>	<b>81</b>
4.1	Experimental . . . . .	81
4.2	Part 1: Zero field measurement . . . . .	82
4.2.1	Experimental results and analysis . . . . .	82
4.2.2	Discussion . . . . .	89
4.3	Part 2: Measurement in magnetic field (H  z) . . . . .	90
4.3.1	Experimental results, analysis, and discussion . . . . .	90
4.4	Conclusion . . . . .	92
<b>5</b>	<b>Magnetic resonance - lineshape studies on Mn<sub>12</sub>-acetate</b>	<b>95</b>
5.1	Experiment . . . . .	95
5.2	Mn <sub>12</sub> -acetate in Voigt geometry . . . . .	96
5.2.1	<i>zfc</i> and <i>fc</i> measurement with linearly polarized radiation in Voigt geometry . . . . .	96
5.3	Mn <sub>12</sub> -acetate in Faraday geometry . . . . .	100
5.3.1	Mn <sub>12</sub> -acetate in Faraday geometry measured with linearly polarized radiation . . . . .	100
5.3.2	Faraday geometry: in magnetic field measurement with circularly polarized radiation. . . . .	110
5.4	Conclusion . . . . .	113
<b>6</b>	<b>Magnetic quantum tunneling</b>	<b>115</b>
6.1	Description of the experiment and the analysis . . . . .	115
6.1.1	Relaxation experiment . . . . .	115
6.1.2	Relaxation spectra - fitting model . . . . .	119
6.1.3	Angular calibration of the sample holder . . . . .	121
6.1.4	Measurement lists . . . . .	121
6.2	Experimental results . . . . .	121
6.2.1	Temperature dependence of relaxation time: Voigt geometry . . . . .	121
6.2.2	Longitudinal field dependence of relaxation time: Voigt geometry . . . . .	123
6.2.3	Relaxation time dependence of the longitudinal field: Faraday geometry . . . . .	133
6.2.4	Zero field relaxation: Faraday geometry . . . . .	135
6.3	Conclusion . . . . .	137

<i>CONTENTS</i>	5
<b>7 Summary</b>	<b>139</b>
7.1 Results . . . . .	139
7.2 Future plans . . . . .	143
<b>Curriculum vitae</b>	<b>155</b>
<b>List of publications</b>	<b>157</b>
<b>Acknowledgements</b>	<b>159</b>



## List of Abbreviations

$\hat{a}$  = Complex

$\hat{A}$  = Operator

a = Scalar

$\tilde{a}$  = Tensor

**a** = Vector

e.g.= For example = Examp*li* gratia

EM = Electromagnetic

EPR = Electron paramagnetic resonance

ESR = Electron spin resonance

fc = Field cooled

FDMRS = Frequency domain magnetic resonance spectroscopy

FIR = Far infrared

FWHM = Full width at half maximum

HFEPR = High field/frequency electron paramagnetic resonance

i.e.= That is = Id est

INS = Inelastic neutron scattering

LB = Langmuir-Blodgett

L.H.C. = Left hand circular polarization

MM-SUBMM = Millimeter and submillimeter

MR = Magnetic resonance

MQT = Magnetic quantum tunneling

NMR = Nuclear magnetic resonance

QT = Quantum tunneling

r.f. = Radio frequency

R.H.C. = Right hand circular polarization

SMMs = Single molecule magnets

SQUID = Superconducting quantum interference device

zfc= Zero field cooled

ZFS = Zero field splitting





# Abstract

We present the studies of the general material property (time independent) and dynamic property (time dependent) of  $\text{Mn}_{12}$ -acetate single-molecule magnet by using the *frequency-domain magnetic resonance spectroscopy* (FDMRS) technique.

For studies of the material property (time independent), the measurement was done within the frequency range  $6\text{-}12\text{ cm}^{-1}$ , temperature range  $1.9\text{-}15\text{ K}$ , and magnetic field  $0\text{-}6\text{ T}$ . We report the zero field splitting (ZFS) parameters and g-value anisotropy. We also report that the environmental effects, such as the effects of the internal field (e.g. dipolar field) and the inhomogeneous distribution of the main ZFS parameter, which both give contributions to the linebroadening mechanism in  $\text{Mn}_{12}$ -acetate.

We also studied the magneto-optical effects in the  $\text{Mn}_{12}$ -acetate sample e.g. the orientation effect of the magnetic field and the wave propagation direction, the magnetic state of the sample (demagnetized and magnetized states,) and the polarization of the radiation (e.g. linear, and left hand circular, and right hand circular polarizations), on the magnetic transition lineshape. As a result, we found the Faraday effect in the  $\text{Mn}_{12}$ -acetate system which suggests an application as the molecular rotator.

For the dynamic studies (time dependent), we performed relaxation measurements at low temperature ( $1.75\text{-}3.3\text{ K}$ ) and in magnetic fields up to  $6\text{ T}$ . We studied the relaxation time as function of the temperature, applied magnetic field, and magneto-optical geometries. We observed both thermally activated and magnetic quantum tunneling relaxations. We qualitatively and quantitatively investigated the distribution of the relaxation time in the magnetic field domain via the phonon-assisted spin tunneling process.

In conclusion, these results show that the FDMRS technique is a promising tool to study the magnetic resonance and mesoscopic quantum phenomena in the field of single-molecule magnets in the future.



# Kurzfassung

## Ergebnisse

Das mesoskopische System  $\text{Mn}_{12}$ -Acetat ist der am meisten untersuchte Einzelmolekülmagnet. Es besteht aus Austausch-gekoppelten paramagnetischen Metallion-Komplexen, die quantenmechanische Effekte wie das rein molekulare magnetische Quantentunneln aufweisen.  $\text{Mn}_{12}$ -Acetat besteht aus 8  $\text{Mn}^{3+}$  und 4  $\text{Mn}^{4+}$  Ionen, die antiferromagnetisch gekoppelt sind und zum Hochspin-Grundzustand  $S=10$  führen. Die Mangan Ionen sind durch Brückenverbindungen von Oxid- und Acetatliganden umgeben wodurch jedes einzelne Molekül von den anderen abgeschirmt ist.  $\text{Mn}_{12}$ -Acetat besitzt eine große, einaxial magnetische Anisotropie, die zu einer Nullfeld-Energiebarriere (Koerzitivfeld) von 65 K gegen magnetisches Umpolen führt;  $+ \rightarrow -$  oder  $- \rightarrow +$ . Die Umpolung der Magnetisierung kann über drei verschiedene Prozesse erfolgen: thermische Aktivierung, Quantentunneln und thermisch unterstütztes Tunneln. Eine detaillierte Beschreibung der Eigenschaften von  $\text{Mn}_{12}$ -Acetat wird in Kapitel 1 gegeben.

In den letzten zehn Jahren gab es einige hundert Veröffentlichungen über das  $\text{Mn}_{12}$ -Acetat-System, wobei die unterschiedlichsten Messtechniken, namentlich Elektronenspin-Resonanz (electron paramagnetic resonance, EPR bei veränderlichem äußeren Magnetfeld), Kernspin-Resonanz (NMR), SQUID-Magnetometrie, inelastische Neutronenstreuung (INS) u.s.w., angewendet wurden. Dennoch bleiben sehr viele offene Fragen und ungelöste Probleme, die es wert sind, mit bisher noch nicht angewandten Techniken betrachtet zu werden. In dieser Arbeit führen wir als alternative Methode die Elektronenspinresonanz mit veränderlicher Frequenz der elektromagnetischen Strahlung ein, die sogenannte *frequency-domain magnetic resonance spectroscopy* (FDMRS). Mit dieser Technik ist es möglich, sowohl die statischen (zeitunabhängigen), als auch die dynamischen (zeitabhängigen) Eigenschaften des Einzelmolekülmagneteten  $\text{Mn}_{12}$ -Acetat zu untersuchen. Sowohl die elektrodynamischen Eigenschaften von Festkörpern als auch die der magnetischen Resonanz werden in Kapitel 2 beschrieben.

Mit unserer Apparatur können wir externe Magnetfelder von  $H = 0 - 8$  T in einem Temperaturbereich von 1,5 - 300 K anlegen. Die Ausbreitungsrichtung der elektromagnetischen Welle ( $\mathbf{q}$ ) und die Richtung des äußeren magnetischen Feldes ( $\mathbf{H}_{\text{ext}}$ ) können dabei in verschiedenen Anordnungen zueinander angelegt werden, woraus zwei verschiedene Mess-Geometrien, nämlich die Voigt- ( $\mathbf{q} \perp \mathbf{H}_{\text{ext}}$ ) und die Faraday-Geometrie ( $\mathbf{q} \parallel \mathbf{H}_{\text{ext}}$ ), resultieren. Die Frequenz der elektromagnetischen Strahlung kann in einem Frequenzbereich von 1 - 48  $\text{cm}^{-1}$  ( $= 30 - 1440$  GHz, was einer Wellenlänge von 208  $\mu\text{m}$  - 10 mm entspricht) entweder durchgestimmt oder festgehalten werden. Eine komplette

Beschreibung der FDMRS Apparatur und der Messmethode findet sich in Kapitel 3.

Während bei der EPR-Technik oft Wellenleiter benötigt werden breitet sich die Strahlung bei der FDMRS-Technik im freien Raum aus. Dadurch können wir die Polarisierung der Strahlung kontrollieren, also linear, elliptisch oder zirkular polarisiertes Licht anwenden. Einen Bericht über derartige magneto-optische Messungen am Einzelmolekülmagneten  $\text{Mn}_{12}$ -Acetat gab es bislang nicht. Der andere große Vorteil der FDMRS ist, dass man individuelle magnetische Übergänge untersuchen kann, während beispielsweise bei der SQUID-Messung nur die Gesamtmagnetisierung gemessen wird. Außerdem ist bei EPR-Messungen immer ein externes Magnetfeld notwendig, während wir bei der FDMRS sowohl Nullfeld-Messungen als auch Messungen mit externem Feld machen können. Gerade die Eigenschaft, dass man einzelne magnetische Übergänge mit und ohne äußeres Feld bei verschiedenen Polarisierungen studieren kann, macht die FDMRS sehr interessant. Zusätzlich können wir mit der FDMRS die einzelnen magnetischen Übergänge bei ihrem magnetischen Relaxationsprozess beobachten. In diesem Fall können wir eine Echtzeit-Analyse durchführen, wodurch wir sowohl die Linienform als auch die Relaxationszeit der Übergänge erhalten.

In dieser Arbeit verwenden wir die FDMRS, um die magnetischen Übergänge zwischen den  $|\pm 10\rangle \rightarrow |\pm 9\rangle$ ,  $|\pm 9\rangle \rightarrow |\pm 8\rangle$  und  $|\pm 8\rangle \rightarrow |\pm 7\rangle$  Niveaus zu studieren. Wir verwenden die Fresnel-Formeln für Übergänge, um die Spektren anzufitten und erhalten so die elektrodynamische Antwortfunktionen der Materialien, nämlich die komplexe dielektrische Funktion ( $\hat{\epsilon}$ ) und die komplexe magnetische Permeabilität ( $\hat{\mu}$ ). Bei der Analyse benutzen wir den Zusammenhang  $\mu = 1 + \Delta\mu \cdot g(\nu)$  zwischen der komplexen Permeabilität ( $\hat{\mu}$ ) und dem Beitrag der magnetischen Mode ( $\Delta\mu$ ).

Im Kapitel 4 präsentieren wir temperaturabhängige Transmissionsmessungen ohne äußeres Magnetfeld. Wir erhalten daraus die Nullfeldaufspaltungs-Parameter (zero field splitting, ZFS):  $D = -0,389 \pm 0,01 \text{ cm}^{-1}$ ,  $B = -7,65 \pm 0,05 \times 10^{-4} \text{ cm}^{-1}$  und  $C = \pm 2 \times 10^{-5} \text{ cm}^{-1}$ . Diese Ergebnisse stimmen sehr gut mit denen aus etlichen anderen anderen Messmethoden überein. Dabei konnten beispielsweise bei der Hochfeld Elektronenspinresonanz (HF-EPR) die Ergebnisse nur durch Extrapolationen aus Magnetfeldmessungen erzielt werden, während man nur mit der FDMRS oder der INS die Resultate direkt ohne äußeres Feld bekommen kann. Bei der INS werden aber einige Gramm einer deuterierten Probe benötigt, während man für die FDMRS nur etwa 100 Milligramm (entweder Einkristalle oder Polykristalle) braucht. Die FDMRS Messungen sind schnell und die Ergebnisse werden direkt aus einer realen Nullfeld-Messung erhalten.

Neben den ZFS Parametern fanden wir noch zusätzlich heraus, dass die Temperaturabhängigkeit des Beitrag der magnetischen Mode dem Gesetz einer Boltzmann-Verteilung gehorcht. Die Absorptionslinien können wesentlich besser mit Gauß-förmigen als mit Lorentz-förmigen Linien angefitet werden. Die Gauß-Form ist ein Hinweis auf eine inhomogene Verbreiterung die zumindest teilweise von lokalen Variationen des Nullfeldaufspaltungs-Parameters (ZSF) (D-Verteilung) im  $\text{Mn}_{12}$ -Acetat herrührt. Die Breite der Gauß-Linie ( $\sigma$ ) erweist sich als temperaturabhängig, was ein Anzeichen für den Beitrag eines internen Dipolfeldes an der Linienverbreiterung ist. Die Resonanzfrequenz dagegen ist temperaturunabhängig, was bedeutet, dass die Temperatur im untersuchten Temperaturbereich die Nullfeldaufspaltungs-Parameter nicht beein-

flusst. Als nächstes untersuchten wir die magnetischen Übergänge bei angelegtem äußeren Magnetfeld. Dabei fanden wir eine Verschiebung der Absorptionslinien als Funktion des Zeeman-Splitting-Terms:  $g\mu_B m \cdot H_{\text{ext}}$ . Wir erhalten aus der Berechnung der durchschnittlichen Form der graphischen Darstellung der Resonanzfrequenzen als Funktion des Magnetfeldes einen Wert von  $g_{\parallel} = 1,93$ . Dieser g-Faktor stimmt gut mit dem aus HFEPR-Messungen erhaltenen überein.

Im Kapitel 5 untersuchten wir die Linienform des  $|\pm 10\rangle \rightarrow |\pm 9\rangle$  Übergangs von  $\text{Mn}_{12}$ -Acetat Einkristallen in Voigt- und Faraday-Geometrie. Da wir in der Lage waren, Nullfeld-Messungen an Proben durchzuführen, die entweder ohne äußeres Magnetfeld (zero field cooled, *zfc*), oder unter Einfluß eines äußeres Magnetfeld gekühlt worden waren (field cooled, *fc*), waren Tieftemperatur-Messungen ( $T = 1,75 - 3,3$  K) sowohl an nichtmagnetisierten (*zfc*) als auch an magnetisierten (*zfc*) Proben möglich. In den beiden Geometrien fanden wir große Unterschiede in der Linienform je nach Magnetisierungs-Zustand der Probe. Wir entwickelten ein Modell zur Beschreibung die Linienform der magnetischen Resonanz-Übergänge im  $\text{Mn}_{12}$ -Acetat System unter all diesen Bedingungen. Die Unterschiede in der Linienform können durch das Auftreten Nichtdiagonal-Elemente im magnetischen Permeabilitäts-Tensor in den magnetisierten Proben beschrieben werden. Der Permeabilitäts-Tensor ist eine Folge der Wechselwirkung zwischen der elektromagnetischen Strahlung, dem äußeren Magnetfeld und dem magnetischen Zustand der anisotropen Probe in den verschiedenen magnetooptischen Geometrien.

In Voigt-Geometrie untersuchten wir entmagnetisierte (*zfc*) und magnetisierte (*fc*) Proben mit linear polarisiertem Licht ohne äußeres Magnetfeld. Dabei fanden wir eine symmetrische Gauß-Linie im *zfc* und eine asymmetrische Gauß-Linie im *fc* Fall. Außerdem fanden wir eine leichte Verschiebung der Linie um  $\approx 0,1 \text{ cm}^{-1}$  zwischen den *zfc* und *fc* Proben. Diesen Effekt erklären wir mit Beiträgen innerer Felder wie zum Beispiel Dipolfelder oder Hyperfein-Felder ( $\approx 0,02 - 0,03 \text{ cm}^{-1}$ ) und dem Effekt der nichtdiagonalen Permeabilität  $\approx 0,07 \text{ cm}^{-1}$ . Der zweite genannte Beitrag durch nichtdiagonale Elemente in der Permeabilität ist eine Konsequenz des magnetisierten Zustands der Probe. Die Tatsache, dass die Asymmetrie der Gauß-Linie der magnetisierten Probe bei der Nullfeld-Messung auftritt ein Hinweis, dass diese Asymmetrie nicht von der Verkipfung der weichen Achse des Kristalls herrührt, sondern viel mehr vom D-Strain.

In Faraday-Geometrie führten wir die Transmissions-Messungen mit linear und zirkular polarisiertem Licht durch. Dabei konnten wir Unterschiede in den Linienformen bei linkszirkular polarisiertem (left hand circularly, L.H.C.), rechtszirkular polarisiertem (right hand circularly, R.H.C.) und linear polarisiertem Licht feststellen. Im Falle linear polarisierten Lichts fanden wir symmetrische Gauß-Linien bei *zfc*  $\text{Mn}_{12}$ -Acetat. Im *fc* Fall bleibt die Linienform gleich, besitzt aber nur die Halbe Intensität im Vergleich zu den Voigt-Spektren. Platziert man einen Analysator vor dem Detektor wird die Linienform deutlich verändert, neben der Resonanzlinie selbst werden zwei zusätzliche Minima sichtbar. Mit dem linear polarisierten Licht konnten wir auch den Faraday-Effekt beobachten, bei dem bei der Transmission die Hauptachse der Polarisation als Funktion der Strahlungsfrequenz gedreht wird. Die Faraday-Drehung reicht bei einer Probendicke von 0,5 mm von  $-100^\circ$  bis  $100^\circ$ . Deshalb schlagen wir vor,

dass ein  $\text{Mn}_{12}$ -Acetat Einkristall als molekularer Polarisations-Transformer verwendet werden kann.

Unter der Verwendung von zirkular polarisiertem Licht in der Faraday-Geometrie fanden wir eine einzelne Gauß-Absorptionslinie sowohl bei  $zfc$  als auch bei  $fc$   $\text{Mn}_{12}$ -Acetat genau wie in der Voigt-Geometrie. Die Absorption hängt aber von der Magnetisierungs-Richtung der Probe und von der Drehrichtung des zirkular polarisierten Lichts (L.H.C. oder R.H.C.) ab. Zum Beispiel, wenn die Probe durch ein  $+H_{\text{ext}}$  Feld magnetisiert wurde tritt die Resonanz nur bei L.H.C. Licht auf, bei  $-H_{\text{ext}}$  Feld magnetisierter Probe nur bei R.H.C. Licht. Dieses Ergebnis kommt von der optischen Auswahlregel:  $\Delta m = +1$  für L.H.C. und  $\Delta m = -1$  für R.H.C. Licht. Die Absorption in der unmagnetisierten Probe tritt sowohl bei L.H.C. als auch bei R.H.C. auf.

Zur Auswertung der Linienform-Messungen entwickelten wir ein Modell, das die Linienform in den beiden Geometrien in Abhängigkeit von der Magnetisierung beschreibt. Damit konnten wir sowohl qualitativ als auch quantitativ die Elektrodynamik des  $\text{Mn}_{12}$ -Acetat Systems mit Hilfe des Effekts der Lichtpolarisation und den magnetooptischen Geometrieeffekten auswerten.

In Kapitel 6 untersuchten wir die dynamischen Eigenschaften, die *Relaxation der Magnetisierung* von  $\text{Mn}_{12}$ -Acetat. Während eines Relaxations-Prozesses wechselt der Spin vom "Spinup"- (+) in den "Spindown"- (-) Zustand oder umgekehrt.

Wir untersuchten mit der FDMRS-Technik die drei verschiedenen Relaxationsprozesse im Temperaturbereich von 1,75 - 3,3 K, in Magnetfeldern von 1,6 - 2,63 T und in den beiden Geometrien (Voigt, Faraday). Dabei fanden wir heraus, dass die Relaxation viel mehr von der Temperatur und dem Magnetfeld als von der Geometrie abhängt. Im Temperaturbereich zwischen 1,75 und 3,3 K hängt die Relaxation sehr stark nach dem Arrhenius-Gesetz von der Temperatur ab. Bei Magnetfeldern zwischen 1,6 und 2,63 T beobachten wir 2 Minima in der Relaxationszeit. Das erste Minimum liegt bei etwa 1,85 T, das zweite bei etwa 2,3 - 2,35 T. Diese zwei Minima treten bei einem Magnetfeld  $H_n^{mm'} \approx 0,45n$  mit  $n = 4, 5$  auf, durch das Energieniveaus auf beiden Seiten des Doppelmuldenpotenzials in Übereinstimmung gebracht werden.

Wir spalteten die Relaxations-Messungen in zwei Teil-Messungen auf: Im ersten Teil geht es um die Relaxations-Spektren bei variierter Frequenz, im zweiten Teil um die Relaxations-Zeiten bei verschiedenen Magnetfeldern.

Für die frequenzabhängigen Messungen entwickelten wir ein theoretisches Modell zur Analyse der zeitabhängigen Spektren sowohl in der Voigt- als auch in der Faraday-Geometrie. Damit können die Linienformen der Relaxationsspektren gut beschrieben werden. Dabei führten wir den Besetzungs-Faktor ein, der ein Maß dafür ist, welcher Anteil der Spin-Besetzung zur Intensität der Absorptionslinie beiträgt. Wir fanden einen exponentiellen Zusammenhang zwischen Besetzungs-Faktor und Zeit, woraus man die Relaxationszeit erhalten kann. In Voigt-Geometrie beobachteten wir während des Relaxationsprozesses eine Verschiebung der Resonanzlinie und eine Veränderung der Breite der Gauß-Linie. Wir nehmen an, dass die Verschiebung vom lokalen Dipolfeld und den nichtdiagonalen Elementen des magnetischen Permeabilitäts-Tensors herrühren.

Im zweiten Teil stellen wir die Abhängigkeit der Relaxationszeit vom äußeren Magnetfeld ( $H_z$ ) dar. Wir beobachten zwei unterschiedliche Relaxations-Mechanismen;

thermische Aktivierung mit geringerer und thermisch unterstütztes Tunneln mit sehr viel höherer Relaxationsrate. Unsere Relaxationszeit-Messungen verglichen wir mit den Resultaten aus magnetometrischen Messungen und fanden eine gute Übereinstimmung.

Die Relaxationszeit-Abhängigkeit vom Magnetfeld konnten wir qualitativ und quantitativ mit dem Modell eines Phononen-gestützten Spin-Tunnelns beschreiben. Wir berechneten die Relaxationszeit aus den drei Beiträgen: Der Zeit, nötig zur Spin-Phonon-Kopplung ( $m \rightarrow m \pm 1, \pm 2$ ), der Zeit des Tunnelns ( $m \rightarrow m'$ ) und der Zeit für den ( $m' \rightarrow m' \pm 1, \pm 2$ ) Prozess. Der Parameter des longitudinalen Feldes ( $H_z$ ) wird durch die Energieniveau-Parameter ersetzt. Nach diesem Modell hat die Relaxationszeit-Verteilung die Form einer Lorentz-Linie um das Feld  $H_n^{mm'}$ , bei dem sich die Energieniveaus kreuzen.

Der Spin-Tunnelprozess geschieht auf verschiedenen Pfaden: dem Hauptpfad und dem Satelliten. In dieser Arbeit identifizieren wir die Tunnel-Pfade durch Simulation Relaxationszeit-Verteilung mit einer einzelnen Lorentz-Linie mit der höchsten Amplitude und der größten Linienbreite. Bei der vierten Kreuzung ( $H_{z,theo} \approx 1,8$  T), sind die Hauptpfade (6,-2) mit der höchsten Amplitude und (4,0) mit der größten Linienbreite.

Die Untersuchung des Relaxations-Phänomens mit Hilfe der FDMRS kann sehr viele Details, wie die Relaxationszeit, ihre Temperatur- und Magnetfeldabhängigkeit, die Dynamik der Relaxationsspektren oder den Einfluss des Tunnelns auf die Linienformen der Einzelnen Übergänge liefern. Für den letzt genannten Fall allerdings haben wir bislang den realen Mechanismus, wie das Tunneln die einzelnen Relaxationsspektren beeinflussen kann, noch nicht völlig verstanden.

Zusammenfassend kann man sagen, dass die FDMRS-Technik eine sehr vielversprechende Methode zur Untersuchung sowohl der statischen als auch der dynamischen Methode des Einzelmolekülmagneten  $Mn_{12}$ -Acetat darstellt.

## Ausblick

Der Einzelmolekülmagnet  $Mn_{12}$ -Acetat und seine analogen Komplexe bieten möglicherweise einen Zugang zu ultimativen Datenspeichern extrem hoher Speicherdichte. Das liegt an der wohldefinierten Größe im Nanometerbereich die als einzelne magnetische Domäne wirkt. Die Moleküle müssen dazu geeignet angeordnet und einzeln adressierbar gemacht werden, sodaß jedes Molekül als ein Bit Informationsspeicher dienen kann. Einige Forschergruppen versuchten, die Moleküle auf Polymerschichten auf metallischen oder halbleitenden Substraten anzubringen. Durch diesen Trend bewegt sich die  $Mn_{12}$ -Acetat-Forschung in Richtung der zweidimensionalen (2D) mesoskopischen Physik. Beispielsweise könnte die Untersuchung der Halbleiter-Eigenschaften und das MQT-Phänomen einer dünnen  $Mn_{12}$ -Acetat Schicht ein sehr interessantes Gebiet sein. Die Eigenschaften dünner Schichten hängen auch stark von den Substrat-Materialien und deren Oberflächen-Eigenschaften ab. Nachdem FDMRS sowohl elektrische, als auch magnetische Eigenschaften der Materialien erfassen kann, kann sie, neben den im Rahmen dieser Arbeit beschriebenen Anwendungen, auch in diesem Gebiet eine vielversprechende Methode sein.





# Chapter 1

## Introduction to Molecular magnets

### 1.1 An overview

*Mesoscopic physics* is the physics of a large system that shows quantum effects. It lies at the frontier between the microscopic and the macroscopic world. The microscopic regime normally contains the building block of atoms, and molecules. The macroscopic regime contains the objects whose behavior can be treated with classical mechanics. Macroscopic and mesoscopic systems are similar in the sense that they contain a large number of atoms or molecules. The difference is that we can predict the behavior of the objects in the macroscopic regime through the average properties of the materials. In mesoscopic regime, the object is so small that its fluctuations around the average become important which provides the signature of the classical motion of its quantum counterpart. Research on mesoscopic systems has led to the discovery of many new phenomena such as quantum tunneling of the Cooper pairs of electrons in the Josephson junctions, quantum tunneling of the electrons in quantum dots system, quantum tunneling of the magnetization, quantum phase interference, quantum coherence and quantum decoherence, quantum spin collective phenomena, etc.

Mesoscopic systems can be made either by making macroscopic objects smaller or by increasing the size of microscopic particles. Since mesoscopic system often deals with the objects in nanometer size, it is thought as a subdiscipline of *nanoscience*. One very interesting class of mesoscopic materials are molecular magnets. Their magnetic properties are in between the quantum spins and bulk magnets. The fascinating quantum effects that shown in these materials are the quantum tunneling of the magnetization [1], quantum coherence [2, 3, 4], quantum avalanches [5, 6], quantum size effects, quantum interference [7], etc.

Molecular magnets are the molecular systems which contain organic groups combined with transition metal or rare earth ions. There are several categories of the molecular magnets. One of them is the exchanged coupled clusters. The prime examples are  $\text{Mn}_{12}$ -acetate,  $\text{Fe}_8$ ,  $\text{Ni}_{12}$ ,  $\text{V}_{15}$ , etc. They show very interesting quantum phenomena at low temperatures such as slow relaxation of the magnetization. They exhibit magnetic hysteresis similar to bulk magnets. However, this behavior is purely from molecular origin. Hence, they can be called *single molecule magnets* (SMMs). Note

that similar systems such as the Prussian blues, polycyanamides, and spin crossover systems, which exhibit the photoswitching phenomenon, are also the molecular magnets but they are not in SMMs category since they do not exhibit the slow magnetic relaxation.

SMMs contains four to thirty paramagnetic ions, normally from the first period of the transition metals, that are bridged by simple ligands such as oxide, hydroxide, halide, or carboxylate ligands. Owing to its organic ligand shell, each molecule is well shielded from the others. The exchange interaction among these ions is often antiferromagnetic. In some cases, it can lead to ferrimagnetic large spin ground states, since the magnetic moments of the individual ions are not cancelled out.

### 1.1.1 Magnetic anisotropy and spin Hamiltonian

Not only the large spin, but also the *magnetic anisotropy* of the SMMs is important. The magnetic anisotropy is the dependence of magnetic properties on the preferred direction. It can be anisotropy in the response of the system to a magnetic field ( *g* value anisotropy) or in zero field (zero field splitting). There are two origins of the zero field splitting (ZFS). For the single ions, spin-orbit coupling is the main contribution. It induces a mixing of excited state orbital angular momentum into the ground state. For the clusters, the dipolar interaction between paramagnetic ions is also a main contribution.

An easy way to describe the magnetic anisotropy term is to use the *spin Hamiltonian*. Here we replace the real wavefunction by spin wavefunction and the real Hamiltonian by an effective spin Hamiltonian. So that we consider the energies of the spin states only. The spin Hamiltonian takes the crystal symmetry into consideration together with the directions of the appropriate axes relative to where the anisotropy is present. This approach allows all parameters to be substituted by spin variables, which can be obtained from the experimental data. Therefore, a suitable magnetic anisotropy Hamiltonian that can describe these two contributions together can be written in the simplest case as

$$\mathbf{H}_A = \mathbf{S} \cdot \tilde{\mathbf{D}} \cdot \mathbf{S}, \quad (1.1)$$

where  $\tilde{\mathbf{D}}$  is a symmetric traceless tensor. The above equation can be rewritten as [8, 9, 10]

$$\mathbf{H}_A = D[\mathbf{S}_z^2 - S(S+1)/3] + E(\mathbf{S}_x^2 - \mathbf{S}_y^2), \quad (1.2)$$

where  $D$  and  $E$  are the axial and rhombic anisotropy constants which are related to the principal values  $D_{uu}$  ( $u=x,y,z$ ) of the  $\tilde{\mathbf{D}}$  tensor via

$$D = 3D_{zz}/2, \quad (1.3)$$

$$E = |D_{xx} - D_{yy}|/2. \quad (1.4)$$

If  $S \geq 2$ , the higher terms are required. In orthorhombic symmetry, the axes (x,y,z) may be chosen in different ways. In the higher axial symmetry system (eg. tetragonal, cubic), the rhombic parameter  $E$  is zero.

Note that in several publications, instead of Eq. 1.2, they often use the *extended Stevens operators* system, where the magnetic anisotropy Hamiltonian can be written as

$$\mathbf{H}_A = \sum_{k,q} B_k^q \mathbf{O}_k^q(\mathbf{S}_x, \mathbf{S}_y, \mathbf{S}_z), \quad (1.5)$$

where  $\mathbf{O}_k^q$  are operators which are functions of  $\mathbf{S}_{x,y,z}$ .  $k$  corresponds to the site symmetry ranging from  $-q, \dots, q$ .  $B_k^q$  are corresponding anisotropy parameters.

Compare Eq. 1.2 and Eq. 1.5, we have [10]

$$D = 3B_2^0, \quad (1.6)$$

$$3E = 3B_2^2. \quad (1.7)$$

Up to the fourth order term  $B_4^q$ , the terms  $B_4^0$  and  $B_4^4$  are nonzero for tetragonal symmetry. For orthorhombic symmetry, the terms  $B_4^0$ ,  $B_4^2$ , and  $B_4^4$  are nonzero.

In molecular magnetism, Eq. 1.2 and Eq. 1.5 are often used together. The complete magnetic anisotropy Hamiltonian up to the fourth order can be expressed as

$$\mathbf{H}_A = D[\mathbf{S}_z^2 - S(S+1)/3] + B_4^0 \mathbf{O}_4^0 + E(\mathbf{S}_x^2 - \mathbf{S}_y^2) + B_4^2 \mathbf{O}_4^2 + B_4^4 \mathbf{O}_4^4, \quad (1.8)$$

where the first two terms are the axial terms while the last three terms are the transverse terms. The axial terms change the energies of the states, while the transverse terms changes the character of the states (i.e. mixing the states).

If there is an applied field ( $\mathbf{H}$ ) in the system, the Hamiltonian in Eq. 1.8 will include the extra Zeeman term

$$\mathbf{H}_{Zee} = g\mu_B S_z H_z + g\mu_B S_{x,y} H_{x,y}, \quad (1.9)$$

where the first term is the axial term and the second term is the transverse term.

### 1.1.2 Double-well energy potential

From Eq. 1.8, if the axial magnetic anisotropy is negative, the cluster becomes bistable, meaning that the spin has two preferable directions, namely *spin up* and *spin down*. Let  $m$  represent the projection of the spin along the uniaxial direction, for example  $z$ -direction. The spin energy potential forms the **double-well potential** type. One well represents the  $+m$  states, where  $m = 0, \dots, +S$  and another well represents  $-m$  states, where  $-m = 0, \dots, -S$ .  $S$  is the total spin ground state. The barrier energy

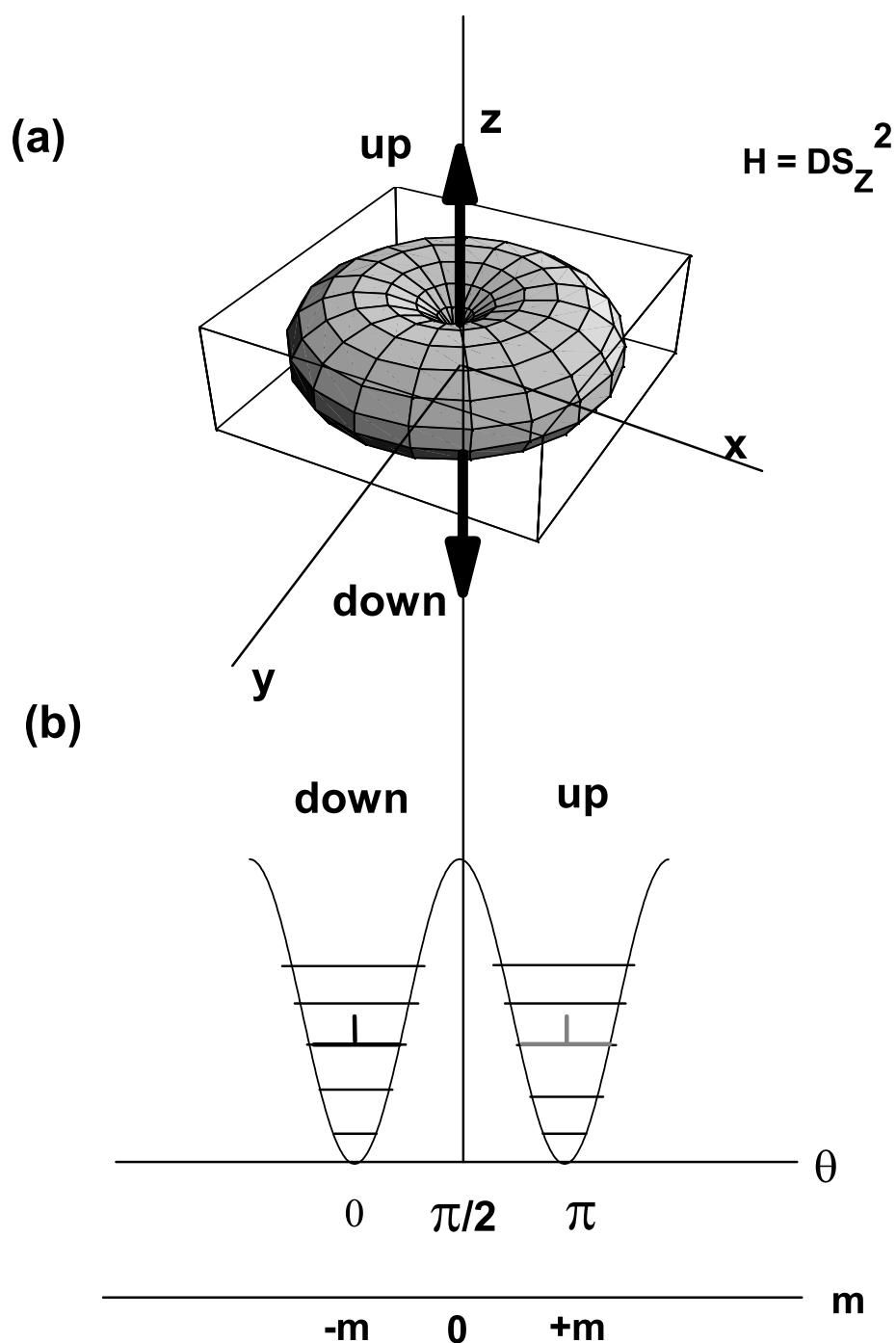


Figure 1.1: at  $H=0$ ; (a) Spherical plot of spin energy ( $H = DS_z^2$ ) in  $(-D \sin^2 \theta, \theta = 0 - \pi, \phi = 0 - 2\pi)$  coordinate. (b) The projection of the spin energy from (a) on to  $(E, \theta)$  coordinate.  $S_z$  can be mapped from  $S_z = \sqrt{S(S+1)} \cos \theta$ . The localized behavior of the wave function coefficients  $c_m$  are shown as thick black and gray solid lines. (See text)

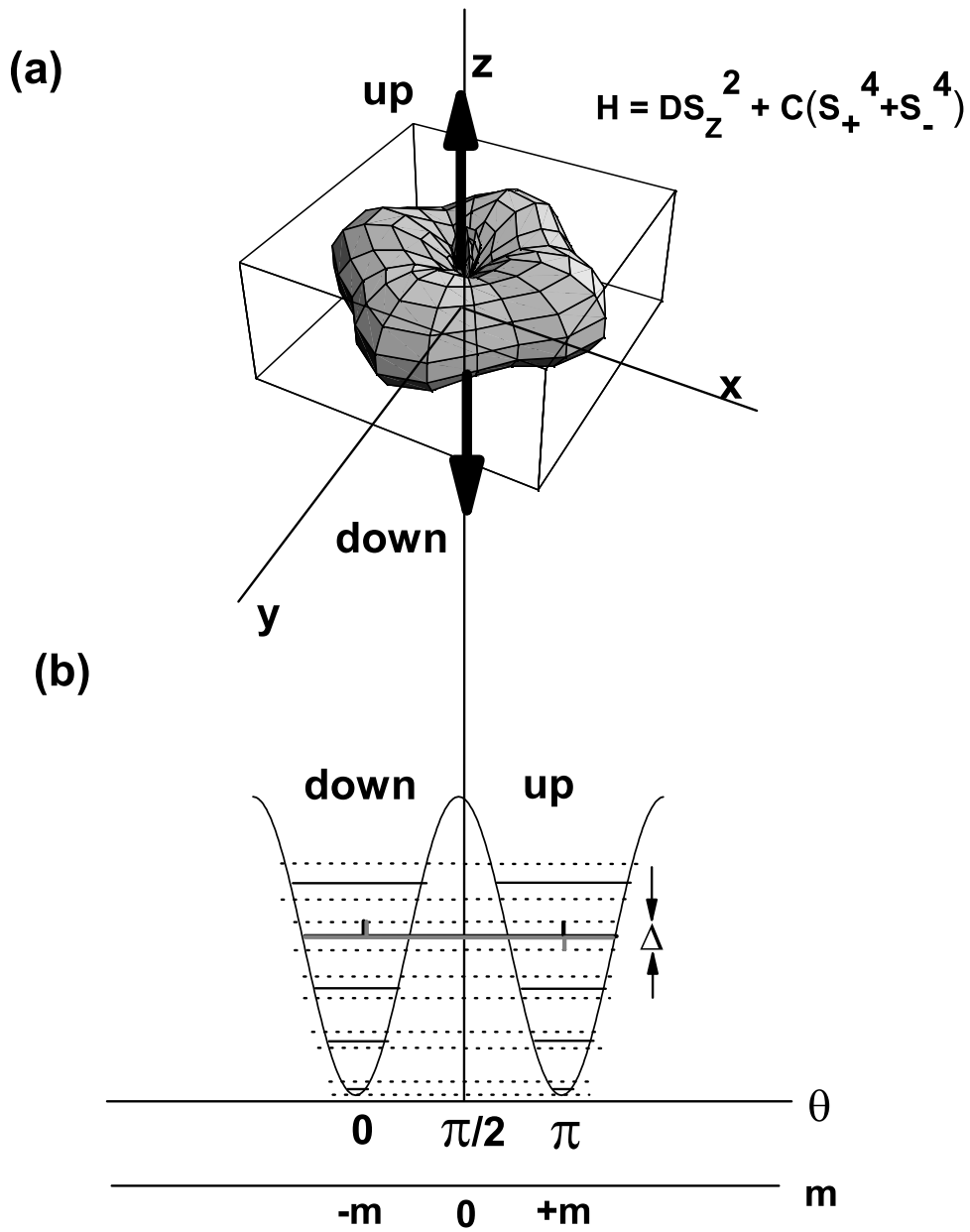


Figure 1.2: at  $H=0$ ; (a) Spherical plot of spin energy included both longitudinal and transverse term ( $H = DS_z^2 + C(S_+^4 + S_-^4)$ ). (b) The projection of the spin energy from (a) on to  $(E, \theta)$  coordinate.  $m$  quantum number can be mapped from  $m = \sqrt{S(S+1)} \cos \theta$ . Here the delocalized behavior of the wave function coefficients  $c_m$  is shown. The thick black line represents symmetric wave function. The thick gray line represents antisymmetric wave function. (See text)

that separated those two energy states, can be estimated from the spin Hamiltonian Eq. 1.8.

To have a view of the double-well potential, in a simplest case, we use the simplest form of the anisotropy Hamiltonian. Eq. 1.8 becomes  $H = DS_z^2$ , where we neglect all the higher anisotropy terms. In Fig. 1.1(a),  $S_z = \sqrt{S(S+1)} \cos \theta$  is plotted in a spherical coordinate,  $(-D \sin^2 \theta, \theta = 0 - \pi, \phi = 0 - 2\pi)$ . Fig. 1.1(a) is mapped to Fig. 1.1(b) via the  $(E, \theta)$  coordinate, which becomes the double well potential energy diagram. The barrier height of the double well potential can be estimated as  $E = Dm^2$ .

At high temperature, the system couples with the heat bath (phonon). The phonons induce the spin transitions under the selection rule;  $\Delta m = \pm 1, \pm 2$ . The spin hop across the energy barrier. This mechanism is called *thermally activated relaxation*. The relaxation time ( $\tau$ ) required in this thermal process follows the Arrhenius law;

$$\tau = \tau_0 \exp(-U/T), \quad (1.10)$$

where  $U$  is the barrier energy.  $\tau_0$  is the time constant of the exponential function.  $T$  is the temperature.

If the spin Hamiltonian contains the transverse term. For example, it contains the lowest transverse term which is  $E(\mathbf{S}_x^2 - \mathbf{S}_y^2)$ , see Eq. 1.8. The energy diagram can be redrawn as shown in Fig. 1.2(a). The transverse term induces the *tunneling splitting* ( $\Delta$ ). It exists between each pair of the matching energy levels between both side of the double-well potential, as shown in Fig. 1.2(b).

If we apply the magnetic field to the system, the magnetic field (the axial term in Eq. 1.9) will lower the energy barrier and the double-well potential becomes asymmetric. The transverse term in Eq. 1.9 will enlarge the tunnel splitting.

However, if the temperature of the system is low enough and if the energy levels in the opposite side of the double-well potential are matched, either in the zero field or in the applied magnetic field, *magnetic quantum tunneling* (MQT) can occur. In order to understand the MQT, we have to understand the basic idea of *Quantum tunneling* (QT) first.

### 1.1.3 Theory of quantum tunneling and magnetic quantum tunneling

QT is a quantum effect in which a particle can tunnel through the potential energy barrier where classical physics conclude that a classical particle does not have enough energy to do so. The tunneling phenomenon is an important consequence of quantum mechanics.

Let us consider a particle with the energy  $E$  in the one dimensional potential well  $V(x)$ .

$$E = \frac{p^2}{2M} + V(x), \quad (1.11)$$

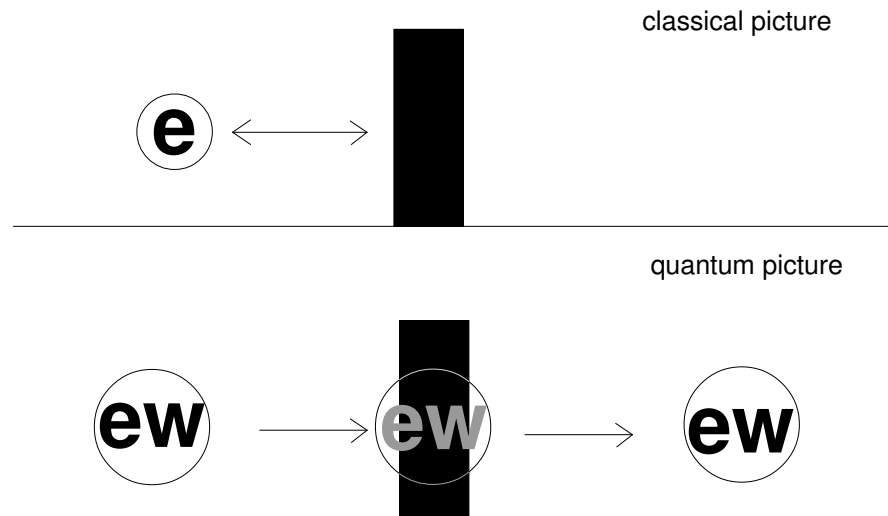


Figure 1.3: Upper figure shows the classical picture of an electron and the energy barrier. If the energy of the electron is less than the barrier energy. The electron can not cross the barrier. Lower figure shows the quantum picture of an electron wave and the energy barrier. The electron wave has some finite probability to tunnel (transmit) through the barrier even though its energy is less than the barrier energy.

where  $x$  is position of the center of mass of a particle,  $p$  is momentum conjugate to  $x$ , and  $M$  is an effective mass.

Let  $V$  is the maximum height of the potential barrier. In classical mechanics, if  $E < V$ , the particle remains in the potential well. If  $E > V$ , the particle can escape from the potential well. In quantum system, the particle can escape from the well even in the case  $E < V$ . In this case, the particle tunnel through the barrier and emerge with the same energy  $E$ . This is due to the fact that the distance  $x$  is not a conserved quantity and the particle has a wave property in a quantum system. Hence, the tunneling is allowed. The root of the tunneling phenomena is the *kinetic energy* in a particle tunneling case. Switching off the tunneling can be done by increasing the effective mass  $M \rightarrow \infty$ . However, by doing this, the system becomes classical since the energy density becomes continuous. Therefore, quantum tunneling is always there in a quantum system.

However, it is different in the *spin system*. The energy form contains no kinetic part. Let us consider the simplest Hamiltonian of a spin system with an easy axis anisotropy,

$$H = -DS_z^2 + H', \quad (1.12)$$

where the first term is an anisotropy energy, and the second term contains the terms which do not commute with  $S_z$ . In the limit of  $H' \rightarrow 0$ ,  $S_z$  is a conserved quantity, meaning that the transitions between the eigenstates of  $S_z$  are not allowed. In this

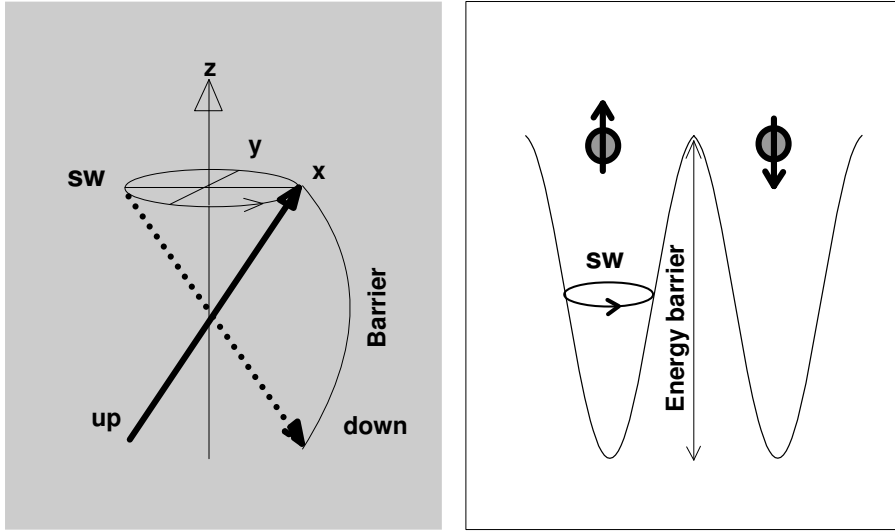


Figure 1.4: Schematic diagram of the spin tunneling (magnetic quantum tunneling). Left figure shows the circular precession of the spin wave (sw) together with the magnetization vector in the up state (solid arrow) passing to the down state (dotted arrow). Right figure shows the double-well potential energy of the spin wave. The up and down wells are separated by the energy barrier.

case, there is no tunneling. Unlike in the classical case, the system does not have to become classical to turn off the tunneling phenomenon. To turn on the tunneling, it can be done by introducing the transverse terms which do not commute with  $S_z$ , e.g. a transverse magnetic field, or a transverse anisotropy. Keep in mind that in the spin system, we only consider the spin wave function part not the spatial wave function part. *Hence, the quantum tunneling in the spin system is the magnetization tunneling through a potential barrier, which happens in an angular space.* See Fig. 1.4.

To quantify the magnetic quantum tunneling (MQT) phenomenon in the spin system, first we have to consider the view of the double well potential energy diagram. The first criteria for spin tunneling is that both sides of the barrier have the same energy. Second criteria is that the transverse term exists which does not commute with  $S_z$ .

To understand how the transverse term can induce tunneling, the convenient way is to look at the spin wave function. First, we express the eigenstates  $|\psi\rangle$  in the basis of the eigenstates  $|m\rangle$  of  $S_z$  as follows:

$$|\psi\rangle = \sum_m c_m |m\rangle, \quad (1.13)$$

where  $m = -S, \dots, +S$ ,  $c_m$  is the symmetric or antisymmetric coefficient of the state  $|m\rangle$ .

Due to the existence of transverse anisotropy term such as  $C(S_+^4 + S_-^4)$ , or  $E(S_x^2 - S_y^2)$ , the  $m$  states are no longer the eigenstates of the system. Therefore, the states  $|\psi\rangle$  of the system are not a set of doublets of the localized states but rather of



the delocalized states. We show the localized behavior of  $c_m$  coefficients in Fig. 1.1. The spin Hamiltonian only contains axial terms. The wave function coefficients  $c_m$  in Eq. 1.13 are localized for both symmetric and antisymmetric cases. See the thick black and gray lines in Fig. 1.1(b). For the delocalized state, the wave function coefficients  $c_m$  in Eq. 1.13 are no longer localized but rather tunnel between the energy barrier for both symmetric and antisymmetric cases. See the thick black and gray lines in Fig. 1.2(b).

We assume that each doublet can consist of a symmetric state  $|\psi_s\rangle$  with symmetric coefficient  $c_{+m} = c_{-m}$ , and an antisymmetric state  $|\psi_a\rangle$  with antisymmetric coefficient  $c_{+m} = -c_{-m}$ . These two states are separated by an energy gap  $\Delta = E_a - E_s$ . In the ground doublet, the good approximation for those states are

$$|\psi_a\rangle = \frac{1}{\sqrt{2}}(|+S\rangle - |-S\rangle), \quad (1.14)$$

$$|\psi_s\rangle = \frac{1}{\sqrt{2}}(|+S\rangle + |-S\rangle). \quad (1.15)$$

The state that is localized on one side of the barrier can now be expressed as a superposition of the actual eigenstates as

$$|+S\rangle = \frac{1}{\sqrt{2}}(|\psi_s\rangle + |\psi_a\rangle), \quad (1.16)$$

$$|-S\rangle = \frac{1}{\sqrt{2}}(|\psi_s\rangle - |\psi_a\rangle). \quad (1.17)$$

If the system is prepared at time,  $t=0$  such that,  $\psi(t=0) = |+S\rangle$ . The time evolution of this system simply obeys the Schrödinger equation as

$$\psi(t) = \frac{1}{\sqrt{2}} \exp(it \frac{E_s + E_a}{2\hbar}) [|\psi_s\rangle \exp(+it \frac{\Delta}{2\hbar}) + |\psi_a\rangle \exp(-it \frac{\Delta}{2\hbar})]. \quad (1.18)$$

This implies that the time evolution of the state shows coherent oscillations of the spin between the state  $|+S\rangle$  and  $|-S\rangle$  with oscillating frequency  $\omega_T = \Delta/\hbar$ . In this model, the spins coherently tunnel back and forth through the barrier. The energy gap  $\Delta$  is called the *tunnel splitting*. However, in reality, the system can couple to the environment, for instance, external fields, or internal fields such as hyperfine field or dipolar field, the phonon bath, etc. The coupling energy is many orders of magnitude larger than the tunnel splitting caused by the off-diagonal terms in most molecular magnets. Consequently, the tunneling is not coherent but rather incoherent.

#### 1.1.4 Experimental evidences for magnetic quantum tunneling

The first story of MQT began when C. Paulsen and J.G. Park found the evidence of MQT from the steps in the magnetization relaxation experiment. Specific heat

measurement confirmed that the steps found in the hysteresis are associated with superparamagnetism [11]. M.A. Novak and R. Sessoli unexpectedly found the field dependence of the relaxation time in dynamic susceptibility measurements [11]. It has significantly fast rates at some specific value of the magnetic field applied in z-direction ( $H_z$ ). Later, J.R. Friedman *et al.* found the space steps at some specific value of  $H_z$  in the hysteresis loops from the dynamic hysteresis experiment [1].

The field tuned resonant tunneling appears in AC susceptibility measurement [12]. It was found that the relaxation rate followed the Arrhenius law and the barrier height varied with the applied field. The field tuned resonant tunneling was also performed by NMR result [13] and specific heat measurement results [14, 15]. It has been proved that the resonance condition is invariant under the transverse field to at least fourth order in perturbation theory [1].

However, it was found that if the magnetic field is not at the resonance value, the small transverse field can get back the tunneling [12]. E.M. Chudnovsky and J.R. Friedman have explained the transverse field effect through the *nonresonance tunneling*. In this case, there is no energy barrier. The tunnel splitting becomes comparable to level spacing. Recently, the effects of transverse field have been studied widely for both theoretically and experimentally schemes. D.A. Garanin and E.M. Chudnovsky have published the effects of  $H_x$  to the tunneling rate caused by hyperfine and axis misalignment [16]. Later, they introduced the theory of transverse field effected tunneling which is caused by the lattice dislocation [17, 18].

AC susceptibility data and DC magnetic relaxation data indicated the relaxation time that follows an Arrhenius law down to 2.1 K [5, 11, 19, 20, 21]. The relaxation time constant  $\tau_0$  in the Arrhenius equation is  $10^{-7} - 10^{-9}$  sec. Below 2 K, the relaxation time is deviated from the Arrhenius law [5, 20, 22, 23], where the relaxation time approaches toward the temperature independent behavior. At low temperature, thermal activation becomes exponentially difficult, while the tunneling becomes exponentially easier. The crossover between these two temperature regimes was theoretically studied by D.A. Garanin *et al.* [16, 24, 25]. They proposed that as the temperature is decreased, the dominant tunneling levels shift to lower energies either continuously (*second order transition*) or abruptly (*first order transition*) under the limit  $S \rightarrow \infty$  and  $T \rightarrow 0$ . The crossover regime was experimentally observed at  $\approx 1$  K by the micro-Hall-effect magnetometry technique [26].

For the past few years, the main interest in this field is the details studies of the tunnel splitting which is a driving force for MQT [27, 28]. The tunnel splitting of this system was first calculated by D.A. Garanin *et al.* [16]. They found the tunneling between levels near the top of the barrier is faster than the bottom levels. Tunnel splitting increases in several orders of magnitude from lower to upper states. If the transverse field increases, the relaxation rate also increases. There are many issues involving the studies of the relaxation process in details. The applied transverse field [29], the crystal defects such as dislocations [30], the transverse component of the hyperfine field [16, 31, 32], the spin-orbit-vibron interaction [33] influence the spin tunneling in  $Mn_{12}$ -acetate system. Spin phonon coupling is also involved in the tunneling mechanism in the thermal assisted tunneling regime [16, 34, 35].

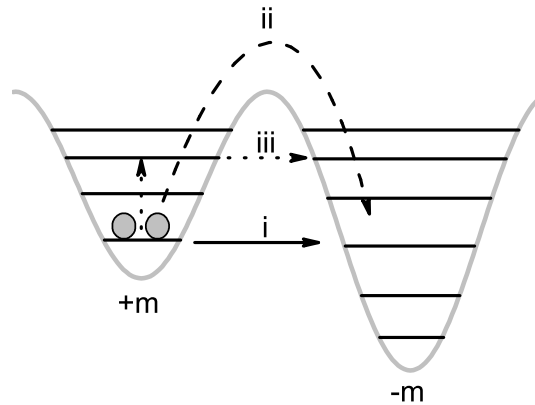


Figure 1.5: A schematic diagram of the relaxation phenomena; (i) Quantum tunneling regime, (ii) Thermally activated regime, (iii) Thermally assisted quantum tunneling regime. (See text).

### 1.1.5 Magnetic relaxation

Depending on the temperature, one of the relaxation mechanisms (thermally activated relaxation or MQT relaxation) will become important. If the system is at high temperature but the energy levels are matched, then the relaxation can occur through either thermal activation or MQT. However, the thermal activation process is faster and dominant in the high temperature regime than the MQT process. In the special case, the system can lie between those two relaxation regimes, namely, *thermally assisted quantum tunneling* regime. The relaxation occurs with the helps of both thermal activation and MQT processes. The most common case is the *phonon-assisted spin tunneling*. The spins first couple to the heat bath and move to the higher energy states. If the energy of those states are matched with ones at the other side of the well, then the spins can tunnel through the energy barrier. See Fig. 1.5.

### 1.1.6 Theoretical concepts of phonon-assisted spin tunneling

Normally thermally activation over the barrier is accompanied by transitions from the bottom energy level to the top energy level. This kind of process requires the energy to be exchanged between  $\mathbf{S}$  and the other degrees of freedom of the whole system, for example:

i) The fluctuating part of the dipole-dipole interaction between different magnetic clusters which could cause the spin relaxation was proved to be inefficient to cause the spin relaxation [21, 36] by using the diluting sample.

ii) Nuclear spins produce hyperfine field on electronic spin system. Its transverse term can enhance the tunneling. However, it will be treated as a part of the transverse field term,  $H_T$ .

iii) Spins interact with phonons and photons. In the case of the presence of both

phonons and photons. The photon part can be neglected since the light velocity is much faster than the sound velocity, making the photon density of states much smaller than the phonon's. The spin-phonon energy is large enough to be considered at low temperature without Raman scattering concerned.

### Spin Hamiltonian: included spin-phonon coupling

In this part, we will formulate the spin-phonon Hamiltonian ( $H_{sp}$ ) and determine the spin-phonon coupling constant ( $g_i$ ). First, we rewrite a single spin Hamiltonian of  $\text{Mn}_{12}$ -acetate system in Eq. 1.67 including the spin-phonon coupling as

$$H = H_a + H_z + H_T + H_{sp} \quad (1.19)$$

$H_a = DS_z^2$  is the longitudinal anisotropy term,  $H_z = g\mu_B S_z H_z$  is the longitudinal Zeeman term,  $H_T = C(S_+^4 + S_-^4)/2 + g\mu_B S_x H_x$  is the transverse term, and  $H_{sp}$  is defined as the spin-phonon coupling term which can be generally formulated as

$$H_{sp} = \sum_i Q_i \otimes F_i, \quad (1.20)$$

where  $Q_i$  is spin operator and  $F_i$  is phonon operator.

The idea of spin-phonon coupling assisted tunneling has been formulated intensively for many years [8]. D.A. Garanin and E.M. Chudnovsky first implemented this idea in  $\text{Mn}_{12}$ -acetate system [16]. Shortly after, many have followed their works [34, 37]. Here we assume that the phonon in molecular magnet systems contains two transverse modes and one longitudinal mode.

The basic concept of spin coupled with phonon is based on the studies of energy transfer between spin system and the phonon bath. The whole system is an isolated system. Therefore, the energy has to be conserved. The lowest order spin-phonon interactions, which is allowed by time-reversal symmetry, is *linear* in phonon operator and *bilinear* in spin operator. The simplest interaction is due to the rotation of an anisotropy axis by a *transverse phonon*. We leave the longitudinal phonon mode since it appears at the plasma frequency, which is not in our case.

If  $\mathbf{n}$  is an arbitrarily oriented anisotropy axis, then the anisotropy term,  $H_a$  to the first order, can be rewritten as

$$H_a = D(\mathbf{n}S^2), \quad (1.21)$$

where the the fourth-order term ( $BS_z^4$ ) is much smaller and is neglected here. A transverse phonon can change the vector  $\mathbf{n}$  by

$$\delta\mathbf{n} = \delta\phi \times \mathbf{n}, \quad (1.22)$$

where  $\delta\phi$  is a local rotation of the lattice and  $\mathbf{u}$  is the lattice displacement where

Strain function	One-ion spin operators of spherical tensor operators
$\frac{1}{2}[\epsilon_{xx} - \epsilon_{yy}]$	$\frac{1}{2}[S_x^2 - S_y^2]$
$\epsilon_{xy}$	$\frac{1}{2}[S_x S_y + S_y S_x]$
$\epsilon_{yz}$	$\frac{1}{2}[S_y S_z + S_z S_y]$
$\epsilon_{xz}$	$\frac{1}{2}[S_x S_z + S_z S_x]$

Table 1.1: Isomorphism for elastic strain components and one-ion spin operators.[38]

$$\delta\phi = \frac{1}{2}\nabla \times \mathbf{u}. \quad (1.23)$$

Normally if we have the displacement of the lattice, it is necessary to determine the strain tensor. The linear strain tensor is defined by

$$\epsilon = \nabla \mathbf{u}. \quad (1.24)$$

Let  $\alpha, \beta = x, y, z$ . We can determine the symmetric linear strain tensor as

$$\epsilon_{\alpha\beta} = \frac{1}{2}\left(\frac{\partial u_\alpha}{\partial \beta} + \frac{\partial u_\beta}{\partial \alpha}\right), \quad (1.25)$$

and the antisymmetric linear strain tensor as

$$\omega_{\alpha\beta} = \frac{1}{2}\left(\frac{\partial u_\alpha}{\partial \beta} - \frac{\partial u_\beta}{\partial \alpha}\right). \quad (1.26)$$

We use an equation 1.20 combined with the formulas for the strain functions, one-ion spin operators given as shown in table 1.1, and the antisymmetric strain term. We can write the spin-phonon coupling term allowed by tetragonal symmetry of Mn<sub>12</sub>-acetate crystal as (Refer to [34, 38])

$$\begin{aligned} H_{sp} = & g_1(\epsilon_{xx} - \epsilon_{yy}) \otimes (S_x^2 - S_y^2) + \frac{1}{2}g_2\epsilon_{xy} \otimes \{S_x, S_y\} + \\ & + \frac{1}{2}g_3(\epsilon_{xz} \otimes \{S_x, S_z\} + \epsilon_{yz} \otimes \{S_y, S_z\}) + \\ & + \frac{1}{2}g_4(\omega_{xz} \otimes \{S_x, S_z\} + \omega_{yz} \otimes \{S_y, S_z\}), \end{aligned} \quad (1.27)$$

where the notation  $\{S_x, S_y\}$  is  $[S_x S_y + S_y S_x]$ . After we substitute  $S_\pm = S_x \pm iS_y$  in the above equation, we have

$$\begin{aligned}
H_{sp} &= \frac{1}{2}g_1(\epsilon_{xx} - \epsilon_{yy}) \otimes (S_+^2 + S_-^2) + \frac{i}{4}g_2\epsilon_{xy} \otimes (S_-^2 - S_+^2) + \\
&+ \frac{1}{4}g_3[(\epsilon_{xxz} - i\epsilon_{yz}) \otimes \{S_+, S_z\} + (\epsilon_{xz} + i\epsilon_{yz}) \otimes \{S_-, S_z\}] + \\
&+ \frac{1}{4}g_4[(\omega_{xz} - i\omega_{yz}) \otimes \{S_+, S_z\} + (\omega_{xz} - i\omega_{yz}) \otimes \{S_-, S_z\}].
\end{aligned} \tag{1.28}$$

Due to the modulation of crystal field by phonon, we denote  $g_i=1,2,3,4$  as the spin-phonon coupling constants which can be determined as

$$\begin{aligned}
g_1 &= |g_2| = D, \\
|g_3| &= g_4 = 2D.
\end{aligned} \tag{1.29}$$

Recall that  $D$  is the anisotropy constant. For proof of equation 1.29, refer to [34, 39].

Finally, we have formulated the spin-phonon Hamiltonian ( $H_{sp}$ ) by assuming that the spin Hamiltonian contains only the first order longitudinal anisotropy term ( $DS_z^2$ ) and found that the coupling constants ( $g_i$ ) in  $H_{sp}$  are related to the anisotropy constant ( $D$ ). We note that  $g_{1,2}$  cause the transition with  $\Delta m = \pm 2$  and  $g_{3,4}$  with  $\Delta m = \pm 1$ . In the next Section, we will formulate the tunnel splitting in order to further calculate the tunneling rate.

## Tunnel splitting

Recall that the transverse terms in the spin Hamiltonian are the terms that cause the tunnel splitting. These terms mix the eigenstates  $|m\rangle$  and  $|m'\rangle$  of longitudinal terms together. The mixing of these two eigen states can give symmetric and anti-symmetric final state with different energy, where the energy difference is called *tunnel splitting*. The tunnel splitting can make the tunneling of the magnetization through the barrier possible. To calculate the tunnel splitting energy (which is the inverse of the *tunneling rate*), it might be interesting to follow the following story.

In quasiclassical limit where  $S \gg 1$ , the tunneling rate from ground state for different values of  $H_z$  was calculated by E.M. Chudnovsky and L. Gunther [40] using the *instanton* technique. M. Enz and R. Schilling have developed more sophisticated version of the instanton approach to spins, in order to obtain ground state tunneling splitting with the prefactor [41]. Later, O.B. Zaslavskii used more simple method based on the mapping onto a particle problem [42]. J.L. van Hemmen and A. Sütő have formulated the Wentzel, Kramers, and Brillouin- WKB method for spin systems to calculate the tunneling rates for excited states [43, 44]. Note that WKB method is a semi-classical treatment to explain the tunneling. Scharf *et al.* have proposed an approach using a particle mapping but subsequent with WKB approximation to refine the results of the energy splitting in the excited levels. However, it is limited to small  $H_x$  [45]. In case of small  $H_x$ , it is possible to directly calculate the energy splitting using high order perturbation theory. For early applications refer to I.Ya. Korenblit *et al.* who studied ground state splitting of rare earth system [46]. The successful

calculation for the Mn<sub>12</sub>-acetate system came with D.A. Garanin who could derive the splitting energy for all levels of  $m$  [47]. However, he used only one perturbation parameter which is  $H_T = H_x S_x$ . It gives the transition only  $\Delta m = \pm 1$ . In this case, the tunnel splitting energy can be formulated as

$$\Delta_{m,m'}^{(n)} = \frac{2D}{[2m-n-1]^2} \left( \frac{(S+m-n)!(S+m)!}{(S-m)!(S-m+n)!} \right)^{(1/2)} \left( \frac{g\mu_B H_T}{2D} \right)^{(2m-n)}, \quad (1.30)$$

where  $n = m - m'$ . Recall that  $H_T = H_x S_x$  for the above formula.

To have  $\Delta m = \pm 4$ , M. Leuenberger *et al.* have used double perturbation parameters which includes the  $B_4$  term giving  $\Delta m = \pm 4$  in the transverse Hamiltonian [34]

$$H_T = \frac{C}{2}(S_+^4 + S_-^4) + g\mu_B H_x S_x. \quad (1.31)$$

In a small transverse field, the tunnel splitting  $\Delta_{mm'}$  can be solved in an elementary way using time-independent perturbation theory in higher order as

$$\Delta_{mm'} = 2 \frac{V_{m,m-1}}{\epsilon_{m-1} - \epsilon_m} \frac{V_{m-1,m-2}}{\epsilon_{m-2} - \epsilon_m} \dots V_{-m'+1,-m'}, \quad (1.32)$$

where the step  $\Delta m = \pm 1$  is allowed. Then, by using resolvent techniques [34, 48] to generalize the equation 1.32. It gives  $\Delta m$  as any arbitrary steps.

$$\Delta_{mm'} = 2 \left| \sum_{m_1 \dots m_N, m_i \neq m, m'} \frac{V_{m,m_1}}{\epsilon_m - \epsilon_{m_1}} \prod_{i=1}^{N-1} \frac{V_{m_i, m_{i+1}}}{\epsilon_m - \epsilon_{m_{i+1}}} V_{m_N, m'} \right|, \quad (1.33)$$

where  $V$  is a *Hermitian* operator having a real eigen value (not complex).  $V$  is defined as;  $V_{m+1,m} = \langle m+1 | hS_x | m \rangle = \frac{\hbar}{2} [(s-m)(s+1+m)^{\frac{1}{2}}]$  and  $N$  is the lowest order of the degenerate perturbation. The summation in Eq. 1.33 can be thought as the sum over different paths in Hilbert space between  $|m\rangle$  and  $|m'\rangle$ .

We insert  $H_T$  in the potentials  $V_{m_i, m_{i+1}}$ . The two-state Hamiltonian yields

$$\tilde{H}_T = \varepsilon_m |m\rangle \langle m| + \Delta_{m,m'}/2 |m\rangle \langle m'| + (m \leftrightarrow m'), \quad (1.34)$$

where  $\varepsilon_m = E_m + g\mu_B \delta H_z m$ . See Fig. 1.6. See  $E_m$  in Eq. 5.24.  $\delta H_z$  is

$$\delta H_z = H_z^{mm'} - H_z = 0. \quad (1.35)$$

See  $H_z^{mm'}$  in Eq. 1.69 ( $H_z^{mm'} = \frac{nD}{g\mu_B} [1 + \frac{B}{D}(m^2 + m'^2)]$ ).  $|m\rangle$  and  $|m'\rangle$  are degenerate when  $\delta H_z = 0$ . The energy eigen value ( $E_T$ ) can be written as

$$E_T = 1/2[\varepsilon_m + \varepsilon_{m'} \pm \sqrt{(\varepsilon_m - \varepsilon_{m'})^2 + \Delta_{m,m'}^2}]. \quad (1.36)$$

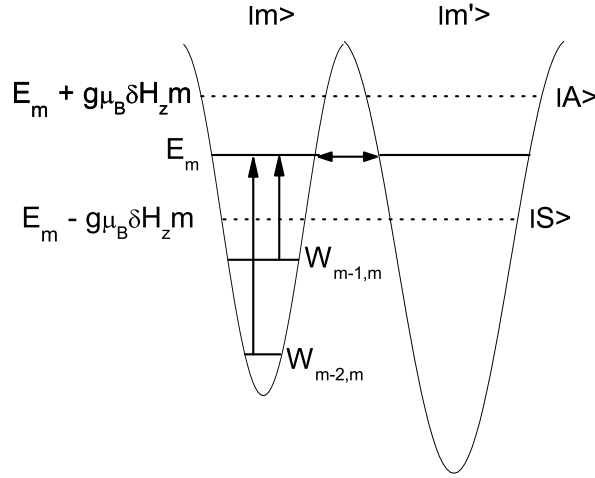


Figure 1.6: The tunneling diagram between the energy levels  $E_m \rightarrow E_{m'}$  within the tunneling gap (dashed line) caused by the energy difference between the antisymmetric state ( $|A\rangle$ ) and symmetric state ( $|S\rangle$ ).  $W_{m-1,m}$  and  $W_{m-2,m}$  are the transition rates (See Eq.1.51-1.52).

### The density matrix equation (DME) for relaxation system

DME is used to study the resonant tunneling in a moderate spin system. Because there is a lost for a natural account in tunneling problem in the quasiclassical approaches for the real macroscopic system. First, we shall know some basic properties of the density matrix [49].

### Density matrix and its properties

To consider a mixture of states  $|\psi_n\rangle$ , ( $n=1,2,3,\dots$ ), with statistical weight  $W_n$ . The density operator (or *statistical operator*) which can describe the mixture can be written as

$$\rho = \sum_n W_n |\psi_n\rangle\langle\psi_n|. \quad (1.37)$$

Next  $\rho$  operator needs to be expressed in a matrix form. To this end, the convenient basis states are chosen as,  $|\phi_1\rangle, |\phi_2\rangle, |\phi_3\rangle, \dots$ . They are orthonormal ( $\langle\phi_n|\phi_m\rangle = \delta_{nm}$ ) and complete ( $\sum_n |\phi_n\rangle\langle\phi_n| = 1$ ). By superposing all the states, we have

$$\rho = \sum_{nm'm} W_n a_{m'}^{(n)} a_m^{(n)*} |\phi_{m'}\rangle\langle\phi_m|. \quad (1.38)$$



By taking matrix elements of equation 1.38 between state  $|\phi_j\rangle$  and  $|\phi_i\rangle$ , and applying the orthonormality, we have the set of the following elements

$$\langle \phi_i | \rho | \phi_j \rangle = \sum_n W_n a_i^{(n)} a_j^{(n)*}, \quad (1.39)$$

where  $i$  and  $j$  run over all basis which finally gives  $\rho$  operator from equation 1.37 into a matrix form. It is called the *density matrix*.

Because we use  $|\phi_n\rangle$  as the basis states, therefore we will present the elements of the density matrix as  $|\phi_n\rangle$ .

Here are some important properties of the density matrix.

**i)**  $\rho$  is

$$\langle \phi_i | \rho | \phi_j \rangle = \langle \phi_j | \rho | \phi_i \rangle^*. \quad (1.40)$$

**ii)** Reckon that  $W_n$  is the probability of finding the system in the state  $|\phi_n\rangle$  and  $|a_m^{(n)}|^2$  is the probability to find  $|\psi_n\rangle$  in state  $|\phi_m\rangle$ . Then we shall have the probability to find the system in state  $|\phi_m\rangle$  as *diagonal element*

$$\rho_{mm} = \sum_n W_n |a_m^{(n)}|^2. \quad (1.41)$$

**iii)**  $\rho_{mm} \geq 0$

**iv)** The probability  $W(\psi)$  to find the system in state  $|\psi\rangle$  after the measurement is

$$W(\psi) = \langle \psi | \rho | \psi \rangle. \quad (1.42)$$

**v)** Since  $\sum_n W_n = 1$ , then the trace of  $\rho$  is  $\text{tr } \rho = 1$ .

**vi)** If  $Q$  is any operator, the expectation value of  $Q$  is given by the trace of the product of  $\rho$  and  $Q$ . In general case, we shall drop the normalization then we have

$$\langle Q \rangle = \frac{\text{tr}(\rho Q)}{\text{tr} \rho}. \quad (1.43)$$

The properties of a system can be found by calculation of the expectation values of suitable operators. Since the expectation value of any operator can be obtained by equation 1.43, therefore, we shall say that the density matrix contains all physically significant information of the system.

**vii)** Now we shall consider the time evolution of the mixtures of the states. By applying the Shrödinger relation, we have

$$i\hbar \frac{\partial \rho(t)}{\partial t} = [H(t), \rho(t)], \quad (1.44)$$

with the commutator

$$[H(t), \rho(t)] = H(t)\rho(t) - \rho(t)H(t). \quad (1.45)$$

The relation in Eq. 1.43 and Eq. 1.44 are the heart of the density matrix theory. They are simultaneous solution which can lead to equations of motion for the observable.

### Density matrix for spin-phonon coupling: Generalized master equation

We consider a system in a contact with its surroundings, exchanging energy, or polarization. If its initial state in a nonequilibrium state. After some time later, the state gradually goes to an equilibrium state. Such a gradual and irreversible evolution into an equilibrium state is called *relaxation process*.

By using a density matrix equation, we can describe the evolution of the spin system coupled to an equilibrium heat bath of phonons where the diagonal elements  $\rho_{mm} = N_m$  describe population of the spin energy levels. If a transverse field or another level mixing perturbation are applied, nondiagonal elements appear with the slow dynamics describing the tunneling process.

Here we derive only a master equation that can describe the relaxation of the spin due to the tunneling. Our model is the spin coupling to a heat reservoir of phonons. The phonon heat bath is in thermodynamics equilibrium which can be described by a canonical density matrix  $\rho_{ph}$  for free phonons. We can write down the full Hamiltonian representing the whole interested system again as

$$H = H_0 + H_{sp} + H_{ph}, \quad (1.46)$$

where  $H_0 = H_a + H_z$  (see Eq. 1.19).  $H_{sp}$  represents the spin bath, and  $H_{ph}$  represents phonon heat bath.

The relaxation of the magnetization obeys

$$\dot{\rho}_{mm'} = \frac{i}{\hbar}[\rho, H_0]_{mm'} + \delta_{mm'} \sum_{n \neq m} \rho_n W_{mn} - \gamma_{mm'} \rho_{mm'}. \quad (1.47)$$

The Eq. 1.47 is called the *generalized master equation*. To formulate Eq. 1.47, refer to [49]. The diagonal elements ( $m = m'$ ) of Eq. 1.47 give the master equation

$$\dot{\rho}_m = \frac{i}{\hbar}[\rho, H_0]_{mm} + \sum_{n \neq m} \rho_n W_{mn} - \rho_m \sum_{n \neq m} W_{nm}, \quad (1.48)$$

and the off-diagonal elements ( $m \neq m'$ ) are given by

$$\dot{\rho}_{mm'} = \frac{i}{\hbar}[\rho, H_0]_{mm'} - \gamma_{mm'} \rho_{mm'}. \quad (1.49)$$

The diagonal term gives the probability to find the level  $|m\rangle$  occupied at time  $t$ . The probability increases in time due to the transitions from *all other levels*  $|n\rangle$  to  $|m\rangle$ . Vice versa, It also decreases due to transitions from  $|m\rangle$  to  $|n\rangle$ . Hence, we can calculate the rate change in the diagonal elements as

$$\dot{\rho}_{mm'} = \text{Gain in } |m\rangle - \text{Loss in } |m\rangle, \quad (1.50)$$

where  $\dot{\rho}_{mm'} = \langle m | \dot{\rho} | m' \rangle$ .  $W_{mn}$  is the Fermi golden rule describing the transition rate from all other states  $|m\rangle$  to  $|n\rangle$  and vice versa for  $W_{nm}$  which can be explicitly written as

$$W_{m\pm 1, m} = \frac{D^2 s_{\pm 1}}{12\pi\rho c^5 \hbar^4} \frac{(E_{m\pm 1} - E_m)^3}{e^{\beta(E_{m\pm 1} - E_m)} - 1}, \quad (1.51)$$

$$W_{m\pm 2, m} = \frac{17D^2 s_{\pm 2}}{192\pi\rho c^5 \hbar^4} \frac{(E_{m\pm 2} - E_m)^3}{e^{\beta(E_{m\pm 2} - E_m)} - 1}, \quad (1.52)$$

where  $D$  is the anisotropy constant,  $E_m$  is the energy of level  $m$  (see Eq. 5.24), and

$$s_{\pm 1} = (s \mp m)(s \pm m + 1)(2m \pm 1)^2, \quad (1.53)$$

$$s_{\pm 2} = (s \mp m)(s \pm m + 1)(s \mp m - 1)(s \pm m + 2). \quad (1.54)$$

Refer to [34] for more details. The mass density  $\rho$  of  $\text{Mn}_{12}$ -acetate is  $1.83 \times 10^3$  kg/m<sup>3</sup>, and the sound velocity  $c$  is  $\approx 1.45 - 2 \times 10^3$  m/s.

Note that we only calculate the rate changes due to the population gain and loss in a certain  $m$  state causes by the spin coupling with phonon bath under the selection rule  $\Delta m = \pm 1, \pm 2$ . In the next section, we will calculate the rate changes by including the effect of tunneling between  $m$  and  $m'$ .

### Density matrix for spin-phonon coupling including spin tunneling: Master equation

To evaluate the generalized master equation (Eq. 1.47) with the spin tunneling term, we insert  $\tilde{H}_T$  from Eq. 1.34 into the generalized master equation (Eq. 1.47). We obtain *the master equation* with the diagonal and off-diagonal element as

$$\dot{\rho}_m = \frac{i\Delta_{mm'}}{2\hbar}(\rho_{mm'} - \rho_{m'm}) - W_m\rho_m + \sum_{n \neq m, m'} W_{mn}\rho_n, \quad (1.55)$$

and

$$\dot{\rho}_{mm'} = -\left(\frac{i}{\hbar}\varepsilon_{mm'} + \gamma_{mm'}\right)\rho_{mm'} + \frac{i\Delta_{mm'}}{2\hbar}(\rho_m - \rho_{m'}), \quad (1.56)$$

where  $\varepsilon_{mm'} = \varepsilon_m - \varepsilon_{m'}$  (see Eq. 1.34). Since the tunneling process is incoherent, we can neglect the time dependence of the offdiagonal elements, eg.  $\dot{\rho}_{mm'} = 0$ . Inserting the stationary solution of Eq. 1.56 into Eq. 1.55 yields the complete master equation

$$\dot{\rho}_m = -W_m\rho_m + \sum_{n \neq m, m'} W_{mn}\rho_n + \Gamma_m^{m'}(\rho'_m - \rho_m), \quad (1.57)$$

where

$$\Gamma_m^{m'} = \Delta_{mm'}^2 \frac{W_m + W_{m'}}{4\varepsilon_{mm'}^2 + \hbar^2(W_m + W_{m'})^2}, \quad (1.58)$$

where  $\Gamma_m^{m'}$  is the transition rate from state  $|m\rangle$  to  $|m'\rangle$ . It is induced by tunneling process and phonon damping. The quantity  $\Gamma_m^{m'}$  has a Lorentzian shape as a function of  $\varepsilon_{mm'}$  which is the subfunction of the external magnetic field  $H_z$ . The Lorentzian has a very sharp peak at the resonance field.

Up to this part, we can write down the generalized master equation in Eq. 1.47 and the master equation in Eq. 1.57. The first one explains the transition within  $m$  states by spin-phonon induced process. In the latter one, the spin tunneling process from  $m \leftrightarrow m'$  is included, in which its tunneling is described as the Lorentzian  $\Gamma_m^{m'}$  function.

### Relaxation time

To evaluate the relaxation time, we need to numerically diagonalize the master equation. We rewrite the master equation 1.57 as

$$\dot{\vec{\rho}}(t) = \tilde{W}\vec{\rho}(t). \quad (1.59)$$

Here we represent  $\vec{\rho}(t)$  as the diagonal elements of  $\rho$ . For the system with several relaxation path ( $i$ ), the rate matrix  $W$  has its eigenvalues  $w_i$  where  $i=1,2,3,\dots,21$ . The dominant relaxation time of the system is

$$\tau = \max_i \left\{ -\frac{1}{\text{Re } w_i} \right\}. \quad (1.60)$$

It is not obvious to calculate  $\tau$  according to the above equation. Alternatively we estimate the value of  $\tau$  near the resonance.

For  $H_z \geq 0$ , we use

$$1/\tau = \frac{1}{1 + e^{\beta(E_{-s} - E_s)}} \frac{e^{\beta(E_{m_i} - E_s)}}{\Omega_{m_i}^{m_i+1}}, \quad (1.61)$$

and for  $H_z \leq 0$  we use

$$1/\tau^* = \frac{1}{1 + e^{\beta(E_s - E_{-s})}} \frac{e^{\beta(E_{m_i} - E_{-s})}}{\Omega_{m_i+1}^{m_i}}, \quad (1.62)$$

where  $\Omega_{m_i}^{m_i+1}$  is  $\Gamma_{m_i}^{m_i+1}$ .

The relaxation rate in equation 1.61 can be rewritten as (see [34])

$$1/\tau = \frac{1}{1 + e^{\beta(E_{-s} - E_s)}} \left( \frac{e^{\beta(E_{m+2} - E_s)}}{W_{m,m+2}} + \frac{e^{\beta(E_{m'} - E_s)}}{W_{m'-2,m'}} + \frac{e^{\beta(E_m - E_s)}}{\Gamma_m^{m'}} \right). \quad (1.63)$$

Note that the relation between the transition probability to go up  $W_m^{m+2}$  and to decay down  $W_{m+2}^m$  is

$$\frac{W_{m,m+2}}{W_{m+2,m}} = e^{\beta(E_{m+2} - E_m)}. \quad (1.64)$$

The linewidth of the relaxation rate peak in Eq. 1.63 can be estimated as

$$w' = \frac{2^{3/2} \Delta_{mm'}}{|m - m'| g \mu_B}. \quad (1.65)$$

Finally, we obtain the relaxation rate of the phonon assisted spin tunneling process (see Eq. 1.63 and Fig. 1.6) with the first two terms describe the time required in the transitions within the same  $m$  and the last term describes the transitions between  $m \leftrightarrow m'$  levels. The last term which is due to the tunneling term is the main term giving the Lorentzian lineshape (see  $\Gamma_{m_i}^{m_i+1}$  function) to the relaxation time in the field domain curve. We will use Eq. 1.63 in Chapter 6 in order to explain our experimental relaxation time.

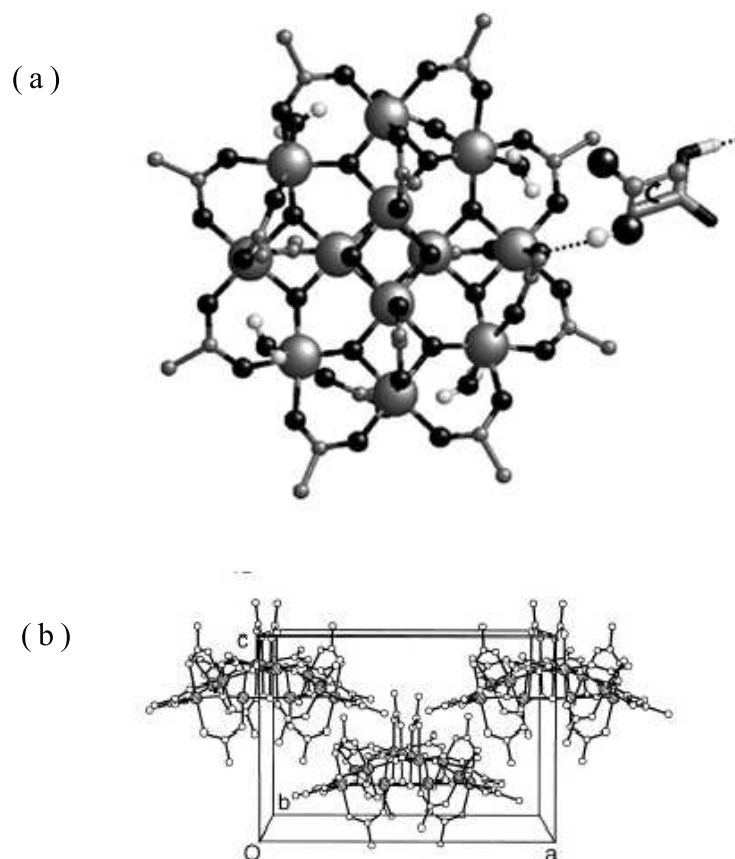


Figure 1.7: (a) Structure of  $\text{Mn}_{12}$ -acetate molecule; manganese atoms - large spheres, oxygen atoms - black spheres, carbon atoms - gray spheres, and hydrogen atoms - white spheres. The inner big spheres are  $\text{Mn}^{4+}$  ions where the outer big spheres are  $\text{Mn}^{3+}$  ions. The acetic acid can make a hydrogen bond (dash line) to the manganese core on two different axes (curve arrow) and on different positions. (b) Unit cell of  $\text{Mn}_{12}$ -acetate (See text)

## 1.2 Examples of the molecular magnets

### 1.2.1 Mn<sub>12</sub>-acetate

Mn<sub>12</sub>-acetate is the prime example of single molecule magnets. Several interesting phenomena have been found in this system such as the magnetic quantum tunneling (MQT) which is a typical mesoscopic effect. Mn<sub>12</sub>-acetate stands for [Mn<sub>12</sub>O<sub>12</sub>(CH<sub>3</sub>COO)<sub>16</sub>(H<sub>2</sub>O)<sub>4</sub>]·2CH<sub>3</sub>COOH·4H<sub>2</sub>O]. It is a high spin coordination cluster with total spin ground state S=10. This has been confirmed by low-field magnetic measurements [50]. It was first synthesized by Lis and characterized by X-ray diffraction methods [51]. The structure of Mn<sub>12</sub>-acetate is shown in Fig. 1.7(a) which was confirmed experimentally by polarized neutron scattering [52] and theoretically by electronic-structure calculations [53]. The core of the molecule is composed of four Mn<sup>4+</sup> ions forming a ferromagnetic sublattice with spin s=3/2 each, surrounded by a crown of eight Mn<sup>3+</sup> ions forming a ferromagnetic sublattice of spin s=2 each. These two ferromagnetic sublattices are strongly antiferromagnetically coupled through the oxygen ligands, giving a total collective spin S=10 ground state.

The unit cell of Mn<sub>12</sub>-acetate crystals is shown in Fig.1.7(b). This molecular clusters form a molecular crystal of tetragonal S<sub>4</sub> symmetry with the lattice constants  $a = 1.732$  nm and  $b = 1.239$  nm. One unit cell contains two Mn<sub>12</sub>O<sub>12</sub> molecules surrounded by four water molecules and two acetic acid molecules. The molecules are isolated from each other by the acetate shell. The symmetry of the molecules and the lattice results in a strong uniaxial anisotropy along the  $c$ -axis. The symmetry disallows second order transverse anisotropy. The anisotropy barrier of each molecule is about 65 K which blocks the magnetic moment along the  $c$ -axis. It exhibits an effective magnetic moment  $M = gS\mu_B = 20\mu_B$  at low temperature. The magnetism of this coordinative cluster is of purely *spin origin* because of the quenching of the orbital moment by the crystal field. The  $S = 10$  spin ground state is split into 21 components, with the two degenerate states  $m = \pm 10$  being the ground states.

Since Mn<sub>12</sub>-acetate has tetragonal symmetry, hence the term  $B_4^2$  is zero but not  $B_4^0$  and  $B_4^4$ . The rhombic constant is also zero ( $E = 0$ ). We can rewrite the Hamiltonian in Eq. 1.8 for the tetragonal symmetry as

$$\mathbf{H}_A = D[\mathbf{S}_z^2 - S(S+1)/3] + B_4^0\mathbf{O}_4^0 + B_4^4\mathbf{O}_4^4. \quad (1.66)$$

If  $O_4^0 = 35S_z^4 - 30S(S+1)S_z^2 + 25S_z^2 - 6S(S+1) + 3S^2(S+1)^2$ , and  $O_4^4 = 1/2(S_+^4 + S_-^4)$  [54], then a convenient spin Hamiltonian of Mn<sub>12</sub>-acetate including the Zeeman terms can be formulated as

$$H = DS_z^2 + BS_z^4 + g\mu_B\mathbf{S}_z\mathbf{H}_z + C(\mathbf{S}_+^4 + \mathbf{S}_-^4)/2 + g\mu_B\mathbf{S}_{x,y}\mathbf{H}_{x,y}, \quad (1.67)$$

where  $D$ ,  $B$ , and  $C$  are anisotropy constants of Mn<sub>12</sub>-acetate system. The first three terms in Eq. 1.67 are the axial terms while the last two terms are the transverse terms. Note that the spin operator  $S_{\pm}$  is equivalent to  $(S_x \pm iS_y)$ . The anisotropy

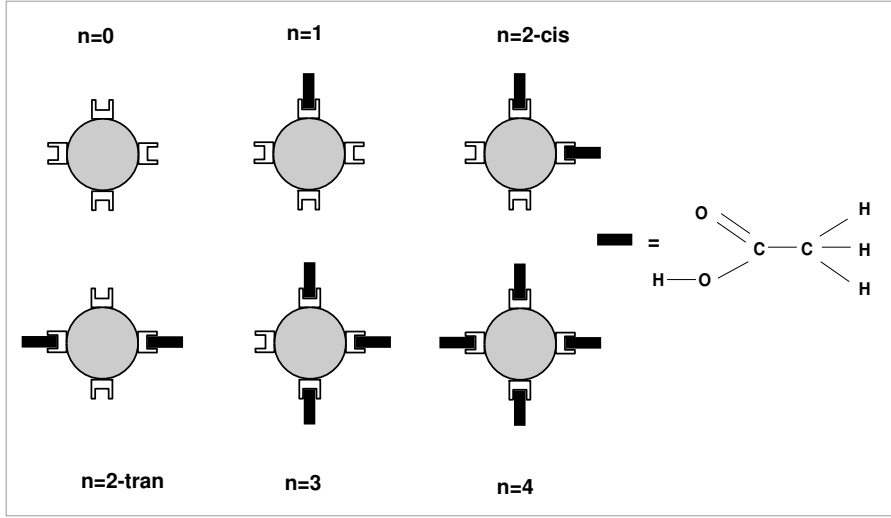


Figure 1.8: Six isomers of Mn<sub>12</sub>-acetate molecule are shown. The circles represent Mn<sub>12</sub>-acetate molecules.  $n$  is a number of acetic acid molecules which are represented by black rectangular shape [58].

constants can be obtained by using different techniques [54, 55, 56]. It was found that  $D \approx -0.56$  K,  $B \approx -1.1 \times 10^{-3}$  K, and  $C \approx \pm 3 \times 10^{-5}$  K.  $DS^2$  is typically around 60-70 K.

Eq. 1.67 contains no  $E$  term because it is not allowed by the tetragonal symmetry. However in the real crystal, there is the strong stress of the dislocations in the Mn<sub>12</sub>-acetate [57]. It leads to the extra transverse  $E$  term. The average value for  $E \approx 22$  mK [57].

The other origin of the  $E$  term also was discussed by A. Cornia *et al.* [58]. The idea of the isomer-model was proposed via the disorder of the acetic acid of crystallization induces the distortion of the Mn(III) sites. See Fig. 1.8. There are six different ways, namely six isomers, that the acetic acid can make the hydrogen bond to the manganese core. In Fig. 1.8, there are four isomers ( $n=1$ ,  $n=2$ -cis,  $n=2$ -trans, and  $n=3$ ) that have symmetry lower than tetragonal, leading to a nonzero  $E$  term. Only two isomers ( $n=0$ , and  $n=4$ ) have tetragonal symmetry. Moreover, six different isomers give different anisotropy constants  $D$ , and  $E$  values. The isomer property of Mn<sub>12</sub>-acetate leads to the distribution in the anisotropy constants which influences the line broadening in the magnetic resonance spectra [59].

To have an idea how the energy levels of the double-well potential look like, we use Eq. 1.67 without the transverse terms as a simplest case. The energy ( $E_m$ ) of each level  $m$  can be written as

$$E_m = Dm^2 + Bm^4 + g\mu_B H_z m. \quad (1.68)$$

According to Eq. 5.24, there is a condition of the magnetic field for matching of two energy levels ( $m, m'$ ) in the opposite wells, where  $m = 0, 1, 2, \dots, 10$  and  $m' =$



0, -1, -2, ..., -10. For  $E_m = E_{m'}$ ,

$$H_{mm'} = \frac{nD}{g\mu_B} \left[ 1 + \frac{B}{D} (m^2 + m'^2) \right], \quad (1.69)$$

where  $n = m + m'$ , where  $n=0,1,2,\dots,10$ .  $H_{mm'}$  is so called the *resonance field*.

### 1.2.2 Other molecular magnets

Beside  $\text{Mn}_{12}$ -acetate, there are many other molecular magnet systems that show interesting mesoscopic quantum phenomena. For example,  $\text{Fe}_8$  system also exhibits MQT [7]. It was first synthesized in the group of Wieghardt in 1984 [60]. Pure quantum tunneling behavior below 0.35 K was discovered in this system due to its large transverse anisotropy [61]. Later  $\text{Fe}_8$  was widely studied and topological constructive-destructive interference of the spin phase (Berry phase) was found in the transverse field dependence of the relaxation rate [7].

Molecular clusters with the complete antiferromagnetic cancellation of their spin giving  $S=0$  ground state are also interesting. In the last few years some of the antiferromagnetic ring-shaped clusters, which exhibit quantum-size effects, have been intensively studied [62, 63, 64, 65]. For example, large iron(III) rings can be a model of 1D-quantum antiferromagnets. These are the best candidates for investigating the properties of larger assemblies of interacting metal ions at the simplest level. In addition, mesoscopic quantum coherence might be observed in the form of coherence tunneling of the sublattice magnetization (the Néel vector) between classically degenerate directions over many periods [66].

Today, the number of new magnetic clusters that are synthesized and investigated increases exponentially. In manganese complex family, many compounds have been studied such as  $\text{Mn}_4$  [67],  $\text{Mn}_7$  with  $S=11$  [68],  $[\text{Mn}_8\text{O}_8]^{8+}$  with  $S=16$  [69],  $\text{Mn}_9$  with  $S=11/2$  [70],  $\text{Mn}_{10}$  with  $S=12$  [71]. Recently, larger clusters than  $\text{Mn}_{12}$ -acetate have been produced such as  $[\text{Mn}_{18}]^{2+}$  with  $S=13$  [72],  $\text{Mn}_{21}$  with  $S=17/2$  [73],  $\text{Mn}_{25}$  with  $S=51/2$  [74],  $\text{Mn}_{30}$  with  $S=5$  [75],  $\text{Mn}_{84}$  with  $S=6$  [76]. In the range of iron complexes, beside  $\text{Fe}_8$ , there are many iron compounds that have been investigated such as  $\text{Fe}_4$  [77, 78],  $\text{Fe}_2$ ,  $\text{Fe}_6$ ,  $\text{Fe}_{17}$ , and  $\text{Fe}_{19}$  [79, 80, 81, 82]. Many other inorganic based molecular magnets such as cyano-bridged complexes [83], cobalt based complexes [84, 85], nickel based complexes [86, 87], and copper based complexes [88] are also being investigated.

## 1.3 Molecular magnets in applications

Beside their significant properties to test the fundamental quantum theory and nanoscale magnetism prospects [1, 89], molecular magnets may have important technological applications as the nanoscale storage [90], qubits for quantum computation [67, 91, 92, 93], and the molecular electronics and magnetic devices [94, 95, 96, 97].

The  $\text{Mn}_{12}$ -acetate molecular magnet and its analogous clusters offer potential access to ultimate high density data storage devices, due to its well defined nanoscale size

and identically molecular structure with a single magnetic domain [2, 93, 98]. However, to achieve this role, the molecules need to be oriented properly in order to be addressed individually, where each molecule can be used as a bit of information. This can be done by arranging the molecules onto the thin film surface. An early attempt was to arrange  $\text{Mn}_{12}$ -acetate molecules into a well organized multilayer film by using Langmuir-Blodgett (LB) technique [99, 100]. In this work,  $\text{Mn}_{12}$ -acetate was embedded in multilayer fatty acid (behenic acid) where  $\text{Mn}_{12}$ -acetate formed an intercalated layer between the two headgroups of adjacent fatty acids. However this technique is very unstable when the  $\text{Mn}_{12}$ -acetate film is transferred to other substrates. The next approach is based on the preparation of the polymeric thin films which is made from polycarbonate matrix, and  $\text{Mn}_{12}$ -acetate complex [101]. This method is more reliable and simpler methodology than the LB technique.

However, at that time there has been no success to organize  $\text{Mn}_{12}$ -acetate molecules onto the conducting substrates. Until, there is a report by A. Cornia that depositing  $\text{Mn}_{12}$ -acetate-derivative molecules onto gold surface with monolayer or submonolayer coverage is possible [94]. The molecule can be addressed individually by the scanning probe microscope. Nanopatterning of aggregates of  $\text{Mn}_{12}$ -acetate with size and distance control on multiple length scale ranging from ten nanometers to millimeters was demonstrated by using the stamp-assisted deposition of the molecules technique [102].

Spin coating  $\text{Mn}_{12}\text{Cl}$  onto the silicon wafer is also already achieved [85]. In this work, the magnetic hysteresis of the tunneling current is reported, implying that magnetic character of the molecule influences the current transport in the single molecule level. The other interesting report is about depositing  $\text{Mn}_{12}$ -acetate molecules into the mesoporous silica as the magnetically addressed structure [103]. This work can also open the opportunity of the molecular magnet as the new functional materials.

However, due to its storage application, the problem of how to implement the process of reading and writing is still a major discussion [104]. It has been proposed to use these molecular clusters as qubit systems for quantum computers [91, 93]. It is also independently reported that it is feasible to encode and read-out the states of the molecular clusters by the interaction between the polarizing clusters and injected electrons [105].

Beside the molecular electronics application, recently, the superradiance effect (0.1-0.5 THz) from the avalanches of the magnetization reversal  $\text{Mn}_{12}$ -acetate was observed by J. Tejada *et al.* [106, 107, 108]. The electromagnetic radiation sources in the THz range are very rare. This suggests a new application of the molecular magnets as a new THz source. Consequently this field is very active. Lots of experimental results and sophisticated theories are reported.

## 1.4 Motivation of the Thesis

In this Thesis, we are interested in  $\text{Mn}_{12}$ -acetate system, since it is one of the prime examples of the single molecule magnets that shows the slow relaxation mechanism at reasonably low temperature (in order of a few seconds at 4 K, or a few months at 2 K). Therefore, its quantum tunneling dynamics are easily investigated with most

techniques without the use of a dilution refrigerator. The single crystal of this sample is also physically and chemically stable. So far, there are many techniques that have been applied to Mn<sub>12</sub>-acetate system e.g. the magnetometry technique [11, 27, 109, 110, 111, 112, 113], electron paramagnetic resonance (EPR) [54], nuclear magnetic resonance (NMR) [13, 114, 115, 116], muon spin resonance ( $\mu$ SR) [116], specific heat measurement [3], magnetic circular dichroism technique [117].

However, most of the MQT evidences were measured by the SQUID magnetometer. Nevertheless, this technique can not measure the local magnetization from each individual magnetic transitions but rather measure the magnetization of the whole system. In this point of view, the optical spectroscopy technique such as EPR has a better advantage since it can access each magnetic transition individually. However, in the typical EPR setup, the magnetic field is scannable while the frequency of the radiation is fixed. This technique can not directly observe the relaxation of the magnetization. Beside, EPR requires an applied magnetic field. In order to measure the zero field splitting parameters by using EPR technique, the results are extrapolated from the results in the magnetic fields, which might be inaccurate.

Therefore, we would like to introduce our new technique; Frequency-Domain Magnetic Resonance Spectroscopy (FDMRS), which is a frequency domain technique, to study both physical and relaxation properties in Mn<sub>12</sub>-acetate system. Firstly, FDMRS works either in zero or applied magnetic field. Therefore, compared to typical EPR technique, FDMRS can directly measure the zero field splitting parameters in the zero magnetic field.

Secondly, FDMRS can locally measure the magnetic transition compared to the typical SQUID magnetometer. MQT measured by SQUID is the macroscopic results. In contrast, by using FDMRS, we can observe the relaxation from the individual magnetic transitions. Beside we can obtain the relaxation time, we can also do the lineshape studies of the magnetic transitions during the relaxation process. Lineshape studies (such as linewidth, and lineshape) can give much fruitful information about the effects of the environmental (such as dipolar field, and hyperfine field) to the magnetic resonance transitions. Therefore, it is very interesting to measure the relaxation time and observe the environmental effect to the relaxation process at the same time.

Thirdly, our FDMRS setup can be arranged into two different magneto-optical geometries (Voigt and Faraday). The typical EPR setup requires the waveguide, therefore, the wave geometry is no longer important in this system since it is difficult to control the polarization of the radiation. In FDMRS, the radiation travels in free space, therefore the radiation polarization is remained. So far, there is no full reports on the magneto-optical studies on Mn<sub>12</sub>-acetate system. Since Mn<sub>12</sub>-acetate exhibit the bistability of the magnetization, therefore studying this system by using different light polarizations (linear or circular polarization) in different magneto-optical geometries, we might explore the new results in this field.

Therefore, we would like to apply FDMRS technique to qualitatively and quantitatively study Mn<sub>12</sub>-acetate molecular magnet system for both physical and relaxation characteristics.

## 1.5 Thesis outline

After we have introduced the general properties of the molecular magnets in this Chapter, in Chapter 2, we introduce the basic idea of the electrodynamics in which we will explain how the electromagnetic wave interacts with the matters and how the magnetic resonance works.

In Chapter 3, we introduce FDMRS technique for its history, detailed setup and operation, detailed measurement and spectra analysis.

In Chapter 4, we report the results in zero field and in magnetic field measurements on the static properties of  $\text{Mn}_{12}$ -acetate such as the zero field splitting (ZFS) parameters, g-value anisotropy, magnetic mode contribution, etc.

In Chapter 5, we report the magneto-optical properties of  $\text{Mn}_{12}$ -acetate.

In Chapter 6, we focus on the relaxation measurements in which we will report our observations on MQT phenomenon.

Chapter 7 is the summary of this Thesis in which the future works are included.

## Chapter 2

# Electromagnetic wave propagation and the magnetic resonance phenomenon

The main aim of this Thesis is to apply frequency-domain magnetic resonance spectroscopy (FDMRS) method to observe the magnetic transitions and magnetic relaxation (including the tunneling process) in molecular magnets. In order to understand our results throughout the whole Thesis, it is important to understand some basic concepts of electromagnetic (EM) wave propagation in a magnetic medium, and magnetic resonance (MR) theory. This Chapter is divided into two parts.

In the first part, we discuss the general concept of the basic EM wave propagation theory. First we discuss the wave equations in space, in a medium and at the interface. Then we make a note on the polarization property of the radiation and the wave propagation geometries with respect to the applied magnetic field direction; Voigt and Faraday geometry. Later we will go through more details of how the medium responds to the radiation where we introduce the material parameters such as dielectric permittivity and magnetic permeability. We also include the derivation of these parameters for each wave propagation case (Voigt and Faraday). Note that most works in this Thesis are done in **CGS** units.

For the second part, we discuss basic MR theory including MR mechanism, transition probability and transition absorption line.

## 2.1 Electromagnetic wave propagation

### 2.1.1 Electromagnetic waves in space

Electromagnetic (EM) waves are defined as a time and space varied combination of alternating electric and magnetic fields. J.C Maxwell was the first who successfully derived the electric and magnetic field relation through the famous Maxwell equations. In the vacuum, time ( $t$ ) and space ( $\mathbf{r}$ ) varying Maxwell equations in the revised version are written in (CGS units) as

$$\nabla \times \mathbf{E}(\mathbf{r}, t) + \frac{1}{c} \frac{\partial \mathbf{B}(\mathbf{r}, t)}{\partial t} = 0, \quad (2.1)$$

$$\nabla \cdot \mathbf{B}(\mathbf{r}, t) = 0, \quad (2.2)$$

$$\nabla \times \mathbf{B}(\mathbf{r}, t) - \frac{1}{c} \frac{\partial \mathbf{E}(\mathbf{r}, t)}{\partial t} = \frac{4\pi}{c} \mathbf{J}(\mathbf{r}, t), \quad (2.3)$$

$$\nabla \cdot \mathbf{E}(\mathbf{r}, t) = 4\pi\rho(\mathbf{r}, t), \quad (2.4)$$

where  $\mathbf{E}$  is the electric field strength,  $\mathbf{B}$  is the magnetic induction,  $c$  is the light velocity ( $3 \times 10^8 \text{ ms}^{-1}$ ),  $\mathbf{J}$  is the current density, and  $\rho$  is the charge density. These parameters are dependent of spatial ( $\mathbf{r}$ ) and time ( $t$ ). By assuming that the waves are monochromatic, the solutions of the above Maxwell equations in vacuum are

$$\mathbf{E}(\mathbf{r}, t) = \mathbf{E}_0 \exp \{i(\mathbf{q} \cdot \mathbf{r} - \omega t)\}, \quad (2.5)$$

$$\mathbf{B}(\mathbf{r}, t) = \mathbf{B}_0 \exp \{i(\mathbf{q} \cdot \mathbf{r} - \omega t)\}, \quad (2.6)$$

where  $\mathbf{q}$  is the wave vector, and  $\omega$  is the wave frequency.

### 2.1.2 Electromagnetic waves in a medium

The Maxwell equations for a medium are written as

$$\nabla \times \mathbf{E}(\mathbf{r}, t) + \frac{1}{c} \frac{\partial \mathbf{B}(\mathbf{r}, t)}{\partial t} = 0, \quad (2.7)$$

$$\nabla \cdot \mathbf{B}(\mathbf{r}, t) = 0, \quad (2.8)$$

$$\nabla \times \mathbf{H}(\mathbf{r}, t) - \frac{1}{c} \frac{\partial \mathbf{D}(\mathbf{r}, t)}{\partial t} = \frac{4\pi}{c} \mathbf{J}_{\text{cond}}(\mathbf{r}, t), \quad (2.9)$$

$$\nabla \cdot \mathbf{D}(\mathbf{r}, t) = 4\pi\rho_{\text{ext}}(\mathbf{r}, t), \quad (2.10)$$

where  $\mathbf{D}$  is the displacement field which can be explained as the response of a solid to an electric field  $\mathbf{E}$  and written as  $\mathbf{D} = \hat{\epsilon}\mathbf{E}$ .  $\hat{\epsilon} = \epsilon' + i\epsilon''$  is the dielectric permittivity.  $\mathbf{H}$  is the magnetic field strength, which is associated with the magnetic induction  $\mathbf{B}$  by  $\mathbf{B} = \hat{\mu}\mathbf{H}$ .  $\hat{\mu} = \mu' + i\mu''$  is the magnetic permeability.  $\mathbf{J}_{\text{cond}}$  is conduction current in a medium related with  $\mathbf{E}$  via the conductivity  $\hat{\sigma}$  as  $\mathbf{J}_{\text{cond}} = \hat{\sigma}\mathbf{E}$ .  $\hat{\sigma} = \sigma' + i\sigma''$ .  $\rho_{\text{ext}}$  is external charge from outside.

The solutions of wave equations in an infinite medium (to avoid boundary and the edge effects) with no free charge ( $\rho_{\text{ext}} = 0$ ) and no external current ( $J_{\text{ext}} = 0$ ) are

$$\mathbf{E}(\mathbf{r}, t) = \mathbf{E}_0 \exp \{i(\mathbf{q} \cdot \mathbf{r} - \omega t)\}, \quad (2.11)$$

$$\mathbf{H}(\mathbf{r}, t) = \mathbf{H}_0 \exp \{i(\mathbf{q} \cdot \mathbf{r} - \omega t)\}. \quad (2.12)$$

The response functions of the medium to the EM waves such as  $\epsilon$ ,  $\mu$ , and  $\sigma$  are important as material parameters. The main optical properties of the medium are

the *real* refractive index ( $n$ ) and the extinction coefficient ( $k$ ) which are used for the propagation and dissipation of the EM wave in the medium. To relate the material parameters and the optical response function, we define a new response function called the *complex* refractive index ( $\hat{N}$ )

$$\hat{N} = n + ik = [\hat{\epsilon}\hat{\mu}]^{1/2}, \quad (2.13)$$

$$n^2 - k^2 = \epsilon'\mu'. \quad (2.14)$$

The important relation between  $n$  and  $k$  expressed through the phase difference is

$$\tan \phi = \frac{k}{n}. \quad (2.15)$$

We define the relation between the propagation wave vector ( $\mathbf{q}$ ) and the complex propagation wave vector ( $\hat{q}$ ) as

$$\mathbf{q} = \hat{q}\mathbf{n}_q, \quad (2.16)$$

where  $\mathbf{n}_q$  is the unit wave vector defined as  $\mathbf{n}_q = \mathbf{q}/|\mathbf{q}|$ . The dispersion relation between  $\omega$  and  $\hat{q}$  can be written as

$$\hat{q} = \frac{\omega}{c}\hat{N} = \frac{n\omega}{c} + i\frac{k\omega}{c}. \quad (2.17)$$

Substituting equation 2.17 into equation 2.11, we obtain separately real and imaginary parts of the wave that go through the medium as

$$\mathbf{E}(\mathbf{r}, t) = \mathbf{E}_0 \exp\{i\omega(\frac{n}{c}\mathbf{n}_q \cdot \mathbf{r} - t)\} \exp\{-\frac{\omega k}{c}\mathbf{n}_q \cdot \mathbf{r}\}. \quad (2.18)$$

We can see here that the real part of the complex wave vector  $\mathbf{q}$  represents a travelling wave while the imaginary part expresses the attenuation term. The first exponent describes the fact that the velocity of light is reduced to  $c/n$ . The second exponent gives the damping term. This is also true for the magnetic field wave since it has the same  $\mathbf{q}$ .

### 2.1.3 Electromagnetic waves at the interface

To this point, we have already explained how the EM waves propagate through the medium. Now we have to discuss what will happen to the waves at the interface. For simplicity, we use the infinite thickness medium as the example. At the interface between medium 1 and medium 2, part of the wave is transmitted and part is reflected. Fig. 2.1 shows the transmission and reflection wave diagram. We use Fresnel formulas to describe both transmission and reflection wave phenomena. Here

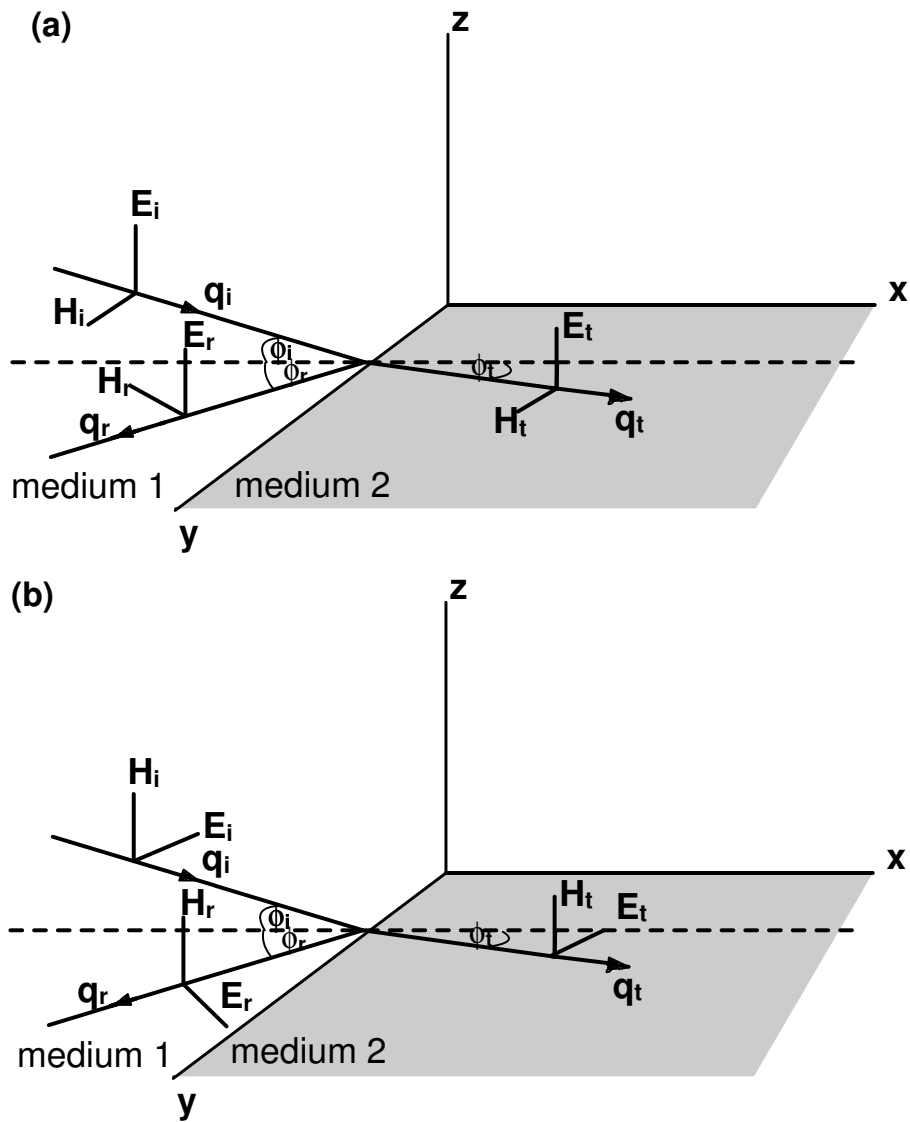


Figure 2.1: Reflection and transmission of an electromagnetic wave at the interface between the medium 1 and medium 2; (a) with the electric field ( $\vec{E}$ ) perpendicular to the  $xy$ -plane of incidence where the magnetic field ( $\vec{H}$ ) lies in the  $xy$ -plane. (b) with electric field ( $\vec{E}$ ) parallel to the  $xy$ -plane of incidence where the magnetic field ( $\vec{H}$ ) is perpendicular to the  $xy$ -plane.



we define the following notation;  $\mathbf{E}_i = E_{0i} \exp\{i(\mathbf{q} \cdot \mathbf{r} - \omega_i t)\}$  is the incident wave,  $\mathbf{E}_r = E_{0r} \exp\{i(\mathbf{q} \cdot \mathbf{r} - \omega_r t)\}$  is the reflected wave, and  $\mathbf{E}_t = E_{0t} \exp\{i(\mathbf{q} \cdot \mathbf{r} - \omega_t t)\}$  is the transmitted wave. The angle  $\phi_i$  is an incident angle of  $\mathbf{q}_i$ ,  $\phi_r$  is reflected angle of  $\mathbf{q}_r$ ,  $\phi_t$  is transmitted angle of  $\mathbf{q}_t$  in the plane- $\mathbf{xy}$ .  $\mu'_1$  and  $\mu'_2$  are the real part of the magnetic permeability of the medium 1 and the medium 2, respectively.  $\hat{N}$  is the complex refractive index. In the case of  $\mathbf{E}_i$  perpendicular to the  $\mathbf{xy}$ -plane of incidence, the complex transmission and reflection coefficients are

$$\begin{aligned} \hat{t}_\perp &= \frac{E_{0t}}{E_{0i}}, \\ &= \frac{2\mu'_1 \cos \phi_i}{\mu'_1 \cos \phi_i + \sqrt{(\hat{N}^2 - \sin^2 \phi_i)}}, \end{aligned} \quad (2.19)$$

$$\begin{aligned} \hat{r}_\perp &= \frac{E_{0r}}{E_{0i}}, \\ &= \frac{\mu'_1 \cos \phi_i - \sqrt{(\hat{N}^2 - \sin^2 \phi_i)}}{\mu'_1 \cos \phi_i + \sqrt{(\hat{N}^2 - \sin^2 \phi_i)}}. \end{aligned} \quad (2.20)$$

If  $\mathbf{E}_i$  is in the plane of incidence  $\mathbf{xy}$ , we obtain the Fresnel formulas for  $\mathbf{E}_i$  parallel to the plane of incidence  $\mathbf{xy}$

$$\begin{aligned} \hat{t}_\parallel &= \frac{E_{0t}}{E_{0i}}, \\ &= \frac{2\mu'_1 \hat{N} \cos \phi_i}{\hat{N}^2 \cos \phi_i + \mu'_1 \sqrt{(\hat{N}^2 - \sin^2 \phi_i)}}, \end{aligned} \quad (2.21)$$

$$\begin{aligned} \hat{r}_\parallel &= \frac{E_{0r}}{E_{0i}}, \\ &= \frac{\hat{N}^2 \cos \phi_i - \mu'_1 \sqrt{(\hat{N}^2 - \sin^2 \phi_i)}}{\hat{N}^2 \cos \phi_i + \mu'_1 \sqrt{(\hat{N}^2 - \sin^2 \phi_i)}}. \end{aligned} \quad (2.22)$$

Further reading can be found in [118].

### 2.1.4 Polarization

Before we continue to the next section (dielectric and magnetic properties of the medium), It would be useful to know some basic ideas about the polarization principle of EM waves because the interaction between the EM radiation and the matter can be sensitive to some external parameters i.e. light polarization, magnetic field direction, direction of light propagation, etc.

#### Linear Polarization

If a wave moves in the  $\mathbf{z}$  direction and its electric field component oscillates in the  $\mathbf{x}$  direction, it is said to be linearly polarized in the  $\mathbf{x}$  direction. The wave equations can

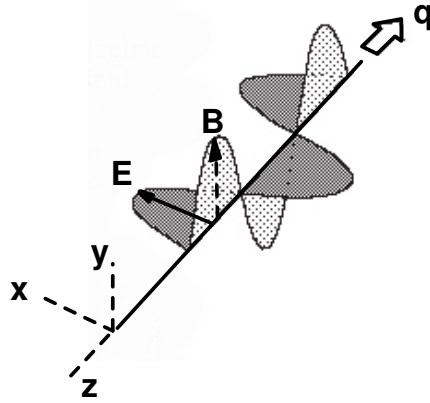


Figure 2.2: Wave diagram shows *linearly polarized* wave in  $\mathbf{x}$  direction.

be expressed as

$$\mathbf{E} = E_0 \mathbf{x} \cos(qz - \omega t), \quad (2.23)$$

$$\mathbf{B} = B_0 \mathbf{y} \cos(qz - \omega t), \quad (2.24)$$

$$\frac{\omega}{q} = c. \quad (2.25)$$

A similar solution is obtained for a wave that moves in the  $\mathbf{z}$  direction with its electric field component oscillating in the  $\mathbf{y}$  direction. Such a wave is said to be linearly polarized in the  $\mathbf{y}$  direction.

$$\mathbf{E} = E_0 \mathbf{y} \cos(qz - \omega t), \quad (2.26)$$

$$\mathbf{B} = B_0 \mathbf{x} \cos(qz - \omega t). \quad (2.27)$$

$$\frac{\omega}{k} = c \quad (2.28)$$

### Circular Polarization

We also can make circularly polarized light by adding  $x$  and  $y$  linearly polarized light but make them out of phase in time by  $90^\circ$ . A right circularly polarized wave is described by

$$\mathbf{E} = E_0 [\mathbf{x} \cos(qz - \omega t) + \mathbf{y} \sin(qz - \omega t)], \quad (2.29)$$

$$\mathbf{B} = B_0 [\mathbf{y} \cos(qz - \omega t) - \mathbf{x} \sin(qz - \omega t)]. \quad (2.30)$$

Similarly, a left circularly wave looks like

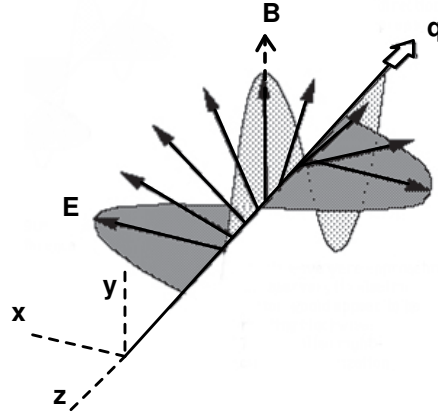


Figure 2.3: Wave diagram showing a *circularly polarized* wave. If approaching an observer, the electric vector ( $\mathbf{E}$ ) of this wave would appear to be rotating clockwise and this is called right hand circular polarization.

$$\mathbf{E} = E_0[\mathbf{x} \cos(qz - \omega t) - \mathbf{y} \sin(qz - \omega t)], \quad (2.31)$$

$$\mathbf{B} = B_0[\mathbf{y} \cos(qz - \omega t) + \mathbf{x} \sin(qz - \omega t)]. \quad (2.32)$$

We can also have linearly polarized wave by adding right and left circularly waves together with the equal amplitude and the right phase shift.

### 2.1.5 Wave propagation geometries

When an external d.c. magnetic field ( $\mathbf{H}_{ext}$ ) is applied to the system, different wave propagation directions of the r.f. radiation exist with respect to the direction of the applied magnetic field. In this Thesis, we concern two types of such the arrangements namely Voigt and Faraday geometry. We introduce these following parameters of the r.f. radiation; propagation wave vector ( $\mathbf{q}$ ), electric field component ( $\mathbf{e}$ ), and magnetic field component ( $\mathbf{h}$ ).

#### Voigt geometry

Voigt geometry is described as having  $\mathbf{q} \perp \mathbf{H}_{ext}$ . We can set  $\mathbf{e}$  parallel or perpendicular to  $\mathbf{H}_{ext}$ . Similar considerations for  $\mathbf{h}$ . It can be expressed in an orthogonal geometry as

$$(\mathbf{q} \parallel \mathbf{y}) \perp (\mathbf{H}_{ext} \parallel \mathbf{h} \parallel \mathbf{z}), \quad \mathbf{e} \parallel \mathbf{x}, \quad (2.33)$$

$$(\mathbf{q} \parallel \mathbf{y}) \perp (\mathbf{H}_{ext} \parallel \mathbf{e} \parallel \mathbf{z}), \quad \mathbf{h} \parallel \mathbf{x}. \quad (2.34)$$

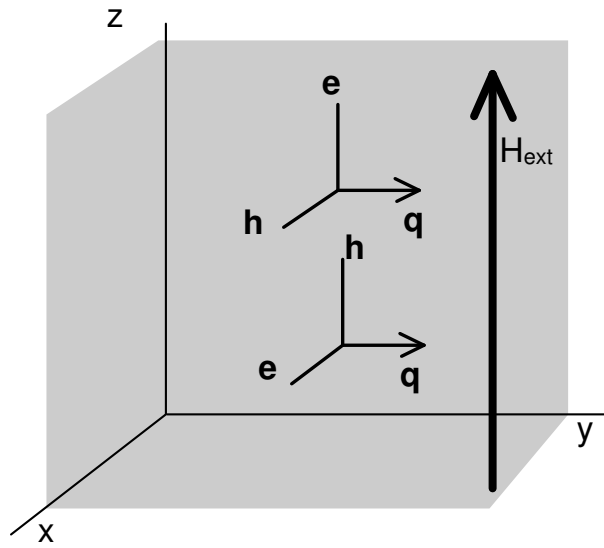


Figure 2.4: Voigt geometry where electromagnetic wave ( $\mathbf{e}, \mathbf{h}$ ) with propagation direction ( $\mathbf{q}$ ) perpendicular to the bias d.c. field  $\mathbf{H}_{ext}$ ;  $\mathbf{q} \perp \mathbf{H}_{ext}$ .

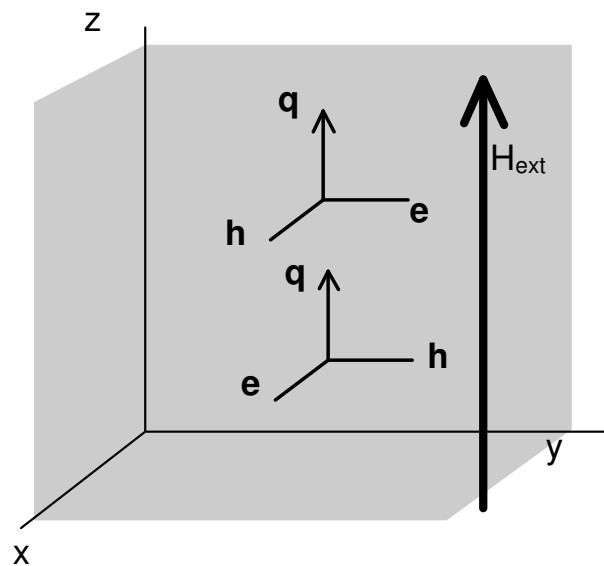


Figure 2.5: Faraday geometry where electromagnetic wave ( $\mathbf{e}, \mathbf{h}$ ) with propagation direction ( $\mathbf{q}$ ) parallel to the bias d.c. field  $\mathbf{H}_{ext}$ ;  $\mathbf{q} \parallel \mathbf{H}_{ext}$ .

### Faraday geometry

Faraday geometry is described as  $\mathbf{q} \parallel \mathbf{z} \parallel \mathbf{H}_{ext}$ . We can have the following cases:

$$\mathbf{q} \parallel \mathbf{H}_{ext} \parallel \mathbf{z}, (\mathbf{e} \parallel \mathbf{x}) \perp (\mathbf{h} \parallel \mathbf{y}) \perp \mathbf{H}_{ext}, \quad (2.35)$$

$$\mathbf{q} \parallel \mathbf{H}_{ext} \parallel \mathbf{z}, (\mathbf{e} \parallel \mathbf{y}) \perp (\mathbf{h} \parallel \mathbf{x}) \perp \mathbf{H}_{ext}. \quad (2.36)$$

The schematic of Voigt and Faraday geometry is shown in Fig. 2.4 and Fig. 2.5. Here we can see that in Faraday geometry,  $\mathbf{h}$  strongly couples to  $\mathbf{H}_{ext}$  giving us a strong magneto-optical effect, so called the Faraday effect, where the plane of polarization of the light is rotated from the initial plane position. This geometry has been widely used to measure the magnetization in ferromagnetic and ferrimagnetic materials [119, 120]. Note that, there is also a coupling between  $\mathbf{h}$  and  $\mathbf{H}_{ext}$  in Voigt geometry but small compared to the Faraday case. See Fig. 2.4 for example, the torque between  $\mathbf{h}$  and  $\mathbf{H}_{ext}$  is maximum for the upper radiation while it is minimum for the lower radiation scheme. In Faraday case, see Fig. 2.5,  $\mathbf{h}$  is always perpendicular to  $\mathbf{H}_{ext}$  for both radiation schemes giving the maximum torque always. As a result, the magneto-optic effect in Voigt geometry is less sensitive to the mode of light polarization than in Faraday geometry, which we shall see in the later Section.

### 2.1.6 Dielectric permittivity and magnetic permeability tensor of the second rank

We have already introduced the properties of the medium such as dielectric permittivity ( $\epsilon$ ), magnetic permeability ( $\mu$ ), and conductivity ( $\sigma$ ) in Section 2.1.2. In this section, we will discuss in more details about the properties of these quantities. In this Thesis, we will omit  $\sigma$  quantity since it is not in our particular interests.

In physics, normally we have three types of quantities: scalar, vector, and tensor. Tensor is the quantity connected to any possibly defined reference direction. The  $n$  rank tensor defined as  $3^n$  components. Scalar and Vector can be classified as a tensor of zero and first rank respectively. The tensor of a second rank defined by nine numbers. It follows from the tensor algebra that the quantity, connecting the other two physical quantities for example between f-rank and g-rank tensor quantities, will have the [f+g] rank tensor. For example, dielectric permittivity is a second-rank tensor quantity because it connects the dielectric displacement and the electric field, each of which is a first-rank tensor quantity. That is why the dielectric permittivity tensor is a second-rank tensor quantity. The same rule applies to the other physical quantities which are in the second-rank form such as electrical conductivity, thermal conductivity, permittivity, permeability, etc. Further reading refer to [121].

In an *isotropic* medium, the  $\epsilon$ ,  $\mu$ , and  $\sigma$  quantities are scalars but more general, the mediums are *anisotropic* such as the crystal and these quantities are in a second rank tensor form. Here we will discuss for each case:

### Dielectric permittivity

Dielectric permittivity ( $\epsilon$ ) is a measure of how much a medium changes when it interacts to an electric field. In an *isotropic* medium, ( $\epsilon$ ) is scalar quantity defined as  $\epsilon = \mathbf{D}/\mathbf{E}$  where  $\mathbf{D}$  is displacement field and  $\mathbf{E}$  is electric field, which are parallel to each other. In the *anisotropic* medium, it is called *permittivity tensor* defined as  $\tilde{\epsilon} = \mathbf{D}/\mathbf{E}$  where  $\mathbf{D}$  are no longer parallel to  $\mathbf{E}$ . For example, we can write the second rank permittivity tensor in the crystal as

$$\tilde{\epsilon} = \begin{pmatrix} \epsilon_{xx} & \epsilon_{xy} & \epsilon_{xz} \\ \epsilon_{yx} & \epsilon_{yy} & \epsilon_{yz} \\ \epsilon_{zx} & \epsilon_{zy} & \epsilon_{zz} \end{pmatrix}. \quad (2.37)$$

Note that the tensor multiplication is the same as in matrix or vector multiplication. For example, we can write

$$D_x = \epsilon_{xx}E_x + \epsilon_{xy}E_y + \epsilon_{xz}E_z. \quad (2.38)$$

In case, if the medium has

$$\epsilon_{ij} = \epsilon_{ji}, \quad (2.39)$$

then this results in *diagonal* permittivity tensor in a properly defined coordinate frame (with principal axes)

$$\tilde{\epsilon} = \begin{pmatrix} \epsilon_{xx} & 0 & 0 \\ 0 & \epsilon_{yy} & 0 \\ 0 & 0 & \epsilon_{zz} \end{pmatrix}. \quad (2.40)$$

The medium is uniaxial when any two pairs are equal  $\epsilon_{xx} = \epsilon_{yy} \neq \epsilon_{zz}$  and biaxial when  $\epsilon_{xx} \neq \epsilon_{yy} \neq \epsilon_{zz}$ . In this Thesis, we keep the dielectric permittivity as a constant value due to very strong magnetic absorption in Mn<sub>12</sub>-acetate sample.

### Magnetic permeability

Similarly considerations are valid for the magnetic permittivity ( $\mu$ ), which is the degree of magnetization of a medium in response to a magnetic field. In an *isotropic* medium,  $\mu$  is a scalar quantity defined as  $\mu = \mathbf{B}/\mathbf{H}$  where  $\mathbf{B}$  is and  $\mathbf{H}$  are parallel. In an *anisotropic* medium, it is called *permeability tensor* defined as  $\tilde{\mu} = \mathbf{B}/\mathbf{H}$  where  $\mathbf{B}$  are no longer parallel to  $\mathbf{H}$ . For example, we can write the second rank permeability tensor in the crystal as

$$\tilde{\mu} = \begin{pmatrix} \mu_{xx} & \mu_{xy} & \mu_{xz} \\ \mu_{yx} & \mu_{yy} & \mu_{yz} \\ \mu_{zx} & \mu_{zy} & \mu_{zz} \end{pmatrix}. \quad (2.41)$$

The permeability tensor ( $\tilde{\mu}$ ) was first derived by D. Polder [122]. Here we will follow his work to have some fruitful ideas about the tensor quantities  $\tilde{\mu}$ . Polder

derived  $\tilde{\mu}$  through the ferromagnetic resonance in ferrites. When ferrites are subjected to a d.c. polarizing field in the  $\mathbf{z}$  direction, the spin direction of the electron cloud makes an angle  $\theta$  with respect to the  $\mathbf{z}$  axis. We defined  $\mathbf{P}$  as the angular momentum, and  $\mathbf{m}$  is the magnetic moment of the electron. If a uniform magnetic flux density ( $\mathbf{B} = B_{ext}\mathbf{z} = \mu_0 H_{ext}\mathbf{z}$ ) is applied, we can write the torque acts on the electron as

$$\begin{aligned} \frac{d\mathbf{P}}{dt} &= \mathbf{T} \\ &= \mu_0 \mathbf{m} \times \mathbf{H} \\ &= -\mu_0 |\gamma| \mathbf{P} \times \mathbf{H} \\ &= \omega_L \times \mathbf{P}, \end{aligned} \quad (2.42)$$

where  $\omega_L = |\gamma| B_{ext}$  is the Larmor precession frequency and  $\gamma$  is the ratio of the spin magnetic moment to the spin angular momentum or said to be  $q/m_e = 1.759 \times 10^{11}$  C/Kg.

We emphasize again that the first assumption is the d.c. magnetic field ( $\mathbf{H}_{ext}$ ) is applied in  $\mathbf{z}$  direction. Now we apply r.f. microwave radiation ( $\mathbf{h}$ ) as an additional perturbation creating a (small) time harmonic wave field of frequency  $\omega$ . This r.f. wave can approach the material from any direction. The time dependent term is  $exp\{i\omega t\}$ . Now the total magnetic field is

$$\mathbf{H} = \mathbf{H}_{ext} + \mathbf{h}exp\{i\omega t\} = H_{ext}\mathbf{z} + \mathbf{h}exp\{i\omega t\}, \quad (2.43)$$

where  $h \ll H_{ext}$  and the material is a large sum of individual moments with identical spin. Thus it follows the the magnetization ( $\mathbf{M} = \tilde{\chi} \cdot \mathbf{H}$ , where  $\tilde{\chi}$  is the magnetic susceptibility tensor)

$$\mathbf{M} = \mathbf{M}_s + \mathbf{m}exp\{i\omega t\} = M_s\mathbf{z} + \mathbf{m}exp\{i\omega t\}, \quad (2.44)$$

where  $\mathbf{M}_s$  is the saturated state and  $\mathbf{m}$  is the magnetization induced by the perturbation r.f. field. The torque in equation 2.42 now can be rewritten as

$$\frac{d\mathbf{M}}{dt} = -\mu_0 |\gamma| \mathbf{M} \times \mathbf{H}. \quad (2.45)$$

By substituting forms for  $\mathbf{M}$  and  $\mathbf{H}$ , the Eq. 2.45 becomes

$$\begin{aligned} \frac{d\mathbf{m}}{dt} &= -|\gamma| \mu_0 (\mathbf{m} \times \mathbf{H}_{ext} + \mathbf{M}_s \times \mathbf{h} + \mathbf{m} \times \mathbf{h}), \\ &\simeq -|\gamma| \mu_0 (\mathbf{m} \times \mathbf{H}_{ext} + \mathbf{M}_s \times \mathbf{h}), \end{aligned} \quad (2.46)$$

where each component yields

$$m_x = i \frac{\omega_L}{\omega} (m_y - M_s \frac{h_y}{H_{ext}}), \quad (2.47)$$

$$m_y = i \frac{\omega_L}{\omega} (M_s \frac{h_x}{H_{ext}} - m_x), \quad (2.48)$$

$$i\omega m_z = 0. \quad (2.49)$$

We have assumed that the time dependence is  $\exp\{i\omega t\}$  and  $M_s$  and  $H_{ext}$  lie along  $\mathbf{z}$  direction. We solve for  $\mathbf{M}$  in terms of  $\mathbf{H}$  and then derive the resulting form of the permeability tensor by using  $\mathbf{B} = \mu_0(\mathbf{H} + \mathbf{M}) = \tilde{\mu} \cdot \mathbf{H}$ , where  $\mu_0$  is magnetic permeability in vacuum. We then obtain

$$b_x = \mu_0 h_x + \frac{\mu_0 \omega_L \omega_s}{\omega_L^2 - \omega^2} h_x - i \frac{\mu_0 \omega \omega_s}{\omega_L^2 - \omega^2} h_y, \quad (2.50)$$

$$b_y = \mu_0 h_y + \frac{\mu_0 \omega_L \omega_s}{\omega_L^2 - \omega^2} h_y + i \frac{\mu_0 \omega \omega_s}{\omega_L^2 - \omega^2} h_x, \quad (2.51)$$

where  $\omega_L = |\gamma| B_{ext}$  is the Larmor precession due to the applied d.c. field.  $\omega_s = \mu_0 |\gamma| M_s$  depends on the materials. Now we can write the permeability tensor for the ferrite-type materials where external d.c. magnetic field applied in  $\mathbf{z}$  direction as

$$\tilde{\mu}_{H_{ext}||z} = \begin{pmatrix} \mu_{xx} & \mu_{xy} & \mu_{xz} \\ \mu_{yx} & \mu_{yy} & \mu_{yz} \\ \mu_{zx} & \mu_{zy} & \mu_{zz} \end{pmatrix} = \begin{pmatrix} \mu_{xx} & \mu_{xy} & 0 \\ \mu_{yx} & \mu_{yy} & 0 \\ 0 & 0 & \mu_0 \end{pmatrix}, (H_z) \quad (2.52)$$

where

$$\mu_{xx} = \mu_{yy} = \mu_0 \left( 1 + \frac{\omega_L \omega_s}{\omega_L^2 - \omega^2} \right), \quad (2.53)$$

$$\mu_{xy} = -\mu_{yx} = i \frac{\mu_0 \omega \omega_s}{\omega_L^2 - \omega^2}. \quad (2.54)$$

We can rewrite Eq. 2.52 in a conventional way as

$$\tilde{\mu}_{H_{ext}||z} = \mu_0 \begin{pmatrix} \mu & -i\kappa & 0 \\ i\kappa & \mu & 0 \\ 0 & 0 & 1 \end{pmatrix}, \quad (2.55)$$

where  $\mu$  and  $\kappa$  are defined as

$$\mu = 1 + \frac{\omega_L \omega_s}{\omega_L^2 - \omega^2}, \quad (2.56)$$

$$\kappa = \frac{\omega \omega_s}{\omega_L^2 - \omega^2}. \quad (2.57)$$

If the material is biased by the magnetic field in another orthogonal direction. The permeability tensor will be transformed due to the change in coordinates. Hence, if we have  $\mathbf{H}_{ext} = H_{ext} \mathbf{x}$ , the permeability tensor will be



$$\tilde{\mu}_{H_{ext}\parallel x} = \begin{pmatrix} \mu_0 & 0 & 0 \\ 0 & \mu_{yy} & \mu_{yz} \\ 0 & \mu_{zy} & \mu_{zz} \end{pmatrix}, (H_x) \quad (2.58)$$

If  $\mathbf{H}_{ext} = H_{ext}\mathbf{y}$ , the permeability tensor will be

$$\tilde{\mu}_{H_{ext}\parallel y} = \begin{pmatrix} \mu_{xx} & 0 & \mu_{xz} \\ 0 & \mu_0 & 0 \\ \mu_{zx} & 0 & \mu_0 \end{pmatrix}, (H_y) \quad (2.59)$$

### Effective magnetic permeability

The macroscopic or measurable quantity of  $\tilde{\mu}$  is called *effective permeability* ( $\mu_{eff}$ ). This scalar quantity only depends on the geometry of the wave propagation (i.e. Voigt and Faraday) interact with the external magnetic field. To calculate  $\mu_{eff}$ , one needs to look at the *complex propagation* constant ( $\Gamma$ ) for each mode of the wave propagation. First of all, we need the general form of  $\Gamma$ . It can be obtained by writing the Maxwell equations which includes the permeability tensor taken from Eq. 2.55. We then obtain

$$\nabla \times \mathbf{E} = -i\omega\tilde{\mu} \cdot \mathbf{H}, \quad (2.60)$$

$$\nabla \times \mathbf{H} = i\omega\epsilon\mathbf{E}. \quad (2.61)$$

By eliminating the  $\mathbf{E}$  term, we can rewrite Eq. 2.60 as

$$\nabla \times \nabla \times \mathbf{H} = -\nabla^2\mathbf{H} + \nabla(\nabla \cdot \mathbf{H}) = \omega^2\epsilon\tilde{\mu} \cdot \mathbf{H}. \quad (2.62)$$

If we rewrite the plane wave solution of the perturbed r.f. radiation as

$$\mathbf{h} = \mathbf{h}_0 \exp\{-\Gamma(\mathbf{n}_q \cdot \mathbf{r})\}, \quad (2.63)$$

where  $\mathbf{h}$  is magnetic field component of the radiation,  $\mathbf{n}_q$  is the unit wave vector in the direction of propagation,  $\mathbf{r}$  is the displacement vector, and the complex wave propagation constant is  $\Gamma = \alpha + i\beta$ . Then we can rewrite  $\nabla(\nabla \cdot \mathbf{H}) = \Gamma^2(\mathbf{n}_q \cdot \mathbf{h}\mathbf{n}_q)$  which is equivalent to  $\nabla^2\mathbf{H} = \Gamma^2 n_q^2 \mathbf{h}$ . Now we can rewrite Eq. 2.62 as

$$\Gamma^2[-n_q^2\mathbf{h} + (\mathbf{n}_q \cdot \mathbf{h})\mathbf{n}_q] = \omega^2\epsilon\tilde{\mu} \cdot \mathbf{h}. \quad (2.64)$$

Now we need to write down three linear equations of  $h_x$ ,  $h_y$ , and  $h_z$  from Eq. 2.62. First we assume that the magnetic field  $\mathbf{H}_{ext}$  is in  $\mathbf{z}$  direction, propagation vector is in  $\mathbf{xz}$  plane. Therefore we can write  $\mathbf{n}_q$  into  $\{x, y, z\}$  directions as;  $n_{q,y} = 0$ ,  $n_{q,x} = \sin\psi$ , and  $n_{q,z} = \cos\psi$ , where  $\psi$  is the angle between propagation direction and  $\mathbf{H}_{ext}$ . These give us the three component linear equations of  $h_x$ ,  $h_y$ , and  $h_z$  with the vanishing determinant of the coefficients

$$\begin{vmatrix} -\Gamma^2 \cos \psi^2 - \omega^2 \epsilon \mu_0 \mu & i\omega^2 \epsilon \mu_0 \kappa & \Gamma^2 \sin \psi \cos \psi \\ -i\omega^2 \epsilon \mu_0 \kappa & -\Gamma^2 - \omega^2 \epsilon \mu_0 \mu & 0 \\ \Gamma^2 \sin \psi \cos \psi & 0 & -\Gamma^2 \sin \psi^2 - \omega^2 \epsilon \mu_0 \end{vmatrix} = 0 \quad (2.65)$$

where  $\mu$  and  $\kappa$  are defined in Eq. 2.56. If we expand the above determinant, we can obtain a general form of  $\Gamma$  as

$$\Gamma_{\pm}^2 = -\omega^2 \epsilon \mu_0 \frac{(\mu^2 - \mu - \kappa^2) \sin \psi^2 + 2\mu \pm [(\mu^2 - \mu - \kappa^2)^2 \sin \psi^4 + 4\kappa^2 \cos \psi^2]^{1/2}}{2(\cos \psi^2 + \mu \sin \psi^2)}. \quad (2.66)$$

Finally we can determine  $\mu_{eff}$  for each propagation case.

### i) $\mu_{eff,V}$ for Voigt geometry

In Voigt geometry with the external magnetic field ( $\mathbf{H}_z$ ) perpendicular to the wave propagation, the value  $\psi = 90^\circ$ . The propagation constant in Eq. 2.66 is then

$$\Gamma_{\parallel} = \frac{i\omega \epsilon^{1/2}}{c} \left( \frac{\mu^2 - \kappa^2}{\mu} \right)^{1/2}, \quad (2.67)$$

$$\Gamma_{\perp} = \frac{i\omega \epsilon^{1/2}}{c}, \quad (2.68)$$

where  $\epsilon$  represents the dielectric constant with respect to free space. Note that we use  $\Gamma_{\parallel}$  and  $\Gamma_{\perp}$  instead of  $\Gamma_+$  and  $\Gamma_-$  in Voigt case.

We now have  $\Gamma_{\parallel}$  and  $\Gamma_{\perp}$  correspond to two modes of propagations according to Eq. 2.33 and Eq. 2.34. We can discuss as following

$\Gamma_{\parallel}$  is the propagation constant for the case  $(\mathbf{q} \parallel \mathbf{y}) \perp (\mathbf{H}_{\text{ext}} \parallel \mathbf{h} \parallel \mathbf{z})$ ,  $\mathbf{e} \parallel \mathbf{x}$ . In this case, the magnetic field  $\mathbf{h}$  of the radiation does not interact with the spin dipoles.

$\Gamma_{\perp}$  is the propagation constant for the case  $(\mathbf{q} \parallel \mathbf{y}) \perp (\mathbf{H}_{\text{ext}} \parallel \mathbf{e} \parallel \mathbf{z})$ ,  $\mathbf{h} \parallel \mathbf{x}$ . While in this case,  $\mathbf{h}$  can interact with the spin dipoles.

The overall propagation constant can be obtained by multiply  $\Gamma_{\parallel}$  and  $\Gamma_{\perp}$  together, giving the macroscopic permeability as

$$\mu_{eff,V} = \mu_0 \frac{\mu^2 - \kappa^2}{\mu}, \quad (2.69)$$

$$= \mu_{xx} - \frac{\mu_{xy}\mu_{yx}}{\mu_{yy}}. \quad (2.70)$$

ii)  $\mu_{eff,F}$  for **Faraday geometry**

In the case of Faraday geometry, where the propagation vector is parallel to the external magnetic field. Therefore, we have  $\psi = 0^\circ$ ,  $n_{q,x} = n_{q,y} = 0$ ,  $n_{q,z} = 1$ , and  $\mathbf{h} = \mathbf{h}_0 \exp\{-\Gamma z\}$ . Such a special case, we need to write down the linear component equations in Eq. 2.64 again as

$$-\Gamma^2 h_x = \frac{\omega^2}{c^2} \epsilon (\mu h_x - \imath \kappa h_y), \quad (2.71)$$

$$-\Gamma^2 h_y = \frac{\omega^2}{c^2} \epsilon (\imath \kappa h_x + \mu h_y). \quad (2.72)$$

Note that the  $\mathbf{z}$  component has vanished. Let us take the ratio of the above two equations. We have

$$\frac{h_x}{h_y} = \frac{\mu h_x - \imath \kappa h_y}{\imath \kappa h_x + \mu h_y}, \quad (2.73)$$

or

$$h_x = \pm \imath h_y. \quad (2.74)$$

Here the imaginary quantity indicates the phase different between the  $+\imath h_y$  and  $-\imath h_y$  terms. Inserting the above equation into Eq. 2.71, we have

$$\Gamma_{\pm}^2 = -\frac{\omega^2}{c^2} \epsilon (\mu \pm \kappa). \quad (2.75)$$

Now we again have  $\Gamma_+$  and  $\Gamma_-$ . Both corresponds to two modes of propagation according to Ref. 2.35 and 2.36 with respect to  $\mathbf{H}_{\text{ext}}$ , these two modes can be thought as the circularly polarized modes of the radiation, namely *right hand circularly polarization* (R.H.C.) and *left hand circularly polarization* (L.H.C.) mode. The scalar or effective permeability of these two opposite modes can be written as

$$\mu_{(eff, L.H.C.)} = \mu_0 (\mu + \kappa) = \mu_{xx} - \mu_{xy}, \quad (2.76)$$

$$\mu_{(eff, R.H.C.)} = \mu_0 (\mu - \kappa) = \mu_{xx} + \mu_{xy}. \quad (2.77)$$

For further reading, refer to [119, 120, 123, 124].

## 2.2 Magnetic Resonance

For the past section, we have already learnt much about how the electromagnetic waves propagate through the medium plus the optical responses of the materials. In

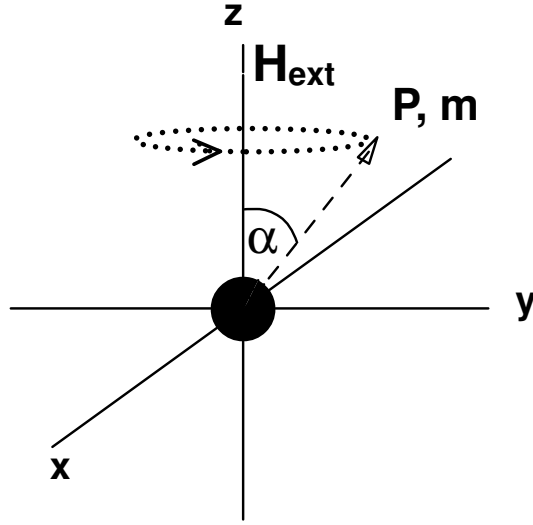


Figure 2.6: Precession of a magnetic moment ( $\mathbf{m}$ ) in a magnetic field  $\mathbf{H}_{ext}$ .  $\mathbf{P}$  is an angular momentum and  $\alpha$  is a precession angle between  $\mathbf{m}$  and  $\mathbf{H}_{ext}$ . See text for more details.

this section, we will go into details for our particularly interesting medium which is the paramagnetic substance. This kind of materials can give us very interesting phenomena so called the *electron paramagnetic resonance* (EPR). Note that there is another main type of magnetic resonance technique called *nuclear magnetic resonance* (NMR). It shares the same phenomena as EPR but for nuclear system and at the radio frequency waves, while EPR is for the electrons and based on the microwave or at slightly higher frequencies. In this Section, we will focus mainly on EPR phenomena but keep in mind that NMR is theoretically based on the same magnetic resonance phenomena.

A paramagnetic medium is defined as a medium which has a very weak or no resultant magnetic moment in the absence of an external magnetic field. However, it can give a net magnetic moment in the direction of an applied field. Its size is also a function of that applied field.

A paramagnetic medium can be composed of the atoms or ions which have permanent magnetic moments. In the case of zero applied field, these atoms or ions are randomly oriented. When the field is applied, there is a redistribution of those atomic (or nuclear) magnetic moments giving the net magnetic moment of the system. The magnetic dipole moment can be written as

$$\mathbf{m} = \gamma \mathbf{P}, \quad (2.78)$$

where  $\mathbf{m}$  is the magnetic dipole moment,  $\mathbf{P}$  is the angular momentum of the electron in paramagnetic atom, and  $\gamma$  is the magnetogyric ratio ( $q/m_e$ ).

When this atom is placed in the magnetic field ( $\mathbf{H}_{ext}$ ), the magnetic dipole moment ( $\mathbf{m}$ ) will precess around the field with an angular velocity

$$\omega_L = |\gamma| \mathbf{H}_{ext}, \quad (2.79)$$

where  $\omega_L$  is so called the Larmor frequency. This precession can produce the oscillatory magnetic dipole moment in any direction perpendicular to the field  $\mathbf{H}_{ext}$ . If there is another oscillatory field ( $H_1 \cos \omega t$ ) perpendicular to  $\mathbf{H}_{ext}$ , there is a chance that  $H_1 \cos \omega t$  can interact with the oscillatory magnetic dipole moment and result in the energy change of the magnetic dipole.

Let  $W$  be the energy of the dipole in the field  $\mathbf{H}_{ext}$

$$W = \mathbf{m} \cdot \mathbf{H}_{ext}. \quad (2.80)$$

A change in component  $m H_{ext} \cos \alpha$  gives the energy change of the magnetic dipole

$$W = \mathbf{m} H_{ext} \cos \alpha = |\gamma| P H_{ext} \cos \alpha. \quad (2.81)$$

To have a transition between  $m$  and  $m'$  levels with  $\Delta M = \pm 1$ , the system requires quantum energy of

$$\hbar \omega = W_m - W_{m'} = |\gamma| \hbar H_{ext}, \quad (2.82)$$

or

$$\omega = |\gamma| H_{ext} = \omega_L. \quad (2.83)$$

The Eq. 2.83 fulfills the resonance condition between the magnetic dipole moment  $\mathbf{m} \cos \omega_L t$  and the oscillatory field  $h \cos \omega t$  leading to the magnetic transition. Such a resonance phenomenon is called *magnetic resonance*.

### 2.2.1 Transition probability and the transition absorption line in the magnetic resonance

One important topic in MR is to find the transition probability ( $P_{m,m'}$ ) of the electron from state  $m \rightarrow m'$ . We can consider this transition as following

$$P_{m,m'} = \gamma^2 H_1^2 |\langle \psi(m) | \hat{S}_{x,y} | \psi(m') \rangle|^2 \delta(\omega_L - \omega), \quad (2.84)$$

where  $|\langle \psi(m) | \hat{S}_{x,y} | \psi(m') \rangle|$  is the matrix element which is found to be zero unless  $m' = m \pm 1$  giving the *selection rule* of the magnetic transition  $\Delta m = \pm 1$ .  $\delta(\omega_L - \omega)$  is the *Dirac delta function* which defined as the function being zero everywhere except at  $\omega = \omega_L$ . In this form, the transition lineshape will be infinitesimally sharp.

However, the Eq. 2.84 can only be justified for a single isolated moment but not in the real macroscopic system. Therefore, we need to introduce the  $g(\omega)$  or  $g(\nu)$  as the *lineshape* term instead of the *Dirac delta function* and the Eq. 2.84 becomes

$$P_{m,m'} = \gamma^2 H_1^2 |\langle \psi(m) | \hat{S}_{x,y} | \psi(m') \rangle|^2 g(\nu). \quad (2.85)$$

The lineshape function has the dimension of time and it is proportional to the frequency ( $\omega = 2\pi\nu$ ). Generally, most of the form of  $g(\nu)$  are Lorentzian or Gaussian type. For the Lorentzian type:

$$g(\nu) = \frac{\nu_L^2}{\nu_L^2 - \nu^2 + i\nu\Delta\nu_L}, \quad (2.86)$$

where  $\nu_L = \omega_L/2\pi$  is the resonance frequency.

For the Gaussian type:

$$g''(\nu) = \left(\frac{\pi}{8}\right)^{1/2} \left(\frac{\nu}{\sigma_L}\right) \left[ \exp\left\{-\frac{(\nu - \nu_L)^2}{2\sigma_L^2}\right\} + \exp\left\{-\frac{(\nu + \nu_L)^2}{2\sigma_L^2}\right\} \right], \quad (2.87)$$

$$g'(\nu) = \left(\frac{2}{\pi}\right) \int_0^\infty \frac{\nu_1 g''(\nu_1)}{\nu_1^2 - \nu^2} d\nu_1, \quad (2.88)$$

where  $g''(\nu)$  is the imaginary term, and  $g'$  is the real term determined via the Kramers-Kronig relation.  $\sigma_L$  is the width of the Gaussian line.

The probability of the transition is symmetric for  $P_{m,m'} = P_{m',m}$  with respect to an interchange of the quantum number  $m$ . This means the *probability* of a transition between two states are equal but not the *number* of the transitions. The latter depends on the population of each states which can be determined by the *Boltzmann factor*, which is written as

$$f(T) = e^{(-E_m/kT)}, \quad (2.89)$$

where  $T$  is the temperature. The total number of the transitions from all transition modes relates to the magnetic permeability ( $\mu$ ) of the material through the following relation

$$\hat{\mu} = 1 + \sum_L \Delta\mu_L \cdot g(\nu)_L, \quad (2.90)$$

where  $L$  is the transition mode which corresponds to each resonance frequency  $\nu_L$  in the system.  $\Delta\mu_L$  is called *the mode contribution to the static magnetic permeability* expressed as

$$\Delta\mu_L = \gamma^2 H_1^2 |\langle \psi(m) | \hat{S}_{x,y} | \psi(m') \rangle|^2 \left\{ N \cdot \frac{e^{(-E_m/kT)} e^{(-E_{m'}/kT)}}{\sum_i e^{E_i/kT} E_{mm'}} \right\}, \quad (2.91)$$

where  $E_{mm'} = (E_{m'} - E_m)$ ,  $\sum_i$  is the sum over all of the contribution modes (e.g. magnetic and phonon), and  $N$  is the number of the magnetic atoms per unit volume of the material which contribute the magnetic moments in the system. Note that we have separated  $g(\nu)$  from the transition probability function in Eq. 2.85 (which is equivalent to the  $\Delta\mu$  function) for simplicity.

# Chapter 3

## Experimental techniques

Up to now, we have learnt about the basic ideas of radiation propagation in a medium and the magnetic resonance (MR) phenomena. In this Chapter, we will concentrate more on the technical details of *frequency-domain magnetic resonance spectroscopy* or FDMRS which will be our main technique for this Thesis.

In the first Section, some historical background of EPR, HFEPR, and FDMRS spectroscopy is introduced. The second Section is about the detailed operation of our FDMRS spectrometer. In the third Section, it is described how to transform the polarization of the electromagnetic radiation from linear to circular polarization. The fourth Section deals with the magnetic cryostat and its low temperature operation. The fifth Section is the sample preparation for FDMRS techniques. The sixth Section is the description of the FDMRS transmission measurement and transmission spectral simulation. The last Section is to compare between the FDMRS phase and transmission measurements.

### 3.1 Historical background of electron paramagnetic resonance spectroscopy

The history of the electron paramagnetic resonance is closely related to the microwave technique history. The first successful magnetic resonance (MR) experiment was performed by E. Zavoisky [125] in 1944. He observed electron paramagnetic resonance (EPR) in  $CuCl_2H_2O$  at 4.76 mT using a frequency of 133 MHz. In 1946, J. Griffiths observed ferromagnetic resonance [126]. At the same time, in 1946, B. Bleaney *et al.* [127] moved up to microwave frequencies to measure the absorption in the ammonia molecule. Later they moved up to the frequencies around 9 GHz (X-band) which became a standard of EPR. Due to the lack of technologies to produce the monochromatic and continuously tunable source at that time, therefore the X-band was found to be the most compromise between cost and availability of high field electromagnets, high frequency radiation sources on one hand, and cavity size, sensitivity and g-value resolution on the other. During these years, EPR has been developed allow solid (single crystal and polycrystalline powders), frozen solution, and liquid solution to be recorded. EPR in the range of 9-35 GHz also has become traditional tool to

obtain structural information of transition metal compounds. Later it has been widely applied in various field such as biology and mineralogy.

There are many reasons for going to higher magnetic fields and higher frequencies. For example, high field EPR (HFEPR) is useful to resolve small g-value anisotropies. In the case of large zero field splitting (ZFS), the EPR-active transitions of integer-spin systems can not be observed at low frequencies. Such systems are called *EPR-silent*, which is due to the fact that the magnetic field of a conventional X-band EPR spectrometer usually does not exceed 2 T and the photon energy corresponds to only  $0.3 \text{ cm}^{-1}$ . Therefore, operating at high frequencies makes it possible to study such large ZFS integer-spin systems. Hence, in the last decade, *high frequency and high field electron paramagnetic resonance* (HFEPR) research efforts in various fields of science at the magnetic field up to 30 T and the frequency up to 700 GHz have increased enormously. Nowadays, HFEPR spectrometers are operated at large scale facilities. Such as the facilities operated at the National High Magnetic Field Laboratory at Tallahassee, USA, the Grenoble High Magnetic Field Laboratory in France, and the newly equipped at Nijmegen High Field Magnet Laboratory in The Netherlands with numerous publications coming out each year [89, 128, 129, 130].

The first HFEPR spectrometers were based on high frequency klystrons. Besides far-infrared (FIR) gas lasers, solid-state devices, like semiconductor Gunn diodes or IMPATT diodes, are employed as high-frequency radiation sources in 90-500 GHz region. Although this covers a wide spectral range, these source can not be continuously swept over a large frequency range. Sweeping of an external magnetic field is therefore required to achieve the resonance condition. This means that ZFS parameters can be determined only by extrapolation from non-zero magnetic fields which can possibly lead to the wrong values.

An alternative method to obtain ZFS parameters is to sweep the frequency and keep the magnetic field at zero or at some fixed values. This technique is called *frequency-domain magnetic resonance spectroscopy* or FDMRS. It was originated by Richards and co-workers[131] in the late 60s who used an infrared Michelson interferometer. This type of far-infrared FIR spectroscopy combined with fixed magnetic fields allows one to observe the parameters of the electronic spins (ZFS and g-values) for systems which are not possible to study by conventional EPR technique. Performing EPR investigations at different frequencies also allows one to study dynamic processes. At different magnetic fields, interactions like the zero-field splitting (ZFS) and the Zeeman splitting have different respective magnitudes. Estimation of ZFS parameters from the extrapolation of the magnetic field measurement data can be inaccurate. Therefore, using FDMRS in zero field allows one to have more accuracy in the determination of the corresponding ZFS parameters. Recently, this technique has been widely applied in many high spin and large ZFS splitting systems [132, 133, 134, 135]. It also has been widely applied to several molecular magnets and molecular compounds system [133, 136, 134]. The detailed operation of *FDMRS* technique will be discussed in a later Section.

The advantages of FDMRS over the other powerful techniques in this scope (to obtain the ZFS parameter in zero magnetic field) such as inelastic neutron scattering (INS) is that in INS, gram amounts of deuterated sample are needed while in FDMRS,



only few hundred milligrams are required, depending on the absorption properties of the materials. INS can be carried out only at a small number of large facilities due to the need of a nuclear reactor or a particle accelerator as the neutron source. However, the advantage of the INS over FDMRS is  $\Delta S = \pm 1$  transitions which are not allowed in EPR or other optical spectroscopies.

## 3.2 Frequency-domain magnetic resonance spectroscopy

During the 1960s, there were major improvements in the development of the backward-wave oscillators (BWOs) as monochromatic and continuously tunable sources. Our success in building a high-frequency domain spectrometer is mainly due to using high frequency BWOs. A BWO [138] is a vacuum tube similar to a magnetron, a klystron or a travelling-wave tube in the sense that electrons are generated and accelerated and transform their kinetic energy to generate electromagnetic waves. Fig. 3.1 shows a schematic diagram of a (high-frequency) backward wave oscillator, the cathode is heated by an electrical heater which is located next to it, and emits electrons. Applying a high voltage accelerates the electrons towards the anode. In order to collimate the electron beam, the source is placed in a permanent magnet. On the way to the anode, the electrons pass over a comb-like fine metallic structure where charges and electric fields modulate the electron velocity and group them in bunches. The acceleration and deceleration causes the electrons to excite and sustain an electromagnetic wave which travels in the direction opposite to the electron beam and exits the source through an oversized waveguide. For a given comb structure, the frequency of this radiation is determined purely by the velocity of the electrons and hence by the magnitude of the high voltage. Thus, changing the voltage allows one to tune the frequency continuously.

The radiation generated by BWOs is coherent, monochromatic and linearly polarized to a high degree. The spectrum of the output power of various BWOs is shown in Fig. 3.2. The frequency range of 1-48  $\text{cm}^{-1}$  is covered by different sources. The low-frequency BWOs (up to 6  $\text{cm}^{-1}$ ) are irreversibly incorporated in a small samarium-cobalt magnet. The high-frequency sources ( $> 180$  GHz) are placed in a 1.2 T permanent magnet which focuses the electron beam.

We let the radiation propagate through free space without using any wave-guide. Fig. 3.3 shows the diagram of our spectrometer setup. It is the typical arrangement of an optical Mach-Zehnder interferometer. The radiation is generated by the BWOs, collimated to a parallel beam and focused onto a detector by set of lenses made of PE or PTFE. The Mach-Zehnder interferometer is formed by two beam splitters and two metal mirrors. For transmission measurements only one arm of the interferometer is in used while for the phase measurements the interferometer is utilized to its full extent. The detector is a Golay cell which has a frequency independent response the whole submillimeter wavelength range. Whereas, a helium-cooled pumped bolometer is used when higher sensitivity is needed. The beam splitters and polarizers are made of closely spaced, parallel tungsten wire grids which reflect the electric field component  $E_{\parallel}$  and

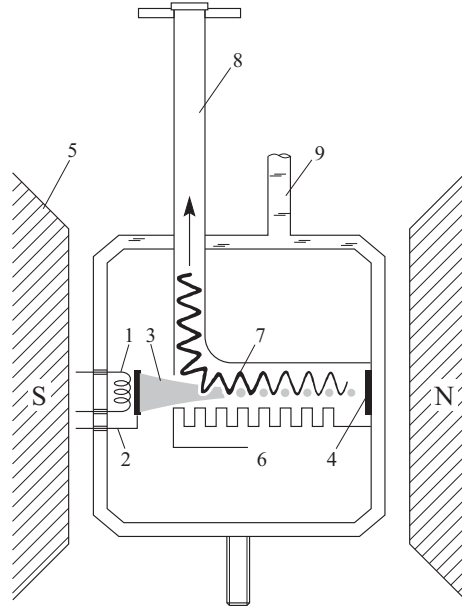


Figure 3.1: Schematic diagram of a backward wave oscillator[138]. 1) heater, 2) emitter(cathode), 3) electron beam, 4) collector(anode), 5) permanent magnet, 6) deceleration system, 7) electromagnetic wave, 8) waveguide, and 9) water cooling.

allow  $E_{\perp}$  to pass through. The lenses are Teflon or fused-Silica type with typical diameter of 5-10 cm and focal length of 5-20 cm. The samples are plane parallel slabs of 3-10 mm in diameter where the thickness can be varied depending on the absorption of the materials. To have a good signal-to-noise ratio, the transmission coefficient should be larger than  $10^{-4} - 10^{-5}$ . For zero-field measurement a homemade helium bath cryostat ( $T=1.5-300$  K) is used, and for zero or in-field measurement ( $T=1.5-300$  K,  $H=0-8$  T) an Oxford Instruments Spectromag 4000 with a split-coil superconducting magnet is used, which is equipped with Large nonabsorbent thin polymer films windows. Both Voigt ( $\mathbf{q} \perp \mathbf{H}_{\text{ext}}$ ) and Faraday ( $\mathbf{q} \parallel \mathbf{H}_{\text{ext}}$ ) geometries can be used (where  $\mathbf{q}$  is the propagational wavevector, and  $\mathbf{H}_{\text{ext}}$  is the external applied magnetic field).

The transmission coefficient ( $Tr$ ), is determined as the ratio of the signal with the sample and without the sample in the quasi-optical channel. For phase-shift measurement, the movable mirror-1 in the reference arm as shown in Fig. 3.3 is adjusted in length to make the beam in both arms interfere destructively at the detector. From the position of mirror-1, the optical phase shift is evaluated as a function of frequency. Practically, resolution can be as good as 0.1 MHz allowing one to map extremely narrow lines. All measurements are computer controlled and performed fully automated on a real time scale of a few seconds.

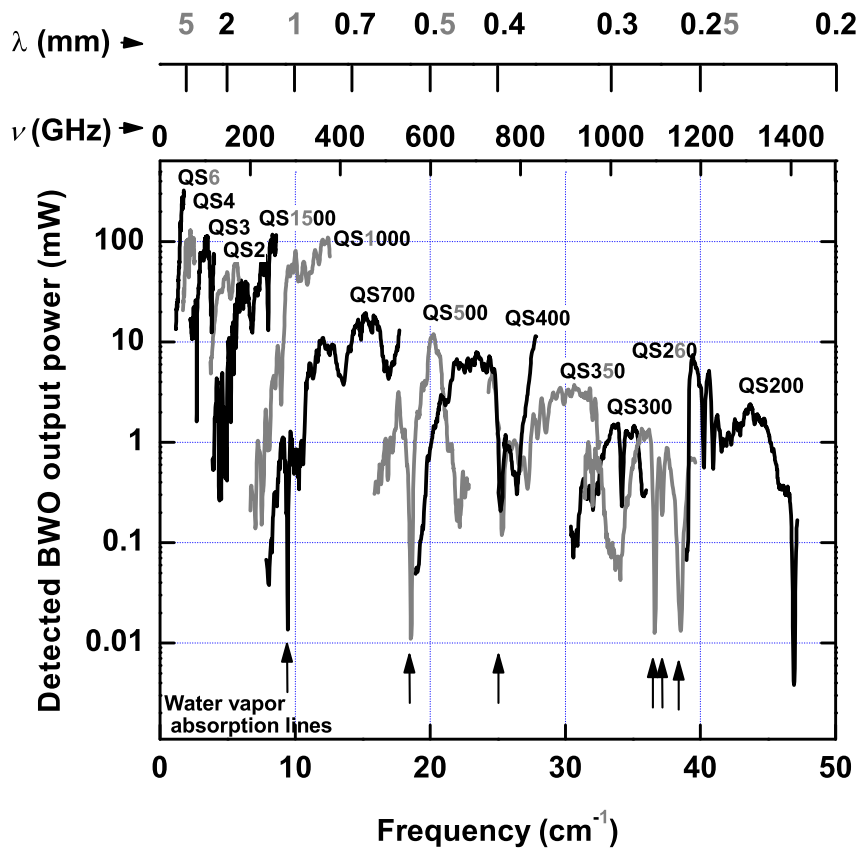


Figure 3.2: Radiation characteristics of BWOs, shown as the output power of various BWOs vs. frequency from 30 GHz to 1400 GHz (1-48  $\text{cm}^{-1}$ ).

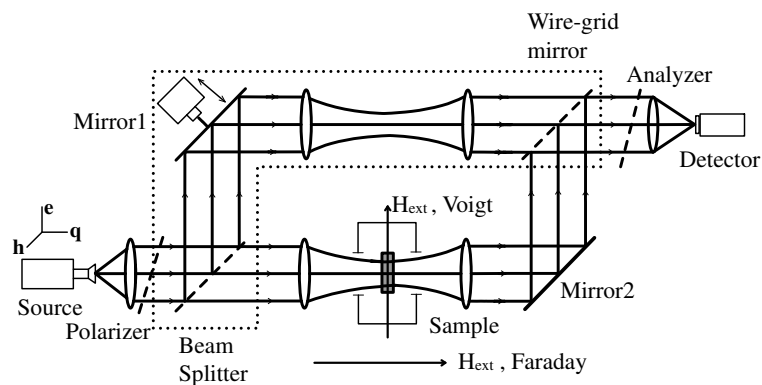


Figure 3.3: Schematic setup of the FDMRS spectrometer. For transmission measurements, the reference arm of the interferometer (in the dash box) is not used. The reference arm is only used for phase measurement. The  $\mathbf{q}$  vector is the direction of the radiation propagation which can be parallel or perpendicular to the external field  $\mathbf{H}_{\text{ext}}$  corresponding to Faraday and Voigt geometry respectively.

### 3.3 Polarization transforming

The type of polarization of the electromagnetic radiation (linear, circular, or elliptic) is determined by the direction of the oscillation plane of electric field vector ( $\mathbf{e}$ ). We use a millimeter-wave quasi-optical polarization transformer which allows the continuous change of the phase difference between two orthogonal components of the electric field vector. As shown in Fig. 3.4, polarizer-1 ( $P_1$ ) creates linearly polarized light at the angle  $\alpha_1 = 0^\circ$  and polarizer-2 ( $P_2$ ) polarizes the radiation at  $\alpha_2 = 45^\circ$ . The polarization transformer consists of a mobile uniform metal mirror and a fixed grid under  $45^\circ$  with beam. The component of the vector  $\mathbf{e}$  parallel to the grid wires will be reflected. The perpendicular  $\mathbf{e}$  component will pass through and reflect at the mirror. By changing the distance  $d$  between the mirror and the wire grid of the polarization transformer, the outgoing beam to the detector will consist of two waves with mutually perpendicular polarization and with phase difference,  $\Delta\phi = 2\pi d\sqrt{2}/\lambda$ . By changing  $d$ , consequently the phase difference,  $\Delta\phi$ , changes. For two orthogonal  $\mathbf{x}$  and  $\mathbf{y}$  components of the electric field;  $e_x$  and  $e_y$  with equal amplitudes the trajectory ( $a$ ) of the  $\mathbf{e}$  vector is given by;

$$e_x^2 + e_y^2 - 2e_x e_y \cos\Delta\phi = a^2 \sin^2\Delta\phi. \quad (3.1)$$

This allows one to get any polarization of the outgoing beam by changing  $\Delta\phi$  or  $d$  at the polarization transformer; linear ( $e_x = (-1)^m e_y$  for  $\Delta\phi = m\pi$  when  $m = 0, \pm 1, \dots$ ), circular ( $e_x^2 + e_y^2 = a^2$  for  $\Delta\phi = \pm\pi/2$ ), or elliptic in all other cases. The phase difference must be  $\pi/2$  and  $3\pi/2$  to create right hand circular (R.H.C.) and left hand circular (L.H.C.) respectively. Experimentally it can also be done by switching polarizer-2 to  $+\pi/4$  and  $-\pi/4$  for R.H.C. and L.H.C. respectively.

We have confirmed our polarization transformation setup by using two mirror-grid transformers namely  $MG_1$  and  $MG_2$ . We used  $MG_1$  to produce circularly polarized light. After that, we used  $MG_2$  to convert back the circular to linearly polarized light in order to confirm that we truly have a real circularly polarized wave from  $MG_1$  with equal amplitude in all direction, not an average signal or an unpolarized signal (refer to theory of polarization in Section 2.1.4). We placed  $MG_2$  right after the cryostat. We checked the output signal as a function of the analyzer angle at  $P_2$ ,  $MG_1$ , and  $MG_2$ . The result is shown in Fig.3.5 which confirms us that we had truly circularly polarized radiation by using the mirror-grid transformer ( $MG_1$ ) ie. with the quality of 98-99% at 300GHz wave, 88-95% in the frequency range of 294-304 GHz. The quality of the circular polarization decreased sharply outside that frequency range. During the experiment we always had to fine tune to obtain the best quality of circularly polarized light at each frequency.

### 3.4 Operating the magnetic cryostat

A commercial magnetic cryostat with a superconducting magnet Oxford Spectromag 4000 was used to perform the temperature measurements (1.5-300 K) in a magnetic field (0-8 T).

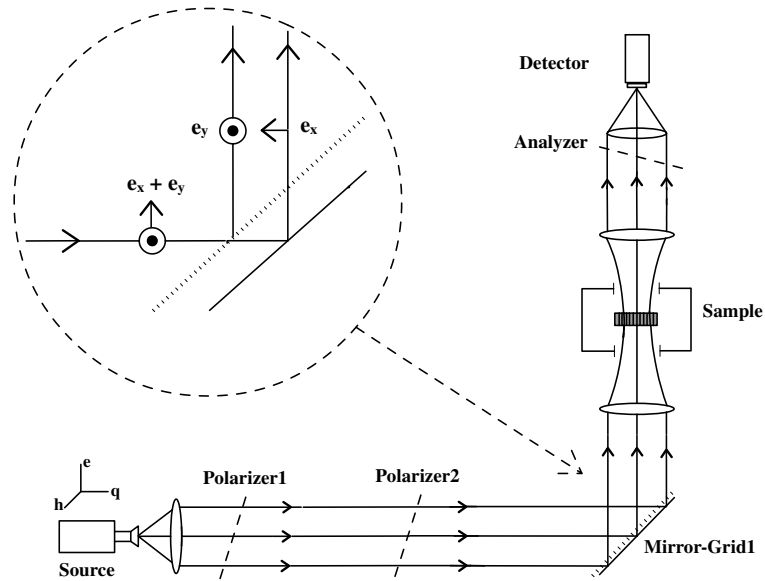


Figure 3.4: Experimental setup in Faraday geometry combined with the use of circularly polarized radiation. The radiation propagates through polarizer-1 ( $P_1$ ) at  $\alpha_1 = 0^\circ$  and polarizer-2 ( $P_2$ ) at  $\alpha_2 = 45^\circ$  having vectorially the orthogonal electric field vector components ( $e_x$  and  $e_y$ ). The mirror-grid transformer (*Mirror-Grid1*) creates the right phase shift between these  $e_x$  and  $e_y$  vectors producing the circularly polarized radiation, (see text).

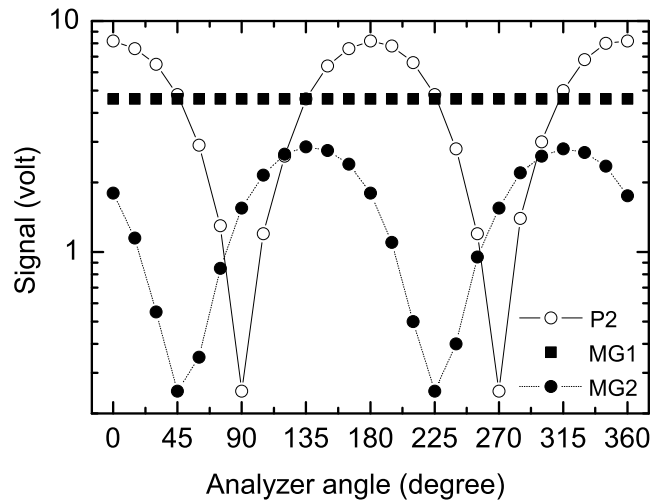


Figure 3.5: Angular dependence of the detector signal after mirror-grid-1 ( $MG_1$ ), mirror-grid-2 ( $MG_2$ ), polarizer-2 ( $P_2$ ), (see text). The beam is linearly polarized at the polarizer-2 ( $P_2$  with  $\alpha = +45^\circ$ ) placed after the polarizer-1 ( $P_1$  with  $\alpha = 0^\circ$ ), the beam is circularly polarized at  $MG_1$ , and the signal is back to linear polarized again at  $MG_2$ .

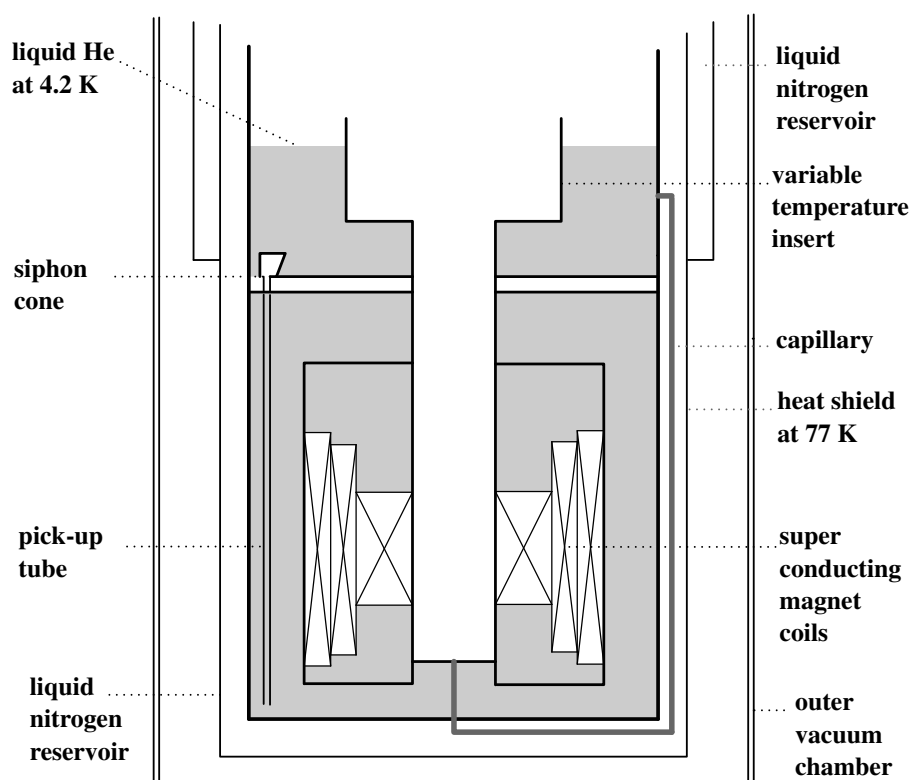


Figure 3.6: Schematic diagram of our Spectromag4000 - magnetic cryostat.

The variable temperature insert (VTI) allows us to adjust the temperature of a sample continuously over a wide range (1.5-300 K). The outer part of VTI is equipped with large windows for the optical access for two opposite sides. The inner part of the VTI insert is vacuum isolated from the liquid helium reservoir. There is a radiation shield between the sample space and the helium reservoir, and a liquid nitrogen reservoir between the helium reservoir and the outer vacuum chamber (OVC) to reduce the heat load.

The sample space is connected to the reservoir by an indium sealed capillary tube and a needle valve. The sample is mounted on a top loading probe which is inserted into the VTI in the flowing helium gas. The liquid helium is drawn from the main reservoir to the sample space through a needle valve which adjusted by a stepping motor to control the flow. The sample temperature can be controlled by balancing the cooling power of the liquid helium flow with the heater controlled by an Oxford Instruments ITC503 temperature controller. The heater and control thermometer were mounted on the sample rod. In principle, the needle valve is also equipped with a heater in order to clear any ice blockage in the small capillaries between the sample space and the reservoir without warming the whole system up to room temperature.

Temperatures below 4.2 K can be reached by reducing the vapor pressure of liquid helium in the sample space. We set the needle valve in order to let the liquid helium fill in the sample space continuously. Having the right flow rate can replace the evaporating liquid and maintain a constant liquid level. The base temperature in this continuous fill mode is 1.7 K.

The magnet consists of a number of coaxial solenoid sections wound using multifilamentary superconducting wire. This magnet is both physically and thermally stable under the large Lorentz forces generated during operation. The superconducting magnet has the ability to be operated in the persistent mode where the superconducting circuit is closed to form a continuous loop and the power supply can be switched off leaving the magnet at field. To have the magnet in the normal or nonsuperconducting state, the switch has to be warmed by the switch heater in order to hold it open. After the magnet reaches the desired field, the induced voltage across the switch drops to zero and all current flows through the magnet. The switch is closed by turning off the heater thus allowing the magnet to return to the superconducting state. Normally we can run the magnet up to 7 T.

## 3.5 Sample preparation

The sample is mounted on the sample holder which is placed in a cryostat. The aperture with the diameter larger than the radiation wavelength is placed in front of the sample. The sample size depends on the size of this aperture. Powder samples are pressed into plane parallel pellets. For single crystals, if the resonance frequency of interest falls around a few wavenumbers then the crystal diameter should be around a centimeter. The typical single crystal size is around a few millimeter, therefore, a mosaics of a few single crystals must be prepared. It can be done by glueing the single crystals on a mylar layer where the main axis of the crystals must point into the same

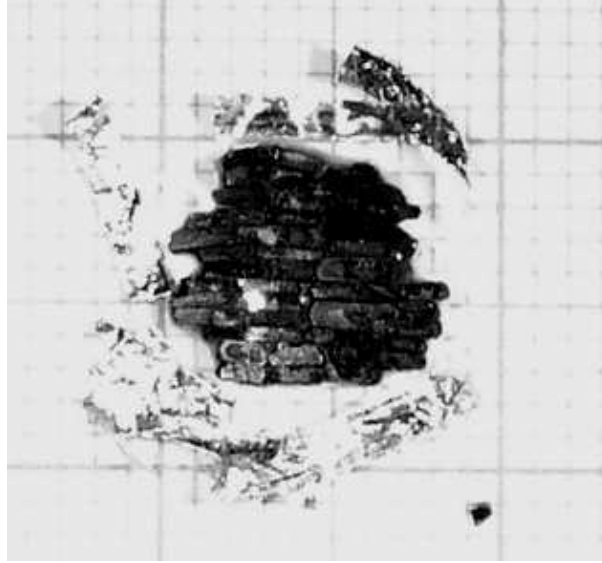


Figure 3.7:  $\text{Mn}_{12}$ -acetate-mosaic of single crystals with 0.5 mm thickness and  $7 \times 7 \text{ mm}^2$  area. The crystals are fixed with epoxy with the main axis in the plane of the mosaic.

direction i.e. parallel or perpendicular to the mylar layer. After the glue had dried, we polished both sides of the mosaic surface in order to have a plane parallel sample. At the last step, we filled in the hole between the imperfectly shaped crystals with the graphite powder in order to avoid standing wave effects from the diffraction and reflection through the holes between the crystals. In this Thesis, we prepared two types of  $\text{Mn}_{12}$ -acetate mosaics as shown in Fig. 3.7 and Fig. 3.8 with the anisotropy axis (main axis) parallel and perpendicular to the mylar plane, respectively. The plane parallel pressed pellet sample is shown in Fig. 3.9. The synthesis method of  $\text{Mn}_{12}$ -acetate crystals was described by Lis[51].

### 3.6 Simulating FDMRS transmission spectra

This Section, we will learn the basic concept of how to analyse the absorption line measured by FDMRS with the background knowledge from Chapter 2 and Chapter 3.

The transmission coefficient spectra ( $Tr$ ) from the FDMRS technique are obtained from the ratio of the transmission measurement from the the sample channel ( $I_{sample}$ ) and empty channel ( $I_{hole}$ ).

$$Tr(\nu) = \frac{I_{sample}(\nu)}{I_{hole}(\nu)}, \quad (3.2)$$

where  $\nu$  is the frequency.

However, simulation of  $Tr(\nu)$  is not simple since it is a complicated function of the complex dielectric permittivity  $\hat{\epsilon}$  and complex magnetic permeability  $\hat{\mu}$ .



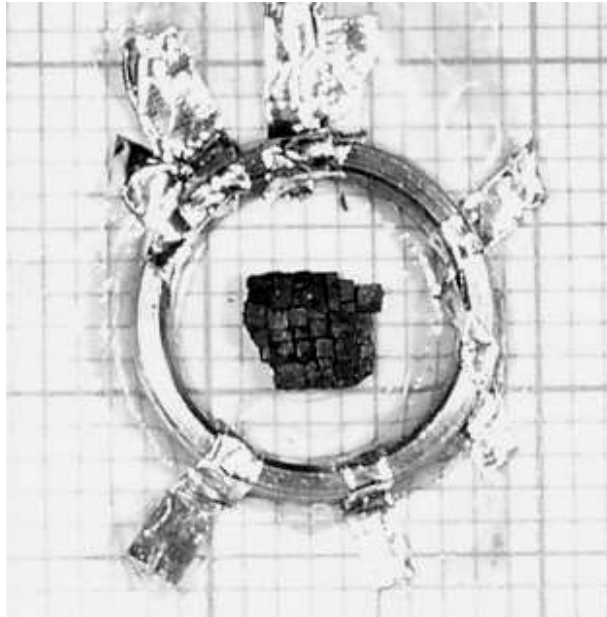


Figure 3.8:  $\text{Mn}_{12}$ -acetate-mosaic of single crystals with 0.5 mm thickness and  $4 \times 4 \text{ mm}^2$  area. They are fixed with epoxy with the main axis perpendicular to the plane.

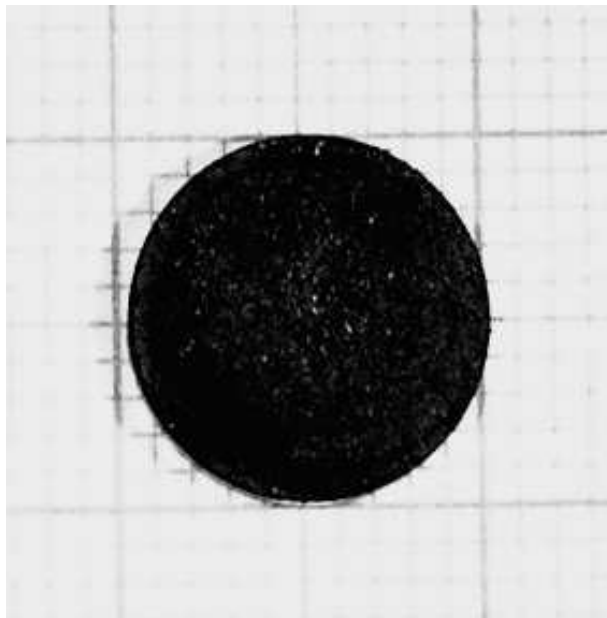


Figure 3.9:  $\text{Mn}_{12}$ -acetate-plane parallel pressed pellet with diameter 10 mm and thickness 1.32 mm.

$$\hat{\epsilon}(\nu) = \epsilon'(\nu) + \imath\epsilon''(\nu), \quad (3.3)$$

$$\hat{\mu}(\nu) = \mu'(\nu) + \imath\mu''(\nu), \quad (3.4)$$

where  $\epsilon'(\nu)$  is the effective dielectric constant,  $\epsilon''(\nu)$  is the dielectric absorption,  $\mu'(\nu)$  is the magnetic permeability, and  $\mu''(\nu)$  is the magnetic absorption. As we have explained in Section 2.1.6, in an anisotropic system,  $\hat{\epsilon}(\nu)$  and  $\hat{\mu}(\nu)$  are tensors, and the latter one is antisymmetric in a case of a magnetized medium.

The optical response functions of the medium normally appear in a pair such as refractive index ( $n$ ) and extinction index ( $k$ ) and are related to the medium properties such as  $\hat{\epsilon}$  and  $\hat{\mu}$ , (refer to Section 2.1.2). If one measures the transmission coefficient ( $Tr$ ) and the phase change ( $\Phi$ ) spectra, one can obtain the medium properties ( $\hat{\epsilon}$ ,  $\hat{\mu}$ ) through those response functions ( $n, k$ ) by the use of the Fresnel formulas given in Eq. 2.19, and Eq. 2.22 (Section 2.1.3), which can be rewritten as [137, 138, 139]

$$Tr(\nu) = E \frac{(1-R)^2 + 4R \sin^2 \psi}{(1-RE)^2 + 4RE \sin^2(Q+\psi)}. \quad (3.5)$$

The phase change  $\Phi$  can be expressed as

$$\Phi = Q + \arctan \frac{ER \sin 2(Q+\psi)}{1-ER \cos 2(Q+\psi)} + \arctan \frac{b}{b^2+a^2+a} - \arctan \frac{b}{a+1}, \quad (3.6)$$

where  $Q$  and  $E$  are function of the real refractive index ( $n$ ), the extinction coefficient ( $k$ ), the frequency ( $\nu$ ), and the sample thickness ( $d$ ).

$$E = \exp\{-4\pi k\nu d\}, \quad (3.7)$$

$$Q = 2\pi n\nu d. \quad (3.8)$$

The complex refractive index ( $\hat{N}$ ) is given by

$$\hat{N} = n + \imath k, \quad (3.9)$$

where the optical response  $\hat{N}$  is related to the materials parameters  $\hat{\epsilon}$  and  $\hat{\mu}$  through

$$n = \frac{\theta_2}{2}, \quad (3.10)$$

$$k = \sqrt{\frac{-\theta_1 + \sqrt{\theta_1^2 + \theta_2^2}}{2}}, \quad (3.11)$$

$$\theta_1 = \epsilon'\mu' - \epsilon''\mu'', \quad (3.12)$$

$$\theta_2 = \epsilon'\mu'' - \epsilon''\mu'. \quad (3.13)$$

Similarly to  $\hat{N}$ ,  $R$  is also a function of  $\hat{\epsilon}$  and  $\hat{\mu}$

$$R = \frac{(a-1)^2 + b^2}{(a+1)^2 + b^2}, \quad (3.14)$$

$$a = \sqrt{\frac{\alpha_1 + \sqrt{\alpha_1^2 + \alpha_2^2}}{2}}, \quad (3.15)$$

$$b = \frac{\alpha_2}{2a}, \quad (3.16)$$

$$\alpha_1 = \frac{\mu'\epsilon' + \mu''\epsilon''}{\epsilon'^2 + \epsilon''^2}, \quad (3.17)$$

$$\alpha_2 = \frac{\mu''\epsilon' + \mu'\epsilon''}{\epsilon'^2 + \epsilon''^2}. \quad (3.18)$$

The last parameter is  $\psi$  which is also a function of  $\hat{\epsilon}$  and  $\hat{\mu}$

$$\psi = \arctan \frac{2b}{a^2 + b^2 - 1}. \quad (3.19)$$

For further analysis, here we simply consider two types of media; a dielectric and a magnetic medium. One with only a dielectric response and one with both dielectric and magnetic responses.

### 3.6.1 Dielectric medium

For a purely *dielectric* medium, there is no magnetic resonance contribution to the absorption process. The optical response can be determined by a pair of optical response functions: such as refractive index ( $n$ ) and extinction index ( $k$ ), real and imaginary part of the dielectric permittivity ( $\epsilon', \epsilon''$ ), or real and imaginary part of optical conductivity ( $\sigma', \sigma''$ ), etc. A typical transmission coefficient spectra of a dielectric sample is shown in Fig. 3.10. The oscillation is caused by the interference of the waves travelling through a plane parallel medium with a thickness comparable to the wavelength. We can numerically evaluate any pair of those material parameters via Eq. 3.5 by assuming that  $\mu'(\nu) = 1$  and  $\mu''(\nu) = 0$ . There is no need to measure the phase spectra in this case. Further reading about dielectric measurements can be found in Ref. [138].

### 3.6.2 Magnetic medium

For *magnetic* medium, the simulation of the transmission coefficient spectra is rather complicated since both dielectric and magnetic properties become important. We need to determine two pairs of unknown parameters; ( $\epsilon', \epsilon''$ ) and ( $\mu', \mu''$ ).

First we determine the dielectric constants. This can be done outside of the resonance line or at temperature where the magnetic resonance line is absent. The dielectric parameters are then kept constant throughout the fit process. For this part of

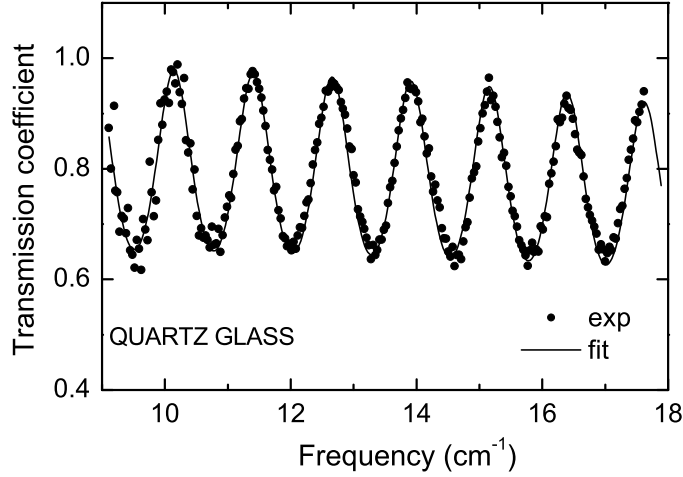


Figure 3.10: Transmission spectrum of a dielectric sample: quartz glass. (See text for the spectrum analysis).

the fit, we assume that  $\mu' = 1$  and  $\mu'' = 0$ . When we obtain these dielectric properties ( $\epsilon'$ ,  $\epsilon''$ ), we can interpolate them in the magnetic resonance region.

Next we fit the magnetic permeability in the magnetic resonance region. We can calculate the quantity  $\hat{\mu}$  from Eq. 2.90, Section 2.2.1. For simplicity, we write this term  $\hat{\mu}$  for one magnetic absorption mode presented as

$$\hat{\mu}(\nu) = 1 + \Delta\mu \cdot g(\nu), \quad (3.20)$$

where all the parameters have been explained in Section 2.2.1.

In the case of  $H \parallel z$ , the permeability tensor can be written as in Eq. 2.52, where  $\mu$  component can be simply written as

$$\hat{\mu}_{xx} = \hat{\mu}_{yy} = 1 + \Delta\mu \cdot g(\nu), \quad (3.21)$$

$$\hat{\mu}_{xy} = -\hat{\mu}_{yx} = \nu\Delta\mu \cdot g(\nu). \quad (3.22)$$

In Voigt geometry, the effective permeability from Eq. 2.70 can be expressed as

$$\hat{\mu}_{eff, V} = 1 + \frac{\Delta\mu \cdot g(\nu)}{1 + \Delta\mu \cdot g(\nu)}. \quad (3.23)$$

In Faraday geometry, the effective permeability from Eq. 2.76-2.77 can be written as

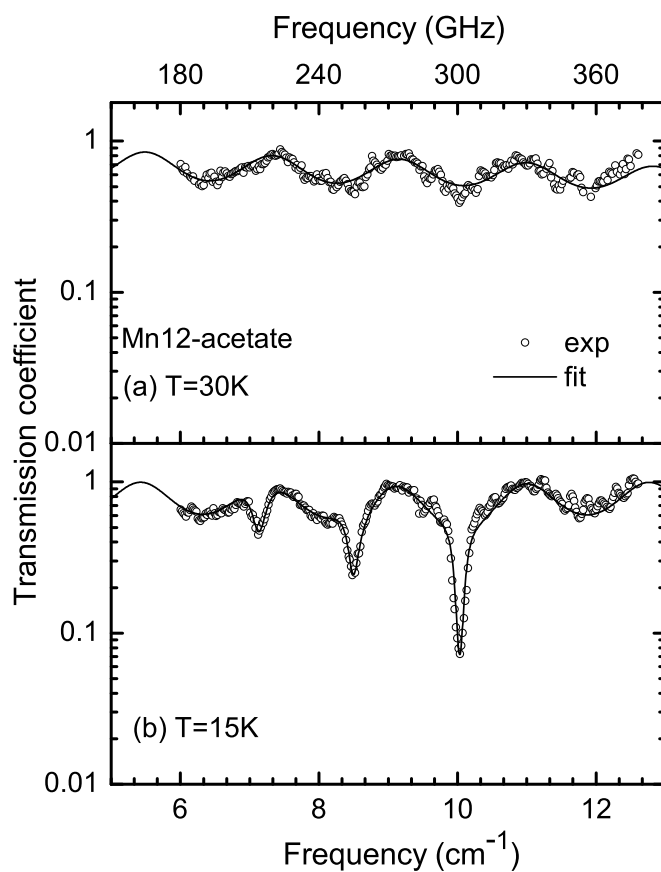


Figure 3.11: Transmission coefficient spectra of the magnetic sample; Mn<sub>12</sub>-acetate (a) at temperature T=30 K, there is no magnetic resonance line (b) at T=15 K, three magnetic resonance lines are observed. (See text for analysis).

$$\hat{\mu}_{eff, F, L.H.C.} = 1 + \Delta\mu \cdot g(\nu) - \imath\Delta\mu \cdot g(\nu), \quad (3.24)$$

$$\hat{\mu}_{eff, F, R.H.C.} = 1 + \Delta\mu \cdot g(\nu) + \imath\Delta\mu \cdot g(\nu). \quad (3.25)$$

Here we have to assume the lineshape function ( $g(\nu)$ ) in Eq. 2.85 to be in either Lorentzian (Eq. 2.86) or Gaussian form (Eq. 2.87-2.88). The last step is to put the above parameters into Eq. 3.5.

For a polycrystalline sample, we need to average the permeability with respect to their orientation ( $\theta$ ) in the applied magnetic field ( $H_z$ ) as follows

$$\hat{\mu}_{xx,yy} = (1 + \Delta\mu \cdot g(\nu)) \cdot (1 + \cos^2 \theta)/2, \quad (3.26)$$

$$\hat{\mu}_{xy,yx} = \pm \imath\Delta\mu \cdot g(\nu) \cdot \cos \theta, \quad (3.27)$$

$$\hat{\mu}_{zz} = (1 + \Delta\mu \cdot g(\nu)) \cdot \sin^2 \theta, \quad (3.28)$$

### 3.7 Phase and transmission measurement

So far we have used only the transmission measurement with the fitting model to extract the magnetic mode parameters and the complex permeability  $\mu'(\nu)$  and  $\mu''(\nu)$ . However, it is possible to directly obtain  $\mu'(\nu)$  and  $\mu''(\nu)$  spectra without any model consideration by using both transmission and phase measurements. In this way, we also can check the validity of our fitting model.

In the phase measurement, both channels of the FDMRS setup are used (refer to Fig. 3.3) and form a two beam polarization interferometer (Mach-Zehnder interferometer). It is operated by moving the movable mobile mirror during the frequency scan. The measurable quantity is a displacement  $\Delta(\nu)$  of the movable mobile mirror. This implies that the spectrometer registers the change in the optical thickness of the sample *vs.* frequency. The phase spectrum  $\phi(\nu)$  of the sample is determined from the difference  $\Delta(\nu) - \Delta_0(\nu)$ .

The transmission spectra is shown in Fig. 3.12(a)-dot. The phase spectrum of the polycrystalline sample in a zero magnetic field is shown in Fig. 3.12(b). The permeability  $\mu'(\nu)$  in Fig. 3.12(d)-(dot) and  $\mu''(\nu)$  spectrum in Fig. 3.12(c) -dot are calculated via the corresponding transmission spectra, phase spectra and preliminary found dielectric constants (in Fig. 3.12(c) and (d)-dash line).

We have compared the result between  $\mu'(\nu)$  and  $\mu''(\nu)$  obtained from experiment (Fig. 3.12(d)-dot and (c)-dot), and calculation (Fig. 3.12(d)-line and (c)-line) to the phase spectrum (Fig. 3.12(b)-dot). The results are in good agreement.

We can see that we do not need to do the phase measurement ( $\Phi$ ) since the simulation of  $Tr$  spectra has already given us the  $\mu', \mu''$  parameters. Nevertheless, to check the accuracy of this  $Tr$  spectra simulation model, one needs to measure the phase shift for the comparison.

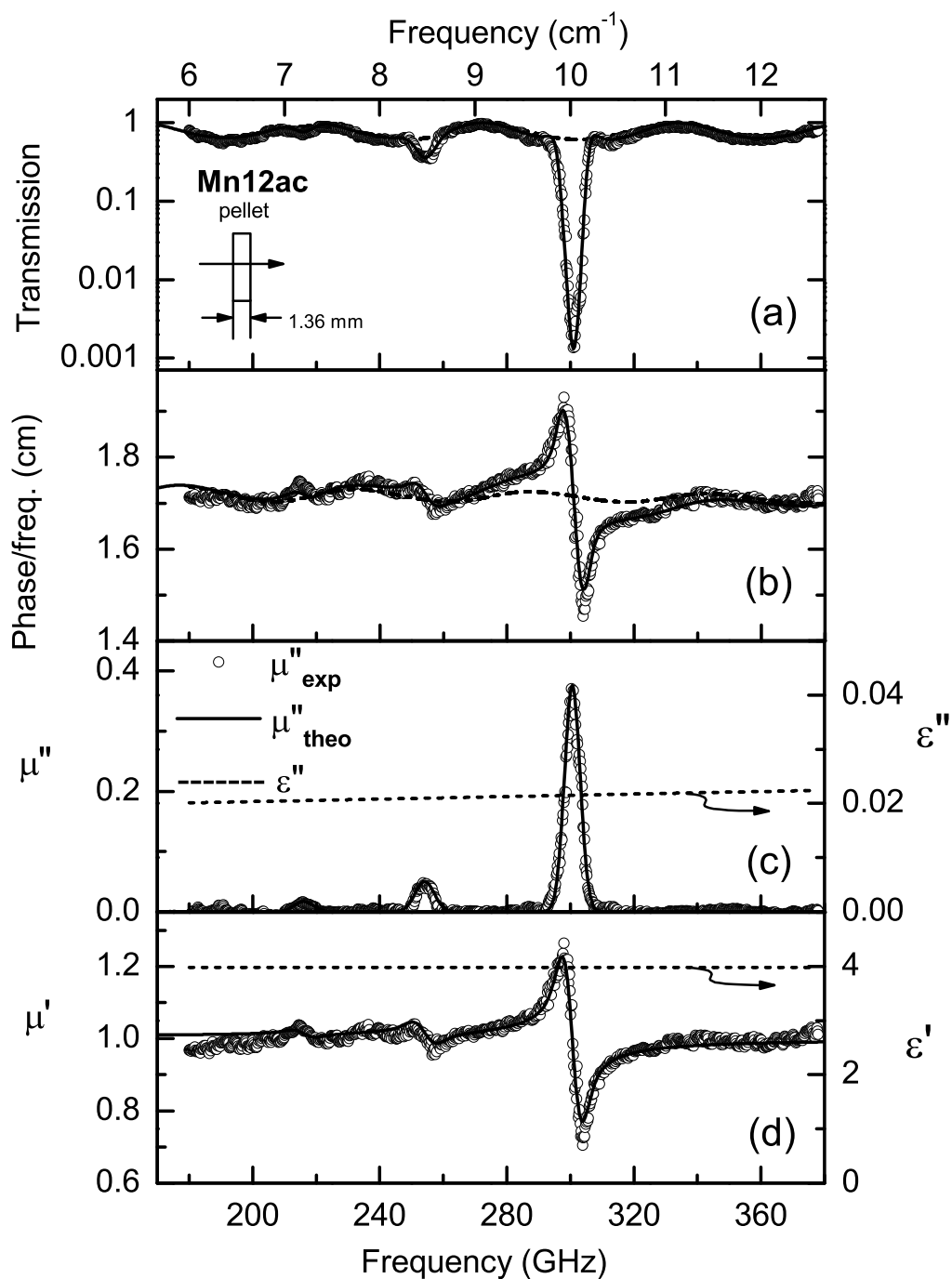


Figure 3.12:  $\text{Mn}_{12}$ -acetate pellet at  $T = 5.2$  K (a) Transmission spectra (b) Phase spectra. (c)+(d) Spectra of the complex permeability  $\mu''$  and  $\mu'$  extracted from transmission and phase spectra by direct calculations. The  $\epsilon'$  and  $\epsilon''$  are obtained directly from the fitting of the transmission line in (a) and are shown as the dash line in (d) and (c) respectively.





# Chapter 4

## Magnetic Resonance in Mn<sub>12</sub>-acetate

In this chapter, we demonstrate that FDMRS is a powerful technique to quantitatively study the material properties of Mn<sub>12</sub>-acetate molecular magnetic clusters. Detailed studies of the transmission spectra measurement of Mn<sub>12</sub>-acetate in zero and non zero applied magnetic field are described. We observed magnetic transitions in the frequency range  $\nu = 6 - 12 \text{ cm}^{-1}$ . We qualitatively and quantitatively study the effects of the temperature and field dependence to the zero field splitting (ZFS) transition in Mn<sub>12</sub>-acetate. The Chapter is divided into two Sections. In the first Section, we studied the temperature dependence of the resonance frequencies, linewidths, and mode contributions to the magnetic permeability in the temperature range 1.9-30 K and in zero magnetic field. In the second Section, we study the field dependence of the ZFS transition in the magnetic field up to 7 T. The studies of the transmission lineshape are very rich in details. The results show the origin of the line broadening in the Mn<sub>12</sub>-acetate clusters.

### 4.1 Experimental

We studied two different types of Mn<sub>12</sub>-acetate samples; (a) plane parallel pressed pellets with a diameter of 10 mm and thicknesses ranging from  $d \sim 0.5 - 2 \text{ mm}$  and (b) a mosaic of single crystals with their easy axes in the plane of the mosaic with a thickness of about 0.5 mm and diameter  $7 \times 7 \text{ mm}^2$  as described in Chapter 3.

Note that in this chapter, we restricted ourselves to the Voigt geometry, where the wave vector of the radiation is perpendicular to the applied magnetic field ( $\mathbf{q} \perp \mathbf{H}_{\text{ext}}$ , see Chapter 3). We used linear polarization radiation within the frequency range  $6 - 12 \text{ cm}^{-1}$ . First we performed the zero field transmission measurement in temperature range of 1.7-30 K. Next we applied an external magnetic field of up to 7 Tesla to zero field cooled samples at temperatures of 1.9-14 K and recorded the transmission spectra. The transmission measurement technique has been described in Chapter 3.

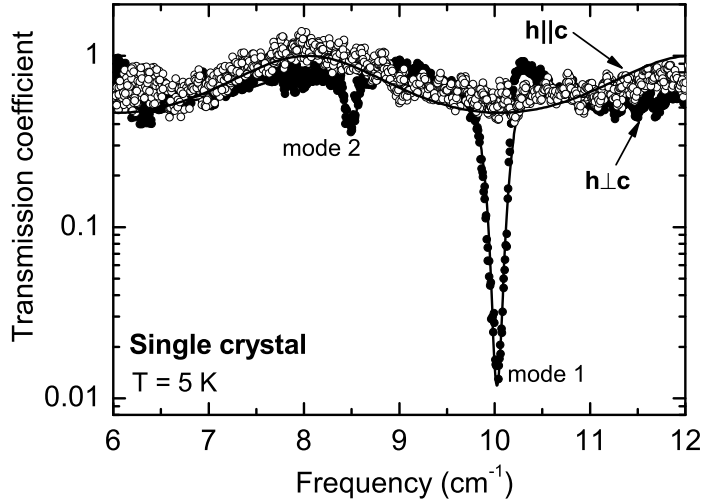


Figure 4.1: Transmission spectra of a 0.5 mm thick mosaic of  $Mn_{12}$ -acetate single crystals for two different directions of magnetic field vector of the radiation:  $\mathbf{h} \perp \mathbf{C}_4$  where the absorption lines are found and  $\mathbf{h} \parallel \mathbf{C}_4$  where there is no absorption line.  $\mathbf{C}_4$  is the easy axis of the  $Mn_{12}$ -acetate crystal.

## 4.2 Part 1: Zero field measurement

### 4.2.1 Experimental results and analysis

#### Checking a mosaic alignment

Before doing any measurement, first we have to check the quality of the crystal alignment of our mosaic sample. We measured the transmission using the radiation with the magnetic field vector  $\mathbf{h}$  parallel and perpendicular to the easy axis  $\mathbf{C}_4$  of the mosaics. The measurement was done at 4 K without applied magnetic field. The result is shown in Fig. 4.1. We found two absorption lines when  $\mathbf{h} \perp \mathbf{C}_4$  and no absorption line when  $\mathbf{h} \parallel \mathbf{C}_4$ . This is due to the magnetic interaction between the magnetic moment ( $\mu$ ) in the sample and the magnetic field vector of the radiation. It causes the magneto-dipolar transition only when  $\mathbf{h} \times \mu \neq 0$ . In other words, from a quantum mechanical point of view, there is a matrix element containing  $\hat{S}_{x,y}$  or  $\hat{S}_{\pm}$ , which causes the magneto-dipolar transition, only when  $\mathbf{h}$  is not parallel to  $\mathbf{C}_4$ . The results in Fig. 4.1 has confirmed us that our crystal alignment is accurate within at maximum a few degrees.

#### Transmission measurement without applied magnetic field

We measured transmission spectra of both  $Mn_{12}$ -acetate mosaic (aligned single crystals) and pellet (polycrystal) samples. Fig. 4.2(a), and Fig. 4.3(a) show the frequency dependent transmission  $Tr(\nu)$  of the  $Mn_{12}$ -acetate single crystals and  $Mn_{12}$ -acetate

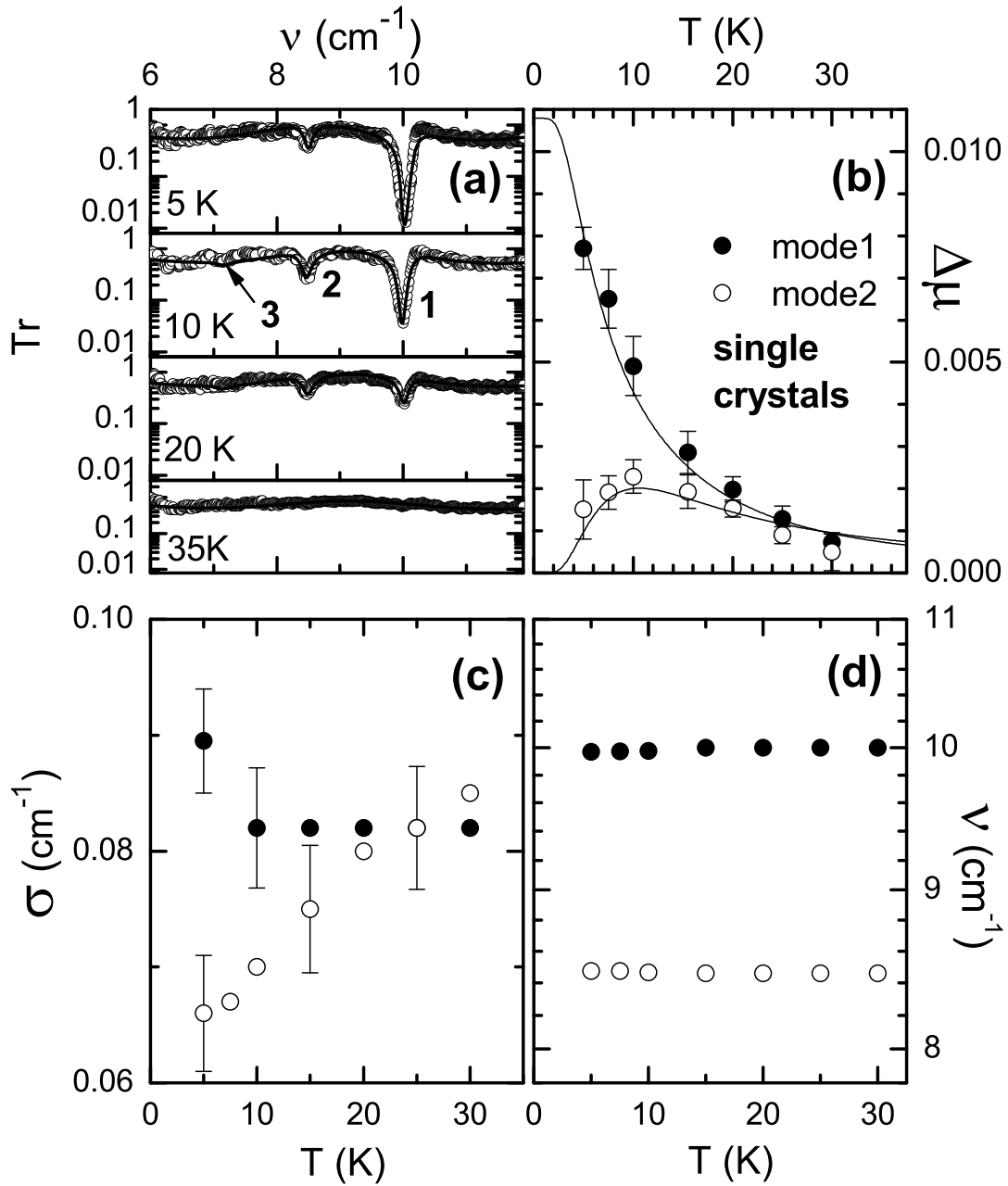


Figure 4.2: Temperature dependence measurement of Mn<sub>12</sub>-acetate single crystal mosaic with a 0.49 mm thickness (a) Transmission coefficient spectra; mode 1 corresponds to the  $|\pm 10\rangle \rightarrow |\pm 9\rangle$  CF transition, mode 2 to  $|\pm 9\rangle \rightarrow |\pm 8\rangle$ , mode 3 to  $|\pm 8\rangle \rightarrow |\pm 7\rangle$ . (b) Mode contribution to the static magnetic permeability of the CF transitions obtained by fitting the transmission spectra as well as calculated. (c) Gaussian linewidths of the transmission spectra as a function of temperature. (d) Magnetic resonance frequency as a function of temperature.

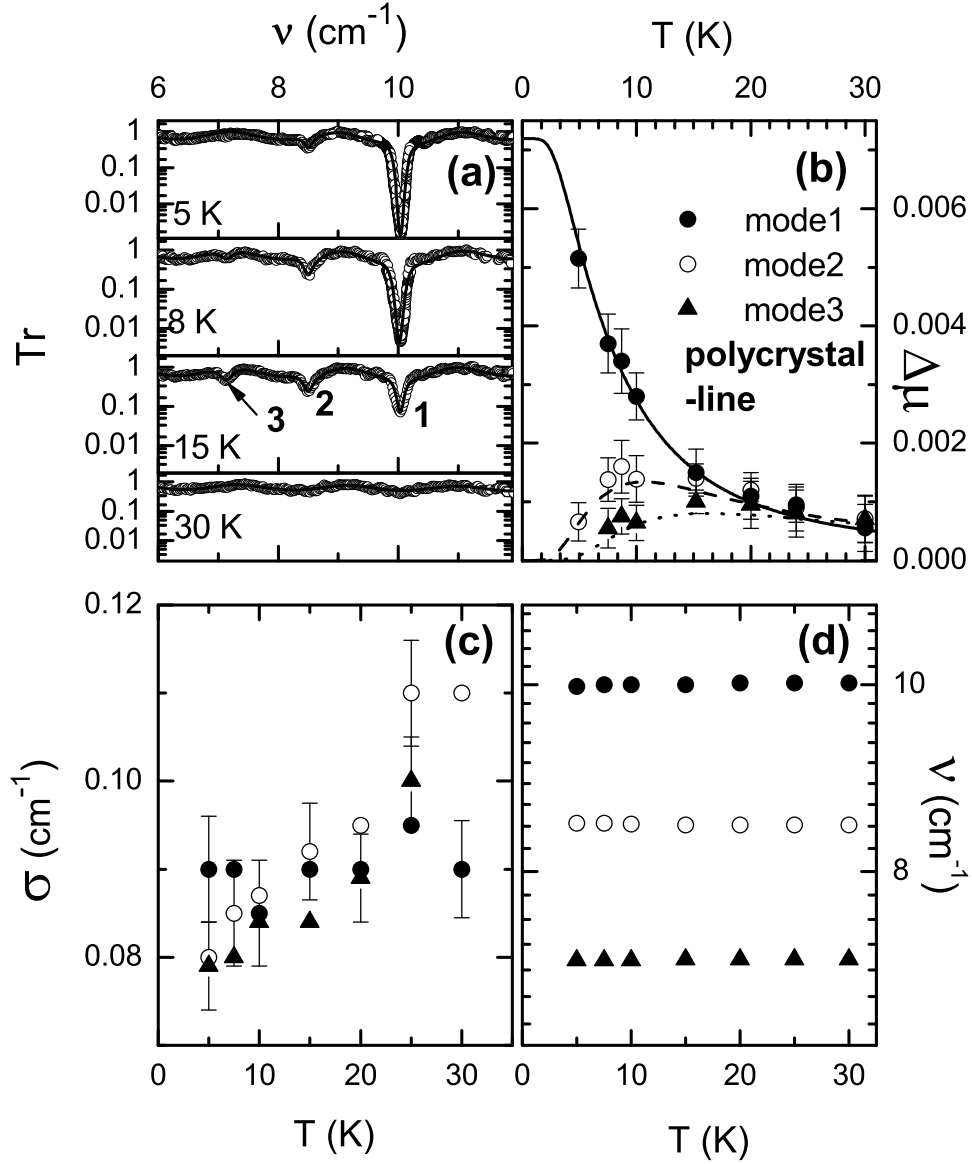


Figure 4.3: Temperature dependence measurement of  $Mn_{12}$ -acetate pellet with a 1.326 mm thickness (a) Transmission coefficient spectra: mode 1 correspond to the  $|\pm 10\rangle \rightarrow |\pm 9\rangle$  CF transition, mode 2 to  $|\pm 9\rangle \rightarrow |\pm 8\rangle$ , mode 3 to  $|\pm 8\rangle \rightarrow |\pm 7\rangle$ . (b) Mode contribution to the static magnetic permeability of the CF transitions obtained by fitting the transmission spectra as well as calculated. (c) Gaussian linewidths of the transmission spectra as a function of temperature. (d) Magnetic resonance frequency as a function of temperature.

pellet recorded at several temperatures (5-35 K). We observed 3 absorption modes in both samples. Note that mode-3 in the single crystal can hardly be observed. This is due to the smaller thickness of the single crystals sample which gives a lower number of the transitions meaning a lower signal compared to the pellet sample.

The three observed modes belong to the magneto-dipolar transitions between; mode-1:  $|\pm 10\rangle$  to  $|\pm 9\rangle$ , mode-2:  $|\pm 9\rangle$  to  $|\pm 8\rangle$ , and mode-3:  $|\pm 8\rangle$  to  $|\pm 7\rangle$  (see Chapter 1). For  $T > 30$  K, these absorption lines are absent. The transmission spectra for both single crystals and pellet are more or less flat, with slight oscillations connected to the interference of the radiation inside the plane parallel sample. As the temperature is lowered a series of narrow absorption lines arise at  $\nu \leq 10$  cm<sup>-1</sup> in the  $Tr(\nu)$  spectra. On reducing the temperature further, the low-frequency lines become weaker while the intensity of the higher frequency line keeps increasing. Below  $T \approx 3$  K only one narrow absorption line (mode-1) remains (approximately at 10 cm<sup>-1</sup>).

In Fig. 4.2(a), and Fig. 4.3(a), the solid lines represent the theoretical fitting spectra using a single Gaussian lineshape per resonance mode. A Lorentzian lineshape does not fit here in our case. The fitting method has been described in Chapter 3. During the fitting process, the dielectric constants were determined by fitting the spectra outside the magnetic lines, using corresponding interference oscillations. To follow the temperature dependence of the absorption lines, their intensities, widths and absorption frequencies from both sample are investigated.

First we investigate the temperature dependence of the line intensity for each mode as a function of the mode contributions ( $\Delta\mu$ ). For  $H=0$ , the total contributions are  $\Delta\mu_{10} = \Delta\mu_{+10} + \Delta\mu_{-10}$ ,  $\Delta\mu_9 = \Delta\mu_{+9} + \Delta\mu_{-9}$ , and  $\Delta\mu_8 = \Delta\mu_{+8} + \Delta\mu_{-8}$  for the observed transitions  $|\pm 10\rangle \rightarrow |\pm 9\rangle$ ,  $|\pm 9\rangle \rightarrow |\pm 8\rangle$ , and  $|\pm 8\rangle \rightarrow |\pm 7\rangle$ , respectively. We have calculated  $\Delta\mu_k$ , where  $k = \pm 10, \pm 9, \pm 8$ , from Eq. 2.89-2.90 which can be here written again as

$$\Delta\mu_k = \gamma^2 H_1^2 |\langle \psi(m) | \hat{S}_{x,y} | \psi(m') \rangle|^2 \left\{ \frac{N \cdot (e^{-E_m/kT} - e^{-E_{m'}/kT})}{\sum_i e^{-E_i/kT} E_{m'm}} \right\}, \quad (4.1)$$

where the parameter details have been described in Section 2.2.1. To obtain the effective permeability, the components of the permeability tensor must be first calculated (see Eq. 2.52 and Eq. 2.70). We have  $\mu_{xx,yy} = \mu_{\perp} = 1 + \Delta\mu \cdot g(\nu)$ ,  $\mu_{xy,yx} = 0$ , and  $\mu_{zz} = \mu_{\parallel} = \mu_0$ . The  $g(\nu)$  function is the lineshape which is better described by Gaussian than Lorentzian type. For Mn<sub>12</sub>-acetate, we calculate the number of atoms per unit volume as  $N = \rho N_a / M$  where density  $\rho = 1.83$  g cm<sup>-3</sup>, number of atoms  $N_a = 6.022 \times 10^{23}$  mol<sup>-1</sup>, and molecular weight  $M = 2059.28$  g mol<sup>-1</sup>. We used  $\gamma = g_{\parallel} \cdot \mu_B$ , where we found  $g_{\parallel} = 1.93$  taken as a fit parameter. We have plotted our results shown in Fig. 4.2(b) and Fig. 4.3(b). The lines represent the theoretical calculated values of  $\Delta\mu_k$ , and the symbols represent the  $\Delta\mu_k$  values obtained as direct fit parameters from the experimental spectra. Both direct calculated  $\mu_k$  and fitted  $\mu_k$  are in good agreement.

In Fig. 4.2(b) and Fig. 4.3(b), we found strong a temperature dependence of  $\Delta\mu_k$ . When lowering the temperature, the intensity of the high frequency mode increases monotonically. While the intensities of the lower frequency modes display maxima at

Parameters	FDMRS [132]	INS [141]	EPR [128]	HFEPFR [54]
$D$ , ( $cm^{-1}$ )	$-0.389 \pm 0.01$	$-0.375 \pm 0.01$	-0.41	$-0.388 \pm 0.02$
$B$ , ( $cm^{-1}$ )	$(-7.65 \pm 0.05) \times 10^{-4}$	$(-8.34 \pm 0.06) \times 10^{-4}$	$6.1 \times 10^{-4}$	$(-7.7 \pm 0.02) \times 10^{-4}$
$C$ , ( $cm^{-1}$ )	$\pm 2 \times 10^{-5}$	-	$\pm 2 \times 10^{-5}$	$\pm 4 \times 10^{-5}$

Table 4.1: Zero field splitting parameters of  $Mn_{12}$ -acetate.

around 10 K for mode-2 and 20 K for mode-3. Below 5 K, these modes practically disappear in our experimental spectra. This can be explained by the level population, which is a function of temperature, and can be described as the Boltzmann distribution function  $exp\{-E_m/kT\} - exp\{E_{m'}/kT\}/[\sum_i exp\{-E_i/kT\}]$ , where  $E_m$  is the energy of  $m$  level and  $i$  is the number of all transition modes (both magnetic and phonon).

Note that, we have added one extra mode around 30-40  $cm^{-1}$  as a correction mode in the partition function ( $\sum_i exp\{E_i/kT\}$ ) of the Boltzmann term for both single crystals and polycrystalline sample, in order to obtain a better fit of the high temperature tail. As shown in Fig. 4.4, the tail of the experimental data (symbols) are fitted much better by adding an extra mode at higher frequency (30-40  $cm^{-1}$ ). The best fit is obtained by adding 38  $cm^{-1}$  mode into the spectrum. This high frequency mode has been observed by far infrared measurements (FIR) [140] and INS measurements [55], and confirmed to be a phonon mode [140]. We also have done the high frequency measurement (up to 70  $cm^{-1}$ ) in the pellet sample using FIR spectrometer. The result is shown in Fig. 4.5. The extra mode are found at 35  $cm^{-1}$ , and 53  $cm^{-1}$ . The 35  $cm^{-1}$  mode which is closed to our estimation at 38  $cm^{-1}$  from the fitting procedure, does not shift in a 7 T magnetic field. There is also no shift for the 53  $cm^{-1}$  mode in the magnetic field. Therefore, we confirm the observed transition mode at 35  $cm^{-1}$  and 53  $cm^{-1}$  as phonon modes.

Next we investigated the resonance frequencies as a function of the temperature. The frequency of all modes  $\nu_k$  are shown in Fig. 4.2(d) and Fig. 4.3(d) for single crystals and polycrystalline sample. For both samples, we observed temperature independence of the resonance frequencies of all three modes in the observed range. This suggests that the temperature does not effect the local environment that causes the ZFS. The observed modes are mode-1 at 10.02  $cm^{-1}$ , mode-2 at 8.50  $cm^{-1}$ , and mode-3 at 7.2  $cm^{-1}$ . We used these values to estimate the ZFS parameters  $D, B, C$  of the spin Hamiltonian  $H_{cf} = DS_z^2 + BS_z^4 + C(S_+^4 + S_-^4)/2$  (see in Chapter 1). We obtained  $D = -0.389 cm^{-1}$ ,  $B = -7.65 \times 10^{-4} cm^{-1}$ , and  $C = \pm 2 \times 10^{-5} cm^{-1}$ .

We have compared our results to INS measurement by Y.Zhong *et al.* [141], EPR measurement by S. Hill *et al.* [128], and HFEPFR measurement by A.L. Barra *et al.* [54] as shown in Table 4.1. Note that, the values in Table 4.1 are recalculated in order to have the same spin Hamiltonian forms and same unit. We found good agreements of ZFS parameters obtained from our FDMRS techniques and the other relevant techniques. In FDMRS and INS techniques, the term  $g\mu_B \mathbf{S} \cdot \mathbf{H}$  is of no importance because we measured in zero magnetic field. However, in HFEPFR or EPR techniques, sweeping magnetic field is needed in order to match the transition energy and the energy of the fixed r.f. field. Therefore, the  $g$ -value can be a crucial parameter in that case.

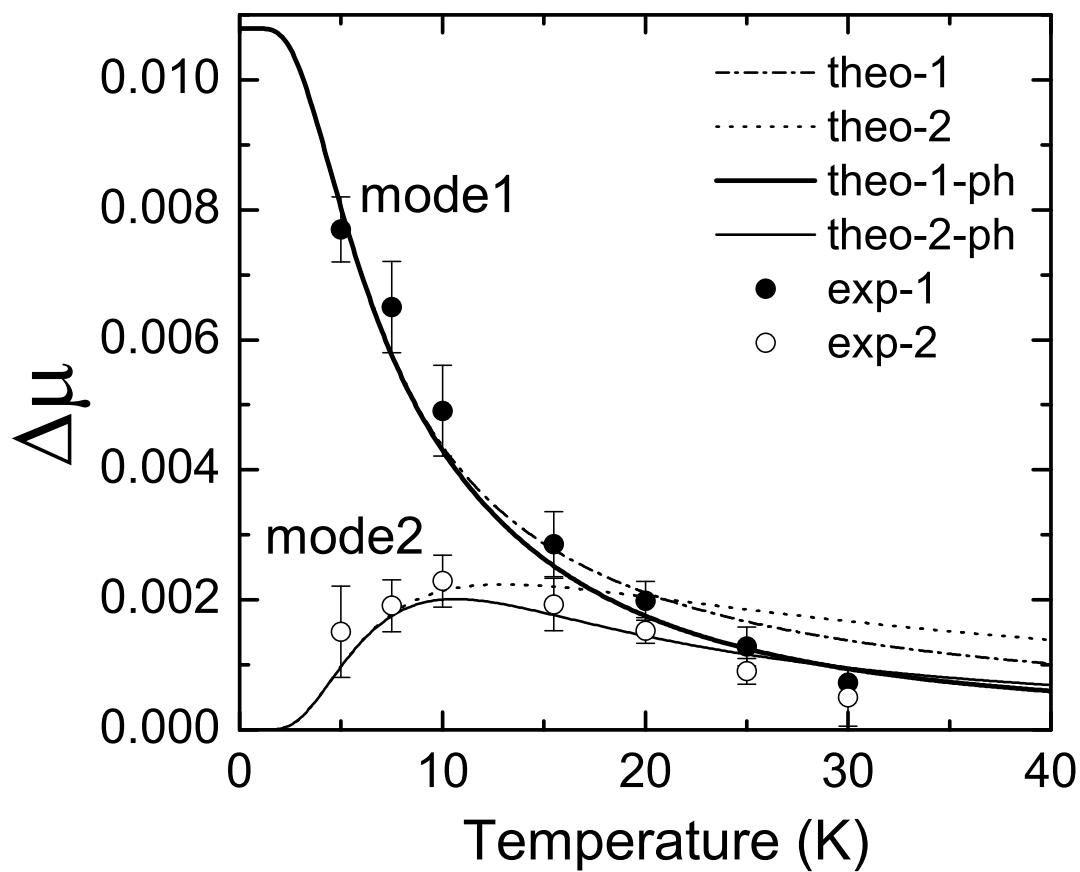


Figure 4.4: Temperature dependence of the mode contributions ( $\Delta\mu$ ) in single crystals sample. Dash lines represent the theoretical calculation without the extra phonon, solid lines represent the theoretical calculation with the extra phonon mode at  $38 \text{ cm}^{-1}$ , and symbols represent the experimental data for transition mode-1 ( $\pm 10 - \pm 9$ ) and mode-2 ( $\pm 9 - \pm 8$ ).

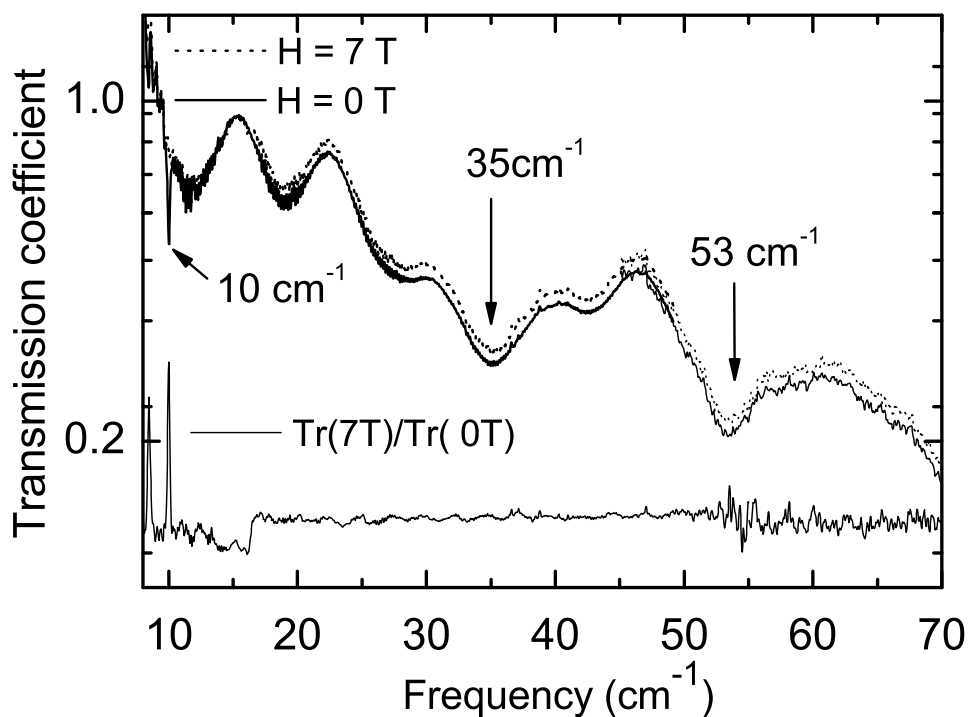


Figure 4.5: The high frequency spectra measured by FIR spectrometer in 0 T and 7 T magnetic field at temperature 10 K of  $Mn_{12}$ -acetate pellet sample. There is no field dependence of the transition modes at  $35\text{ cm}^{-1}$  and  $53\text{ cm}^{-1}$ . The transition line at about  $10\text{ cm}^{-1}$  belongs to the magnetic transition  $|10\rangle \rightarrow |9\rangle$  within the  $S=10$  ground state.



Then we followed the linewidth of each mode as a function of temperature. Here we express the Gaussian linewidth as  $\sigma$ . We have taken  $\sigma_k$  as a fitting parameter while using the theoretically calculated  $\Delta\mu_k$  as a fixed parameter. The result is shown in Fig. 4.2(c) for single crystals, and Fig. 4.3(c) for the polycrystalline sample. The linewidth from the single crystals sample ( $\sigma_{crys} \approx 0.08 - 0.09 \text{ cm}^{-1}$ , therefore  $\text{FWHM}_{single} \approx 2\sqrt{2\ln 2}\sigma \approx 0.188 - 0.212 \text{ cm}^{-1}$  for mode-1) is slightly smaller than the pellet sample ( $\sigma_{pell} \approx 0.09 - 0.10 \text{ cm}^{-1}$ , therefore  $\text{FWHM}_{pell} \approx 0.212 - 0.235 \text{ cm}^{-1}$  for mode-1). The broader line from the pellet compared to the mosaic sample is due to the microcrystals in the pellet which have been subjected to varying stresses that corresponds to slightly broader Gaussian line [142]. For both samples, we found slight temperature dependence of  $\sigma$  for all modes (pronouncedly in mode-2 and mode-3) under the error bar of  $\pm 8\%$  approximately.

## 4.2.2 Discussion

We have found that inclusion of an extra mode at  $38 \text{ cm}^{-1}$  in our theoretical  $\Delta\mu$  calculation significantly improves the high temperature part of the temperature dependence of  $\Delta\mu$ . This mode is not due to any transitions within  $S=10$  ground state. However, it does play a role in the partition function  $\sum_i e^{-E_i}/kT$ , which sums over both magnetic and nonmagnetic levels. M. Hennion *et al.* have also observed high frequency modes at  $40 \text{ cm}^{-1}$ , and  $70 \text{ cm}^{-1}$  in zero field measurement by INS [55]. In the reports of A.B. Sushkov *et al.* [140], the line at  $35 \text{ cm}^{-1}$  has been observed. It does not move in a magnetic field.

The resonance lines have an average Gaussian linewidth of  $\sigma \approx 0.08 - 0.1 \text{ cm}^{-1}$ . Two possible causes for the observed Gaussian broadening are the dipolar fields which is a temperature dependent term, and the distribution in the ZFS parameter ( $D$ ), namely  $D$ -strain, which is a temperature independent term. For the dipolar fields,  $\sigma_{dip}$  estimated by B. Parks *et al.* [144] is around  $\approx 220 \text{ Oe}$  combined with the reported  $\sigma_{hyp} \approx 50-70 \text{ Oe}$  [7, 109], can give the contribution to the linewidth  $\approx 0.03 \text{ cm}^{-1}$  only. This value is not enough to explain our obtained linewidth  $\sigma = 0.08 - 0.1 \text{ cm}^{-1}$ . It implies that the other main contribution to the observed Gaussian linewidth comes from the distribution of the ZFS parameter;  $D$ . It is approximately  $\sigma_{10}^{\pm}/\nu_{10} = \sigma_D/(D + 181B) \approx \sigma_D/D$ ; in our case we have  $\sigma_D \approx 0.01D$  [59, 144]. Note that  $\sigma_{10}^{\pm}$  is the Gaussian linewidth of the transition mode-1 ( $|\pm 10 \rangle \rightarrow |\pm 9 \rangle$ ). The broader distribution from  $D$  parameter compared to the dipolar broadening, is the reason of the limited temperature dependence of the linewidth in  $\text{Mn}_{12}$ -acetate system.

In a real crystal, this  $D$ -strain can be due to the effects such as dislocations [18], or isomer forms within the same single crystal [58]. A. Cornia *et al.* have shown that disorder of acetic acid can induce different coordination surroundings at  $\text{Mn}^{3+}$  ions resulting in six different isomers (see Chapter 1). The three most abundant isomers have  $D = -0.76 \text{ K}$ ,  $-0.778 \text{ K}$ , and  $-0.788 \text{ K}$  giving  $\Delta D/D \approx 0.01$  which is similar to what we have estimated above;  $\sigma_D \approx 0.01D$ . We have used the above three isomers with different  $D$  to quantitatively simulate three isomer absorption lines for the transition mode1 ( $|\pm 10 \rangle \rightarrow |\pm 9 \rangle$ ), where we used the same value of linewidth ( $\sigma$ ) for all lines. As shown in Fig. 4.6, we found the fit is much improved especially at the outer limits

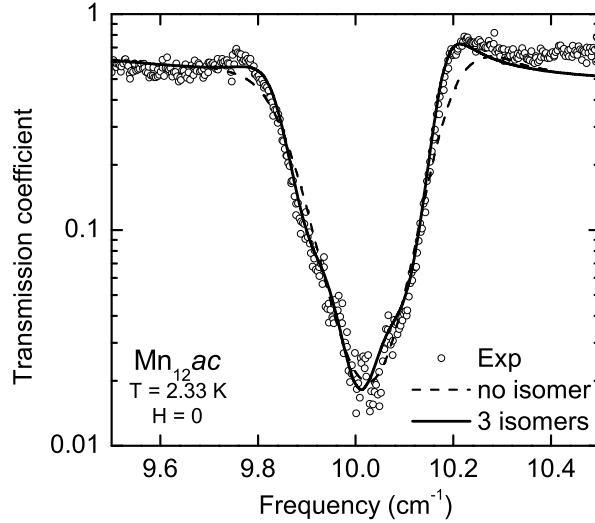


Figure 4.6: Fit of the  $|\pm 10\rangle \rightarrow |\pm 9\rangle$  resonance line of the single crystal sample according to two different models. The dashed line represents a single Gaussian line. The solid line represents the simulation using the ZFS parameters of the three most abundant isomers in the Cornia model [58].

of the absorption line.

However beside D-strain, g-strain which was found in literature to be around  $\sigma_g \approx 0.002g$  [143, 145] can also give a contribution to the linewidth in the in-field measurement. We will discuss this effect in the next section when we apply the external magnetic field.

## 4.3 Part 2: Measurement in magnetic field ( $\mathbf{H} \parallel \mathbf{z}$ )

### 4.3.1 Experimental results, analysis, and discussion

Fig. 4.7 shows transmission spectra recorded on a single crystal mosaic at temperature 14 K with and without applied magnetic field. By applying the external magnetic field, the Zeeman effect causes the magneto-dipolar transitions to split. Two absorption lines, which are degenerate at  $\mathbf{H} = 0$ , move up and down in frequency proportional to the magnetic field (white dot spectra in Fig. 4.7). The absorption line which shifts up in frequency becomes stronger at the expense of its low-frequency counterpart. This behavior can be explained by the distribution of the level population due to the strength of the magnetic field.

First we calculated the frequencies of the split states ( $\pm |m\rangle \rightarrow \pm |m-1\rangle$ ) in the magnetic field. See the Hamiltonian including the applied field in Chapter 1.

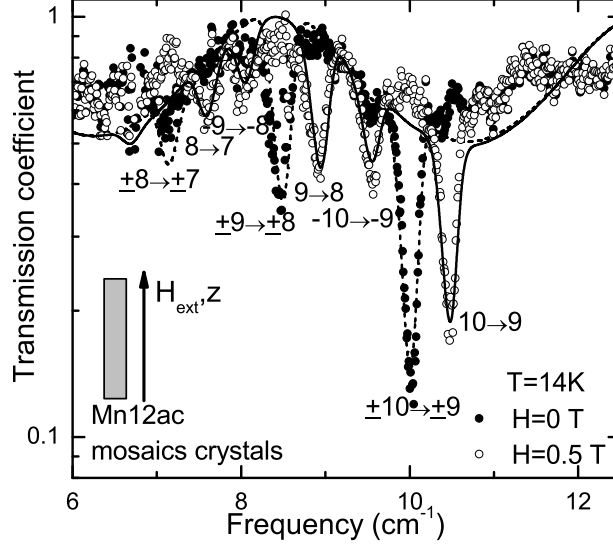


Figure 4.7: Zeeman splitting of the  $|\pm 10\rangle \rightarrow |\pm 9\rangle$  ZFS transition. The 14 K transmission spectra were recorded in the external magnetic field  $\mathbf{H} = 0$  and 0.5 T.

$$h\nu_p = E_{m-1,H} - E_{m,H}, \quad (4.2)$$

$$h\nu_m = E_{-m+1,H} - E_{-m,H}, \quad (4.3)$$

where the frequency  $\nu_p$  and  $\nu_m$  corresponds to the transition  $|+m\rangle \rightarrow |+m-1\rangle$  and  $| -m\rangle \rightarrow | -m+1\rangle$  respectively.  $E_{m,H}$  is the energy of level  $m$  as a function of the applied magnetic field ( $H = H_{ext}$ ).

If the system is disturbed by the magnetic field, the population correspond to the  $p$ -transition ( $|+10\rangle \rightarrow |+9\rangle$ ) and the  $m$ -transition ( $| -10\rangle \rightarrow | -9\rangle$ ) will be biased. Therefore, we introduce the factor ( $p = [0..1]$ ) to correct  $\Delta\mu$  as

$$\Delta\mu = \Delta\mu_p + \Delta\mu_m, \quad (4.4)$$

$$\Delta\mu_p = \frac{\nu_0}{\nu_p} p \Delta\mu_0, \quad (4.5)$$

$$\Delta\mu_m = \frac{\nu_0}{\nu_m} (1-p) \Delta\mu_0. \quad (4.6)$$

The  $p$  and  $1-p$  factor represent how much the population presents in the state  $|+10\rangle$  and  $| -10\rangle$  respectively. Note that, in this case, we fitted  $\Delta\mu$  instead of using the calculated one. We need the correction term  $\nu_0/\nu_p$  and  $\nu_0/\nu_m$  for  $\Delta\mu_p$  and  $\Delta\mu_m$  respectively in  $H \neq 0$ . Since, in  $H = 0$  case,  $\Delta\mu$  is a function of  $1/\nu_0$  (refer to

the term  $1/E_{mm'} = 1/(E_{m'} - E_m) = 1/h\nu_0$  in Eq. 4.1). Therefore, in  $H \neq 0$ , there is a need for the correction term  $\nu_0/\nu'$ , where  $\nu'$  is the transition frequency corresponding to the field  $H \neq 0$ .

Thereafter, we simulated the spectrum by using the same procedure as described in Section 3.6. The simulation spectra for  $H = 0.5$  T of all three observed modes are shown in Fig. 4.7 (white dots). An overview of the Zeeman splitting in a larger field range is given in the Fig. 4.8(a), where the resonance frequencies of the various ZFS transitions are plotted as a function of applied magnetic field up to 6 Tesla. Those average slope corresponds to  $g_{\parallel} = 1.93 \pm 0.02$ .

Up to this point, we can obtain  $g_{\parallel}$  from the slope of the plot in Fig. 4.8(a);  $g_{\parallel} = 1.93 \pm 0.02$  which is close to the value obtained from HF-EPR by A.L. Barra *et al.* [54];  $g_{\parallel} = 1.93 \pm 0.01$ , while  $g_{\parallel} \approx 1.97 - 2.08$  was obtained from EPR by S. Hill *et al.* [128].

In Fig. 4.8(b), we plot Gaussian linewidth of the transition  $|+10 \rangle \rightarrow |+9 \rangle$  and  $|+9 \rangle \rightarrow |+8 \rangle$  of the single crystal mosaics as a function of the applied magnetic field in  $\mathbf{z}$  direction. We found the linewidth independent of the field. Therefore, there is no g-strain in our case, which is in contrast to the report by S. Hill *et al.* [128, 142].

In the case of a polycrystalline sample, the result is shown in Fig.4.9 where the transmission coefficients of the first mode ( $|\pm 10 \rangle \rightarrow |\pm 9 \rangle$ ) are plotted against the applied magnetic field. We found the transmission lines of polycrystal are broader than the single crystals one. Due to the random orientation of the easy axis in the crystals, the lines are much inhomogeneously broadened at the higher field. In this case, we need to average the permeability in Eq. 4.1 with respect to their orientation. The average function is  $\bar{f} = \langle f(\theta_H) \rangle = \frac{1}{2} \int_0^{\pi} f(\theta_H) \sin \theta_H d\theta_H$ , where  $\theta_H$  is the angle between the easy axis and the magnetic field  $H_z$ .

At  $H_z = 0$ , the spectra is symmetric Gaussian. At the higher field, the spectral become asymmetric Gaussian. It is due to the inhomogeneous splitting of the degenerate  $|\pm 10 \rangle$  and  $|\pm 9 \rangle$  state with the frequency ( $\nu_p$  and  $\nu_m$ ) calculated from Eq. 4.2, and Eq. 4.3. In the spin Hamiltonian, we have  $H_z = H \cos \theta_H$  plus the average value of the permeability tensor components. These make the line becomes much broader than the single crystal case. In this case, the line broadening is because of  $H_z = H \cos \theta_H$  term. Different molecules experience different longitudinal fields.

## 4.4 Conclusion

Using a novel type of frequency-swept EPR spectroscopy, we have performed a detailed study of the crystal-field transitions in  $Mn_{12}$ -acetate (for both single crystals and a polycrystalline sample) at temperature  $1.5 \text{ K} < T < 40 \text{ K}$  and magnetic fields up to 7 T in Voigt geometry. The analysis of our experimental data shows that the spectroscopic characteristics of the ZFS transitions in  $Mn_{12}$ -acetate persist for the different kinds of samples. Result from the oriented single crystals (mosaic) and polycrystalline pellets are in a good agreement with each other. We have quantitatively described the observed transmission spectra for both  $H = 0$  and  $H \neq 0$ . We have determined the mode contribution to the static magnetic permeability, linewidth and

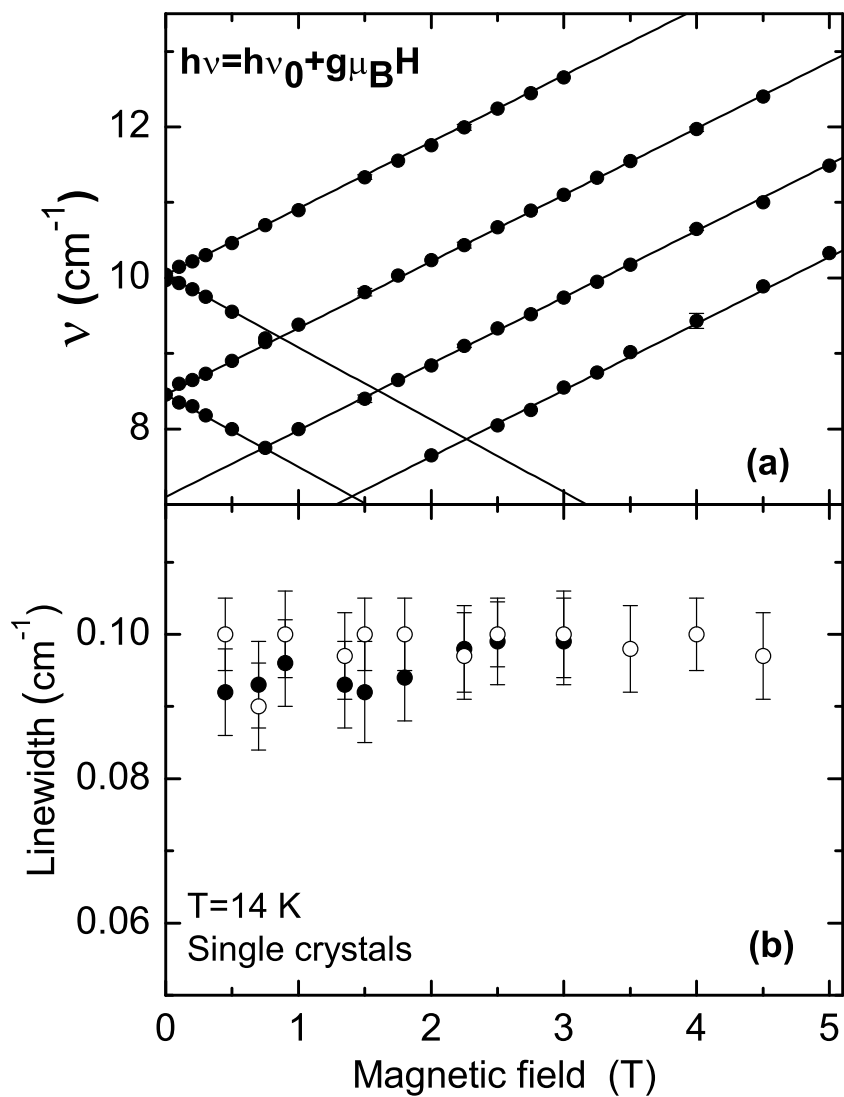


Figure 4.8: (a) Magnetic field dependence of the resonance frequencies of the ZFS transitions in a magnetic field up to 5 T recorded on the single crystal sample. (b) Gaussian linewidth of the transition  $| +10 \rangle \rightarrow | +9 \rangle$  (black dots), and  $| +9 \rangle \rightarrow | +8 \rangle$  (white dots) in the single crystal mosaic at  $T=14$  K, plotted as a function of the magnetic field.

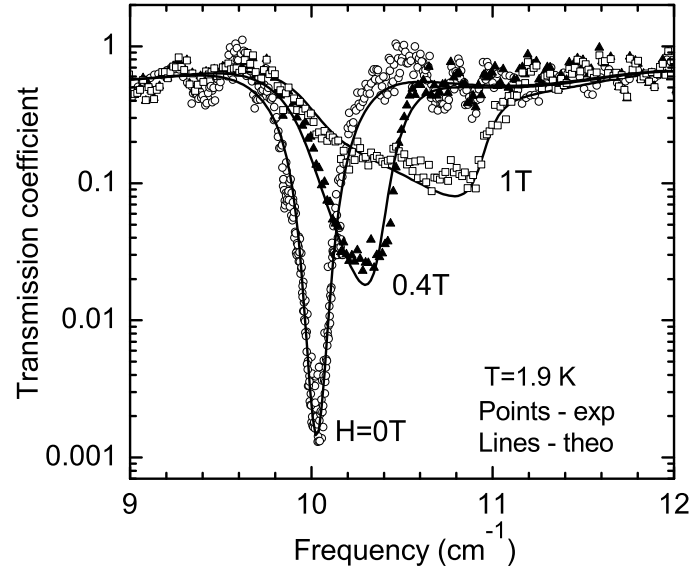


Figure 4.9: Magnetic field dependence of the  $|\pm 10\rangle \rightarrow |\pm 9\rangle$  transition of the pellet of  $Mn_{12}$ -acetate at  $T = 1.9$  K. The solid lines represent theoretical description.

transition frequencies as a function of temperature and magnetic field. We obtained the main characteristics of the ZFS transitions such as ZFS parameters and g-value. We conclude that the contributions to the inhomogeneous broadening of the ZFS transition in  $Mn_{12}$ -acetate are the dipolar field, and the distribution in CF parameter (D-strain) but not g-strain in our case.

# Chapter 5

## Magnetic resonance - lineshape studies on Mn<sub>12</sub>-acetate

In Chapter 4, the material properties of Mn<sub>12</sub>-acetate (ZFS parameters, g-factor, and magnetic permeability contribution) were quantitatively studied in Voigt geometry. In this Chapter, the magneto-optical properties of the same sample are investigated. It is shown that the magnetic resonance lineshapes strongly depend on the relative orientation of the magnetic field, radiation propagation direction and the magnetic state of the sample. These features are mainly due to the magneto-optical properties rather than the magnetic resonance properties of the sample. Measurements were performed in Voigt and Faraday geometry, in magnetized (*fc*) and non-magnetized (*zfc*) states, and by using linearly and circularly polarized radiation. The magnetic resonance lineshapes are described quantitatively and qualitatively. The findings of this Chapter have some important consequences for magnetic resonance measurements in general.

### 5.1 Experiment

The experiments are divided into two main parts according to two different arrangements; Voigt ( $\mathbf{H} \perp \mathbf{q}$ ) and Faraday ( $\mathbf{H} \parallel \mathbf{q}$ ) geometries (see Section 2.1.5). The Mn<sub>12</sub>-acetate samples were separately prepared for each geometry (see Section 3.4). The sample was mounted on a sample holder with the easy axes of the crystals lying parallel to the applied magnetic field. For both geometries, we performed the transmission measurement at low temperature (1.7 – 3.3 K), in order to probe the magneto-dipolar transitions between the lowest lying states ( $|\pm 10\rangle \rightarrow |\pm 9\rangle$ ).

In Voigt geometry, the external field is perpendicular to the radiation propagation,  $\mathbf{H} \perp \mathbf{q}$ . We used linearly polarized radiation with  $\mathbf{h} \perp \mathbf{H}$  to probe the transmission line. First we performed the zero field cooled measurement (*zfc*) by cooling the sample down to 1.7 K without an applied magnetic field. Then, we measured the transmission line. After that, we heated up the sample to 70 K in order to start the field cooled measurement (*fc*). When we reached 70 K, we applied a magnetic field of 2 T. Then we cooled the sample down to 1.7 K in the field. As soon as the temperature had

stabilized, we switched off the field. Finally, we measured the transmission line in zero field again but in the magnetized state. We used only linearly polarized radiation to probe the transmission because the spectrum is not sensitive to the magnetization state of the sample when using circularly polarized radiation in Voigt geometry.

In Faraday geometry as we have explained in Section 2.1.5, there is a very strong coupling between the magnetic vector  $\mathbf{h}$  of the r.f. radiation and the magnetized medium (magnetized by the external magnetic field). Recall that in Faraday geometry, the rotating  $\mathbf{h}$  of circularly polarized radiation is always perpendicular to the external magnetic field, while in Voigt geometry, it is not always the case.

We used linearly polarized radiation to probe the transmission line. We placed an extra analyzer in front of the detector. We will explain the analyzer effect in the analysis and discussion part.

First of all, we performed the zero field and field cooled measurement, similarly to what we have done in Voigt geometry. We found an extreme transformation of the lineshape between magnetized and demagnetized states. Next we set the analyzer in front of the detector at different angles ie.  $0^\circ, +45^\circ, -45^\circ, +90^\circ$ . We measured the transmission line of the sample in *fc* state in zero magnetic field as a function of the analyzer angle.

Secondly, we performed the circular light experiment with *zfc* and *fc* condition at 1.77 K. We measured the transmission spectra using circularly polarized light. We found the absorption line for both L.H.C. and R.H.C. in *zfc* case. In *fc* case, depending on the direction of the field, we found an absorption for L.H.C. but not for R.H.C. if we cooled the sample in  $+H$  and vice versa for  $-H$  field. We did not use the analyzer in this case, since there is no change in the spectra lineshape with and without an analyzer.

## 5.2 $Mn_{12}$ -acetate in Voigt geometry

### 5.2.1 *zfc* and *fc* measurement with linearly polarized radiation in Voigt geometry

#### Experimental results

The results of *zfc* and *fc* measurement in zero magnetic field using linearly polarized radiation at 2.33 K are shown in Fig. 5.1. We found that the resonance line in the *zfc* case lies at a frequency of  $10.002 \text{ cm}^{-1}$  and has a symmetric lineshape. In the *fc* case, the resonance line is around  $10.10 \text{ cm}^{-1}$  and has an asymmetric lineshape. After the *fc* measurement, we kept measuring the transmission spectra at the same temperature, increasing the magnetic field up to 1.8 T. We found that the resonance line remains asymmetrical. The results are shown in Fig. 5.2.

#### Analysis and discussion

For quantitative analysis of the spectra [59], we have to determine the optical response using the effective magnetic permeability in the case of Voigt geometry (see Section



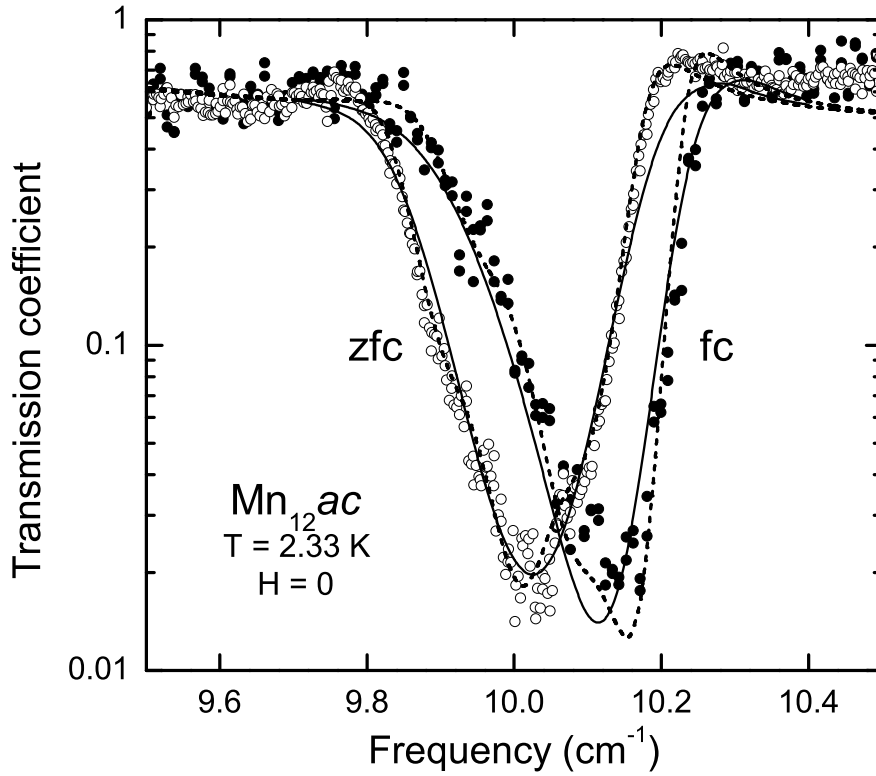


Figure 5.1: Transmission spectra (dots) due to  $|\pm 10\rangle \rightarrow |\pm 9\rangle$  magnetic transitions in the  $Mn_{12}$ -acetate single crystals measured at  $T=2.33$  K and in zero magnetic field. In the *zfc* case, the absorption line is at  $10.002$   $cm^{-1}$  while in the *fc* case, it is shifted to  $10.10$   $cm^{-1}$ . The solid lines show the calculation results using a single Gaussian line model and the dashed lines show the calculation results using the isomer model (see text). The *zfc* line is found to be a symmetric Gaussian whereas the *fc* line is found to be an asymmetric Gaussian.

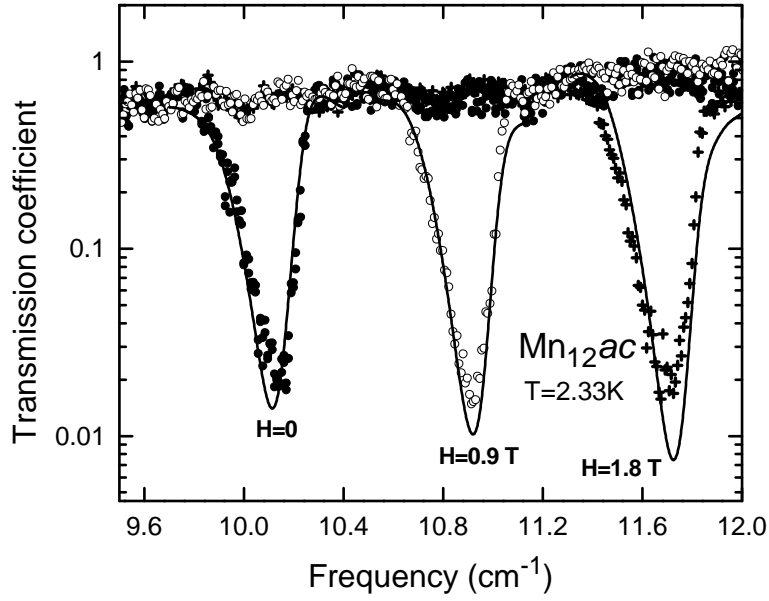


Figure 5.2: Absorption due to the  $|\pm 10\rangle \rightarrow |\pm 9\rangle$  crystal field transition in  $Mn_{12}$ -acetate single crystals at  $T=2.33$  K measured at different magnetic fields. The solid lines represent the calculations using single Gaussian lines.

3.6),

$$\hat{\mu}_{eff} = \hat{\mu}_{xx}(\nu) - \hat{\mu}_{xy}(\nu)\hat{\mu}_{yx}(\nu)/\hat{\mu}_{yy}(\nu), \quad (5.1)$$

where

$$\hat{\mu}_{xx} = \hat{\mu}_{yy} = 1 + \Delta\mu \cdot g(\nu), \quad (5.2)$$

$$\hat{\mu}_{xy} = -\hat{\mu}_{yx} = \nu\Delta\mu \cdot g(\nu), \quad (5.3)$$

where all parameter details have been described in Section 2.2.1 and Section 3.6. In general,  $g(\nu)$  can be Gaussian or Lorentzian lineshape described in Eq. 2.86-2.88.

In the *zfc* case, the external magnetic field is absent, and the average magnetization in the  $Mn_{12}$ -acetate sample is zero. The offdiagonal components ( $\hat{\mu}_{xy}$  and  $\hat{\mu}_{yx}$ ) are therefore zero, while the diagonal components still exist.

In the *fc* case, the external magnetic field is still absent in the zero field measurement. However, we have cooled the sample in a strong field therefore the average magnetization of the sample is not zero. Consequently, the off-diagonal components appear while the diagonal components remain the same as in *zfc* case. Hence, from Eq. 5.1, we obtained the  $\hat{\mu}_{eff}$  for *zfc* and *fc* case as

$$\hat{\mu}_{eff,zfc}(\nu) = 1 + \Delta\mu_{\pm 10} \cdot g(\nu), \quad (5.4)$$

$$\hat{\mu}_{eff,fc}(\nu) = 1 + \frac{\Delta\mu_{+10} \cdot g(\nu)}{1 + \Delta\mu_{+10} \cdot g(\nu)}, \quad (5.5)$$

where all components of permeability tensor have been described in Eq. 5.2, and Eq. 5.3.  $\Delta\mu_{\pm 10}$  refers to the mode contribution in  $zfc$  case, where the transitions can occur from both  $|\pm 10\rangle \rightarrow |\pm 9\rangle$  states. In  $+fc$  case, the transition occurs only from  $|+10\rangle \rightarrow |+9\rangle$  state.

We used the transmission spectra fitting model explained in Section 3.6 combined with the effective magnetic permeability in Eq. 5.4 and Eq. 5.5 to fit our data. We found a better spectral fit with Gaussian lineshapes than with Lorentzian ones. The argument for using Gaussian lineshape due to the distribution of the crystal field parameters has already been discussed in Section 4.2.2.

In Fig. 5.1, those two spectra represent the transitions from state  $|10\rangle \rightarrow |9\rangle$ . We found a frequency shift of  $\approx 0.098 \text{ cm}^{-1}$ , from  $\nu_{10} = 10.002 \text{ cm}^{-1}$  in  $zfc$  case to  $\nu'_{10} = 10.10 \text{ cm}^{-1}$  in  $fc$  case. There are two contributions that cause the line shift; the effect of the magnetic permeability ( $\Delta\nu_{\mu_{eff}}$ ), and the internal field ( $\Delta\nu_{int}$ ).

The shift can be first estimated from the change in the permeability. In Eq. 5.5, the minimum in transmission is where the denominator goes to zero. Therefore, we can estimate the line shift as;  $\bar{\nu} = \nu'_{10}\sqrt{1 + \Delta\mu}$ . From fitting procedure, we found  $\Delta\mu_{+10} \approx 0.008$ . Hence, the change in  $\mu_{eff}$  gives  $\Delta\nu_{\mu_{eff}} = \bar{\nu}_{10} - \nu_{10} \approx 0.07 \text{ cm}^{-1}$ .

The other contribution to the frequency shift is due to the internal dipolar field;  $H_{eff} = H_{ext} + H_{dip} = H_{ext} + \lambda\mathbf{M}$ , where  $\lambda\mathbf{M}$  is the magnetic field proportional to the averaged magnetization  $\mathbf{M}$  ( $\mathbf{M}=0$  in  $zfc$  and  $\mathbf{M}=M_s$  in  $fc$ ).  $\lambda$  is magneto-dipolar tensor, where  $\lambda_{\parallel} \equiv \lambda_{zz}$  and  $\lambda_{\perp} \equiv \lambda_{xx} = \lambda_{yy}$ . Note that in our case, the transverse internal dipolar fields  $\sim \lambda_{\perp}M_{\perp}$  play very small role. Thus we set this value to zero. The frequency shift in  $fc$  state is  $h\nu'_{10} = h\nu_{10} + g\mu_B\lambda_{\parallel}M_s$ . From the fit, we found the internal field about  $0.024 \text{ cm}^{-1}$ , where the average calculated dipolar is predicted to be  $g\mu_B\lambda_{\parallel}M_0 \approx 0.01 - 0.02 \text{ cm}^{-1}$  [109, 31, 115, 98].

Therefore, total frequency shift from the above discussions ( $\Delta\nu_{\mu_{eff}} \approx 0.07 \text{ cm}^{-1}$  and  $\Delta\nu_{int} \approx 0.024 \text{ cm}^{-1}$ ) is  $\approx 0.094 \text{ cm}^{-1}$ . This value is in good agreement with the experimental frequency shift ( $\Delta\nu_{exp} = 0.098 \text{ cm}^{-1}$ ). Note that, the above arguments of the lineshift (the difference in  $\hat{\mu}_{eff}$  and the influence of  $H_{dip}$ ) also valid for the Lorentzian line. Hence, the frequency shift effect can be found in both Gaussian and Lorentzian lineshape. However, the asymmetry of the line in Eq. 5.5 occurs only in the case of a Gaussian lineshape but not Lorentzian lineshape. The Lorentzian lineshape stays symmetric for both  $fc$  and  $zfc$  case. We have simulated the imaginary part of the magnetic permeability ( $\mu''$ ) which corresponds to the magnetic resonance absorption term for both Gaussian and Lorentzian type in the  $fc$  case. An asymmetry of the magnetic resonance line was also observed in EPR measurement of  $Mn_{12}$ -acetate by Hill *et al.*[142]. We simulated the spectra measured in the magnetic field up to 1.8 T as shown as a solid line in Fig. 5.2. The asymmetry still remains in  $fc$  state as we have predicted.

Note that, generally the intensity of the resonance line is a function of resonance frequency. The amplitude of the field is reduced by the higher exponential factor  $exp(-2\pi k/n)$  per wavelength in the medium. As shown in Fig. 5.2, the theoretical transmission line is deeper at higher frequency. However we do not see this effect in our experimental data. It is possibly due to experimental limitations e.g. parasitic radiation in the cryostat.

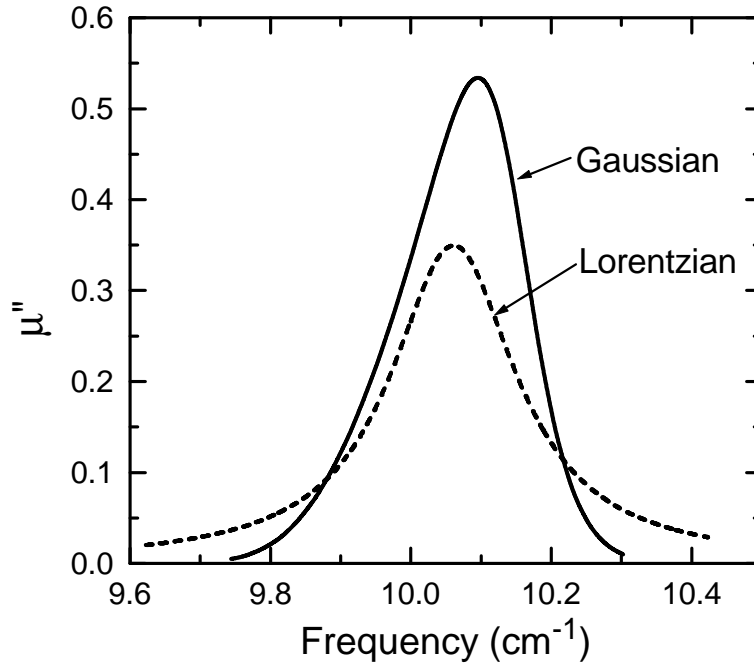


Figure 5.3: Imaginary part of magnetic permeability( $\mu''$ ) compared between Gaussian and Lorentzian lineshape at zero magnetic field ( $H=0$ ) for  $fc$  state.

Qualitatively, there are several contributions to the inhomogeneous broadening of CF-transitions such as the random distribution of magneto-dipolar fields [109, 145, 142], hyperfine fields [109, 146, 147], tilting of the anisotropy axes of single  $Mn_{12}$ -acetate molecules from  $c$ -axis [148], local variations of CF parameters (D-strains) [58, 59, 18, 142, 145] etc. However in our case, the tilt of the easy axis of  $Mn_{12}$ -acetate from the direction of the magnetic field can hardly play a role, since in our observation, the asymmetry does not vanish in zero external magnetic field.

## 5.3 $Mn_{12}$ -acetate in Faraday geometry

### 5.3.1 $Mn_{12}$ -acetate in Faraday geometry measured with linearly polarized radiation

In this Section, we performed the measurement in Faraday geometry with linearly polarized light. An additional analyzer is placed in front of the detector. Without the analyzer, we have half the intensity signal compared to Voigt spectra. This will be explained later in the Section. When an analyzer is introduced, the lineshape changes dramatically. We studied the influence of the magnetic states ( $zfc$  and  $fc$ ) and the angular dependence of an analyzer to the magneto-optical lineshape in Faraday geometry.

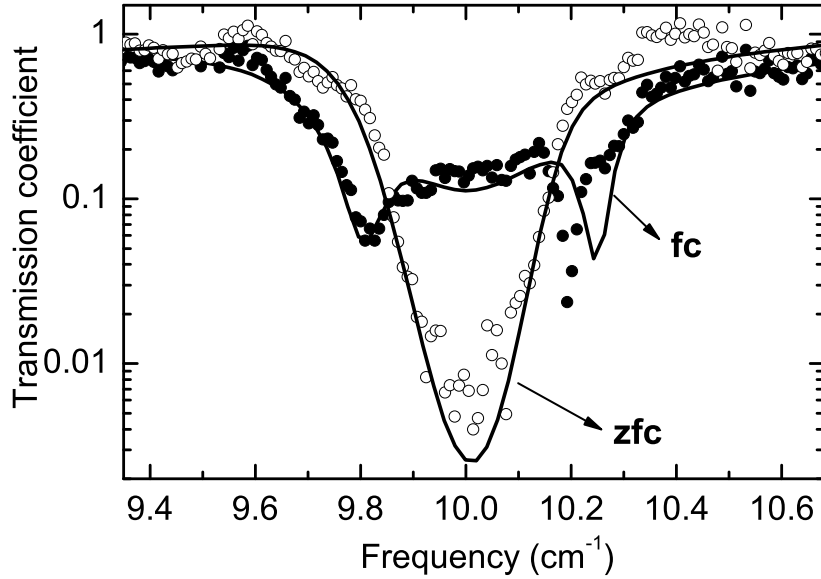


Figure 5.4: Transmission spectra from  $|\pm 10\rangle \rightarrow |\pm 9\rangle$  states in Faraday geometry measured at temperature 3.3 K and in magnetic field 0 T. Black dots and white dots represent the zero field cooled *zfc* and field cooled *fc* measurement respectively. Lines represent the theoretical calculation. (See text)

### Experimental results

We used linearly polarized light to probe the transmission spectra of the  $|\pm 10\rangle \rightarrow |\pm 9\rangle$  transitions. First, we placed the analyzer set at  $0^\circ$  in the front of the detector. We cooled the sample from room temperature down to 3.3 K in zero magnetic field (*zfc* measurement). When the temperature was stabilized, we measured the transmission spectra. The result is shown in Fig. 5.4 (white dots). The line shape is similar to the one obtained from *zfc* measurement in Voigt geometry. The resonance frequency of *zfc* state is at  $10.02 \text{ cm}^{-1}$ .

Then we heated the sample to 80 K and then applied the magnetic field to 2 T. We started to cool the sample down again to 3.3 K in 2 T field (*fc* measurement). When temperature reached 3.3 K, we switched the field to zero and immediately measured the transmission line. The result is in Fig. 5.4 (black dots). We can clearly see that, the lineshape in *fc* state is significantly different from the *zfc* one. The absorption intensity is half of the *zfc* spectra. However, the resonance frequency remains unchanged at  $10.02 \text{ cm}^{-1}$ . A slight asymmetry between the two minima of the *fc* lineshape is due to the fact that the analyzer angle is slightly off from  $0^\circ$ .

Next we measured the *fc* transmission spectra in the zero magnetic field using different analyzer angles ( $0^\circ$ ,  $+45^\circ$ ,  $-45^\circ$ ,  $90^\circ$ ) at temperature 1.77 K. The results are shown in Fig. 5.5 where we found that the peculiar lineshape structure depends on the analyzer angle.

### Analysis and discussion

Recall that the magnetic field ( $\mathbf{H}$ ) is oriented along the  $z$ -direction. Therefore, we can write the same magnetic permeability tensor as Eq. 2.52, where all magnetic permeability components are defined as Eq. 5.2 and Eq. 5.3. If we use linearly polarized light which its  $\mathbf{q}$  vector parallel to  $\mathbf{H}$ , we can view this as a combination of two circularly polarized wave (left and right hand) as explained in Section 2.1.6. The effective magnetic permeability in Faraday geometry using linearly polarized light can be written as Eq. 3.24-3.25. However in this Section, they will be rewritten as

$$\hat{\mu}_{(eff, left)} = 1 + \frac{1}{2}(1-p) \Delta\mu_{10} \cdot g(\nu) - i\frac{1}{2}p\Delta\mu_{10} \cdot g(\nu), \quad (5.6)$$

$$\hat{\mu}_{(eff, right)} = 1 + \frac{1}{2}(1-p)\Delta\mu_{10} \cdot g(\nu) + i\frac{1}{2}p\Delta\mu_{10} \cdot g(\nu), \quad (5.7)$$

where  $g(\nu)$  is the lineshape function (see Section 2.2.1). The notation *left* belongs to L.H.C. wave and *right* belongs to R.H.C. wave.  $p$  is a population factor defined as a difference between the populations in the  $|+10\rangle$  and  $|-10\rangle$  states. We set  $p = 1$  for *fc* case and  $p = 0$  for *zfc* case.

We fitted the spectral using  $g(\nu)$  as a Gaussian lineshape. The sample thickness is 0.75 mm. The fixed parameters for both cases (*zfc* and *fc*) are the dielectric constant  $\epsilon = 4.9$ , linewidth  $\sigma_G \simeq 0.09 \text{ cm}^{-1}$ , and mode contribution  $\Delta\mu \simeq 0.0085$ . The effective permeability for each case can be discussed as follows:

#### i) Zero field cooled case (*zfc*) - demagnetized state

In this case, we have  $p=0$  then the effective magnetic permeability can be rewritten as following

$$\hat{\mu}_{(eff, zfc, left)} = 1 + \frac{1}{2}\Delta\mu_{10} \cdot g(\nu), \quad (5.8)$$

$$\hat{\mu}_{(eff, zfc, right)} = 1 + \frac{1}{2}\Delta\mu_{10} \cdot g(\nu). \quad (5.9)$$

We can see that in *zfc* case, the effective permeability of L.H.C. and R.H.C. radiation are the same, meaning that the absorption are equal. The offdiagonal terms (imaginary terms) are also zero for both cases.

#### ii) Field cooled case (*fc*) - magnetized state

We have  $p = 1$ , then the effective magnetic permeability can be rewritten as (see Eq. 5.6 and Eq. 5.7)

$$\hat{\mu}_{(eff, fc, left)} = 1 - i\frac{1}{2}\Delta\mu_{10} \cdot g(\nu), \quad (5.10)$$

$$\hat{\mu}_{(eff, fc, right)} = 1 + i\frac{1}{2}\Delta\mu_{10} \cdot g(\nu). \quad (5.11)$$

In the  $fc$  case, we can see that the effective permeabilities for L.H.C. and R.H.C. radiation are not the same, meaning that the absorption is different. See the example in Fig. 5.8(a). The offdiagonal terms (imaginary terms) are present in both cases.

To analyze the Faraday transmission spectra in general, first we have to consider the following optical parameters for L.H.C. and R.H.C. wave (see Section 2.1.2).

$$n_{left}^2 - k_{left}^2 = \epsilon' \mu'_{(eff, left)}, \quad (5.12)$$

$$2n_{left}k_{left} = \epsilon' \mu''_{(eff, left)} - \epsilon'' \mu'_{(eff, left)}, \quad (5.13)$$

$$n_{right}^2 - k_{right}^2 = \epsilon' \mu'_{(eff, right)}, \quad (5.14)$$

$$2n_{right}k_{right} = \epsilon' \mu''_{(eff, right)} - \epsilon'' \mu'_{(eff, right)}. \quad (5.15)$$

The real part of the dielectric constant ( $\epsilon'$ ) is taken to be equal for both waves. The imaginary part ( $\epsilon''$ ) is zero in our case. The difference is in the permeability terms (see Eq. 5.6-5.7). The phase shift at the boundary of the transmitted to the incident wave of L.H.C. and R.H.C. radiation can be approximated as

$$\phi = \arctan \frac{-k}{n+1}, \quad (5.16)$$

$$\phi_p = \arctan \frac{-k_{left}}{n_{left}+1}, \quad (5.17)$$

$$\phi_m = \arctan \frac{-k_{right}}{n_{right}+1}. \quad (5.18)$$

For more than one boundary, the  $\phi$  formula has a complicated form [118].

In general, the transmission spectra can be calculated from Eq. 3.5. In Faraday case, we separate the transmission spectra for the two circularly polarized waves;  $Tr_p$  for the transition from  $|+10\rangle \rightarrow |+9\rangle$  and  $Tr_m$  for the transition from  $|-10\rangle \rightarrow |-9\rangle$ , since they both interact with the magnetic sample in Faraday geometry in a different manner. Recall that in the present geometry, the magnetic field component ( $\mathbf{h}$ ) of the radiation is perpendicular to the applied d.c. field ( $\mathbf{H}$ ). The precession of  $\mathbf{h}_{L.H.C.}$  and  $\mathbf{h}_{R.H.C.}$  is in opposite directions.

Due to the different angle of an analyzer, the signal at the detector is an angular sum of the complex transmission  $Tr_p$  and  $Tr_m$  respects to their amplitude and phase. Here we can mathematically summarize the sum of the complex transmitted waves as a function of the analyzer angle as follows (see diagram in Fig. 5.6).

$$Tr_0 = \left| \frac{Tr_p + Tr_m}{2} \right|^2, \quad (5.19)$$

$$Tr_{90} = \left| i \frac{Tr_p - Tr_m}{2} \right|^2, \quad (5.20)$$

$$Tr_{+45} = \left| \frac{\frac{Tr_p + Tr_m}{2} \cos 45 - i \frac{Tr_p - Tr_m}{2} \sin 45}{\cos 45} \right|^2, \quad (5.21)$$

$$Tr_{-45} = \left| \frac{\frac{Tr_p + Tr_m}{2} \cos 45 + i \frac{Tr_p - Tr_m}{2} \sin 45}{\cos 45} \right|^2, \quad (5.22)$$

where the sum has to take into account both amplitude and phase. See Fig. 5.6.

To explain the results in Fig. 5.4-(dots), we can discuss as follows:

In the *zfc* case, both  $Tr_p$  and  $Tr_m$  spectra have the same amplitude (Eq. 5.8-5.9) and phase (Eq. 5.17-5.18), where  $n_{left} = n_{right}$  and  $k_{left} = k_{right}$ . The interference result (Eq. 5.19) becomes a normal spectral shape as appears in Voigt geometry. However in the *fc* case,  $Tr_p$  and  $Tr_m$  spectra do not have the same amplitude (Eq. 5.10-5.11) and phase (Eq. 5.17-5.18), where  $n_{left} \neq n_{right}$  and  $k_{left} \neq k_{right}$ . The interference result (Eq. 5.19) is totally different from the *zfc* case. The simulation results are shown in Fig. 5.4-(lines). Qualitative details of the lineshape analysis will be discussed later in this Section.

As far as our knowledge, there is no report on the transmission measurement of  $Mn_{12}$ -acetate in Faraday geometry. The significant change of the lineshape from magnetized (*fc*) to demagnetized state (*zfc*) in Faraday geometry can be connected to the role of the offdiagonal terms in the permeability tensor. Note that, the offdiagonal terms are related to the interaction between the light and the magnetization in the sample. In Faraday geometry, there is no frequency shift effect in the *fc* case as in Voigt geometry. The resonance frequencies of the *zfc* and *fc* state lie at the same frequency at  $10.02 \text{ cm}^{-1}$ . Due to the effective permeability of L.H.C. and R.H.C. radiation contain the opposite sign of the offdiagonal terms. See Eq. 5.6 and Eq. 5.7. Therefore the frequency shift due to the offdiagonal terms is cancelled out.

In Fig. 5.5-(dots), the results of the angular dependence of an analyzer angle are shown. We measured the transmission in *fc* case but in zero field. The analysis is based on the *fc* case as we have discussed in the earlier part. We sum  $Tr_p$  and  $Tr_m$  spectra using Eq. 5.19-5.22 depending on the analyzer angle. The simulation of the spectra for each analyzer angle is shown in Fig. 5.5-(solid lines). Qualitatively, the peculiar lineshape can be understood as follows.

In order to understand the effect of the analyzer, first we have to know the physical form of our radiation in xy-coordinate. To do so, we have to look at the electric field term. The electric field vectors  $\mathbf{E}_p$  and  $\mathbf{E}_m$  of  $Tr_p$  and  $Tr_m$  transmission radiation can be written as

$$\mathbf{E}_p \propto \frac{|Tr_p|}{2} \exp i(\phi_p - \alpha), \quad (5.23)$$

$$\mathbf{E}_m \propto \frac{|Tr_m|}{2} \exp i(\phi_m - \alpha), \quad (5.24)$$

where the first term  $\frac{|Tr_{p,m}|}{2}$  corresponds to the amplitude and the exponential term corresponds to the phase.  $\alpha$  is an analyzer angle.  $\phi_p$  and  $\phi_m$  are the phase changes of the transmitted radiation (refer to Eq. 5.17-5.18). Note that, the size of the individual  $\mathbf{E}_p$  and  $\mathbf{E}_m$  vectors are not variance when they are plotted as a function of the phase angle. It means they both remain their circularly polarization but a sum between  $\mathbf{E}_p$  and  $\mathbf{E}_m$  vector does not necessary to keep their circular polarization, depending on their amplitude and their phase difference.

If  $|\mathbf{E}_p|$  and  $|\mathbf{E}_m|$  represent the size of the electric field vectors  $\mathbf{E}_p$  and  $\mathbf{E}_m$  respectively, then:



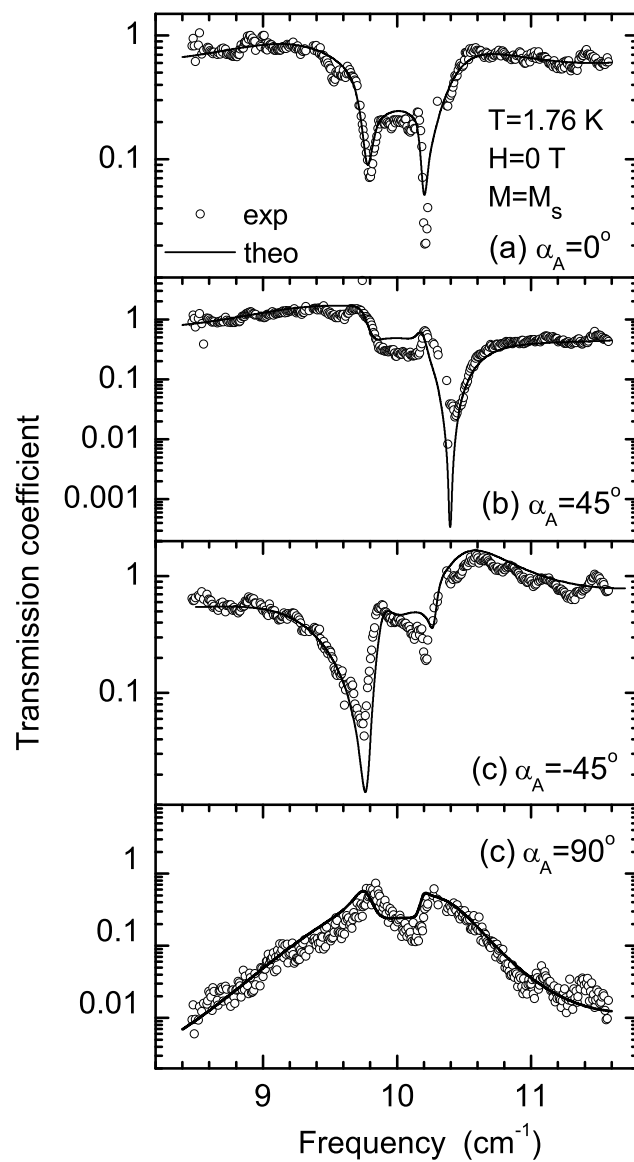


Figure 5.5: Transmission spectra of a 0.75 mm thick mosaic of  $Mn_{12}$ -acetate single crystals in zero magnetic field and at 1.77 K. Each spectra belongs to the analyzer angle at  $0^\circ, +45^\circ, -45^\circ, +90^\circ$ .

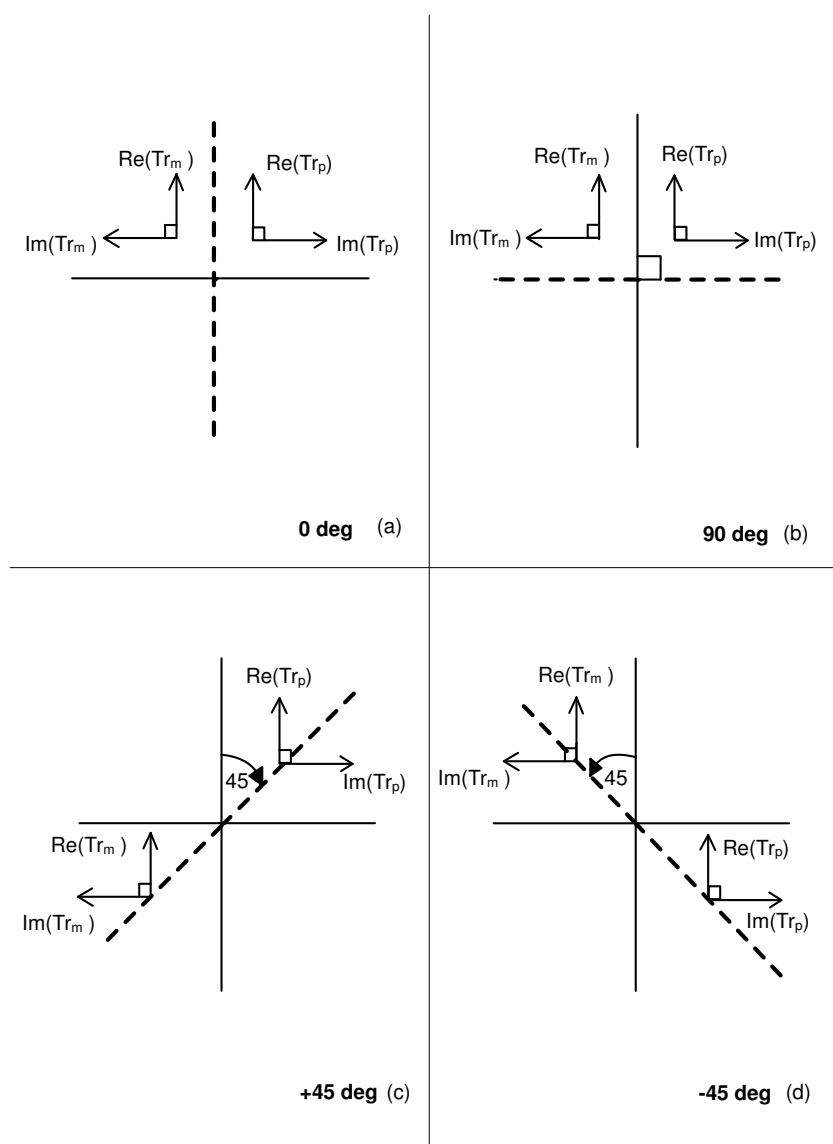


Figure 5.6: Schematic diagram shows the sum of two opposite circular mode spectra ( $Tr_p$  and  $Tr_m$ ) on the polar coordinate at different analyzer angles (dashed lines). Recall that  $Tr_p$  and  $Tr_m$  are complex quantities and can be represented as a combination between real and imaginary vectors under the right angle (arrow lines). However they have the opposite phase, therefore their imaginary vectors are in the opposite directions. The analyzer is also represented in the polar coordinate ( $\theta = 0^\circ - 360^\circ$ ). Only the vectors which have the parallel component to the analyzer can go through and then interference, otherwise, they are blocked. (See Eq. 5.19- 5.22 for quantitative formulas).

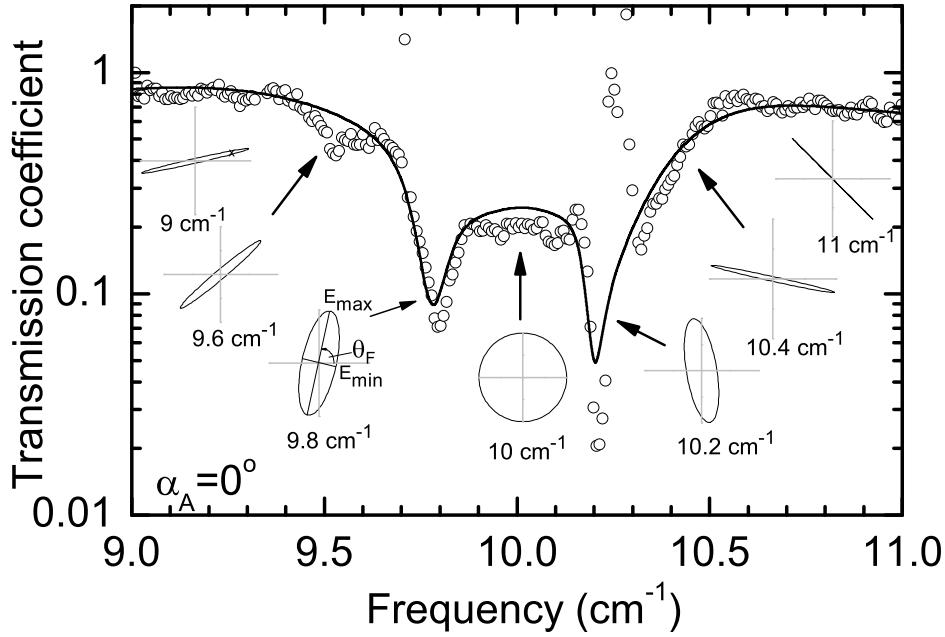


Figure 5.7: Faraday transmission spectra measured at 1.77 K and at the analyzer angle  $\alpha = 0^\circ$ , which lies horizontal. The small diagrams show the sum between the intensity of the  $E_p$  and  $E_m$  spectra for the phase angle 0-360° at certain frequencies. (see text).

case *i*. If  $|\mathbf{E}_p| = |\mathbf{E}_m| \rightarrow \mathbf{E}_p + \mathbf{E}_m$  is linear polarized.

case *ii*. If  $|\mathbf{E}_p| \neq |\mathbf{E}_m| \rightarrow \mathbf{E}_p + \mathbf{E}_m$  is elliptic polarized.

case *iii*. If  $|\mathbf{E}_p| = 0$  or  $|\mathbf{E}_m| = 0 \rightarrow \mathbf{E}_p + \mathbf{E}_m$  is circular polarized.

At the frequency near and at the resonance frequency, there is a rotation of the major axis of the radiation leaving the sample which is called the Faraday rotation with the rotating angle ( $\theta_F$ ). It can be expressed as

$$\theta_F = \left( \sqrt{\epsilon' \mu_{(eff, left)}} - \sqrt{\epsilon' \mu_{(eff, right)}} \right) \frac{\omega}{2c} d. \quad (5.25)$$

The dielectric constants and effective permeability are referred to Eq. 5.10-5.15.  $\omega$  is the wave frequency.  $c$  is the light speed.  $d$  is the thickness of the sample. The simulation of the Faraday angle as a function of frequency is shown in Fig. 5.8(b)-(line). The Faraday rotation calculated from the experimental spectra is shown in Fig. 5.8(b)-(dots). The calculation is based on the following formula.

$$\tan 2\theta_F = \frac{Tr_{45} - Tr_{-45}}{4Tr_0 - Tr_{+45} - Tr_{-45}}. \quad (5.26)$$

The derivation of the above formula is through the coordinate transformation from xy-coordinate to the coordinate of the main axes of the elliptic. See the inset diagram in Fig. 5.8(c).

The radiation leaving the sample has a polarization form as a vector sum of  $\mathbf{E}_{sum} = \mathbf{E}_p + \mathbf{E}_m$  with the phase difference taken into account, see Eq. 5.23- 5.24. During the  $360^\circ$  rotation of the phase of the light, the minimum and maximum value of the electric field vector of  $\mathbf{E}_{sum}$  are  $E_{min}$  and  $E_{max}$  respectively. The ellipticity can be defined as

$$Ellipticity = \frac{E_{min}^2}{E_{max}^2}. \quad (5.27)$$

The simulation of the ellipticity using the simulated  $Tr_p$  and  $Tr_m$  spectra from Fig. 5.8(a) is shown in Fig. 5.8(c)-(solid line). The calculation of the ellipticity using the experimental spectra from Fig. 5.5 is shown in Fig. 5.8(c)-(dots). Note that in the experimental spectra, the ellipticity is not close to unity. This is due to imperfect polarization of the radiation.

To quantitatively analyze the Faraday spectra, let us consider the situation before the linearly polarized light enters the sample. At this stage, the linear light can be viewed as a sum of the same phase and the same amplitude of L.H.C. and R.H.C. light. When the light pass through the sample, the following situation can occur:

i. At nonresonance frequencies, there is no absorption for both circular modes. Both waves are transmitted with equal amplitude and phase. Their combination is linearly polarized light (Fig. 5.8(c)), where the ellipticity is close to zero, meaning that it is linearly polarized. From Fig. 5.8(b), Faraday angle ( $\theta_F$ ) is zero, implying that the polarization vector of the transmitted wave is parallel to the incident one.

ii. At the resonance frequency  $\approx 10 \text{ cm}^{-1}$ , only L.H.C. light interacts with the sample, while R.H.C. light does not. Referring to Fig. 5.8(a), L.H.C. is virtually completely absorbed, whereas R.H.C. is not. In this case, the radiation leaving the sample is the R.H.C. light only. See Fig. 5.7 at frequency of  $10 \text{ cm}^{-1}$ , and Fig. 5.8(c), where the ellipticity is close to unity for the simulated spectra. Therefore, the signal at the detector placed after the analyzer is equal in all angular directions. The real resonance line at  $10 \text{ cm}^{-1}$  remains the same in all cases of the analyzer angle (Fig. 5.5(a)-(d)). In Fig. 5.8(b), the Faraday rotation is also zero due to the fact that circular radiation has no major polarization axis.

iii. In case that the radiation is close but not at the resonance frequency, there is partial absorption for L.H.C. radiation while there is no absorption for R.H.C. radiation. In this situation, the signal after the sample is a sum of the L.H.C. and R.H.C. with unequal amplitudes and different phases. The typical interference result will be elliptically polarized radiation. See Fig. 5.7 at frequency of  $9.8 \text{ cm}^{-1}$  and Fig. 5.8(c). The Faraday rotation is varied, ranging from  $+100^\circ$  to  $-100^\circ$  (see Fig. 5.8(b)).

Depending on the angle of the analyzer ( $\alpha$ ), the detector can observe only the projection of the elliptically polarized wave parallel to the analyzer as shown in Fig. 5.5

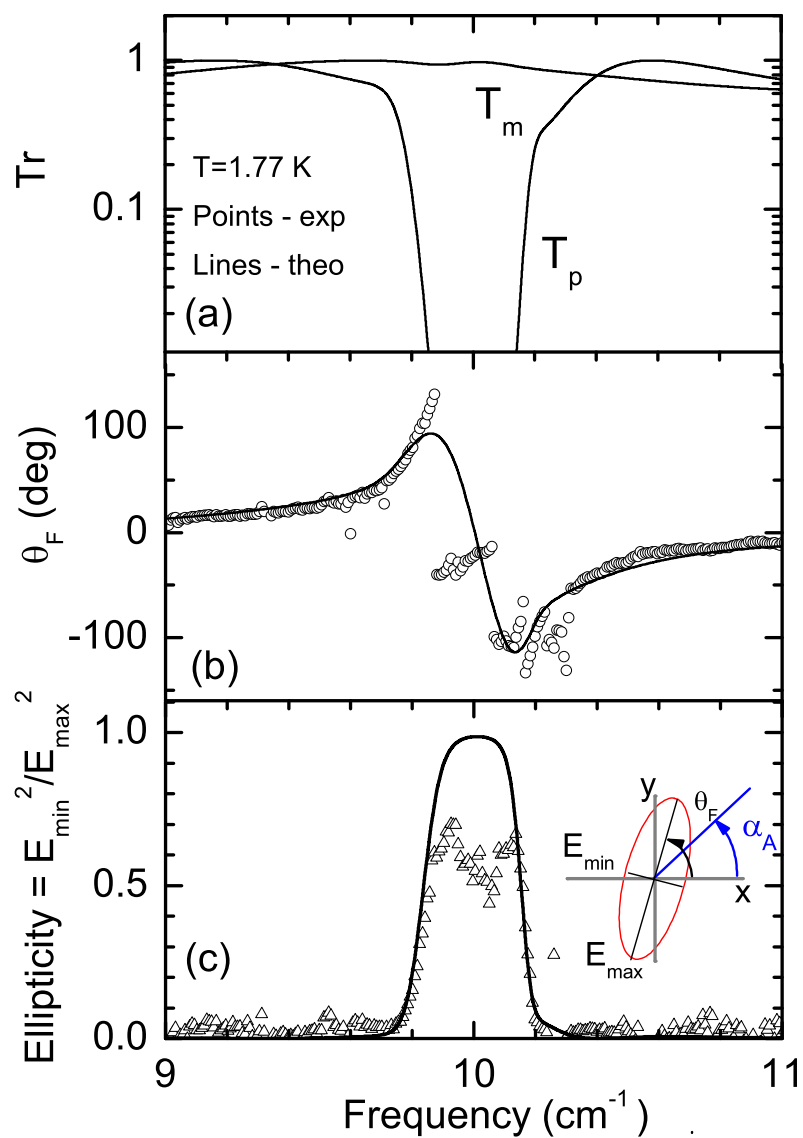


Figure 5.8: (a) Simulation of the individual L.H.C. and R.H.C. transmission spectra  $Tr_p$  and  $Tr_m$ . (b) Simulated and experimentally obtained Faraday rotation angles ( $\theta_F$ ). (c) Simulation and experimental calculation of the ellipticity. (See text)

(a)-(d). In some special cases ie. at some special frequencies, the analyzer cuts through the minor axis of the elliptic light. This results in a minimum in the signal, which can be clearly seen as a *pseudo-peak* at nonresonance frequencies in the transmission spectra. See Fig. 5.7 at frequency of  $9.8 \text{ cm}^{-1}$  for example.

The interference between two circular modes (L.H.C. and R.H.C. radiation) is similar to the *magnetic circular dichroism* phenomena where the rotation of the polarization axis is found due to the different absorption of both circular modes. In the real Faraday effect, the rotation is rather due to the difference in the refraction term, while the absorption term is zero. In our case, the rotation is due to both refraction and absorption terms. The rotation of the major axis of the radiation found in  $Mn_{12}$ -acetate suggests that  $Mn_{12}$ -acetate can be used as a molecular rotator at low temperature with continuous frequencies tuning by the external magnetic field. Moreover at the resonance frequency, we notice that by using the linearly polarized light, we obtain the circularly polarized light. This suggests  $Mn_{12}$ -acetate can be used as a molecular polarization transformer with continuous frequencies. However, the experimental ratio between the L.H.C. and R.H.C. absorption has to be optimized and the very low working temperature has to be taken into account.

### 5.3.2 Faraday geometry: in magnetic field measurement with circularly polarized radiation.

#### Experimental results

In this Section, we performed the transmission measurement by using circularly polarized radiation. The polarization transforming technique has been described in Section 3.3. Note that, in principle circular polarization can be obtained only at a fixed frequency. However, in our case we scan the frequency in a small range of 310-350 GHz ( $\approx 10.33 - 11.67 \text{ cm}^{-1}$ ). We still obtain good quality of the circular polarization at and near the resonance frequency ( $\pm 5 \text{ GHz}$ ) was 90-98%. At the frequencies  $\pm 20 \text{ GHz}$  from the resonance frequency, the quality of the circular polarization drops to 60%.

First, we measured the *zfc* sample in a magnetic field 0 T at 1.77 K using R.H.C. and L.H.C. light. We found the absorption for both polarizations as shown in Fig. 5.9.

Next we measured the transmission spectra at 1.77 K in +1 T magnetic field. We found the absorption line at  $10.94 \text{ cm}^{-1}$  for L.H.C. radiation only but not for R.H.C. radiation. See Fig. 5.10(a). Then we cooled the sample in -1 T, and measured the transmission spectra at 1.77 K. We found the absorption line for R.H.C. at  $10.94 \text{ cm}^{-1}$  but not L.H.C. radiation in this case. See Fig. 5.10(b).

#### Analysis and Discussion

The analysis for both *zfc* and *fc* can be treated similarly to Section 5.3.1. The transmission lineshape from the circular polarized radiation appears to be a single line which is different from the case of using linear polarized radiation where the absorption line is in a complex interference form. Because we only used one circular mode at a

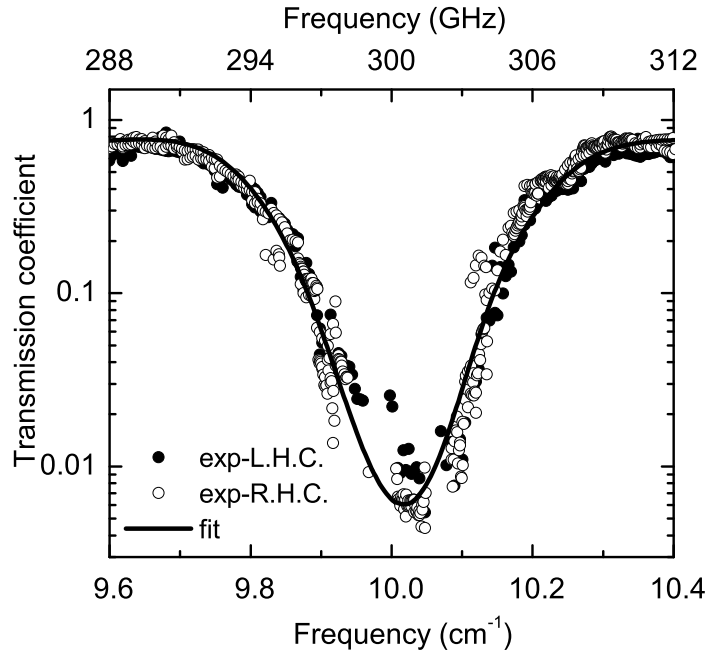


Figure 5.9: Transmission coefficient spectra of *zfc*  $Mn_{12}$ -acetate sample at 1.77 K in zero field. The absorption from both L.H.C. and R.H.C. radiation are observed.

time, therefore, there will be no interference between two individual spectra ( $Tr_p$  for L.H.C. and  $Tr_m$  for R.H.C.) as in Section 5.3.1.

In the *zfc* case, the effective magnetic permeability of the system can be written as Eq. 5.8 and Eq. 5.9, where there is no offdiagonal term. Both L.H.C. and R.H.C. light have the equal absorption probability ( $1/2\Delta\mu_{10}$ ). Transmission spectra can be calculated separately for each individual mode ( $Tr_p$  and  $Tr_m$ ). Since both circular modes have the same absorption and same resonance frequency, therefore the simulated spectra ( $Tr_p$  and  $Tr_m$ ) are the same in both amplitude and phase as shown in Fig. 5.9-(solid line).

In *+fc* case, we follow the effective magnetic permeability in Eq. 5.10 for L.H.C. light and Eq. 5.11 for R.H.C. light for +1 T *fc* case. L.H.C. light has the absorption term  $\Delta\mu_{10}$  because the all spin population is in the  $|+m\rangle$  state. R.H.C. light has zero absorption because no spin population is in the  $| -m\rangle$  state. Therefore, we can see only the absorption in L.H.C. light but not R.H.C. light. The simulation of the transmission spectra of L.H.C. absorption ( $Tr_p$ ) is shown in Fig. 5.10(a)-(solid line).

In *-fc* case, we follow Eq. 5.10 for R.H.C. light and Eq. 5.11 for L.H.C. light. In this case, R.H.C. light has the absorption proportional to  $\Delta\mu$  but L.H.C. has zero absorption, since all the spin population is in the  $| -m\rangle$  state. Hence, the absorption is possible for R.H.C. only. The  $Tr_m$  spectra simulation result is depicted in Fig. 5.10(b)-(solid line).

According to the optical selection rules, only the circular wave with left hand

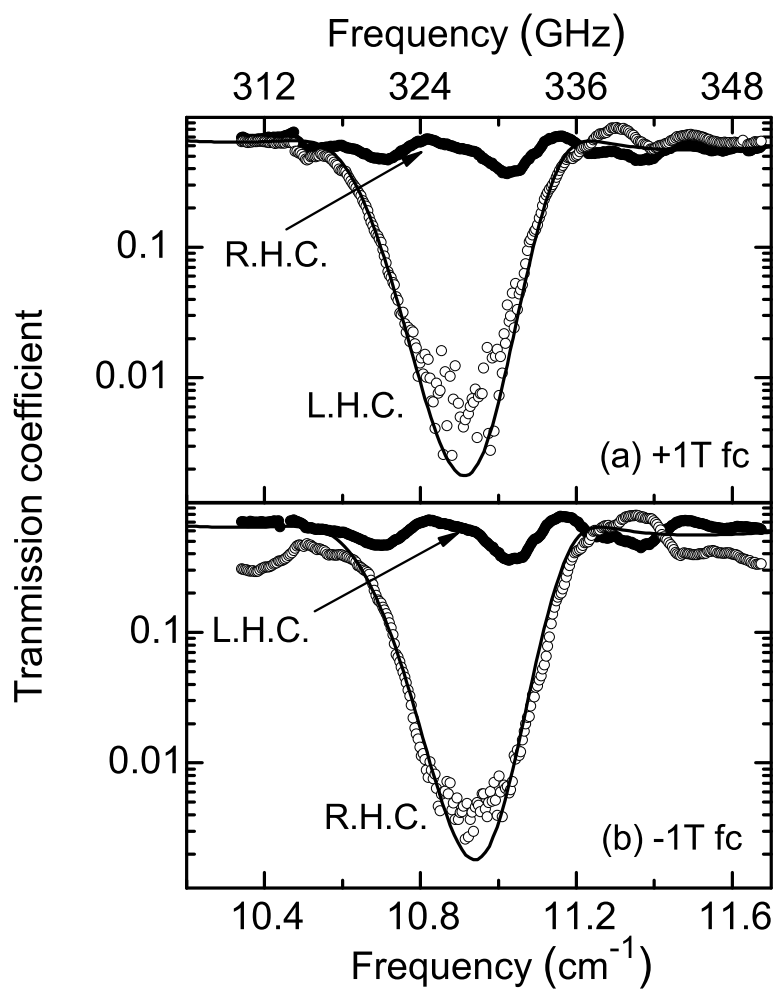


Figure 5.10: Transmission coefficient spectra at 1.77 K (a) At -1 T, only the absorption line from R.H.C. radiation is observed. (b) At +1 T, only the absorption line from L.H.C. radiation is observed.



polarized state can transfer the right energy, and spin angular momentum ( $\Delta m_s = +1$ ) to those molecules sitting in the  $|+m\rangle$  state. Similarly to the right hand polarized state, it can transfer energy and spin momentum  $\Delta m_s = -1$  to those molecules sitting in the  $| -m \rangle$  state [119, 120, 149]. This is the reason why in the linearly polarization case and without the analyzer, we have half of the intensity signal compared to the circular case.

## 5.4 Conclusion

We have studied the magneto-optical effects on the transmission lineshape of  $\text{Mn}_{12}$ -acetate sample in both Voigt and Faraday geometry. We found that the lineshapes are very much sensitive to the magnetic field direction, radiation propagation direction and the magnetic states of the sample (*zfc* and *fc* cases). In Voigt geometry, the symmetry in *zfc* state and the asymmetry in *fc* state of transmission lineshape gives us evidence of the inhomogeneity of CF splitting parameters (see also Chapter 4). The lineshift gives us information on the internal dipolar field. In Faraday geometry, the lineshape in *zfc* and *fc* states are totally different. The transformation of the lineshape has its own advantage in which will be discussed in the next Chapter. As a result, we can see that careful magneto-optical lineshape studies can become important. Moreover, we also show that strong Faraday rotation is observed in the  $\text{Mn}_{12}$ -acetate molecular magnet. Compared the results from our FDMRS setup (frequency domain) to some EPR setup (field domain regime) e.g. without the cavity, our spectra are much more sensitive to the magneto-optical effect than in a single pass transmission HFEPR spectra. In HFEPR setup, the radiation can sometimes lose its polarization properties since it travels in an oversized wave guide. While in our case, the radiation travels in free space in our quasi-optical setup. Therefore, we have more flexibility and controllability to study the magneto-optical effects than in the HFEPR experiment.



# Chapter 6

## Magnetic quantum tunneling

In this Chapter, we investigate the magnetic quantum tunneling (MQT) phenomenon in  $\text{Mn}_{12}$ -acetate molecular magnet via the relaxation measurement by using the frequency-domain magnetic resonance (FDMRS) technique. We optically probe the individual transitions, e.g.  $|+10\rangle \rightarrow |+9\rangle$  and  $|-10\rangle \rightarrow |-9\rangle$ , during the relaxation process, while the other techniques such as the magnetometer cannot locally access. Since we can set up two different geometries (Voigt and Faraday geometries) which give us distinctively different transition lineshapes, the relaxation experiments are performed in both geometries. We study the effect of temperature, applied magnetic field, internal field, the magnetization state to the relaxation time. We develop a model to describe the relaxation spectra and the relaxation time obtained from the FDMRS technique. We also qualitatively and quantitatively describe the relaxation mechanism from our results through the phonon assisted spin tunneling model e.g. relaxation path, and relaxation rate. In the last Section, we have added the zero field relaxation measurement in the Faraday geometry, in order to study the internal field in the  $\text{Mn}_{12}$ -acetate system via the magneto-optics analysis.

### 6.1 Description of the experiment and the analysis

#### 6.1.1 Relaxation experiment

Using the FDMRS technique, relaxation measurements can be performed. First we prepare *polarized system* by using a bias dc magnetic field, in order to obtain all the population in the same side of the double-well potential.

The general measurement procedure was as follows. We cooled the system from high temperature to low temperature in  $+H$  field in order to obtain all the population in  $|+m\rangle$  quantum well (see Fig. 6.1(a)). When the temperature is stabilized ( $\pm 0.005$  K), we invert the field to  $-H$  in less than two minutes. At this stage, the system is in a *nonequilibrium* state, which means the spin population will start to move to the lower energy levels (see Fig. 6.1(b)). We immediately started to measure the transmission coefficient spectra focusing on both  $|\pm 10\rangle \rightarrow |\pm 9\rangle$  transition resonance lines. We kept measuring the transmission spectra as a function of time until the system is back to the equilibrium state where the relaxation process is finished (see

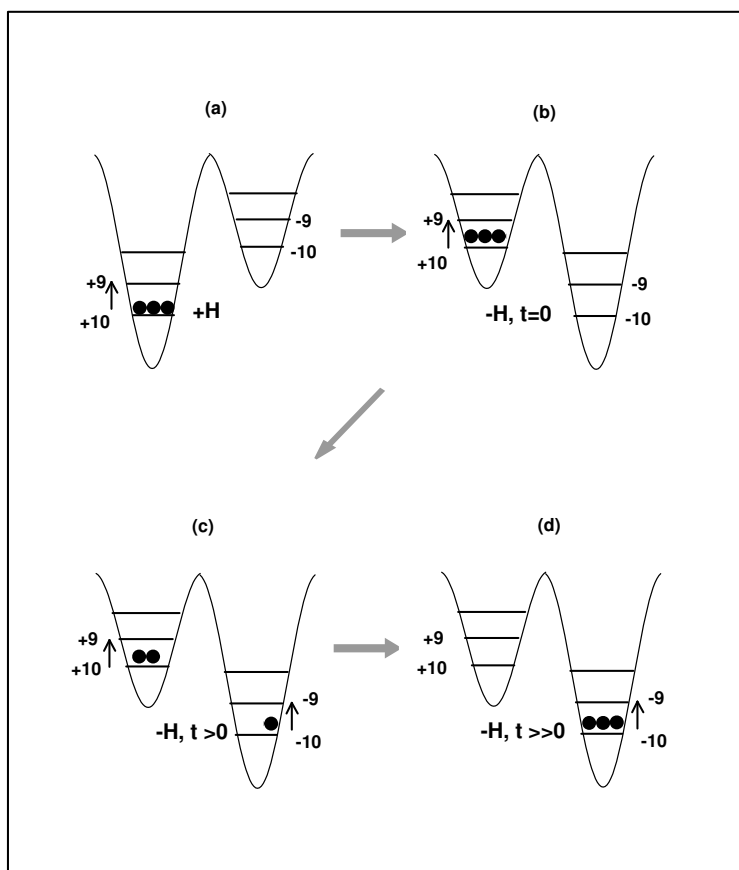


Figure 6.1: Schematic diagram showing the relaxation experiment in a magnetic field. (a) First the system is polarized using  $+H$  magnetic field. (b) Next the system is converted to a metastable state by inverting the magnetic field to  $-H$ . (c) The system relaxes over time and the spin population moves to the ground state. (d) At the end of the relaxation process, the system is back to an equilibrium state again. The arrows show transitions observed in the spectra.

Fig. 6.1(d)). The measurement temperature is  $< 1.95$  K. Example of the relaxation spectra of the transition  $|+10\rangle \rightarrow |+9\rangle$  and  $|-10\rangle \rightarrow |-9\rangle$  measured in magnetic field 1.85 T and at 1.77 K are shown in Fig. 6.3(a) and (b) respectively.

In the zero field relaxation (ZFR) case, the relaxation experiment is the same with the previous case except the relaxation measurement is in zero magnetic field and in Faraday geometry. See Fig. 6.2. The lineshape is dramatically changed in  $zfc/fc$  measurements which gives us an advantage to study the  $ZF$  relaxation. This is a consequence from the results in Chapter 5. In this case, the population in both side of the potential well is equalized (see Fig. 6.2(d)). Example of the relaxation spectra of the transition  $|\pm 10\rangle \rightarrow |\pm 9\rangle$  measured in zero magnetic field and at 3.3 K is shown in Fig. 6.16(a).

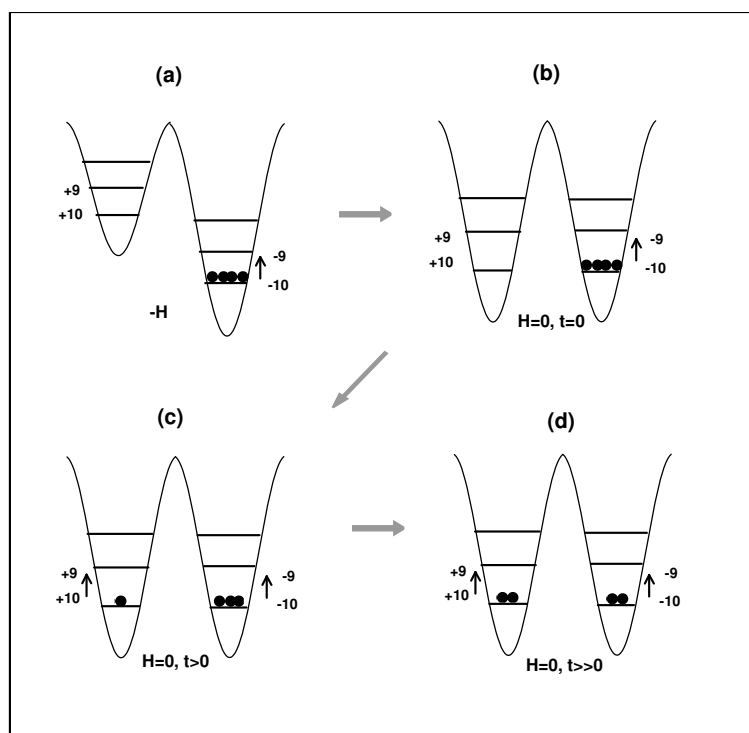


Figure 6.2: Schematic diagram showing the relaxation experiment in a *zero* magnetic field. (a) First the system is polarized using  $+H$  magnetic field. (b) Next the system is converted to a metastable state by inverting the magnetic field to zero. (c) The system relaxes over time and the spin population moves to the ground state. (d) At the end of the relaxation process, the system is back to an equilibrium state again where the population is equal in both side of the double-well. The arrows show transitions observed in the spectra.

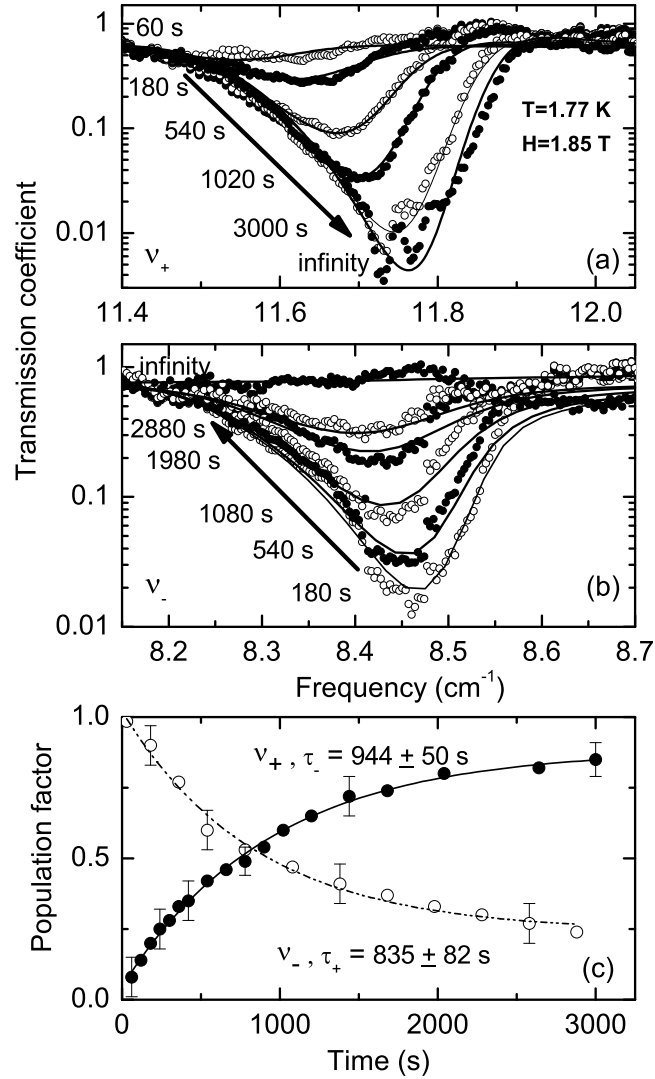


Figure 6.3: Magnetic resonance spectra recorded on a single crystals sample of  $Mn_{12}$ -acetate in Voigt geometry at various delay times. (a) The resonance line due to the  $|+10\rangle \rightarrow |+9\rangle$  transition. (b) the resonance line due to the  $|-10\rangle \rightarrow |-9\rangle$  transition (c) population factors of the metastable  $|-10\rangle$  state ( $q$ , (white dots)) and the lower energy  $|+10\rangle$  state ( $p$ , black dots).

### 6.1.2 Relaxation spectra - fitting model

To fit Voigt and Faraday relaxation spectra, we use the model described below:

**i.** We fit the appropriate mode permeability ( $\Delta\mu$ ) and Gaussian linewidth ( $\sigma$ ) using the spectra in the equilibrium state (e.g. before convert the magnetic field) and then set them as fixed parameters for the whole set of the relaxation spectra.

**ii.** The only fitting parameter is the population factor ( $p$  or  $q$ ) with time dependent behavior.

$$q = 1 - p, \quad (6.1)$$

where  $p$  is the population of  $|+10\rangle$  state.  $q$  is the population of  $|-10\rangle$  state. We take  $p = 0$  and  $q = 1$  at  $t = 0$  and  $p = 1$  and  $q = 0$  at  $t = \infty$  as the boundary condition. These factors are very important since they describe the dynamics of the system and quantitatively describe the spin population during relaxation process. Fitting these quantities gives us the relaxation time.

**iii.** The mode contributions of the  $|+10\rangle \rightarrow |+9\rangle$  and of  $|-10\rangle \rightarrow |-9\rangle$  transitions to the magnetic permeability ( $\Delta\mu_{\pm 10}$ ) can be separated and expressed as

$$\Delta\mu_{+10} = p \cdot \Delta\mu_{10} \cdot \frac{\nu_0}{\nu_{+0}}, \quad (6.2)$$

$$\Delta\mu_{-10} = q \cdot \Delta\mu_{10} \cdot \frac{\nu_0}{\nu_{-0}}, \quad (6.3)$$

where  $\Delta\mu_{10}$  is the mode contribution of the ground state transition in the equilibrium system without applied field ( $H = 0$ ). It can be obtained experimentally or theoretically (see Chapter 4). The last term is the correction factor for  $\Delta\mu_{10}$  in the case of the applied magnetic field is presented ( $H \neq 0$ ) (see Section 4.3.1).  $\nu_0$  is the resonance frequency in  $H = 0$ .  $\nu_{+0}$  and  $\nu_{-0}$  are the resonance frequency of  $|+10\rangle \rightarrow |+9\rangle$  and  $|-10\rangle \rightarrow |-9\rangle$  transitions in the field, respectively.

**iv.** We will use the effective permeability for Voigt and Faraday geometry as follows:

*Effective permeability for Voigt geometry*

$$\mu_{eff, V, fc} = 1 + \frac{(\Delta\mu_{+10} \cdot g_{+10}(\nu) + \Delta\mu_{-10} \cdot g_{-10}(\nu))}{1 + (\Delta\mu_{+10} \cdot g_{+10}(\nu) + \Delta\mu_{-10} \cdot g_{-10}(\nu))}, \quad (6.4)$$

where  $g(\nu)$  is the Gaussian lineshape function.

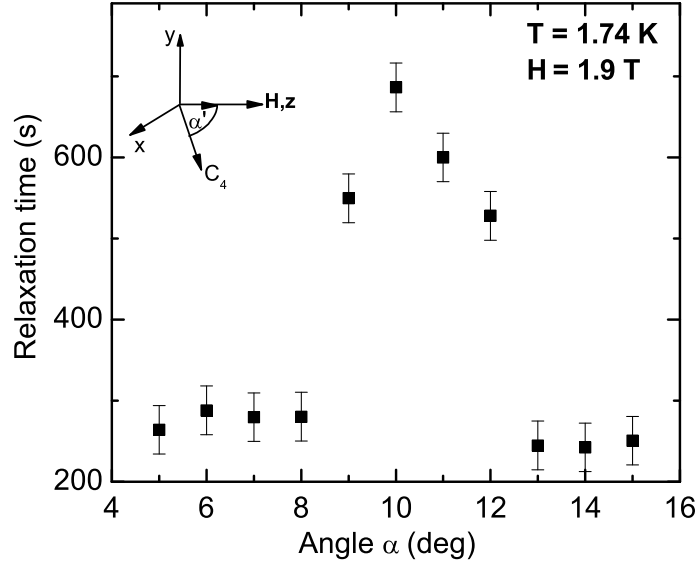


Figure 6.4: Relaxation time is plotted as a function of the tilt  $\alpha$  angle between the crystal easy axes and the applied field. The measurement was performed at temperature 1.74 K and longitudinal field 1.9 T.

*Effective permeability for Faraday geometry*

$$\mu_{eff, F, fc, left} = 1 + \Delta\mu_{+10} \cdot g_{+10}(\nu) + i\Delta\mu_{+10} \cdot g_{+10}(\nu), \quad (6.5)$$

$$\mu_{eff, F, fc, right} = 1 - \Delta\mu_{-10} \cdot g_{-10}(\nu) + i\Delta\mu_{-10} \cdot g_{-10}(\nu), \quad (6.6)$$

where  $\mu_{(eff, F, fc, left)}$  and  $\mu_{(eff, F, fc, right)}$  are the effective permeability corresponding to the left hand and right hand circular light respectively.

v. The energy level ( $E_m$ ) of the system is corrected due to the presence of the internal field as following;

$$E_m = Dm^2 + Bm^4 - g_z\mu_B m[H_z + H_{dip}] (p - q), \quad (6.7)$$

where  $p - q$  term is the time dependent population differenc of  $|+10\rangle$  and  $|-10\rangle$  states which is taken as a measure for the magnetization of the system during the relaxation.

vi. To describe the transmission coefficient spectra, we used the formulas described in Section 3.6. For Faraday geometry, in the case of using the analyzer and linearly polarized light, the transmission coefficient spectra can be simulated according to Section 5.3.1-5.3.2.



The examples of the spectra fitting (solid line) for Voigt spectra measured at 1.85 T and 1.77 K are shown in Fig. 6.3(a)-increasing spectra and Fig. 6.3(b)-decreasing spectra. The examples of the spectra fitting (solid line) for Faraday spectra are shown in Fig. 6.14(a).

**vii.** To obtain the relaxation time, we plotted  $p$  and  $q$  population factor as a function of time. See Eq. 6.2 - Eq. 6.4. The results are shown in Fig. 6.3(c) for Voigt measurement and Fig. 6.14(b) for Faraday measurement. We fitted each exponential curve to a single exponential in order to obtain the relaxation time ( $\tau$ ).

### 6.1.3 Angular calibration of the sample holder

We have mentioned before that the sample alignment is very important since the transverse field can play a crucial role (see Chapter 1). Therefore, we calibrated the position ( $\alpha$ ) angle between the sample holder and the magnetic field ( $H$ ) in order to minimize the angle ( $\alpha'$ ) between an easy axis of the crystal and the magnetic field ( $H_z$ ). Note that this can be done only in the  $\mathbf{xz}$ -plane (see the inset in Fig. 6.4). The calibration process is done by recording the relaxation time as a function of the angle in  $\mathbf{xz}$ -plane. For every  $\alpha = 6^\circ - 16^\circ$ , we keep the temperature and field constant at  $T=1.74$  K and  $H_z=1.9$  T. The results are shown in Fig. 6.4. The maximum relaxation time, meaning least transverse field, belongs to the  $\alpha = 10^\circ$  which will be the calibration angle in our system for the whole Chapter.

### 6.1.4 Measurement lists

Up to this point, we have explained briefly how to perform the relaxation experiment in general. Before going into the experimental part, here is an overview of the experiments performed in this Chapter.

- i. Temperature dependence of the relaxation time: Voigt geometry.
- ii. Longitudinal field dependence of the relaxation time: Voigt geometry.
- iii. Longitudinal field dependence of the relaxation time: Faraday geometry.
- iv. Zero field relaxation: Faraday geometry.

## 6.2 Experimental results

### 6.2.1 Temperature dependence of relaxation time: Voigt geometry

We measured the temperature dependence of the relaxation process in magnetic field 1.9 T. Recall that we still used the same calibration angle  $\alpha = 10^\circ$  in order to exclude accidental transverse field effects. We measured the relaxation spectra for each temperature from 1.68-1.87 K in a 1.9 T magnetic field. The detailed analysis of

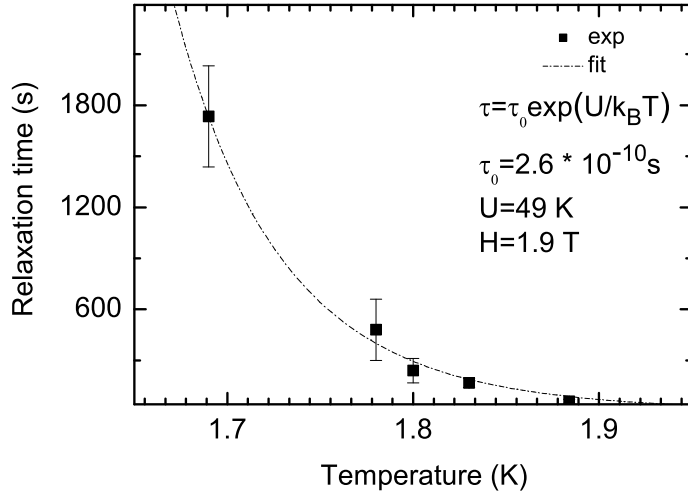


Figure 6.5: Temperature dependence of the relaxation time at  $H_z = 1.9$  T field. The experimental data (dots) have been fitted with Arrhenius function (dashed line) with the relaxation time constant  $\tau_0 = 2.6 \times 10^{-10}$  s, and the barrier height energy 49 K.

the relaxation time is explained in Section 6.1.2. The results (dots) are shown in Fig. 6.5. We can clearly see that the relaxation time is exponentially dependence on the temperature. We fitted the data in Fig. 6.5 (dashed line) using the Arrhenius law;  $\tau = \tau_0 \exp(U/k_B T)$ , since the temperature of the system is in the thermal activation regime.

From Fig. 6.5, we found the characteristic decay time  $\tau_0 = 2.6 \times 10^{-10}$  s, and the barrier height energy  $U = 49 \pm 2$  K at  $H=1.9$  T. Theoretically, we can estimate the *effective barrier height energy* ( $U$ ) in the magnetic field 1.9 T through  $U = E_2 - E_{10} \approx 47$  K.  $E_2$  is the highest energy level for system in 1.9 T field.  $E_2$  and  $E_{10}$  are estimated from Eq. 6.7, where  $p = 1$  and  $q = 0$ .  $D = 0.56$  K, and  $B = 1.1 \times 10^{-3}$  K are taken from the results in Chapter 4. The theoretical barrier height energy,  $U_{(H=1.9\text{ T}),theo} \approx 47$  K, is closed to the experimental value obtained from Fig. 6.5,  $U_{(H=1.9\text{ T}),exp} \approx 49 \pm 2$  K.

According to the literatures, the relaxation time constant ( $\tau_0$ ) is typically around  $10^{-7} - 10^{-9}$  s from the magnetization measurements [109, 151]. However, we found  $\tau_0 \approx 2.6 \times 10^{-10}$  s from our FDMRS technique. Our larger  $\tau_0$  can be due to the fact that  $\tau_0$  and  $U$  are not independent parameters in the fitted process, meaning that this method is not the best way to obtain the precise decay time parameter and the barrier height energy.

## 6.2.2 Longitudinal field dependence of relaxation time: Voigt geometry

### Results and Analysis

In this part, we measured relaxation spectra in a longitudinal magnetic field ( $H_z = 1.6 - 2.65$  T) at 1.77 K, and at  $\alpha$  angle  $10^\circ$ . We observed both i) the growing resonance line due to the  $|+10\rangle \rightarrow |+9\rangle$  transition and ii) the dying resonance line of the  $| -10\rangle \rightarrow | -9\rangle$  transition. The relaxation results of both growing spectra ( $\nu_+$ ) and dying spectra ( $\nu_-$ ) measured at  $H_z = 1.85$  T are shown in Fig. 6.3(a) and (b)-(dots) as examples. The arrows show the development with time. The spectrum at time infinity was measured before converting the magnetic field from -H to +H. In Fig. 6.3(a), we observe that the absorption intensity increases and that the resonance frequency shifts to the higher frequencies, while in Fig. 6.3(b), we observed the absorption intensity decreases and the spectra shifts to lower frequencies.

The relaxation time of Voigt relaxation spectra can be analyzed as in Section 6.1.2. The overall relaxation time curve as a function of the longitudinal field ( $H_z$ ) is plotted in Fig. 6.6. Black dots, and white dots belong to the relaxation time calculated from Voigt-increasing spectra, and Voigt-decreasing spectra at 1.77 K respectively. The stars represent relaxation time from Faraday-increasing spectra at 1.86 K which will be discussed in the next Section.

The relaxation curve in Fig. 6.6 shows pronounced minima at certain fields of 1.85 T and between 2.3-2.35 T. The first minimum is belong to the fourth crossing field, which can be theoretically estimated as  $H_{mm'}^{4th} = 4 \times 0.45 = 1.8$  T. It corresponds a relaxation time of  $\tau \approx 5000$  s. The second minimum is belong to the fifth crossing field, which can be theoretically estimated as  $H_{mm'}^{5th} = 5 \times 0.45 = 2.25$  T. Note that at the fifth crossing, the relaxation occurs too fast to measure. Apart from these minima, the relaxation time slowly decreases as a function of applied field due to the lower effective energy barrier.

### Theoretical analysis on the relaxation time

In order to understand the relaxation mechanism, we have to simulate the contributions from both thermal relaxation and thermal assisted quantum tunneling.

#### Thermal activation regime

Normally, to estimate the relaxation time in the slow regime, namely *thermal activated relaxation*, we use the Arrhenius law;  $\tau_{ther} = \tau_0 \exp(-U/k_B T)$ . By substitution of  $U$  as a function of  $H_z$ , we obtain

$$\tau_{ther} \approx \tau_0 \exp\left(\frac{Dm^2 + Bm^2 + g\mu_B m H_z}{k_B T}\right). \quad (6.8)$$

The temperature  $T=1.77$  K is kept constant. In this case, we found  $\tau_0 = 4 \times 10^{-7}$  s in order to fit  $\tau_{ther}$ , which is a background relaxation time in Fig. 6.6.

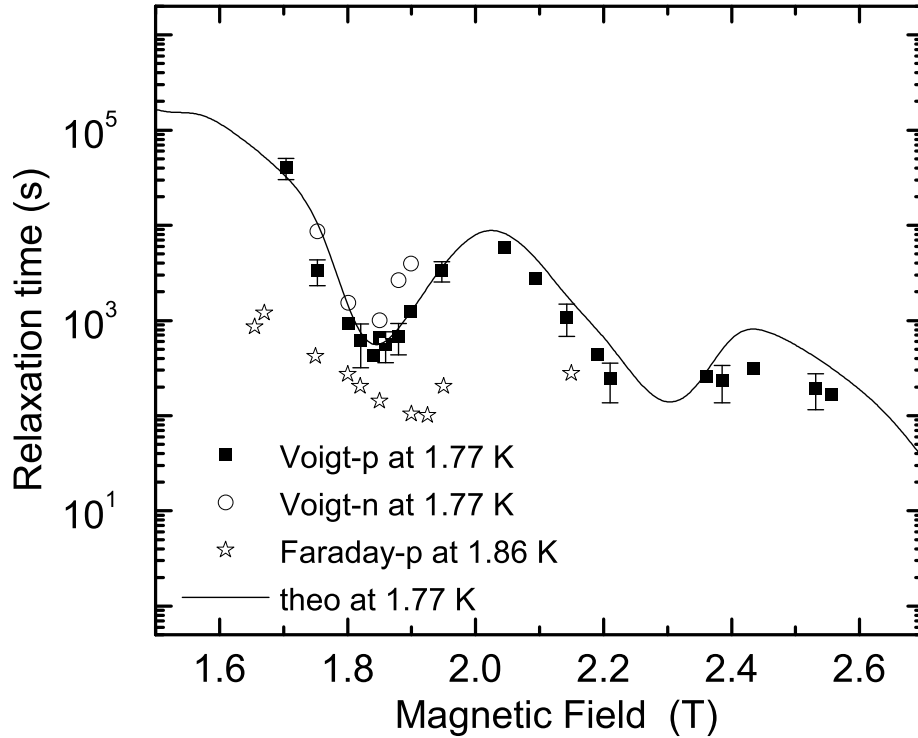


Figure 6.6: Longitudinal field dependence of the relaxation time. Dots belong to Voigt geometry data measured at 1.77 K [white dots: disappearing resonance line (Voigt-n), black dots: appearing resonance line (Voigt-p)]. White stars belong to Faraday geometry data measured from the appearing resonance line (Faraday-p) at 1.86 K. Solid line represents the calculated relaxation time from the phonon assisted spin tunneling combined with the thermal activation process. The solid line is calculated by using the magnetic field resolution of 0.06 T.

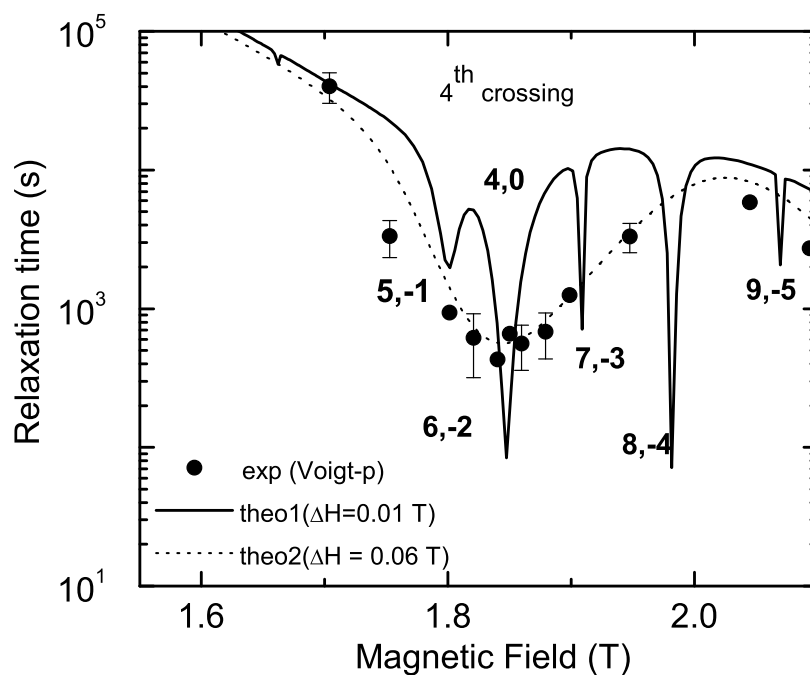


Figure 6.7: Longitudinal field dependence of the relaxation time. Dots belong to Voigt geometry data (appearing resonance line) measured at 1.77 K. Lines represent the calculated relaxation time from the phonon assisted spin tunneling combined with the thermal activation process. The solid line and the dashed line are calculated by using the magnetic field resolution ( $\Delta H_z$ ) of 0.01 T and 0.06 T respectively.

$n$	$m$	$m'$	tunnel splitting , $\Delta_{mm'}$ (mK)
0	4	-4	$45k_B$
1	3	-2	$45k_B$
2	5	-3	$45k_B$
3	4	-1	$130k_B$
4	6	-2	$40k_B$

Table 6.1: The dominant paths  $(m, m')$  and their corresponding tunnel splitting energy ( $\Delta_{mm'}$ ) for each resonance  $n$ , where  $n = m + m'$ . [34]

### Thermal assisted tunneling regime

Next we simulate the fast relaxation time regime (solid line in Fig. 6.6). We can discuss the procedure as follows;

In our calculation for every main crossing field ( $n^{th}$ ), it has one dominant relaxation path (see Table 6.1). To calculate the relaxation rate  $1/\tau$ , we need to estimate the relaxation time contributed by the spin-phonon coupling between  $m \rightarrow m + 2$ ,  $m' \rightarrow m' - 2$  levels, and spin tunneling between  $(m, m')$  resonance path. Note that the relaxation time induced by thermal transition due to phonon with  $\Delta m = \pm 2$  is much more dominant than from  $\Delta m = \pm 1$ . The relaxation time can be summarized as Eq. 1.63, which can be written here again as

$$1/\tau = \frac{1}{1 + e^{\beta(\epsilon_{-s} - \epsilon_s)}} \left( \frac{e^{\beta(\epsilon_{m+2} - \epsilon_s)}}{W_{m, m+2}} + \frac{e^{\beta(\epsilon_{m'} - \epsilon_s)}}{W_{m'-2, m'}} + \frac{e^{\beta(\epsilon_m - \epsilon_s)}}{\Gamma_m^{m'}} \right), \quad (6.9)$$

where the first two terms are the relaxation due to spin-phonon coupling with the relaxation rate  $W_{m, m+2}$  and  $W_{m'-2, m'}$ . The last term is the relaxation due to the quantum tunneling with the relaxation rate  $\Gamma_m^{m'}$ .  $\epsilon_s$  and  $\epsilon_{-s}$  are the energy of the ground state level  $s = 10$ . The relaxation time ( $\tau$ ) has a single Lorentzian lineshape because the  $\Gamma_m^{m'}$  term which has a Lorentzian lineshape is dominate. See also Eq. 1.63.

$$\Gamma_m^{m'} = \Delta_{mm'}^2 \frac{W_m + W_{m'}}{4\varepsilon_{mm'}^2 + \hbar^2(W_m + W_{m'})^2}. \quad (6.10)$$

The linewidth of the Lorentzian peak can be estimated as [34]

$$w' = \frac{\sqrt{2^{3/2} \Delta_{mm'}}}{|m - m'| g\mu_B}, \quad (6.11)$$

where all parameters details are explained in Chapter 1. Note that  $\Delta_{mm'}$  is the tunnel splitting energy corresponds to the tunneling path  $(m, m')$ . The relaxation rate ( $1/\tau$ ) has a single Lorentzian lineshape respects to  $H_z$  applied field because of the term  $\Gamma_m^{m'}$ . It contains the  $\varepsilon_{mm'}$  term, which is proportional to  $\delta H_z$ . See Eq. 1.34,  $\varepsilon_m =$

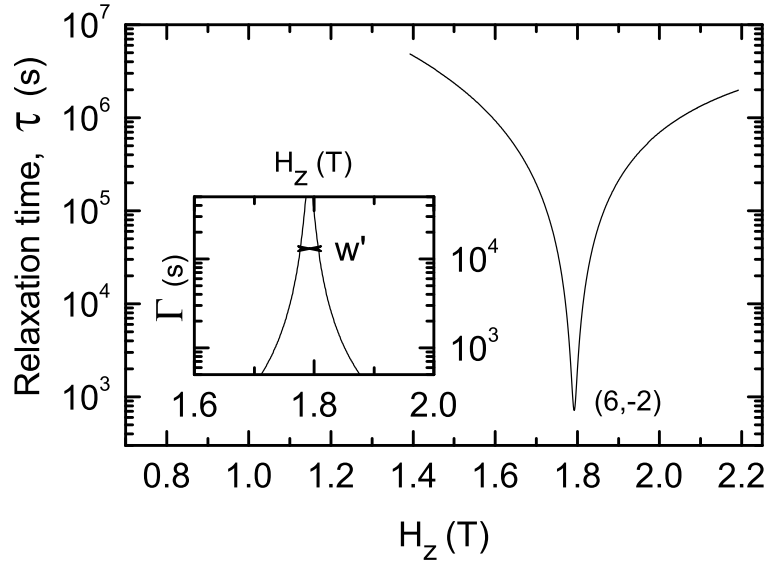


Figure 6.8: The calculated relaxation time ( $\tau$ ) of the tunneling path (6,-2) as a function of the magnetic field ( $H_z$ ), see Eq. 6.9. The inset shows the Lorentzian lineshape of the  $\Gamma_{6,-2}$  function, see Eq. 6.11 with the linewidth  $w' = 42$  mT. (See text).

$\epsilon_m + g\mu_B\delta H_z m$ . To tunnel, the spin has to be in a certain energy level within the tunnel splitting gap.

For example at the fourth resonance, the main resonance path is (6,-2) [34, 152]. We first simulated the Lorentzian line from  $\Gamma_6^{-2}$  function according to Eq. 6.10. The simulation is shown in the inset of Fig. 6.8. Next we calculate the relaxation rate,  $1/\tau_{(6,-2)}$  by insert  $\Gamma_6^{-2}$  term into Eq. 6.9. Finally we can calculate the relaxation time,  $\tau_{(6,-2)}$ . The simulation is shown in Fig. 6.8. We found the linewidth of the relaxation time of the (6,-2) peak  $\approx 42$  mT, which is closed to the value obtained by Ref. [34]. The sensitive parameter in the fit procedure is the sound velocity  $c$  term since it enters with the 5th power (see Eq. 1.51-1.52). We found  $c \approx 1.8 \times 10^3$  m/s.

Normally, beside the main resonance path, there are also the other minority (narrower Lorentzian) resonance paths contribute in the relaxation process. These narrower Lorentzian lines are called the satellite peaks. See Fig. 6.7 (solid line). They are a direct consequences of the fourth order anisotropy ( $BS_z^4$ ) in the spin Hamiltonian which leads to the transition  $\Delta m = \pm 4$  and the transverse field  $H_x = H_z \sin \alpha$  term due to the misalignment angle  $\alpha$  (see the inset diagram in Fig. 6.4) leads to the transition  $\Delta m = \pm 1$ . In this Thesis, we do not perform the calculation of these transverse terms but directly take the results via the tunnel splitting energy term from Ref. [34, 152] since it is not a simple method. See Eq.1.34. Refer to Ref. [16, 37, 152, 153] for more details.

In our calculation, we took the satellite paths from [34]. For example at fourth

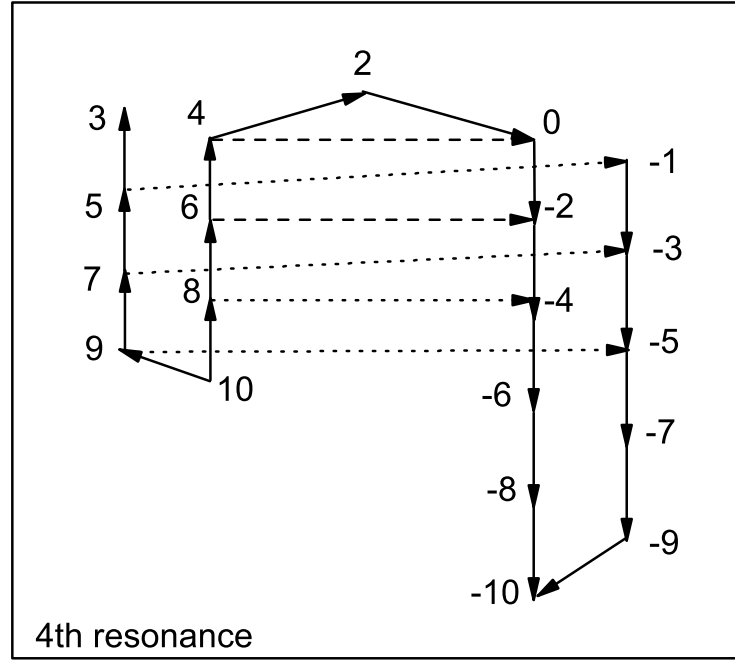


Figure 6.9: Reduced diagram of the relaxation path from the 4th resonance is shown. Solid lines show the *thermal transitions* (phonon induced). Dashed lines show the main tunneling path. Dotted lines show the tunneling due to satellite paths. (See text). Note that level +1 is not shown here because it is very close to the barrier and has no important role in the tunneling mechanism.

crossing, the tunneling path diagram is shown in Fig. 6.9. From the simulation (Fig. 6.7), the main resonance of the fourth crossing is the (6,-2) path due to its minimum relaxation time with linewidth (42 mT). The (4,0) path is considered to be another important resonance path since it has the biggest linewidth (90 mT) but its relaxation time is significantly slower than of the path (6,-2).

In Fig. 6.6, and Fig. 6.7, the lines are the results of summing all the possible relaxation paths together using the Kirchoff's rule of the electrical resistance ( $1/\tau = \sum_i 1/\tau_i$ , where  $i$  represents the number of the relaxation paths). At the non-resonance field, thermal activated relaxation time (Eq. 6.8) is taken into account as the background. Note that in Fig. 6.6, the theoretical line is calculated by using 0.01 T magnetic field resolution, while in Fig. 6.7 we use 0.06 T field resolution.

In general, the resonance field ( $H_{mm'}$ ) can be approximated from Eq. 1.23. For different resonance paths, the resonance fields are slightly different. The magnetic field interval  $d$  between a satellite peak and its associate main resonance peak can be directly obtained as

$$d(m_1 - m'_1, m_2 - m'_2) = \left| \frac{nB}{g\mu_B} (m_1^2 + m_1'^2 - m_2^2 - m_2'^2) \right|, \quad (6.12)$$



where  $(m_1, m'_1)$  represents the main resonance path and  $(m_2, m'_2)$  represents the satellite path.  $n = m_1 + m'_1 = m_2 + m'_2$ . For example, between the far left peak (5,-1) and the far right peak (8,-4), we obtained the magnetic field interval  $d \approx 0.2$  T by using Eq. 6.12. This value coincides well with the FWHM linewidth of the experimental data peak of the fourth resonance (black dots in Fig. 6.6). Our experimental linewidth value (measured at 1.77 K) also agrees well with the results at 1.8 K from Ref. [154].

In this Thesis, we only studied the relaxation mechanism of the fourth and fifth crossing since their relaxation time scale is optimized for our FDMRS technique. Too fast or too slow relaxation time scale is beyond the limitation of the technique. At the 5th resonance, the minimum relaxation time is too fast to observe. Therefore, in this Thesis it is beyond our scope to discuss the parity effect due to the odd and even resonances of the spin quantum tunneling [155].

### Discussion: Magnetic field dependence of the resonance frequency shift

We investigated the frequency shift ( $\Delta\nu_{\pm} = \nu_{\pm}^{\infty} - \nu_{\pm}^0$ ) behavior of the resonance line. For instance, the Voigt relaxation spectra in Fig. 6.3(a)-(b) at 1.85 T, the resonance line moves from 11.65 to 11.76  $\text{cm}^{-1}$  with  $\Delta\nu_{+} = 0.11 \text{ cm}^{-1}$  for  $\nu_{+}$  spectra and from 8.46 to 8.34  $\text{cm}^{-1}$  with  $\Delta\nu_{-} = 0.12 \text{ cm}^{-1}$  for  $\nu_{-}$  spectra.

Recall that the frequency shift in the static case measured in Section 5.2.1 is a contribution of the shift from the dipolar field ( $\Delta\nu_{dip}$ ) and the shift from the offdiagonal permeability term ( $\Delta\nu_{off}$ ). However, the shift from  $\Delta\nu_{dip}$  term can be 0.02  $\text{cm}^{-1}$  at most (see Section 5.2.1). The shift from  $\Delta\nu_{off}$  term can be at most 0.07  $\text{cm}^{-1}$ .

However in the dynamic case and during the relaxation process, the situation can be different. Our first assumption is that the shift is due to the distribution in ZFS (D) parameter. The molecules with different D parameters have slightly different relaxation times. For example, the molecules with higher D have slower relaxation time than the molecules with the lower D. Therefore, at the appearing resonance line, the shift moves to the higher frequency as we can see in Fig. 6.3 (a). However, for the disappearing line, the molecules with the smaller D with faster relaxation time should move first but our observation, see Fig. 6.3(b), is opposite. Hence, this assumption is no longer true.

Next assumption, the shift is due to the time dependent local dipolar field. In our model, we have quantitatively corrected the frequency shift due to the *local time dependent dipolar field* term as  $H_{dip} \cdot (p - q)$  in Eq. 6.7. Note that, the time dependent factor arises from  $p$  and  $q$  parameters. In our fit, we used  $H_{dip} \approx 0.0265$  T, which is the value obtained from Section 5.2.1. In Fig. 6.10, we plotted  $H_{dip} \cdot (p - q)$  as a function of time for the relaxation field 1.85 T at 1.77 K. We found the exponential behavior with time constant  $\tau_{dip} = 1073 \pm 70$  s. The exponential behavior comes from the  $p - q$  term which represents the difference in population between  $|+10\rangle$  and  $|-10\rangle$  states in the system.

In Fig. 6.10, we found time dependent dipolar field ranging from -265 to +265 Gauss for a general case by using function  $H_{dip} \cdot (p - q)$  for time  $t = [0.. \infty] \rightarrow p - q = [-1..1]$ . If we consider the situation at the relaxation field at 1.85 T, we can calculate the frequency shift; for example, from  $g\mu_B H_z = 11.68 \text{ cm}^{-1}$  to the demagnetized state

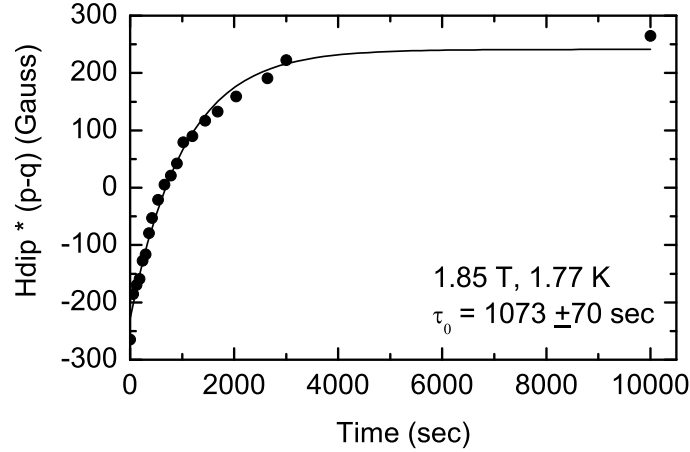


Figure 6.10: Time dependent local dipolar field ( $H_{dip} * (p-q)$ ) plotted as a function of time. The experimental data belongs to the measurement at  $H=1.85$  T,  $T=1.77$  K. (See text).

( $t \approx 0$  s,  $H_{dip} = -265$  Gauss);  $g\mu_B(H_z + H_{dip}) = 11.66$   $\text{cm}^{-1}$ , or to the magnetized state ( $t \approx \infty$ ,  $H_{dip} = +265$  Gauss);  $g\mu_B(H_z + H_{dip}) = 11.70$   $\text{cm}^{-1}$ .

The calculated resonance frequency of  $11.66$   $\text{cm}^{-1}$ , which is due to the dipolar field of  $-265$  Gauss at  $t \approx 0$ , is close to our observed value at  $11.65$   $\text{cm}^{-1}$  in Fig. 6.3(a). However at  $t \approx \infty$ , the resonance  $11.70$   $\text{cm}^{-1}$  which is due to the maximum dipolar field ( $+265$  Gauss), is not enough to explain the observed resonance spectra at  $11.76$   $\text{cm}^{-1}$  in Fig. 6.3(a). The explanation of the additional frequency shift of  $11.76 - 11.7 = 0.06$   $\text{cm}^{-1}$  is from the effect of the offdiagonal magnetic permeability term, see Section 5.2.

However, when we further investigate the frequency shift as a function of  $H_z$ , we found that the above frequency shift discussion is not true for all cases of  $H_z$ . We notice that the frequency shift is dependent on  $H_z$ . See Fig. 6.11 for comparison. At some values of the magnetic field, the frequency shift is less. Therefore, we investigated the frequency shift of the  $|+10\rangle \rightarrow |+9\rangle$  transition during the relaxation for each  $H_z$ . The results are shown in Fig. 6.12. We observed the magnetic field dependence of the frequency shift in the same manner as the field dependence of the relaxation time (refer to Fig. 6.6). The minimum shift ( $0.025$   $\text{cm}^{-1}$ ) corresponds to the magnetic field  $1.93$  T, while the observed resonance field is  $1.85$  T. The other minimum should be between  $2.3$ - $2.35$  T, which we do not have the experimental data due to the fact that the relaxation process is too fast to measure.

As discussed in Section 5.2.1, the frequency shift is due to the time dependent dipolar field ( $\Delta\nu_{dip} = g\mu_B m [H_{dip} * (p-q)]$ ) and the effect of the offdiagonal permeability ( $\Delta\nu_{off} = \nu' \sqrt{1 + \Delta\mu}$ ). However, if the magnetic field approaches the resonance value where the energy levels in  $+m$  and  $-m$  are matched, we observed smallest frequency shift. For instance, at  $1.9$  T, the shift is about  $0.025$   $\text{cm}^{-1}$ , which is approximately

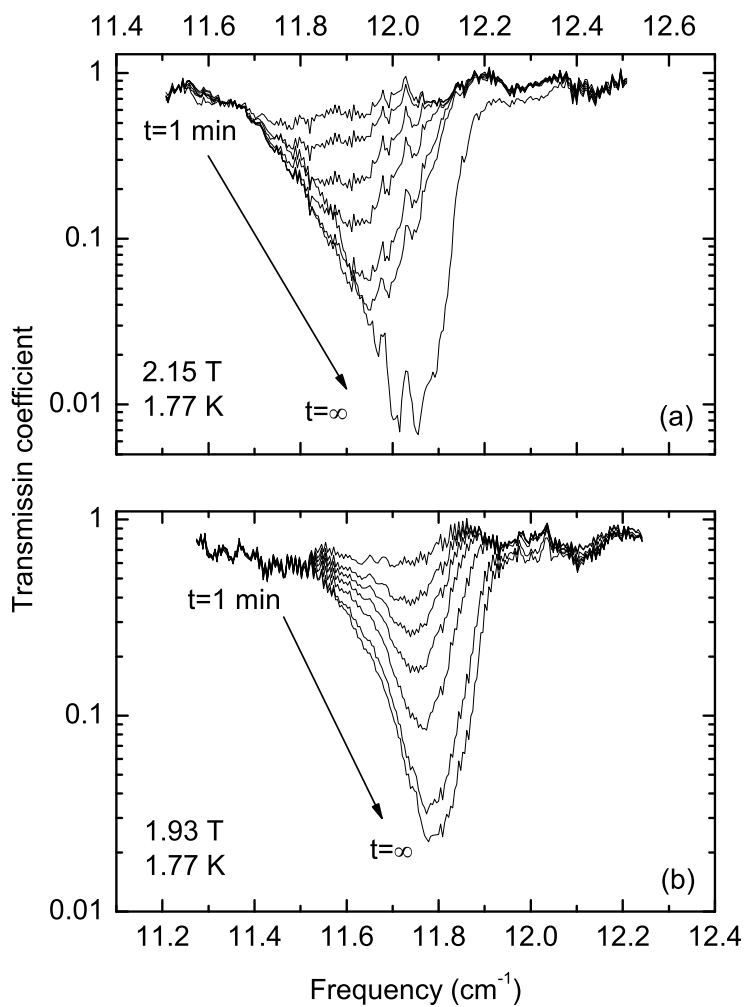


Figure 6.11: Transmission spectra of the transition between  $|+10\rangle \rightarrow |+9\rangle$  levels during the relaxation processes at magnetic field (a)  $H_z = 2.15$  T (b)  $H_z = 1.93$  T.

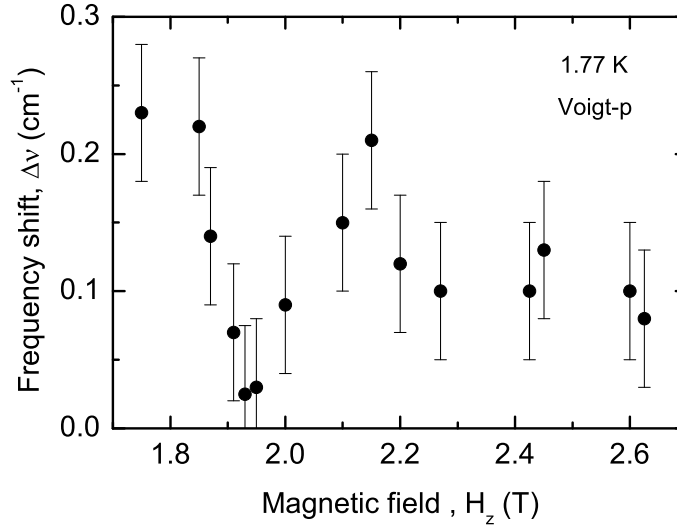


Figure 6.12: Longitudinal field dependent of frequency shift ( $\Delta\nu = \nu_+^\infty - \nu_+^0$ ) during the relaxation process. The data is taken from the spectra set measured at 1.77 K in Voigt geometry.

equal to the maximum calculated dipolar field in Fig. 6.10. Therefore at the resonance field, the dipolar field still remains while the offdiagonal term seems to approach zero.

However, it is difficult to relate the role of the offdiagonal permeability to the resonance field, since they should be rather independent from each others. Due to the big error bar in Fig. 6.12, the quantitative analysis is difficult. Therefore, at this level, we have not understood the field dependence effect to the shift of the resonance line during the relaxation process yet.

### Discussion: The change of linewidth during the relaxation

In principle during the fit procedure, we found that, in order to improve the fit, the linewidth was changed slightly. We investigated the FWHM linewidth of the resonance lines due to the  $|+10\rangle \rightarrow |+9\rangle$  transition before converting the field (which is equivalent to  $t = \infty$ ) as a function of the longitudinal field  $H_z$ . We chose to investigate FWHM instead of Gaussian linewidth ( $\sigma$ ) because we can identify FWHM more precisely than  $\sigma$ . The results are shown in Fig. 6.13. Again, we observe the magnetic field dependence of the linewidth in the same way as in Fig. 6.6 and Fig. 6.12. The minimum linewidth (FWHM =  $2.35 \text{ cm}^{-1} \rightarrow \sigma = 2/\sqrt{2\ln 2} = 0.92 \text{ cm}^{-1}$ ) belongs to the field 1.9 T. The other minimum should be in between 2.2-2.4 T.

From Chapter 4, we found the line broadening in the  $\text{Mn}_{12}$ -acetate system is mainly due to the inhomogeneous distribution of the ZFS parameters (D term). However, it is not clear what causes the field dependence of the linewidth in Fig. 6.13, since the distribution in D is the field independent term. It seems that the linewidth is linked

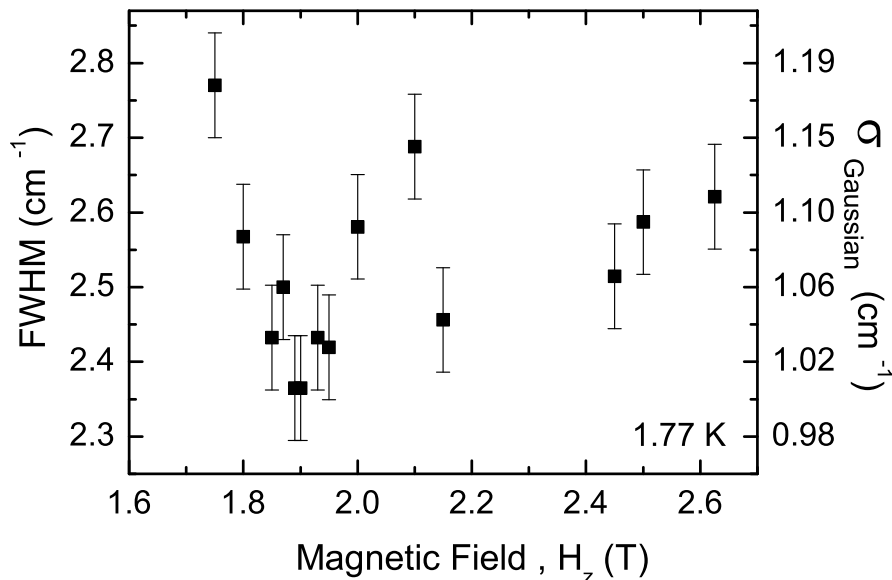


Figure 6.13: Longitudinal field dependent of Gaussian linewidth of the spectra at  $t = \infty$  (equilibrium state). The data is taken from the increasing spectra set (Voigt-p) measured at temperature 1.77 K in Voigt geometry.

to the relaxation mechanism. We currently do not understand this effect.

### 6.2.3 Relaxation time dependence of the longitudinal field: Faraday geometry

#### Experimental results

In Faraday geometry, we repeated the relaxation measurement as a function of the longitudinal applied field ( $H_z = 1.6 - 2.1$  T) as we have done in Voigt geometry. We used the same set up as in Section 5.3.2, where we used linearly polarized light and the analyzer angle at  $0^\circ$ . In this measurement, we only observe the relaxation spectra of the increasing line ( $|+10\rangle \rightarrow |+9\rangle$ ). The example of the Faraday relaxation spectra measured at 1.95 T and 1.86 K are shown in Fig. 6.14(a). The relaxation spectra grow symmetrically, and the resonance frequency does not shift as in the Voigt relaxation case. The relaxation time of the Faraday relaxation spectra can be analyzed as in Section 6.1. The relaxation time curve in Fig. 6.14(b) is well defined by an exponential function. The overall relaxation time curve of the Faraday measurement at 1.86 K as a function of the longitudinal field ( $H_z$ ) is plotted as in Fig. 6.6-(stars).

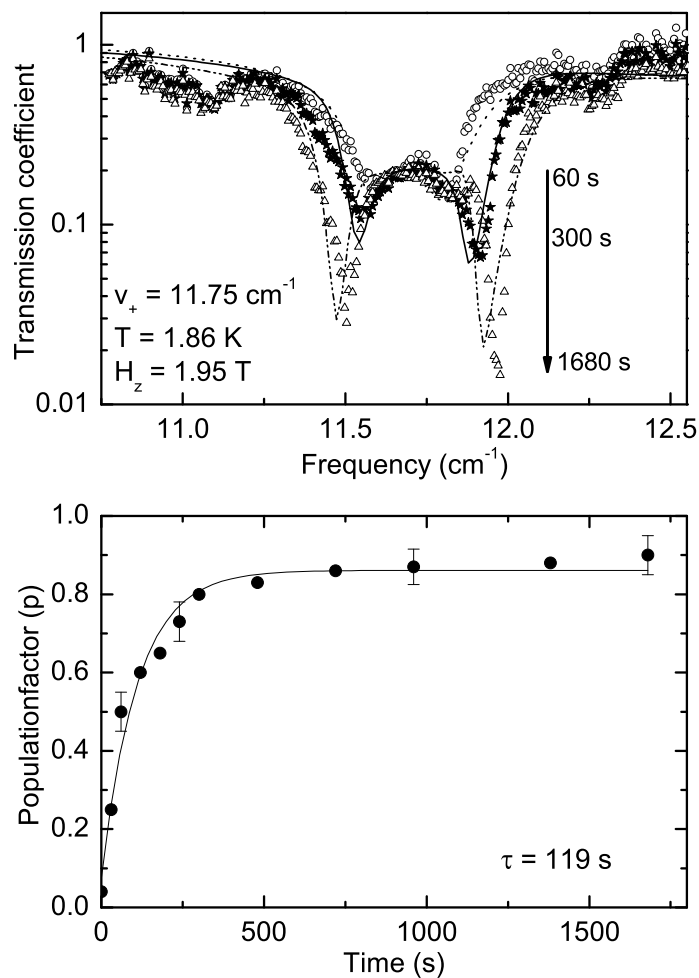


Figure 6.14: Relaxation measurement in Faraday geometry at 1.86 K, 1.95 T. (a) Series of the spectra growth measured right after switching the field to +1.95 T ( $t=1 \text{ min}$ ). (b) population factor  $q$  of the spectra from (a) as a function of time (see text).

## Discussion

The relaxation time of Faraday measurement is slightly lower than from Voigt measurement. Because the measurement in Faraday geometry was performed at slightly higher temperature than the Voigt measurement, the relaxation time, which is exponentially dependent on the temperature, is therefore slightly lower (see temperature dependence behavior of the relaxation time in Fig 6.5). Therefore, the difference in the observed relaxation time is purely from the temperature effect not the geometry effect. The difference in the measurement geometry does not disturb the relaxation time, since the relaxation mechanism is of purely molecular origin and does not depend on the magneto-optical properties of the macroscopic sample.

In Faraday geometry, the spectra grow symmetrically and there is no shift of the resonance frequency compared to Voigt case. The absence of the frequency shift is due to the cancellation of the offdiagonal terms of the L.H.C. and R.H.C. The effect of the frequency shift from the offdiagonal terms are cancelled out when we combine both circular modes together. This is mainly due to the term  $+\mu_{xy}$  and  $-\mu_{xy}$  in the effective permeability. In Voigt case, there is no such a cancellation effect. In other words, in Faraday case, the denominator in the effective permeability does not change as in the Voigt case (see Eq. 5.4-5.5 in comparison).

### 6.2.4 Zero field relaxation: Faraday geometry

#### Experimental results and analysis

Recall that there is a big difference between the lineshape in the *zfc* and *fc* experiment in Section 5.3.1. In this Section, we repeated this experiment but we investigated the changing of the lineshape as a function of time. However, we used the small relaxation field from -0.02 to 0.05 T instead of a strong field. This is because we want to probe the effect of the internal field in the system which is predicted to be in a millitesla range. The experimental details is in Section 6.1.1. See also Fig. 6.2. The measurement was performed at 3.3 K.

The example of the zero field relaxation spectra is shown in Fig. 6.15(a) measured in zero magnetic field. The lineshapes are dramatically changed from the nonequilibrium state (magnetized state) to the equilibrium state (demagnetized state).

The analysis of the relaxation time is the same as in Section 6.1. The lineshape analysis of the nonequilibrium state ( $t=30$  s) and equilibrium state ( $t=1260$  s) were discussed in Section 5.3.1. We fit the zero field relaxation spectra via the population factor  $p$  in Eq. 5.6-5.7. In the nonequilibrium state, we set  $p = 0$ , whereas in the equilibrium state, we set  $p = 1$ . During the relaxation from the nonequilibrium state to the equilibrium state,  $p$  parameter is changed as a function of time. Fig. 6.15(b) shows the time dependent behavior of the population factor  $p$  analyzed from the relaxation spectra in Fig. 6.15(a). It can be well fit with a single exponential function.

We changed the relaxation field from -0.02 to 0.05 T in order to look for the minimum relaxation time. We plotted the overall results in Fig. 6.16. The relaxation time is dependent on the magnetic field with the minimum time belongs to the applied magnetic field of -0.015 to +0.02 T due to the large error bar. These values correspond

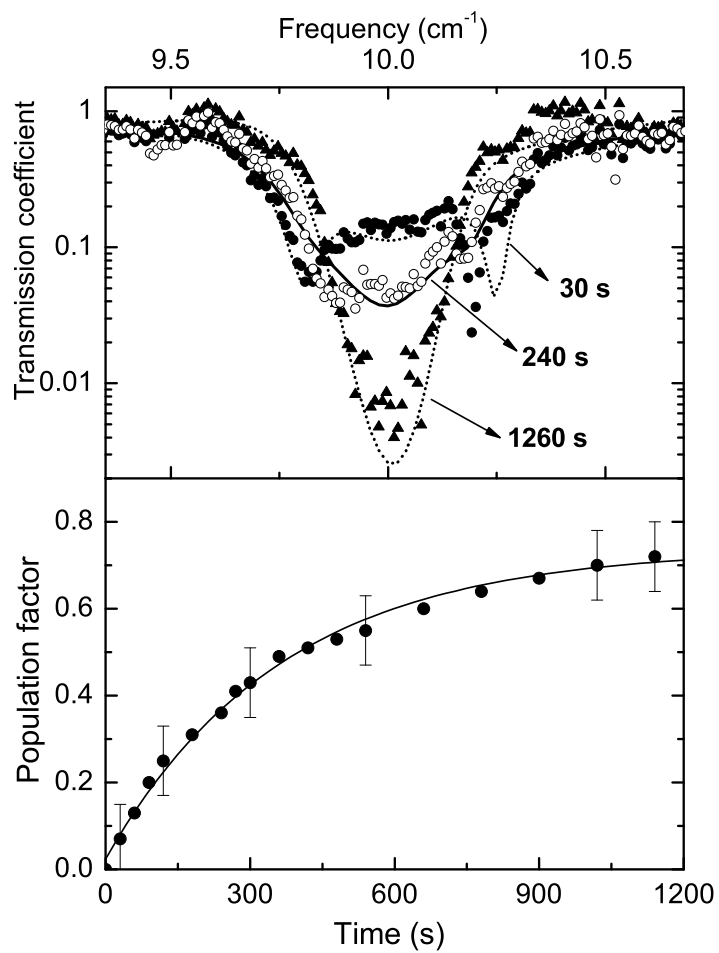


Figure 6.15: Transmission spectra of the transition  $|10\rangle \rightarrow |9\rangle$  levels during the relaxation process in zero field measured at 3.3 K.



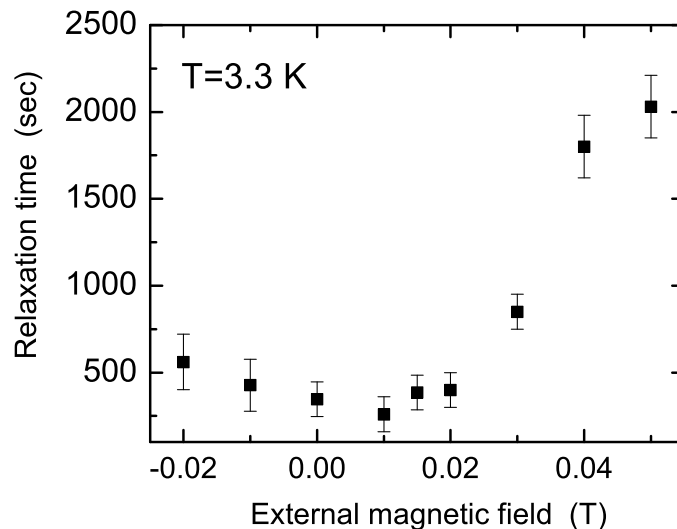


Figure 6.16: The relaxation measurement was performed at temperature 3.3 K in an applied magnetic field (-0.02 to +0.05 T). The relaxation time is plotted as a function of the applied magnetic field ( $H$ ).  $+H$  represent the field is in  $+z$ -direction, and vice versa. The minimum relaxation time corresponds to the applied magnetic field around +0.01 T.

to the real zero field in the system of  $\approx |0.02|$  T, which coincides very well with the dipolar field ( $H_{dip} \approx 0.0265$  T) found from the fit in Section 5.2.1. However, it also can be the remnant field of the superconducting magnets which cannot be distinguished in this case.

## 6.3 Conclusion

We have qualitative and quantitatively studied the magnetic quantum tunneling phenomenon in  $Mn_{12}$ -acetate (mosaics of single crystals) by using FDMRS technique. We performed the measurement within the temperature range of 1.75-3.3 K in both Voigt and Faraday geometries. For both cases, we obtained totally different lineshapes of the relaxation spectra but slightly different relaxation time (relaxation rate), which is due to slightly different temperature. The results indicate that the relaxation mechanism is independent on the measurement geometries but mainly on the temperature of the system and the applied magnetic field. The relaxation time behavior can be fitted nicely with a single exponential function. This implies that our temperature regime is not in the pure quantum tunneling regime but rather in the thermal regime.

We found that for nonresonance relaxation, higher magnetic field induces faster relaxation rate because it makes the energy barrier lower. For resonance relaxation, the relaxation rate is fastest at the certain values of the magnetic field, namely the resonance field, which matches the energy levels between  $(m, m')$  states and induces

the fast quantum tunneling process. We qualitatively and quantitatively explained the relaxation time behavior of both relaxation processes as function of the temperature and the applied magnetic field. We described the distribution of the relaxation time in the field domain via the phonon assisted spin tunneling model. We identified the dominant relaxation path for the tunneling at the fourth level crossing as the (6,-2) path. We observed the effect of the local dipolar field and the offdiagonal terms of the magnetic permeability tensor, which shift the resonance frequency during the relaxation process. However, we have not completely understood the relaxation lineshape studies e.g. the relation between the resonance frequency shift, the changes of the linewidth as a function of the applied magnetic field during the relaxation mechanism. Note that the mentioned results are under large error bars. We do not have the fine evidences that can lead to a precise conclusion at this level.

In conclusion, we believe that the relaxation studies in the frequency domain by using the FDMRS technique can reveal useful local information of the system during the relaxation process. We can directly observe the dynamics of the individual transitions as well as we can observe the quantum tunneling phenomenon whilst the other techniques such as the magnetometry technique cannot. However, the disadvantage of FDMRS technique is that the detailed spectra analysis is rather complicate.

# Chapter 7

## Summary

### 7.1 Results

The Mn<sub>12</sub>-acetate single molecule magnet is the most widely investigated mesoscopic system. It consists of exchanged couple clusters of paramagnetic metal ions, which show the quantum effects similar to the magnetic quantum tunneling of purely molecular origin. Mn<sub>12</sub>-acetate consists of 8 Mn<sup>3+</sup> and 4 Mn<sup>4+</sup> ions, which are antiferromagnetically coupled, giving rise to the large spin ground state, S=10. The manganese ions are bridged by oxide and acetate ligands, in which each molecule is well shielded from the others. Mn<sub>12</sub>-acetate has a large uniaxial magnetic anisotropy, leading to a 65 K zero field energy barrier acting against the magnetization reversal; + → - or - → +. The magnetization reversal can occur via three different processes; thermal activation, quantum tunneling, and thermal assisted tunneling. The full description of Mn<sub>12</sub>-acetate properties can be found in Chapter 1.

In the past ten years, there were around several hundred publications on the Mn<sub>12</sub>-acetate system by using several techniques e.g. electron paramagnetic resonance (EPR in field domain), nuclear magnetic resonance (NMR), SQUID magnetometry, inelastic neutron scattering (INS), etc. Nevertheless, there still is a number of open questions and problems, which are worthwhile to investigate with the help of a different technique. Here, we introduce an alternative EPR technique in a frequency domain, namely *frequency domain magnetic resonance spectroscopy* (FDMRS), to investigate the static (time independent) and the dynamic (time dependent) properties of the Mn<sub>12</sub>-acetate single molecular magnet system. Theoretical background of electrodynamics of solids and magnetic resonance is described in Chapter 2.

In our setup, we can apply an external magnetic field H=0-8 T within the temperature range of 1.5-300 K. We can control the direction of the wave propagation ( $\mathbf{q}$ ) with respect to the direction of the external magnetic field ( $\mathbf{H}_{ext}$ ), resulting in two different geometries, namely Voigt ( $\mathbf{q} \perp \mathbf{H}_{ext}$ ) and Faraday ( $\mathbf{q} \parallel \mathbf{H}_{ext}$ ) geometries. The frequency of the radiation can be either scanned or fixed within the range of 1-48 cm<sup>-1</sup>(= 30-1440 GHz which corresponds to the wavelength of 208 μm - 10 mm). Full description of FDMRS setup and measurement is described in Chapter 3.

In FDMRS the radiation propagation is in free space, while in EPR it often requires

a waveguide. Therefore, we can control the polarization of the radiation e.g. linear, elliptic, and circular polarization. Up to now, no full report on the studies of magneto-optical properties of  $\text{Mn}_{12}$ -acetate single molecular magnet has been produced. The other major advantage of FDMRS is that the individual magnetic transitions are measured, while the whole magnetization of the sample is measured by SQUID technique. Moreover, the magnetic field is always required by EPR, while in FDMRS we can measure both in the zero and nonzero magnetic fields. It is interesting that FDMRS can measure the individual magnetic transitions in zero and nonzero magnetic field environments, with the possibility of using different light polarizations. Moreover, we can use FDMRS to investigate the individual magnetic transition during the magnetic relaxation process. In this case, we can do the real time analysis, where we can obtain both the spectra lineshape and the relaxation time.

In this Thesis, we used the FDMRS technique to study the magnetic transitions of the  $|\pm 10\rangle \rightarrow |\pm 9\rangle$ ,  $|\pm 9\rangle \rightarrow |\pm 8\rangle$ , and  $|\pm 8\rangle \rightarrow |\pm 7\rangle$  levels individually. We used the Fresnel formulas for transmission to fit the spectra and to obtain the electrodynamic response functions of the materials i.e. complex dielectric permittivity ( $\hat{\epsilon}$ ), and complex magnetic permeability ( $\hat{\mu}$ ). We used the equation  $\hat{\mu} = 1 + \Delta\mu \cdot g(\nu)$  to relate between the complex permeability ( $\hat{\mu}$ ) and the magnetic mode contribution ( $\Delta\mu$ ) in the analysis.

In Chapter 4, we performed temperature dependent transmission measurements in the zero magnetic field. In this Thesis, we report the zero field splitting parameters (ZFS);  $D = -0.389 \pm 0.01 \text{ cm}^{-1}$ ,  $B = -7.65 \pm 0.05 \times 10^{-4} \text{ cm}^{-1}$ , and  $C = \pm 2 \times 10^{-5} \text{ cm}^{-1}$ . This result is in agreement with the observations from several other previously used techniques. However, the results from HFEPR were extrapolated from the measurement in the magnetic field. Only FDMRS and INS results were obtained from a real zero field measurement. However, for an INS technique, grams of deuterate sample are required. Our main advantage is that only about a hundred milligrams of the sample (either single crystals or polycrystalline sample) are needed. The FDMRS measurement is fast and the results are directly obtained from a real zero field measurement.

We also obtained the ZFS parameters, and found that the magnetic mode contribution ( $\Delta\mu$ ) obeys the Boltzmann distribution law as a function of the temperature. The resonance lines are well fitted with Gaussian lineshapes rather than with Lorentzian ones. The Gaussian lineshapes indicate that there is an inhomogeneous broadening, which is at least partly due to the local variations in the zero field splitting (ZFS) parameter (D-strain) of  $\text{Mn}_{12}$ -acetate. The Gaussian linewidth ( $\sigma$ ) is found to be temperature dependent, which indicates the contribution of the internal dipolar field to the line broadening. The resonance frequency ( $\nu$ ) is temperature independent, meaning that the temperature does not effect the zero field splitting parameters in the studied temperature range. Next, we studied the magnetic transitions in an applied magnetic field. We observed the lineshift as a function of the Zeeman splitting term;  $g\mu_B m \cdot H_{ext}$ . Here we report the  $g_{\parallel} = 1.93$  obtained by calculating the average slope of the plot of the resonance frequencies as a function of the magnetic field. The g-value is in agreement with the HFEPR measurement.

In Chapter 5, we studied the lineshape of the  $|+10\rangle \rightarrow |+9\rangle$  transition in single

crystalline  $\text{Mn}_{12}$ -acetate samples in Voigt and Faraday geometries. Since we are able to do the zero field measurements on a zero field cooled (*zfc*) and field cooled (*fc*) single crystalline  $\text{Mn}_{12}$ -acetate sample, the measurements were performed in zero field at low temperatures ( $T=1.75\text{-}3.3$  K) on both nonmagnetized (*zfc*) and magnetized (*fc*) samples. In both geometries, we found a large difference in lineshapes depending on the magnetization state of the sample. We have developed a model to describe the lineshape of the magnetic resonance transitions in  $\text{Mn}_{12}$ -acetate system under these conditions. The lineshape differences can be explained by the occurrence of the offdiagonal elements in the magnetic permeability tensor for the case of the magnetized samples. The permeability tensor is a consequence of the interaction between the electromagnetic radiation, the external magnetic field and the magnetic state of the anisotropic sample in different magneto-optical geometries.

In Voigt geometry, we used a linear polarized light to measure the *zfc* (demagnetized sample) and then the *fc* (magnetized sample)  $\text{Mn}_{12}$ -acetate sample in zero magnetic field. We found a symmetric Gaussian lineshape for the *zfc* sample and an asymmetric Gaussian lineshape for the *fc* sample. We found a slight lineshift of  $\approx 0.1 \text{ cm}^{-1}$  between the two samples. This effect is due to the influence of the internal fields such as the dipolar and hyperfine fields ( $\approx 0.02 - 0.03 \text{ cm}^{-1}$ ) together with the contribution of the offdiagonal permeability ( $\approx 0.07 \text{ cm}^{-1}$ ). The latter contribution is a consequence of the appearance of the offdiagonal permeability terms, because the sample is in the magnetized state. The asymmetry of the Gaussian lineshape of the magnetized sample in the zero magnetic field measurement implies that the asymmetry of the line is not due to the tilting of the easy axis of the crystal, but rather due to the effect of the D-strain.

In Faraday geometry, we performed the transmission measurement by using the linearly and circularly polarized lights. We observed the difference in the lineshapes from applying left hand circularly (L.H.C.), right hand circularly (R.H.C.), and linearly polarized light to the  $\text{Mn}_{12}$ -acetate sample. In the linearly polarized case, we found that the absorption line of the *zfc*  $\text{Mn}_{12}$ -acetate has a symmetric Gaussian lineshape. In the *fc* case, the lineshape remains the same, but it has half the intensity compared to the Voigt spectra. By placing an analyzer unit in front of the detector, we observed the change to the lineshape, where the extra two minima are found beside the resonance absorption line. We also found that by using linearly polarized light, we observed the Faraday effect, where the major axis of the light polarization is rotated as a function of the radiation frequencies. The Faraday rotation is found to be ranging from  $+100^\circ$  to  $-100^\circ$  for a given sample thickness of 0.5 mm. This suggests that the  $\text{Mn}_{12}$ -acetate single molecule magnet can be used as a molecular rotator or a molecular polarization transformer.

In the case of using circularly polarized light in Faraday geometry, we found a single Gaussian absorption line from both the *zfc* and the *fc*  $\text{Mn}_{12}$ -acetate sample, as also observed in the Voigt geometry. However, this absorption depends on the direction of the magnetization in the  $\text{Mn}_{12}$ -acetate sample and the rotation direction of the light polarization. In Faraday geometry, the magnetic resonance is sensitive to the circular polarization direction of light (L.H.C. and R.H.C. radiation). For example, if the sample is magnetized with  $+H_{ext}$  field, only L.H.C. light interacts with the

sample. For the sample magnetized in  $-H_{ext}$  field, the absorption line is found by using the R.H.C. light. This result is related to the optical selection rule;  $\Delta m = +1$  for L.H.C., and  $\Delta m = -1$  for R.H.C. radiation. If the sample is demagnetized, the sample interacts with both the L.H.C. and the R.H.C. radiation.

In concluding our lineshape studies, we successfully developed a self-inclusive model to describe the lineshapes for both the geometries (Voigt, and Faraday) and the magnetization states. We have qualitatively and quantitatively studied the electrodynamics of the  $Mn_{12}$ -acetate system via the effects of the light polarization and the magneto-optical geometry.

In Chapter 6, we applied the FDMRS technique to investigate the dynamical properties, namely the *relaxation of the magnetization* of the  $Mn_{12}$ -acetate system. During the relaxation process, the spin changes from the spin up state (+) to a spin down state (-) or vice versa.

We have successfully used FDMRS to observe three different relaxation processes within the temperature range of 1.75-3.3 K, magnetic field range of 1.6-2.63 T, and the two measurement geometries. We found that the relaxation is dependent on the temperature and the applied magnetic field, rather than on the measurement geometry. In the temperature range 1.75-3.3 K, the relaxation time is strongly dependent on the temperature following an Arrhenius function. In the magnetic field 1.6-2.63 T, we observed the two minima of the relaxation time, the first minimum is around 1.85 T, while the second minimum is around 2.3-2.35 T. These two minima correspond with the magnetic field,  $H_n^{mm'} \approx 0.45n$ , where  $n = 4, 5$ , that can match the energy levels on both sides of the double-well energy potential.

During the analysis, we divided our relaxation measurements into two parts; the first part is about the relaxation spectra in the frequency domain, and the second part is about the relaxation time in the field domain.

In the first part, we studied the relaxation spectra in the frequency domain. We have developed a model to analyze the time dependent spectra for both the Voigt and Faraday geometries. Consequently we described the lineshape of the relaxation spectra. We also introduced the population factor, which represents how much of the spin population contributes to the absorption line intensity. We found an exponential relationship between the population factor and the time, from which the relaxation time is obtained. In Voigt geometry, we observed a shift of the resonance line and the change of the Gaussian linewidth during the relaxation process. We suggested that the shift of the resonance line is due to the local dipolar field and the effect of the offdiagonal element in the magnetic permeability tensor.

In the second part, we plotted the relaxation time in the field domain ( $H_z$ ) regime. We observed two distinct relaxation mechanisms; thermal activation with a slower relaxation rate, and thermal assisted tunneling with a much faster relaxation rate. We have compared our relaxation time results to the results obtained by the magnetometric techniques, and we found that these results are in good agreement.

We have qualitatively and quantitatively explained the relaxation time curve in the field domain via the phonon assisted spin tunneling model. We calculated the relaxation time via the three contributions; time required for the spin-phonon coupling ( $m \rightarrow m \pm 1, \pm 2$ ), time required for the tunneling ( $m \rightarrow m'$ ), and time required for

$m' \rightarrow m' \pm 1, \pm 2$  process. The longitudinal field parameter ( $H_z$ ) was substituted into the energy level parameters. In this model, the relaxation time distribution has a Lorentzian lineshape around the level crossing field ( $H_n^{mm'}$ ).

The spin tunneling process occurs via the two different tunneling paths; the dominant path and the satellite path. In this Thesis, we identified these tunneling paths by simulating a single Lorentzian curve of the relaxation time distribution that corresponds to each  $(m, m')$ . The dominant path corresponds to the Lorentzian curve with the highest amplitude and broadest linewidth. At the fourth crossing ( $H_{z,theo} \approx 1.8$  T), the dominant paths with the highest amplitude are found to be (6,-2), whilst the broadest linewidth is found in the (4,0) path.

The study of the relaxation phenomenon by using FDMRS can reveal many detailed findings such as the relaxation time, the system temperature and magnetic field influences, as well as the dynamics of the relaxation spectra and the influences of the tunneling on an individual transition lineshape. However, in the latter case, we have not completely understood the real mechanism of how the tunneling can effect the individual relaxation spectra.

In conclusion, FDMRS technique is a promising technique in the study of both the static and dynamic properties of the Mn<sub>12</sub>-acetate single molecule magnet.

## 7.2 Future plans

Mn<sub>12</sub>-acetate single molecule magnet and its analogous clusters offer potential access to very high density data storage devices. This is due to its well defined nanoscale size and its single magnetic domain properties. To achieve this, the molecules need to be oriented properly in order to be addressed individually, where each molecule can be used as an individual bit of information. Many research groups are now trying to arrange the molecules onto the polymer film, which is combined with the conducting or semi-conducting substrate. Within this trend, the research topics on Mn<sub>12</sub>-acetate are moving towards to the 2-dimensional (2D) mesoscopic physics. A very interesting field involves investigating the semi-conducting properties and the MQT phenomenon of the Mn<sub>12</sub>-acetate thin film, which is spin coated over the conducting substrate. The film properties also strongly depend on the substrate materials and their surface properties. Since FDMRS can study both the electric and the magnetic properties of the materials, FDMRS has potential to be one of the major tools in this field.





# Bibliography

- [1] J.R. Friedman, M. P. Sarachik, J. Tejada, and R. Ziolo, *Phys. Rev. Lett.* **76**, 3830, (1996).
- [2] E. del Barco, N. Vernier, J.M. Hernandez, J. Tejada, E.M. Chudnovsky, and E. Molins, *Europhys. Lett.* **47**, 722, (1999).
- [3] F.L. Mettes, F. Luis, and L.J. de Jongh, *Phys. Rev. B* **64**, 174411, (2001).
- [4] V.V. Dobrovitski, M.I. Katsnelson, and B.N. Harmon, *Phys. Rev. Lett.* **84**, 3458, (2000).
- [5] C. Paulsen, and J.-G. Park, in *Quantum Tunneling of the Magnetization*, Edited by L. Gunther, and B. Barbara, NATO ASI, Series E **301**, (Kluwer, Dordrecht, 1995).
- [6] E. del Barco, J.M. Hernandez, M. Sales, J. Tejada, H. Rakoto, J.M. Broto, E.M. Chudnovsky, *Phys. Rev. B* **60**, 11898, (1999).
- [7] W. Wernsdorfer, and R. Sessoli, *Science* **284**, 133, (1999).
- [8] A. Abragam, and B. Bleaney, in *Electron paramagnetic resonance of transition ions*, (Dover Publication Inc., New York, 1986).
- [9] O. Kahn, in *Molecular Magnetism*, (VCH Publishers Inc., 1993).
- [10] C. Rudowicz, *J. Phys.: Condens. Matter* **12**, L417, (2000).
- [11] M.A. Novak, and R. Sessoli, in *Quantum Tunneling of the Magnetization*, Edited by L. Gunther, and B. Barbara, NATO ASI, Series E **301**, (Kluwer, Dordrecht, 1995).
- [12] F. Luis, J. Bartolomé, J. F. Fernández, J. Tejada, J.M. Hernández, X.X. Zhang, and R. Ziolo, *Phys. Rev. B* **55**, 11448, (1998).
- [13] Z.H. Jang, A. Lascialfari, F. Borsa, and D. Gatteschi, *Phys. Rev. Lett.* **84**, 13, 2977, (2000).
- [14] A.M. Gomes, M.A. Novak, R. Sessoli, A. Caneschi, and D. Gatteschi, *Phys. Rev. B* **57**, 5021, (1998).

- [15] M. Sales, J.M. Hernandez, J. Tejada, and J.L. Martinez, *Phys. Rev. B* **60**, 14557, (1999).
- [16] D.A. Garanin, and E.M. Chudnovsky, *Phys. Rev. B* **56**, 11102, (1997).
- [17] D.A. Garanin, and E.M. Chudnovsky, *Phys. Rev. B* **65**, 094423, (2002).
- [18] E.M. Chudnovsky, and D.A. Garanin, *Phys. Rev. Lett.* **87**, 18, 187203, (2001).
- [19] R. Sessoli, D. Gatteschi, A. Caneschi, and M.A. Novak, *Nature* **365**, 141, (1993).
- [20] B. Barbara, W. Wernsdorfer, L.C. Sampaio, J.G. Park, C. Paulsen, M.A. Novak, R. Ferré, D. Maily, R. Sessoli, A. Caneschi, K. Hasselbach, A. Benoit, and L. Thomas, *J. Magn. Magn. Mater.* **140**, 1825, (1995).
- [21] R. Sessoli, *Mol. Cryst. Liq. Cryst. A* **274**, 145, (1995).
- [22] T. Ohm, C. Sangregorio, and C. Paulsen, *Eur. Phys. J. B* **6**, 195, (1998).
- [23] L. Thomas, A. Caneschi, and B. Barbara, *Phys. Rev. Lett.* **83**, 2398, (1999).
- [24] D.A. Garanin, X. Martinez-Hidalgo, and E.M. Chudnovsky, *Phys. Rev. B* **57**, 13639, (1998).
- [25] G.-H. Kim, and E.M. Chudnovsky, *Europhys. Lett.* **52**(6), 681, (2000).
- [26] L. Bokacheva, A.D. Kent, and M.A. Walters, *Phys. Rev. Lett.* **85**, 4803, (2000).
- [27] J.M. Hernández, X.X. Zhang, F. Luis, J. Bartolomé, J. Tejada, and R. Ziolo, *Europhys. Lett.* **35**, 301, (1996).
- [28] K.M. Mertes, Y. Zhong, M.P. Sarachik, Y. Paltiel, H. Shtrikman, E. Zeldov, E. Rumberger, and D.N. Hendrickson, *J. Appl. Phys.* **89**, 11, 6802, (2001).
- [29] N. Vernier, and G. Bellessa, *Europhys. Lett.* **60**, 148, (2002).
- [30] J.M. Hernandez, F. Torres, J. Tejada, and E. Molins, *Phys. Rev. B* **66**, 161407 (R), (2002).
- [31] F. Hartmann-Boutron, P. Politi, and J. Villain, *Int. J. Mod. Phys. B* **10**, 2577, (1996).
- [32] J.R. Friedman, M.P. Sarachik, and R. Ziolo, *Phys. Rev. B* **58**, 14729(R), (1998).
- [33] M.R. Pederson, N. Bernstein, and J. Kortus, *Phys. Rev. Lett.* **89**, 097202, (2002).
- [34] M.N. Leuenberger, and D. Loss, *Phys. Rev. B* **61**, 1286, (1999).
- [35] I. Chiorescu, R. Giraud, A.G.M. Jansen, A. Caneschi, and B. Barbara, *Phys. Rev. Lett.* **85**, 4807, (2000).

- [36] J. Villain, F. Hartmann-Boutron, R. Sessoli, and A. Rettori, *Europhys. Lett.* **27**, 159, (1994).
- [37] T. Pohjola, and H. Schoeller, *Phys. Rev. B* **62**, 15026, (2000).
- [38] E. Callen, and H.B. Callen, *Phys. Rev. A* **139**, 455, (1965).
- [39] V. Dohm, and P. Fulde, *Z. Phys. B* **21**, 369, (1975).
- [40] E.M. Chudnovsky, and L. Gunther, *Phys. Rev. Lett.* **60**, 661, (1988).
- [41] M. Enz, and R. Schilling, *J. Phys. C* **19**, L711, (1986).
- [42] O.B. Zaslavskii, *Phys. Lett. A* **145**, 471, (1990).
- [43] J.L. van Hemmen, and A. Sütő, *Europhys. Lett.* **1**, 481, (1986).
- [44] A. Sütő, and J.L. van Hemmen, *Physica B* **141**, 37, (1986).
- [45] G. Scharf, W. F. Wreszinski, and J.L. van Hemmen, *J. Phys. A* **20**, 4309, (1987).
- [46] I. Ya. Korenblit, and E.F. Shender, *Sov. Phys. JETP* **48**, 937, (1978).
- [47] D.A. Garanin, *J. Phys. A* **24**, L61, (1991).
- [48] A. Messiah, in *Quantum Mechanics*, (de Gruyter, New York, 1991).
- [49] K. Blum, in *Density Matrix Theory and Applications*, 2nd Ed., (Plenum, New York, 1981).
- [50] A. Caneschi, D. Gatteschi, R. Sessoli, A.L. Barra, L.C. Brunel, and M. Guillot, *J. Am. Chem. Soc.* **113**, 5873, (1991).
- [51] T. Lis, *Acta Crystallogr.* **B36**, 2042, (1980).
- [52] R.A. Robinson, P.J. Brown, D.N. Argyriou, D.N. Hendrickson, and S.M.J. Aubin, *J. Phys.: Condens. Matter* **12**, 2805, (2000).
- [53] Z. Zeng, D. Guenzburger, and D.E. Ellis, *Phys. Rev. B* **59**, 6927, (1999).
- [54] A.L. Barra, D. Gatteschi, and R. Sessoli, *Phys. Rev. B* **56**, 8192, (1997).
- [55] M. Hennion, L. Pardi, I. Mirebeau, E. Suard, R. Sessoli, and A. Caneschi, *Phys. Rev. B* **56**, 8819, (1997).
- [56] A.A. Mukhin, V.D. Travkin, A.K. Zvezdin, A. Caneschi, D. Gatteschi, and R. Sessoli, *Physica B* **284**, 1221, (2000).
- [57] R. Amigó, E. del Barco, LI. Casas, E. Molins, J. Tejada, I.B. Rutel, B. Mommouton, N. Dalal, and J. Brooks, *Phys. Rev. B* **65**, 172403, (2002).

- [58] A. Cornia, R. Sessoli, L. Sorace, D. Gatteschi, A.L. Barra, and C. Daugebonne, *Phys. Rev. Lett.* **89**, 257201, (2002).
- [59] S. Vongtragool, A.A. Mukhin, B. Gorshunov, and M. Dressel, *Phys. Rev. B* **69**, 104410, (2004).
- [60] K. Wieghardt, K. Pohl, I. Jibril, and G. Huttner, *Angew. Chem. Int. Ed. Engl.* **23**, 77, (1984).
- [61] C. Sangregorio, T. Ohm, C. Paulsen, R. Sessoli, D. Gatteschi, *Phys. Rev. Lett.* **78**, 4645, (1997).
- [62] O. Waldmann, R. Koch, S. Schromm, P. Müller, I. Bernt, and R.W. Saalfrank, *Phys. Rev. Lett.* **89**, 24, 246401, (2002).
- [63] F. Cinti, M. Affronte, and A.G.M. Jansen, *Eur. Phys. J. B* **30**, 461, (2002).
- [64] M. Affronte, J.C. Lasjaunias, W. Wernsdorfer, R. Sessoli, D. Gatteschi, S.L. Heath, A. Fort, and A. Rettori, *Phys. Rev. B* **66**, 064408, (2002).
- [65] M. Affronte, J.C. Lasjaunias, and G.L. Abbati, *Phys. Rev. B* **66**, 180405(R), (2002).
- [66] A. Chiolero, and D. Loss, *Phys. Rev. Lett.* **80**, 169, (1998).
- [67] W. Wernsdorfer, N. Aliaga-Alcalde, D.N. Hendrickson, and G. Christou, *Nature* **416**, 406, (2002).
- [68] B. Pilawa, M.T. Kelemen, S. Wanka, A. Geisselmann, and A.L. Barra, *Europhys. Lett.* **43**, 7, (1998).
- [69] A.J. Tasiopoulos, W. Wernsdorfer, B. Moulton, M.J. Zaworotko, and G. Christou, *J. Am. Chem. Soc.* **125**, 15274, (2003).
- [70] C. Boskovic, W. Wernsdorfer, K. Folting, J.C. Huffman, D.N. Hendrickson, and G. Christou, *Inorg. Chem.* **41**, 5107, (2002).
- [71] A. Caneschi, D. Gatteschi, R. Sessoli, and J. Schweizer, *Physica B* **241**, 600, (1998).
- [72] E.K. Brechin, C. Boskovic, W. Wernsdorfer, J. Yoo, A. Yamaguchi, E.C. Sanudo, T.R. Concolino, A.L. Rheingold, H. Ishimoto, D.N. Hendrickson, and G. Christou, *J. Am. Chem. Soc.* **124**, 9710, (2002).
- [73] E.C. Sanudo, W. Wernsdorfer, K.A. Abboud, and G. Christou, *Inorg. Chem.* **43**, 4137, (2004).
- [74] M. Murugesu, M. Habrych, W. Wernsdorfer, K.A. Abboud, and G. Christou, *J. Am. Chem. Soc. (Comm.)* **126**, 4766, (2004).

- [75] M. Soler, W. Wernsdorfer, K. Folting, M. Pink, and G. Christou, *J. Am. Chem. Soc.* **126**, 2156, (2004).
- [76] A.J. Tasiopoulos, A. Vinslava, W. Wernsdorfer, K.A. Abboud, and G. Christou, *Angew. Chem. Int. Ed. Engl.* **43**, 2117, (2004).
- [77] D. Procissi, B.J. Suh, A. Lascialfari, F. Borsa, A. Caneschi, and A. Cornia, *J. Appl. Phys.* **91**, 7173, (2002).
- [78] A. Cornia, A. C. Fabretti, P. Garrisi, C. Mortalò, D. Bonacchi, D. Gatteschi, R. Sessoli, L. Sorace, W. Wernsdorfer, and A.L. Barra, *Angew. Chem. Int. Ed.* **43**, 1136, (2004).
- [79] A.K. Powell, S.L. Heath, D. Gatteschi, L. Pardi, R. Sessoli, G. Spina, F. Del Giallo, and F. Pieralli, *J. Am. Chem. Soc.* **117**, 2491, (1995).
- [80] E. Ruiz, A.R. Fortea, J. Cano, and S. Alvarez, *J. Phys. Chem. Solids* **65**, 799, (2004).
- [81] M. Affronte, R. Sessoli, D. Gatteschi, W. Wernsdorfer, J.C. Lasjaunias, S.L. Heath, A.K. Powell, A. Fort, and A. Rettori, *J. Phys. Chem. Solids* **65**, 745, (2004).
- [82] J.C. Goodwin, R. Sessoli, D. Gatteschi, W. Wernsdorfer, A.K. Powell, and S.L. Heath, *J. Chem. Soc., Dalton Trans.*, 1835, (2000).
- [83] J.J. Sokol, A.G. Hee, and J.R. Long, *J. Am. Chem. Soc.* **124**, 7656, (2002).
- [84] E.C. Yang, D.N. Hendrickson, W. Wernsdorfer, M. Nakano, L.N. Zakharov, R.D. Sommer, A.L. Rheingold, M. Ledezma-Gairaud, and G. Christou, *J. Appl. Phys.* **91**, 7382, (2002).
- [85] M. Murrie, S.J. Teat, H. Stoeckli-Evans, and H.U. Güdel, *Angew. Chem. Int. Ed.* **42**, 4653, (2003).
- [86] R.S. Edwards, S. Maccagnano, E.C. Yang, S. Hill, W. Wernsdorfer, D. Hendrickson, and G. Christou, *J. Appl. Phys.* **93**, 7807, (2003).
- [87] H. Andres, R. Basler, A.J. Blake, C. Cadiou, G. Chaboussant, C.M. Grant, H.U. Güdel, M. Murrie, S. Parsons, C. Paulsen, F. Semadini, V. Villar, W. Wernsdorfer, and R.E.P. Winpenny, *Chem. Eur. J.* **8**, 21, 4867, (2002).
- [88] S. Osa, T. Kido, N. Matsumoto, N. Re, A. Pochaba, and J. Mrozinski, *J. Am. Chem. Soc.* **126**, 420, (2004).
- [89] A.L. Barra, L.C. Brunel, D. Gatteschi, L. Pardi, and R. Sessoli, *Acc. Chem. Res.* **31**, 460, (1998).
- [90] M.R. Cheeseman, V.S. Oganessian, R. Sessoli, D. Gatteschi, and A.J. Thomson, *Chem. Commun.* **17**, 1677, (1997).

- [91] M.N. Leuenberger, and D. Loss, *Nature* **410**, 789, (2001).
- [92] S. Hill, R.S. Edwards, N. Aliaga-Alcalde, and G. Christou, *Science* **302**, 1015, (2003).
- [93] J. Tejada, E.M. Chudnovsky, E. del Barco, J.M. Hernandez, and T.P. Spiller, *Nanotech.* **12**, 181, (2001).
- [94] A. Cornia, A.C. Fabretti, M. Pacchioni, L. Zobbi, D. Bonacchi, A. Caneschi, D. Gatteschi, R. Biagi, U. Del Pennino, V. De Renzi, L. Gurevich, and S.J. van der Zant, *Angew. Chem. Int. Ed.* **42**, 1645, (2003).
- [95] C. Joachim, J.K. Gimzewski, and A. Aviram, *Nature* **408**, 541, (2000).
- [96] H. Park, J.R. Long, D.R. Reichman, and C.B. Murray, NSF-NSEC conference, Grant 0210426, Dec 16-18, (2003).
- [97] D. Zipse, J.M. North, R.M. Achey, N.S. Dalal, S. Hill, R.S. Edwards, E.S. Choi, and J.S. Brooks, *J. Appl. Phys.* **95**, 11, 6900, (2004).
- [98] E.M. Chudnovsky, and J. Tejada, in *Macroscopic Quantum Tunneling of the Magnetic Moment*, (Cambridge University Press, 1998).
- [99] M. Clemente-León, C. Mingotaud, B. Agricole, C.J. Gómez-García, E. Coronado, and P. Delhaès, *Angew. Chem., Int. Ed. Engl.* **36**, 1114, (1997).
- [100] M. Clemente-León, H. Soyer, E. Coronado, C. Mingotaud, C.J. Gómez-García, and P. Delhaès, *Angew. Chem., Int. Ed.* **37**, 2842, (1998).
- [101] D. Ruiz-Molina, M. Mas-Torrent, A.I. Balana, N. Domingo, J. Tejada, M.T. Martínez, C. Rovira, and J. Veciana, *Adv. Mater.* **15**, 42, (2003).
- [102] M. Cavallini, F. Biscarini, J. Gomez-Segura, D. Ruiz, and J. Veciana, *Nano Lett.* **3**, 1527, (2003).
- [103] M. Clemente-León, E. Coronado, A. Forment-Aliaga, P. Amorós, J. Ramírez-Castellanos, and J.M. González-Calbet, *J. Mater. Chem.* **13**, 3089, (2003).
- [104] M.N. Leuenberger, *J. Magn. Magn. Mater.* **272**, 1974, (2004).
- [105] D.S. Hu, and S.J. Xiong, *Int. J. Mod. Phys. B* **17**, 7, 1117, (2003).
- [106] J. Tejada, R. Amigó, J.M. Hernandez, and A. García-Santiago, *J. Magn. Magn. Mater.* **272**, 2131, (2004).
- [107] J. Tejada, E.M. Chudnovsky, J.M. Hernandez, and R. Amigó, *Appl. Phys. Lett.* **84**, 13, 2372, (2004).
- [108] R. Amigó, J.M. Hernandez, A. García-Santiago, and J. Tejada, *Appl. Phys. Lett.* **82**, 25, 4528, (2003).

- [109] B. Barbara, L. Thomas, F. Lioni, L. Chioresu, and A. Sulpice, *J. Magn. Magn. Mater.* **200**, 167, (1999).
- [110] J.A.A.J. Perenboom, J.S. Brooks, S. Hill, T. Hathaway, and N.S. Dalal, *Phys. Rev. B* **58**, 330, (1998).
- [111] L. Gunther, in *Quantum Tunneling of the Magnetization*, Edited by L. Gunther and B. Barbara, NATO ASI, Series E **301**, (Kluwer, Dordrecht, 1995).
- [112] F. Lioni, L. Thomas, R. Ballou, B. Barbara, A. Sulpice, R. Sessoli, and D. Gatteschi, *J. Appl. Phys.* **81**, 4608, (1997).
- [113] A. Cornia, M. Affronte, A.G.M. Jansen, D. Gatteschi, A. Caneschi, and R. Sessoli, *Chem. Phys. Lett.* **322**, 477, (2000).
- [114] Y. Furukawa, K. Watanabe, K. Kumagai, F. Borsa, and D. Gatteschi, *Phys. Rev. B* **64**, 10440, (2001).
- [115] T. Kubo, T. Goto, T. Koshiya, K. Takeda, and K. Awaga, *Phys. Rev. B* **65**, 224425, (2002).
- [116] A. Lascialfari, D. Gatteschi, F. Borsa, A. Shastri, Z.H. Jang, and P. Carretta, *Phys. Rev. B* **57**, 514, (1998).
- [117] N. Domingo, B.E. Williamson, J. Gómez-Segura, Ph. Gerbier, D. Ruiz-Molina, D.B. Amabilino, J. Veciana, and J. Tejada, *Phys. Rev. B* **69**, 052405, (2004).
- [118] M. Dressel, and G. Grüner, in *Electrodynamics of Solids*, (Cambridge University Press, 2002).
- [119] H.W. Katz, in *Solid State Magnetic and Dielectric Devices*, (John Wiley & Sons, INC., 1959).
- [120] B. Lax, and K.J. Button, in *Microwave Ferrites and Ferrimagnets*, (McGraw-Hill, New York, 1962).
- [121] J.F. Nye, in *Physical Properties of Crystals*, (Clarendon Press, Oxford, 1985).
- [122] D. Polder, *Phil. Mag.* **40**, 99, (1949).
- [123] A.V. Solokov, in *Optical Properties of Metals*, edited by O.S. Heavens, (Blackie and Son Limited, 1967).
- [124] D.M. Pozar, in *Microwave Engineering*, (John Wiley & Sons, Inc., 1998).
- [125] E. Zavoisky, *J. Phys. USSR* **9**, 211, (1945).
- [126] J.H.E. Griffiths, *Nature* **158**, 670, (1946).
- [127] B. Bleaney, and R.P. Penrose, *Nature* **157**, 339, (1946).

- [128] S. Hill, J.A.A.J. Perenboom, N.S. Dalal, T. Hathaway, T. Stalcup, and J.S. Brooks, *Phys. Rev. Lett.* **11**, 80, 11, (1998).
- [129] J. Krzystek, L. A. Pardi, L.C. Brunel, D.P. Goldberg, B.M. Hoffman, S. Licoccia, and J. Telser, *Spectrochimica Acta A* **58**, 1113, (2002).
- [130] J.A.A.J Perenboom, S.A.J. Wieggers, P.C.M. Christianen, U. Zeitler, and J.C. Maan, *J. Low Temp. Phys.* **133**, 181, (2003).
- [131] R.R. Joyce, and P.L. Richards, *Phys. Rev.* **179**, 375, (1969).
- [132] A.A. Mukhin, V.D. Travkin, A.K. Zvezdin, S.P. Lebedev, A. Caneschi, and D. Gatteschi, *Euro. Phys. Lett.* **44**, 778, (1998).
- [133] S. Vongtragool, B. Gorshunov, M. Dressel, J. Krzystek, D.M. Eichhorn, and J. Telser, *Inorg. Chem.* **42**, 1778, (2003).
- [134] J. van Slageren, S. Vongtragool, B. Gorshunov, A.A. Mukhin, N. Karl, J. Krzystek, J. Telser, A. Müller, C. Sangregorio, D. Gatteschi, and M. Dressel, *Phys. Chem. Chem. Phys.* **5**, 3837, (2003).
- [135] J. van Slageren, S. Vongtragool, B. Gorshunov, A.A. Mukhin, and M. Dressel, *J. Magn. Magn. Mater.* **e765-e767**, 272, (2004).
- [136] S. Vongtragool, B. Gorshunov, A.A. Mukhin, J. van Slageren, M. Dressel, and A. Müller, *Phys. Chem. Chem. Phys.* **5**, 2778, (2003).
- [137] A.A. Volkov, Yu.G. Goncharov, G.V. Kozlov, S.P. Lebedev, and A.M. Prokhorov, *Infrared Phys.* **25**, 369, (1985).
- [138] G.V. Kozlov, and A.A. Volkov, in *Millimeter and Submillimeter Wave Spectroscopy of Solids*, Edited by G. Grüner, (Springer, Berlin, 1998).
- [139] S. Vongtragool, B. Gorshunov, A.A. Mukhin, J. van Slageren, M. Dressel, and A. Müller, *electronic supplementary information of Phys. Chem. Chem. Phys.* **5**, 2778, (2003).
- [140] A.B. Sushkov, B.R. Jones, J.L. Musfeldt, Y.J. Wang, R.M. Achey, and N.S. Dalal, *Phys. Rev. B* **63**, 214408, (2001).
- [141] Y. Zhong, M.P. Sarachik, J.R. Friedman, R.A. Robinson, T.M. Kelly, H. Nakotte, A.C. Christianson, F. Trouw, S.M.J. Aubin, and D.N. Hendrikson, *J. Appl. Phys.* **85**, 8, 5636, (1999).
- [142] S. Hill, S. Maccagnano, K. Park, R.M. Achey, J.M. North, and N.S. Dalal, *Phys. Rev. B* **65**, 224410, (2002).
- [143] K. Park, M.A. Novotny, N.S. Dalal, S. Hill, and P.A. Rikvold, *Phys. Rev. B* **66**, 144409, (2002).



- [144] B. Parks, J. Loomis, E. Rumberger, E. Yang, D.N. Hendrickson, and G. Christou, *J. App. Phys.* **91**, 7170, (2002).
- [145] K. Park, M.A. Novotny, N.S. Dalal, S. Hill, and P.A. Rikvold, *Phys. Rev. B* **65**, 014426, (2001).
- [146] W. Wernsdorfer, T. Ohm, C. Sangregorio, R. Sessoli, D. Mailly, and C. Paulsen, *Phys. Rev. Lett.* **82**, 3903, (1999).
- [147] I. Tupitsyn and B. Barbara, in *Magnetism: Molecules to Materials III*, Edited by J.S. Miller, and M. Drillon, (Wiley-VCH, Weinheim, 2002).
- [148] K. Park, M.A. Novotny, N.S. Dalal, and P.A. Rikvold, *J. Appl. Phys.* **91**, 7167, (2002).
- [149] J.C. Slater, in *Quantum Theory of Matter*, (McGraw-Hill, 1968).
- [150] B. Barbara, L. Thomas, F. Lioni, I. Chiorescu, and A. Sulpice, *J. Magn. Magn. Mater.* **177-181**, 1324, (1998).
- [151] R. Amigó, J.M. Hernandez, A. García-Santiago, and J. Tejada, *Phys. Rev. B* **67**, 220402(R), (2003).
- [152] C. Park, *J. Korean Phys. Soc.* **43**, 5, 778, (2003).
- [153] H.A. De Raedt, A.H. Hams, V.V. Dobrovitski, M. Al-Saqr, M.I. Katsnelson, and B.N. Harmon, *J. App. Phys.* **91**, 7152, (2002).
- [154] Y. Zhong, M.P. Sarachik, J. Yoo, and D.N. Hendrickson, *Phys. Rev. B* **62**, 9256(R), (2000).
- [155] S. Miyashita, K. Saito, and H. Kobayashi, *Progress of Theoretical Physics* **109**, 5, 741, (2003).
- [156] E.M. Chudnovsky, and D.A. Garanin, *Phys. Rev. Lett.* **79**, 4469, (1997).



## Curriculum vitae

- April 9, 1977      Born in Lampang, Thailand.
- 1992-1995      BeddingField High School, Wilson, NC,  
USA.
- 1995-1999      BSc(Hons), Chiang Mai University,  
Chiang Mai, Thailand.
- 1999-2001      MSc, Nuclear Solid State Physics,  
  
University of Groningen,  
Groningen, The Netherlands.
- Title: *The Application of Rutherford Backscattering  
Spectrometry for Thin Film Analysis.*
- Supervisor: Prof. Dr. Dirk Boerma.
- 2001-2004      PhD student, 1. Physikalisches Institut,  
Universität Stuttgart,  
Stuttgart, Germany.
- Title: *Frequency-Domain Magnetic Resonance  
Spectroscopy on the Mn<sub>12</sub>-acetate Single Molecule  
Magnet.*
- Supervisor: Prof. Dr. Martin Dressel,  
Dr. Joris van Slageren.



# List of Publications

1. S. Grachev, D.M. Borsa, S. Vongtragool, and D.O. Boerma,  
”*The Growth of Epitaxial Iron Nitrides by Gas Flow Assisted MBE*”,  
Surface Science **482-485**, 802-808, (2001).
2. A.D. Rata, S. Vongtragool, D.O. Boerma, and T. Hibma,  
”*Stoichiometry Determination of VO<sub>x</sub> Thin Films by 18O-RBS Spectrometry*”,  
Thin Solid Films **400**, 120-124, (2001).
3. M. Dressel, B. Gorshunov, K. Rajagopal, S. Vongtragool, and A.A. Mukhin ,  
”*Quantum Tunneling and Relaxation in Mn12-Acetate Studied by  
Magnetic Spectroscopy*”,  
Phys. Rev. B **67**(R), 060405, (2003).
4. S. Vongtragool, B. Gorshunov, M. Dressel, J. Krzystek, D.M. Eichhorn, and  
J. Telsler,  
”*Direct Observation of Fine Structure Transitions in a Paramagnetic Nickel(II)  
Complex Using Far-Infrared Magnetic Spectroscopy*”,  
Inorg. Chem. **42**, 1778-1790, (2003).
5. S. Vongtragool, B. Gorshunov, A.A. Mukhin, J. van Slageren, M. Dressel, and

A. Müller,

"*High-Frequency Magnetic Spectroscopy on Molecular Magnetic Cluster V15*",

Phys. Chem. Chem. Phys. **5**, 2778-2782, (2003).

6. J. van Slageren, S. Vongtragool, B. Gorshunov, A.A. Mukhin, N. Karl,

J. Krzystek, J. Telsler, A. Müller, C. Sangregorio, D. Gatteschi, and M. Dressel,

"*Frequency-Domain Magnetic Resonance Spectroscopy of Molecular Magnetic Materials*",

Phys. Chem. Chem. Phys. **5**, 3837-3843, (2003).

7. S. Vongtragool, A. Mukhin, B. Gorshunov, and M. Dressel,

"*Asymmetric Lineshape due to Inhomogeneous Broadening of the Crystal-Field Transitions in Mn12-acetate Single Crystals*",

Phys. Rev. B **69**, 104410, (2004).

8. J. van Slageren, S. Vongtragool, B. Gorshunov, A.A. Mukhin, and M. Dressel,

"*Frequency-Domain Magnetic Resonance Spectroscopy*",

J. Magn. Magn. Mater. **272-276**, e765-e767, (2004).

9. S. Vongtragool, B. Gorshunov, J. van Slageren, M. Dressel, and A.A. Mukhin,

"*Lineshape of Magneto-dipole Transitions and Magnetization Relaxation in Mn12ac*",

J. Magn. Magn. Mater. **272-276**, e769-e770, (2004).

# Acknowledgements

I would like to thank the Graduate College of the Magnetic Resonance, Universität Stuttgart for their educational and financial support during this project.

I would also like to thank my project advisor, Prof. Dr. Martin Dressel, for all his encouragement and support, as well as for ensuring good team work amongst his team of PhD students which helped me greatly in achieving the completion of this project.

I am very grateful to Dr. Boris Gorshunov for all the assistance throughout my project in performance of experiments. His ability as an experimentalist is exceptional, and his hard working attitude have encouraged me all the way from the beginning to the completion of the project. I would like to thank for his friendship, kindness, and for his great sense of humor. Working with him was a great pleasure.

I want to thank Dr. Alexander Mukhin for his help in allowing me to extend my understanding of theoretical physics. His insight into problems involving complicated calculations was invaluable. I greatly appreciate his patience, generosity, and all the time he took to help me to go through all the difficult theoretical problems during the analysis part of this project.

I express my thanks to my thesis advisor, Dr. Joris van Slageren for his scientific insight, which helped me to explore the world of molecular chemistry, and for his highly-developed problem-solving skills. I am also grateful to have been working with Nadescha Kirchner, and Dr. Marc Duran.

Special thanks to the technical support from the crystal laboratory of Prof. Dr. N. Karl for the provision of the large  $Mn_{12}$ -acetate single crystals, and Gabriele Untereiner for ensuring the perfect alignment of these crystals.

I would like to thank all of my colleagues at Prof. Dressel's group, in particular, Phillip Haas, Pedro Zornoza, Belah Salameh, Adriana Matei, Alexej Pashkin, Komalavalli Thirunavukkuarasu, Natalia Drichko, Matthias Fischer, Toby Brandt, Simone Frank, Tobias Müller, Valdeci Mariano, Yue Song, Marc Scheffler, Daniel Faltermeier, Kurt La $\beta$ mann, Christine Kuntscher, Michael Dumm, and Wolfgang Eisenmenger, for their friendship and assistance.

I would like to thank my parents, Anek and Hataikan Vongtragool, and my sister, Sirin Artinian, for all their love and caring. Lots of thanks to Andre Kroupnik for being so supportive during my work on this project.